2008-12-02

Multidimensional Modeling of Solid Propellant Burning Rates and Aluminum Agglomeration and One-Dimensional Modeling of RDX/GAP and AP/HTPB

Matthew Wilder Tanner
Brigham Young University - Provo

BYU ScholarsArchive Citation
Tanner, Matthew Wilder, "Multidimensional Modeling of Solid Propellant Burning Rates and Aluminum Agglomeration and One-Dimensional Modeling of RDX/GAP and AP/HTPB" (2008). *All Theses and Dissertations*. 1643.
https://scholarsarchive.byu.edu/etd/1643

MULTIDIMENSIONAL MODELING OF SOLID PROPELLANT BURNING RATES AND ALUMINUM AGGLOMERATION AND ONE-DIMENSIONAL MODELING OF RDX/GAP AND AP/HTPB

by

Matthew W. Tanner

A dissertation submitted to the faculty of
Brigham Young University
in partial fulfillment of the requirements for the degree of

Doctor of Philosophy

Department of Chemical Engineering
Brigham Young University
December 2008

BRIGHAM YOUNG UNIVERSITY

GRADUATE COMMITTEE APPROVAL

of a dissertation submitted by

Matthew W. Tanner

This dissertation has been read by each member of the following graduate committee and by majority vote has been found to be satisfactory.

Date	Merrill W. Beckstead, Chair
Date	Thomas H. Fletcher
Date	Larry L. Baxter
Date	William C. Hecker
Date	Dean R. Wheeler

BRIGHAM YOUNG UNIVERSITY

As chair of the candidate's graduate committee, I have read the dissertation of Matthew W. Tanner in its final form and have found that (1) its format, citations, and bibliographical style are consistent and acceptable and fulfill university and department style requirements; (2) its illustrative materials including figures, tables, and charts are in place; and (3) the final manuscript is satisfactory to the graduate committee and is ready for submission to the university library.

Date	Merrill W. Beckstead Chair, Graduate Committee

Accepted for the Department

Larry L. Baxter
Graduate Coordinator

Accepted for the College

Alan R. Parkinson
Dean, Ira A. Fulton College of Engineering and Technology

ABSTRACT

MULTIDIMENSIONAL MODELING OF SOLID PROPELLANT BURNING RATES AND ALUMINUM AGGLOMERATION AND ONE-DIMENSIONAL MODELING OF RDX/GAP AND AP/HTPB

Matthew W. Tanner

Department of Chemical Engineering

Doctor of Philosophy

This document details original numerical studies performed by the author pertaining to solid propellant combustion. Detailed kinetic mechanisms have been utilized to model the combustion of the pseudo-propellants RDX/GAP and AP/HTPB. A particle packing model and a diffusion flame model have been utilized to develop a burning rate and an aluminum agglomeration model.

The numerical model for RDX/GAP combustion utilizes a “universal” gas-phase kinetic mechanism previously applied to combustion models of several monopropellants and pseudo-propellants. The kinetic mechanism consists of 83 species and 530 reactions. Numerical results using this mechanism provide excellent agreement with RDX and GAP burning rate data, and agree qualitatively with RDX/GAP pseudo-propellant data.

The numerical model for AP/HTPB combustion utilizes the same universal mechanism, with chlorine reactions added for modeling AP combustion. Including chlorine, there are 106 species and 611 reactions. Global condensed-phase reactions have been developed for six AP percentages between 59% and 80% AP. The AP/HTPB model accurately predicts burning rates, as well as temperature and species profiles.

The numerical burning rate model utilizes a three-dimensional particle-packing model to generate cylindrical particle packs. Particle-size distributions have been modeled using a three-parameter lognormal distribution function. Pressure-dependent homogenization has been used to capture pressure effects and reduce cpu time. A "characteristic" burning path is found through each particle pack. Numerical results showed that different path-finding approaches work better depending on the propellant formulation and combustion conditions. Proposed future work and modifications to the present model are suggested.

The numerical agglomeration model utilizes the same particle packing model and particle-size distribution function as in the burning rate model. Three preliminary models have been developed examining the ideas of pockets, separation distance, and aluminum ignition. Preliminary model results indicate the importance of predicting aluminum particle ignition. In the final model, the surface is regressed numerically through each particle pack. At each surface location, calculations are performed to determine whether aluminum particles combine and/or ignite. Ignition criteria have been developed from the results of the diffusion flame model and an analysis of particle-pack cross-sections. Numerical results show qualitative agreement with each experimentally observed trend. Proposed future work and modifications to the present model are suggested.

ACKNOWLEDGMENTS

I would like to thank the faculty and staff in the Chemical Engineering Department for their guidance during my years at BYU. They were always willing to help whenever I had questions or concerns. I would especially like to thank my advisor, Dr. Merrill Beckstead for his invaluable guidance and counsel. He has shown great patience and vision during my time as a graduate student. He has also been a great friend.

I am grateful to those students who have gone before me and whose research I have continued. I would like to thank my fellow students for the time and association we have had together. Matt Gross, Karthik Puduppakkam, Ephraim Washburn, Dan Smyth, Scott Felt, and many others have greatly contributed to my work.

I am very blessed to have a wonderful family and great friends. I am grateful to my parents and siblings for their love and support, especially to my mom, for all the sacrifices she has made to benefit me. I am also grateful for the support of my brothers, Mark and Hyrum, who were my roommates for a few years. I would also like to thank Bryon Poulter, Nate Pusey, Eric Robinson, Dan Francom, Mike Zarbock, and Fabio Gaertner. I would especially like to thank Clyde and Jana Shepherd for allowing me to stay with them during my final months at graduate school. Lastly, I am grateful to my Heavenly Father and His Son Jesus Christ for the many blessings they have bestowed upon me. They have shaped and guided my life more than I can comprehend.

TABLE OF CONTENTS

LIST OF TABLES

LIST OF FIGURES

NOMENCLATURE

A	pseudo-binder area	[μm^2]
b	parameter in burning rate – flame temperature correlation	
D	particle diameter	[μm]
D_{cut}	agglomerate cutoff diameter	[μm]
E	activation energy	[cal/mole]
f	mass fraction	
F	correction factor in pseudo-binder area calculation	
H	horizontal separation distance	[μm]
H_p	pack height	[μm]
k	reaction rate constant	[1/sec]
L	length	[μm]
m	lognormal scale parameter	
n	pressure exponent	
N	number	
P	pressure	[atm]
r	burning rate	[cm/sec]
r_p	particle radius	[μm]
R	universal gas constant	[cal/mole/K]

S	separation distance	[μm]
t	burning time	[sec]
t_{ign}	ignition delay time	[sec]
T	temperature	[K]
T_b	binder thickness	[μm]

Greek

θ	lognormal location parameter
σ	lognormal shape parameter

Subscript

agg	agglomerate
b	binder
f	flame
h	homogenization cutoff
i	index
j	index
m	mean
n	nominal
o	oxidizer
v	vapor

GLOSSARY

ADN – Ammonium dinitramide, an oxidizer

AMMO – 3-azidomethyl-3-methyl oxetane, an energetic polymer/binder

AN – Ammonium nitrate, an oxidizer

AP – Ammonium perchlorate, an oxidizer

BAMO – Bis(azidomethyl) oxetane, an energetic polymer/binder

Binder – Energetic or non-energetic material used to hold crystalline oxidizer together

BTTN – 1,2,4-butane triol trinitrate, an energetic plasticizer

CL-20 – 2,4,6,8,10,12-hexanitrohexaazaisowurtzitane, an oxidizer

Composite Propellant – Propellant containing a mixture of both oxidizer and binder

CTPB – Carboxy-terminated polybutadiene, a binder

Dark Zone – Spatial region before luminous portion of the flame with relatively constant temperature, attributed to slow nitrogen chemistry

Diffusion Flame – Flame in which fuel and oxidizer must diffuse together for combustion to proceed (i.e. candles)

GAP – Glycidyl azide polymer, an energetic polymer/binder

HMDI – Hexamethylene diisocyanate, a curative

HMX – Cyclotetramethylenetetranitramine, an oxidizer

HNF – Hydrazinium nitroformate, an oxidizer

HTO – Propellant crosslinking agent

HTPB – Hydroxy-terminated polybutadiene, a binder

I_{sp} – Specific impulse (sec), impulse per unit weight

Monopropellant – A single, unmixed ingredient

NG – Nitroglycerin

NMMO – 3-nitratomethyl-3-methyloxetane, an energetic polymer/binder

ONERA – Office National d'Etudes et Recherches Aérospatiales

PBAN – Polybutadiene-acrylic acid acrylonitrile, a binder

PETN – Pentaerythritol tetranitrate, an oxidizer

PHASE3 – Numerical monopropellant and pseudo-propellant combustion code

Premixed Flame – Flame in which fuel and oxidizer are intimately mixed before combustion occurs (i.e. gas ranges and Bunsen burners)

Pseudo-Binder – A homogeneous mixture of binder and very small oxidizer particles that burns with a premixed flame

Pseudo-Propellant – A propellant containing binder and very small oxidizer particles, forming a homogeneous mixture that burn with a premixed flame

PU – Polyurethane, a binder

RDX – Cyclotrimethylenetrinitramine, an oxidizer

SEM – Scanning electron microscope

SST – Separate surface temperature

TAGN – Triaminoguanidine nitrate, an oxidizer

TMETN – Trimethylolethane trinitrate, an energetic plasticizer

TMP – Trimethylol propane, a crosslinking agent

UIUC – University of Illinois at Urbana-Champaign

1 Introduction

Solid propellants are used in many applications, including the space shuttle boosters, missiles, ejector seats, ammunition, and air bags. Each application requires a propellant with a unique composition and combustion properties. A fundamental understanding of solid propellant composition and combustion is necessary for the design engineers who formulate propellants for these and other applications.

1.1 Solid Propellant Composition

Solid propellants consist of one or more particulate ingredients embedded in a binder. Common particulate ingredients include AP, HMX, RDX and aluminum. Common binders include inert (non-energetic), rubber-like binders such as HTPB and PBAN, and energetic binders such as NG and GAP. Pure ingredients are termed monopropellants, homogeneous mixtures of very fine particles in a binder are termed pseudo-propellants, and heterogeneous mixtures of medium-sized and coarse particles in a binder are termed propellants. A typical propellant might contain 30- and 200-micron AP particles in an HTPB binder with an 88/12 AP/HTPB mass ratio. AP propellants typically contain inert binders while non-AP propellants contain energetic binders.

Each of the 30- and 200-micron powders mentioned above actually consists of a broad distribution of particle sizes around an average, or nominal size. Figure 1-1 shows a possible 200-micron distribution. Nominal sizes are also called modes and propellants are characterized as monomodal, bimodal, trimodal or multimodal.

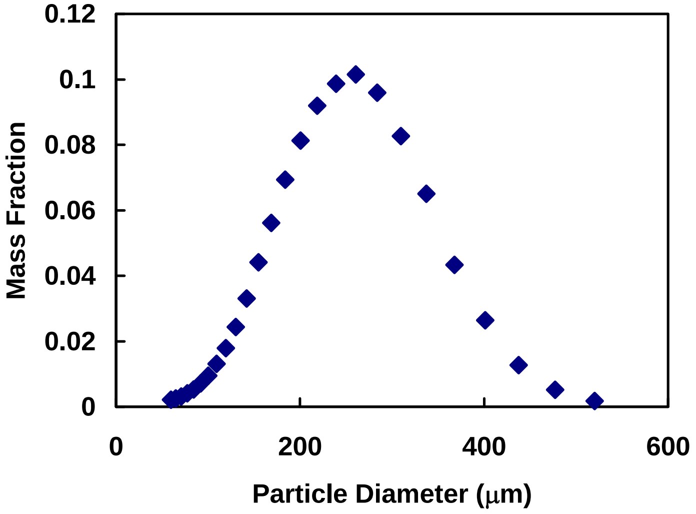

Figure 1-1: 200 μm particle-size distribution.[1]

1.2 Burning Rate

Solid propellants are chosen for specific applications based partly on their combustion properties, the most important of which is usually the surface regression rate, or burning rate. Propellant burning rates determine the rate of gas generation, which determines the pressure inside the motor and the overall thrust. Burning rates are obtained experimentally by burning small propellant strands and measuring the surface regression versus time. The burning rate is affected by changes in composition (ingredients, mass fractions and particle-size distributions) and conditions (pressure and initial temperature). Experimentalists and modelers vary these factors to determine their influence on burning rate as well as other properties and to find the best composition for a given application.

AP is the most common propellant ingredient and has been used for decades. Its popularity is mainly due to its ability to determine a propellant's burning rate. By varying the AP particle-size distribution it is possible to achieve vastly different overall propellant burning rates.

1.3 Aluminum

Aluminum is commonly added to solid propellants to increase specific impulse in rocket motors. As a metal, aluminum is a unique propellant ingredient. Unlike other ingredients, aluminum particles escape the propellant surface unburned or partially burned. Aluminum combustion occurs mostly away from the propellant surface, in the flow field of the motor.

Two common problems with aluminum are incomplete combustion (when partially burned particles exit the motor) and the related problem of slag formation (when particles impinge and collect on the motor wall). These problems are very closely related to the aluminum particle-size distribution in the motor, which in turn is closely related to the size distribution escaping the propellant surface. The main process affecting aluminum particle sizes at the propellant surface is agglomeration, the process through which aluminum particles combine and form agglomerates, which are much larger than the original aluminum particles. The process of aluminum agglomeration occurs only on the propellant surface and ends when the particles lift off the surface and enter the gas phase. The extent of aluminum agglomeration is an important combustion property of solid propellants. The process of agglomeration is affected by changes in propellant composition and combustion conditions. It is measured experimentally and calculated numerically to provide boundary conditions for calculating aluminum particle-size distributions inside motors.

1.4 Numerical Modeling

AP propellant combustion has been studied extensively both experimentally and theoretically in an attempt to understand its unique properties. The most widely accepted theoretical picture was developed in 1970 by Beckstead, Derr, and Price, and is known as the BDP Model.[2,3] Figure 1-2 shows the BDP physical picture. This picture looks at the micro-scale above an AP particle. It proposes that the combustion region above an AP particle and the corresponding binder is composed of three distinct flames: a primary diffusion flame, a premixed monopropellant flame, and a final diffusion flame. The impact of these flames varies with particle size and pressure. A numerical model was also developed based on the BDP flame structure and was successful in accurately predicting many of the unique properties of AP propellants.

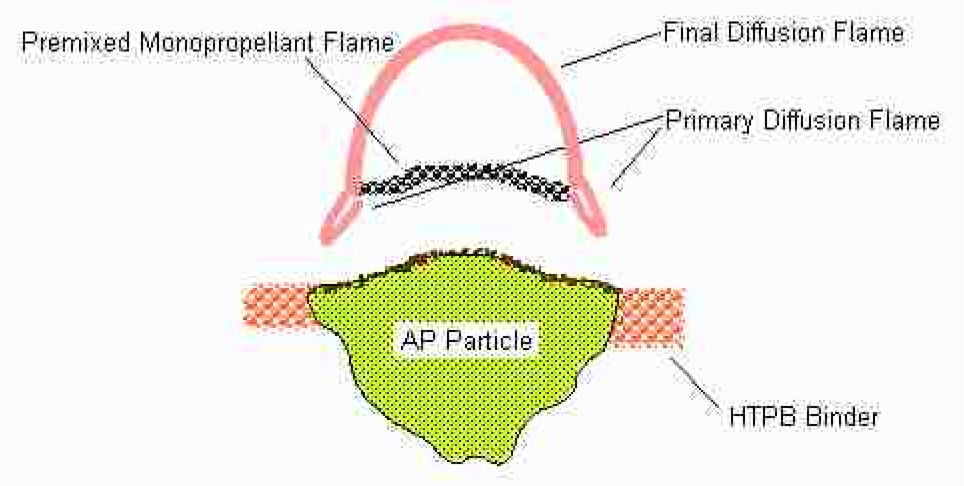

Figure 1-2: BDP flame structure above a burning AP particle and surrounding HTPB binder.[2]

Application of the BDP model to non-AP propellants was relatively unsuccessful, leading to the assumption that diffusion flames are only significant when AP is present and that premixed flames are sufficient for modeling propellants without AP. Models that have used this approach for non-AP propellants have been more successful than those that incorporate the full BDP flame structure. In 1981, Beckstead developed the SST model,[4] which treated the oxidizer and binder as though they burned separately in series, with no diffusion flame interactions. This model worked well for non-AP propellants.

The BDP model was relatively simplistic due to computer technology in 1970. It was one-dimensional and employed simple global kinetics. It also made calculations for only one statistically averaged particle size. To investigate AP propellant flame structure in more detail, a two-dimensional combustion model using detailed gas-phase kinetics has recently been developed by Felt[5,6] and later improved by Gross.[7] Felt's model was the first attempt to apply a detailed gas-phase kinetic mechanism to capture the flame structure of an AP propellant, eliminating many assumptions used in previous models. Calculations appeared to support the BDP concept and provided an even clearer understanding of AP propellant flames. However, this model is very cpu intensive, makes calculations for only one particle and one pressure at a time, and does not capture the complexity of an entire propellant matrix, which includes millions of particles with varying size distributions.

Several recent modeling efforts have focused on two- and three-dimensional particle packs with a more detailed focus on the geometric distribution of the solid phase.[8,9,10,11,12,13] These models typically take large amounts of cpu time to generate a particle pack, and to solve the corresponding conservation equations describing the combustion process. To compensate for the long cpu times, the models employ simplified global kinetics to describe the gas-phase heat release. These models have shown limited agreement with some experimental results.[12] The poor agreement is possibly due to the lack of detail in the kinetic mechanism.

There is a great need for numerical models of solid propellant combustion that incorporate detail in both the solid-phase geometry and the gas-phase reaction mechanism. Past models have been limited by assumptions or simplifications, due in part to computer technology. The most complex models today employ greater detail in either the solid-phase geometry or in the gas-phase kinetics, but not in both. These models do not capture all of the multi-dimensional interactions between ingredients, whether in the morphology of the propellant mixture or in the flame structure during combustion. Therefore, current efforts involve modeling both the solid-phase geometry and gas-phase flame structure in multiple dimensions and using detailed chemical kinetics in the gas phase.

1.5 Project Objectives

The first goal of this study has been to develop a solid propellant burning rate model that improves upon past efforts by incorporating a detailed three-dimensional solid-phase model, PARPACK,[14] and one-dimensional RDX, GAP, and RDX/GAP combustion models that incorporate detailed gas-phase kinetics. These one-dimensional models were developed using PHASE3,[15] a numerical code developed at BYU for calculating premixed combustion properties of monopropellants or pseudo-propellants. The burning rates of AP propellants have not been modeled, due to contractual constraints, but may eventually be included as an extension to the current work. The burning rate model has been designed for RDX/GAP, which is considered to be a typical non-AP propellant.

The second goal of this study has been to develop an aluminum agglomeration model that incorporates detail in the solid phase with PARPACK and in the gas phase with Felt's two-dimensional diffusion flame model, thus capturing the multi-dimensional aspects of propellant mixing and combustion. The agglomeration model is specifically designed for AP propellants, which are typically mixed with aluminum. To enable the development of the agglomeration model, one-dimensional, detailed gas-phase kinetic mechanisms for AP and AP/HTPB combustion have also been developed in this study to calculate burning rates as needed and to provide condensed-phase boundary conditions to Felt's model.

This study was split into four tasks, with the first two being preliminary steps that were required in order to achieve the final two tasks.

- Update a one-dimensional RDX/GAP pseudo-propellant combustion model, using PHASE3, by extending the range of compositions modeled and by further developing the kinetic mechanisms.
- Update a one-dimensional AP/HTPB pseudo-propellant combustion model, using PHASE3, by extending the range of compositions modeled and by further developing the kinetic mechanisms.
- Develop a propellant burning rate model for RDX/GAP propellants.
- Develop an aluminum agglomeration model for AP/HTPB/Al propellants.

1.5.1 RDX/GAP Model

One-dimensional models had previously been developed at BYU for RDX,[15] GAP[16,17] and RDX/GAP[18] using PHASE3. However, the RDX/GAP model only worked over a range of compositions, from 60-100% RDX. In addition, a comprehensive gas-phase reaction mechanism[19] that works for most propellant ingredients has been under development at BYU for several years and had not yet been applied to these ingredients. Therefore, the objectives of this task were:

- Determine the cause of errors for compositions below 60% RDX and make necessary modifications to develop a working model over the entire range of compositions.
- Apply the comprehensive gas-phase mechanism to RDX/GAP using PHASE3.
- Validate the global condensed-phase mechanism for RDX/GAP in conjunction with the new gas-phase mechanism and make necessary modifications.
- Calculate RDX/GAP combustion properties at several compositions between 0% RDX/100% GAP and 100% RDX/0% GAP and at several pressures between 1 and 136 atm.

1.5.2 AP/HTPB Model

One-dimensional modeling of AP/HTPB[20] had been performed previously at BYU using PHASE3, but was very limited. The previous model worked correctly only from 80 to 100% AP. It failed to calculate the final species, final flame temperature, and burning rate at compositions below 80% AP. Due to these limitations, the objectives of this task were:

- Determine the cause of errors for compositions below 80% AP and make necessary changes to develop a working model.
- Apply the comprehensive gas-phase mechanism to AP/HTPB using PHASE3.
- Develop and validate condensed-phase mechanisms for compositions below 80% AP.
- Calculate the combustion properties of AP/HTPB at several compositions below 80% AP.

1.5.3 Propellant Burning Rate Model

The first main objective of the current study was to develop a robust solid propellant burning rate model for RDX/GAP, a typical non-AP propellant, which correctly calculates particle-size effects as well as other important effects. The details of the solid-phase geometry were modeled with PARPACK. One-dimensional models of RDX, GAP, and RDX/GAP were used to calculate monopropellant and pseudo-propellant burning rates as needed. The main steps taken to develop this model were:

- Determine the optimal diameter and height for the cylindrical packs generated by PARPACK in conjunction with the burning rate model.
- Develop an algorithm to find a characteristic, rate-determining path through a particle pack.

- Develop an algorithm to calculate the burning rate of the characteristic path.
- Validate the model by comparison to experimental RDX/GAP burning rate data.

1.5.4 Aluminum Agglomeration Model

The second main objective of the current study was to develop an aluminum agglomeration model for aluminized AP/HTPB propellants that correctly calculates particle-size effects as well as other important effects. The details of the solid phase were modeled with PARPACK. One-dimensional models of AP and AP/HTPB were used to calculate combustion characteristics as needed. The main steps taken to develop this model were:

- Determine the optimal diameter and height for the cylindrical packs generated by PARPACK in conjunction with the aluminum agglomeration model.
- Determine physical criteria for aluminum agglomeration to occur.
- Develop an algorithm for calculating agglomerate sizes resulting from a particle pack, based on the previously determined agglomeration criteria.
- Validate the model by comparison to experimental agglomerate size data.

1.6 Document Outline

Chapter 2 gives an overview of solid propellant combustion, including monopropellant, pseudo-propellant, and propellant combustion, with emphasis on burning rates and aluminum agglomeration. Chapter 3 outlines the work performed in updating the one-dimensional RDX/GAP pseudo-propellant combustion model, including the condensed- and gas-phase mechanism development and model validation, as well as results, conclusions, and recommendations. Chapter 4 outlines the work performed in updating the one-dimensional AP/HTPB pseudo-propellant combustion model, organized similarly to Chapter 3. Chapters 5 and 6 describe the development of a burning rate model for RDX/GAP propellants and an aluminum agglomeration model for AP propellants, respectively. A detailed description of the algorithms is included, as is the utilization of other models, and the results and conclusions. Chapter 7 gives an overall summary of the work performed, along with conclusions and recommendations.

2 Background

Solid propellant combustion can be divided into the following categories: monopropellant combustion, which involves individual ingredients burning separately; pseudo-propellant combustion, which involves propellants with sufficiently fine oxidizer particles that they are considered homogeneous and burn with a premixed flame; and propellant combustion, which involves propellants with multiple particle-size distributions, possibly including aluminum, that are considered heterogeneous and burn with more complex flame structures. Each of these types of propellant combustion is discussed in this section, beginning with relevant experimental and theoretical work on particle packing, burning rate, and aluminum agglomeration.

2.1 Particle Packing

Particle packing is a fundamental part of manufacturing propellants and is important in experimental and numerical studies of propellants. Particle sizes affect processing characteristics, combustion and mechanical properties. Propellant manufacturers must carefully manipulate particle sizes to make propellants for different applications. Propellant chemists must have a detailed knowledge of the particle-size distributions in the propellants they analyze in order to accurately measure particle-size effects. Numerical modelers must accurately describe the same distributions. The more detailed the description, the more accurate numerical predictions and experimental measurements of combustion or other properties can be.

One of the goals of studying propellant packing has been to maximize the propellant specific impulse (I_{sp}), which is proportional to the flame temperature. In the case of AP/HTPB propellants, the maximum I_{sp} is achieved at the stoichiometric ratio of ~90% AP by weight, which is equivalent to ~80% AP by volume. This high volume fraction cannot be achieved with monomodal packing. Bimodal or trimodal packing is required. Propellant packing not only affects the energy of a propellant, but also the burning rate, mechanical properties, combustion instability, aluminum agglomeration, etc. Therefore, it is very important to understand propellant packing.

2.1.1 Experimental Studies

In 1961, McGeary[21] studied packing using steel shot. He determined packing fractions (maximum volume fraction for a given composition) for several bimodal packs. He held the larger sphere diameter constant at 0.124 inches and varied the smaller diameter between 0.0065 and 0.036 inches. His results showed an increase in packing fraction with a decrease in the smaller diameter (or an increase in the size ratio). The highest packing fractions were obtained when the volume ratio of the larger size to the smaller size was 70/30.

Ideas derived from McGeary's work have helped to increase particle packing fractions in propellants, increasing the available energy. Many times, however, achieving specific burning rates or other properties is more important than maximizing the energy. Propellant chemists regularly vary particle sizes and volume ratios to achieve desired burning rates. Much of the relevant experimental work is discussed in the propellant combustion section of this review.

2.1.2 Numerical Studies

There are two main particle packing numerical models used in propellant modeling. These are PARPACK,[14] developed by Davis at ATK Thiokol, and Rocpack,[22] developed by Knott et al. at UIUC. Both models simulate packs of spheres which are placed randomly to represent the random mixing that occurs in propellant manufacturing. The binder is represented by the void space between particles. Both models are capable of simulating multimodal packs of thousands or even millions of spheres. The main differences are in the pack shape and the method of sphere placement.

PARPACK is a Monte Carlo particle packing computer code that simulates cylindrical, multi-modal packs of spherical particles. Figure 2-1 shows two views of a 1000-particle pack with particle diameters ranging from 100 to over 400 microns.

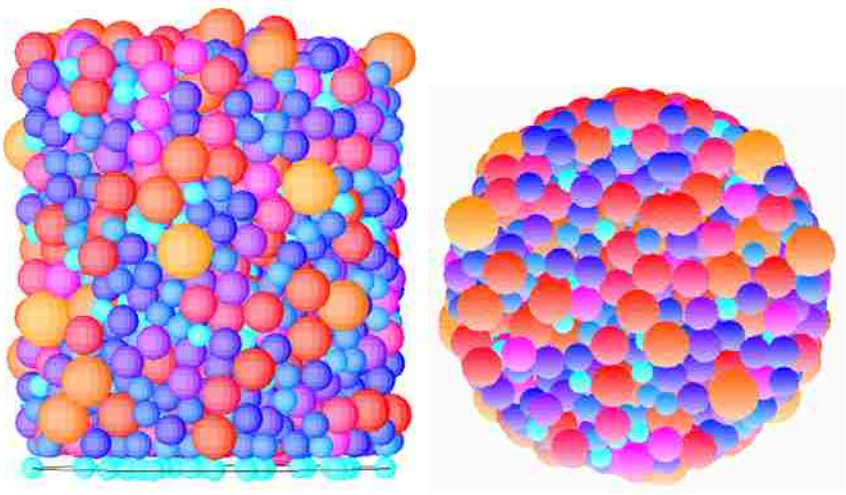

Figure 2-1: Side and top views of a cylindrical pack generated by PARPACK containing 1000 spheres.

User inputs include particle diameters, particle densities, particle-size mass fractions, pack diameter and a maximum number of particles or a maximum cylindrical pack height. Output includes the overall particle volume fraction, volume fractions of individual particle sizes, and the position, type and size of each particle. With PARPACK, particle packs are generated in two steps. First, a pack is generated with the highest possible volume fraction, or packing fraction, that can be achieved by PARPACK for the given formulation. The goal of the first step is to achieve a volume fraction that is higher than the volume fraction of particulate ingredients in the actual propellant being modeled. Second, the overall pack dimensions are expanded to increase the amount of void space, thus decreasing the volume fraction in order to match the actual propellant volume fraction. If the first step results in a volume fraction lower than that of the actual propellant, then PARPACK is incapable of simulating that propellant. PARPACK generates a pack by placing spheres one at a time into a cylinder. Each sphere's diameter is randomly selected from the diameters specified in the input file. The number of times a particular diameter is chosen is based on the specified size distribution. The radial and azimuth coordinates (r, θ) of each sphere are also selected randomly. The z-coordinate is given the lowest possible value that is within the limits of the cylinder and does not result in the overlapping of spheres. In this way, the pack is generated from the bottom up, as if the spheres were being dropped one at a time from random locations above the cylinder.

Rocpack simulates cubic packs. Figure 2-2 shows an angled view of a pack generated by Rocpack. The pack consists of 200-, 50-, and 20-micron distributions of particles. Instead of being dropped into the pack, seed particles are preplaced throughout the cube as random points. Each seed particle is assigned a random growth rate and velocity. It is then allowed to grow and move, colliding with and bouncing off of other particles while conserving momentum. The algorithm stops when a desired volume fraction is achieved or when the pack jams (particles can no longer move).[22] If the pack jams before achieving the desired volume fraction, then Rocpack is incapable of simulating that propellant. The six walls of the cube act as periodic boundary conditions, so a particle exiting through one wall will enter through the opposite wall.

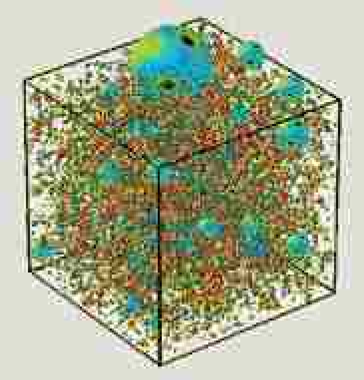

Figure 2-2: Angled view of a cubic pack generated by Rocpack.

Both PARPACK and Rocpack have been validated using McGeary's data and both were successful in matching experimental packing fractions to within ±1%.[14,22] PARPACK has previously been used to model propellant mechanical properties.[14] Rocpack is used to build packs for a combustion model at UIUC. Before these packing models were used, particle packing had been modeled much less extensively. Typically calculations were applied to one average-sized particle for each nominal size. This kind of approach is discussed in the propellant combustion section.

2.2 Monopropellant Combustion

Figure 2-3 shows the three regions or phases of a burning monopropellant. The solid and liquid phases are termed the condensed phases and the liquid phase is also commonly termed the melt layer. Decomposition, evaporation, and gaseous combustion reactions occur as shown. The burning rate is driven by the heat flux to the surface from the gas-phase flame and by the heat released from condensed-phase decomposition reactions.

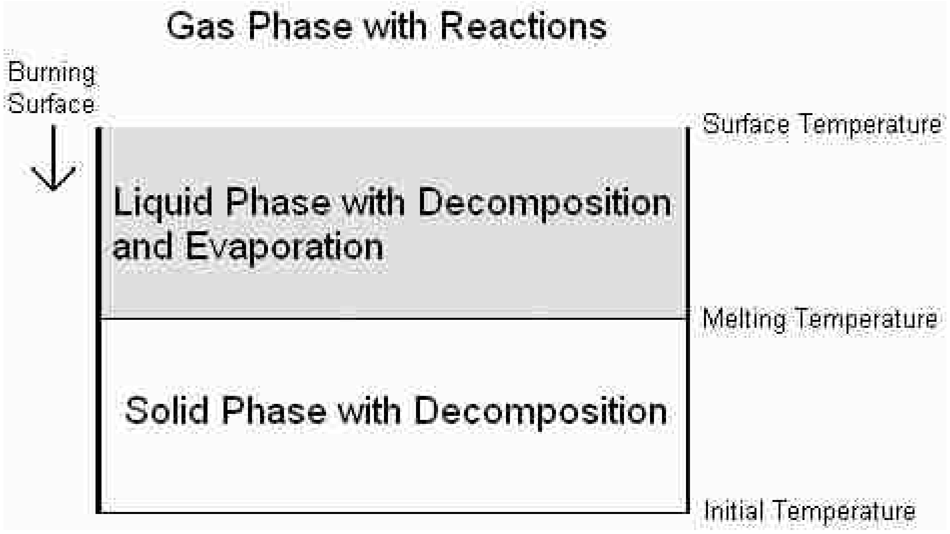

Figure 2-3: Three regions or phases of a burning monopropellant.

The effects of pressure and initial temperature can be understood by an analysis of monopropellant combustion. Figure 2-4 shows both of these effects. As pressure increases, the flame moves closer to the surface and an increase in heat flux to the surface causes an increase in burning rate (mass flux). Different ingredients with different burning rates have similar pressure exponents (slopes). If the initial temperature is increased, both the solid and the ambient gases have more initial energy, which increases the burning rate.

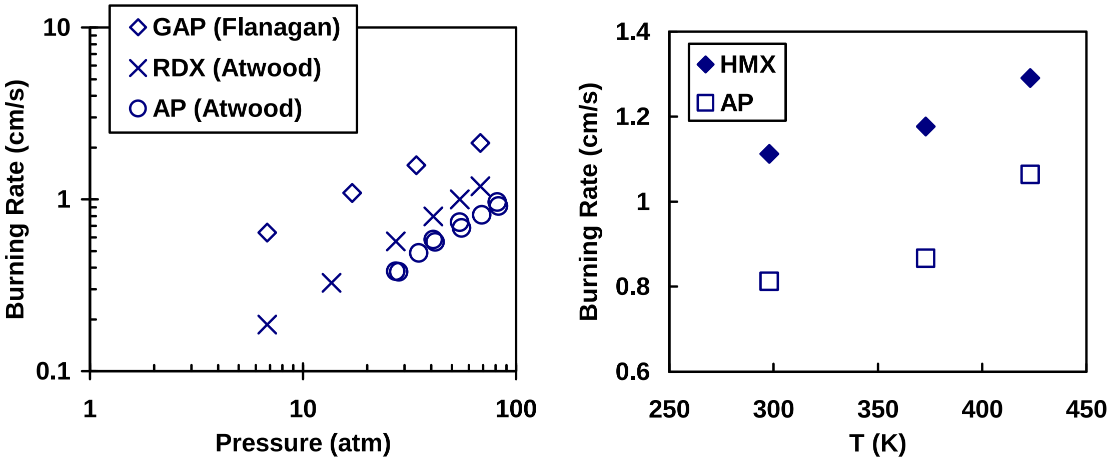

Figure 2-4: Effect of pressure (left) and initial temperature (right) on burning rate for GAP, RDX, AP, and HMX monopropellants.[23,24]

2.2.1 Experimental Studies

The combustion of several monopropellants has been studied experimentally to determine burning rates, surface temperatures, and surface species under different conditions. In 1999, Atwood[23] published burning rate data for common (AP, HMX, RDX) and advanced (CL-20, ADN, HNF) monopropellants. Her work has become a widely used resource for monopropellant burning rate data. Figure 2-5 shows some of Atwood’s data. Propellant samples were placed in a pressurized container that was cooled or heated to the desired temperature. Samples were small enough relative to the chamber size that pressure did not increase during combustion.

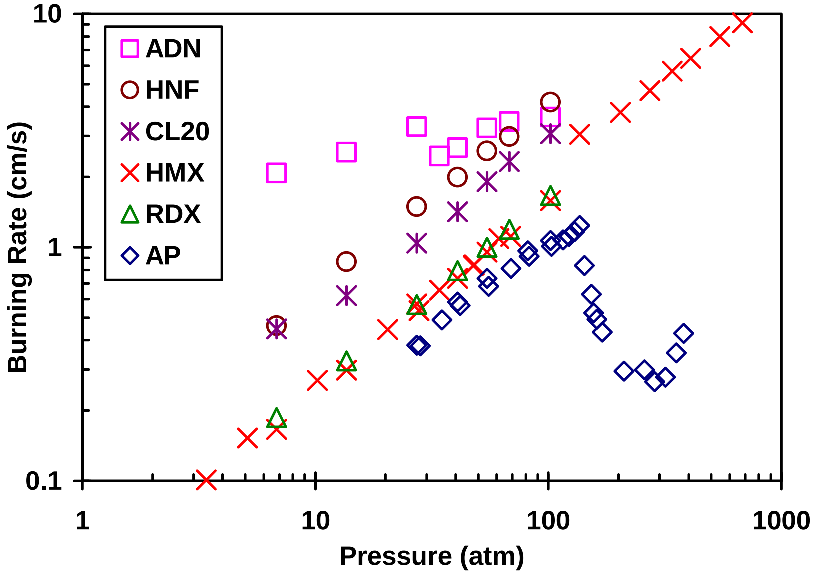

Figure 2-5: Atwood's monopropellant burning rate data.[23]

In the same year, Zenin published burning rate data for HMX.[25] He determined experimentally the heat transfer between the condensed and gas phases, the temperature profiles, and the burning rates. He varied pressure between 1 and 500 atm and initial temperatures between -170 and 100 °C. In 1977, Boggs published HMX burning rate data[26] as well as SEM pictures of the surface after quenching. He used both single HMX crystals and HMX pellets pressed from powder. He found a highly uneven HMX surface due to a bubbly melt layer.

Flanagan[24] and Kubota[27] both published burning rate data for GAP propellants and included GAP monopropellant data in their results. GAP is mixed with a curative (HMDI) and a crosslinking agent (HTO or TMP) to make it solid at room temperature. The burning rate depends on the amount of curative. Flanagan used a typical mixture, about 90% GAP, 9% HMDI, and 1% HTO. Kubota used 84.8% GAP, 12% HMDI and

3.2% TMP. Kubota's burning rates were lower because of the lower GAP and higher curative concentrations.

2.2.2 Numerical Studies

Many early monopropellant combustion models used global kinetic mechanisms for both the condensed and gas phases because of computer capabilities when they were developed. More recently, detailed gas-phase mechanisms have been used. This section focuses on these models.

From 1995 to 1997, Liau et al.,[28] Prasad et al.[29] and Davidson et al.[15] developed similar models for one-dimensional steady-state RDX combustion. Davidson's model, in generic form, is known as PHASE3, and is presented here.

PHASE3 treats RDX combustion as a three-phase system, including solid, liquid and gas phases (Figure 2-3). Combustion is driven by the heat flux to the surface from the gas-phase flame and the condensed-phase heat release. The ODE's describing the melt layer are integrated in space until the surface condition is met. The surface condition may be a user-specified surface temperature or surface void fraction. The surface location can also be calculated using an evaporation submodel. The gas phase is integrated by a modified version of PREMIX[30] in the burner-stabilized mode. The solution is reached when the energy balance at the melt-layer/gas-phase interface is satisfied. Mass flux (burning rate) is an eigenvalue of the solution.

The condensed-phase decomposition mechanism was taken from the literature and slightly modified.[15] It is semi-global with 3 reactions and 8 species. The melt layer description is the weakest part of the model because of the uncertainty of the mechanism and liquid properties. The gas-phase mechanism used is the Yetter RDX mechanism[29] with 45 species and 231 reactions. Figure 2-6 shows Davidson's calculated burning rates using these mechanisms in PHASE3. Agreement with experimental data is excellent.

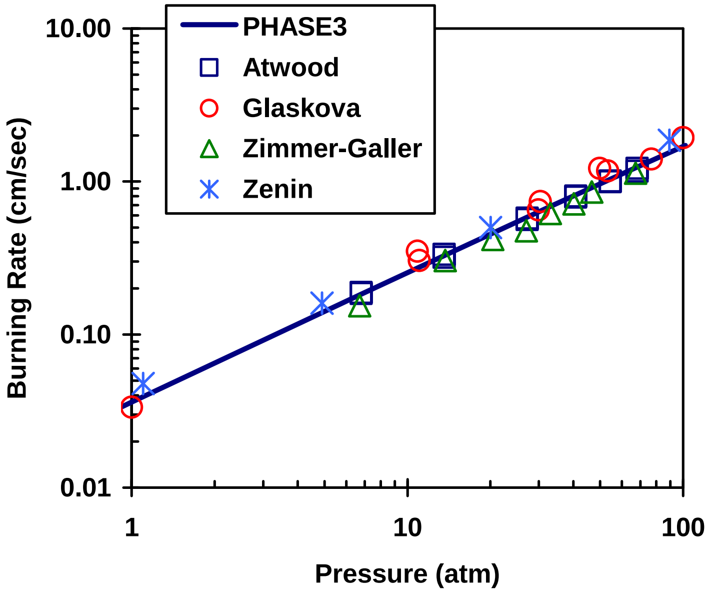

Figure 2-6: Davidson's RDX burning rate predictions compared with data.[23,31,32,33]

In 2000, Miller developed a similar model and applied it to RDX[34,35] and NG.[35] Miller's model is semi-empirical, matching experimental data for species coming off the surface. He justifies this by citing the uncertainty of the condensed-phase description.

Davidson's RDX model has since been adapted to model the combustion of HMX,[36] GAP,[16,17] AP,[37] NG,[19] BTTN,[38] and TMETN.[19] Liau's has been adapted for HMX[39,40] and ADN.[41] Prasad's has been adapted for HMX.[42] To be consistent, a general, all-inclusive gas-phase mechanism[19,43] has been developed at BYU by combining several mechanisms from the literature and removing repeated reactions. This mechanism has worked well for many ingredients. It includes 83 species and 534 reactions. Figure 2-7 shows calculated burning rates for several monopropellants and pseudo-propellants using this mechanism in conjunction with PHASE3.

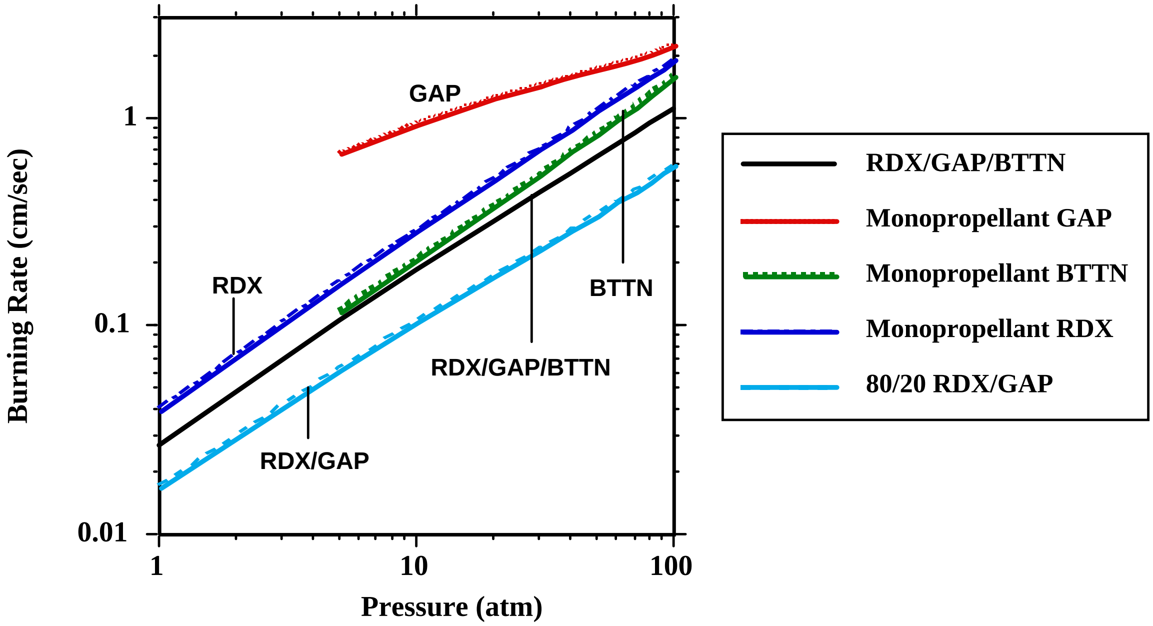

Figure 2-7: Burning rate calculations using the comprehensive gas-phase mechanism.[19]

2.2.3 Pseudo-Propellants

Davidson's and Liau's models have both been adapted to describe pseudo-propellants. Propellants can be considered pseudo-propellants when particles are smaller than ~10 microns, but this number varies with pressure. Davidson's model has been adapted to model AP/HTPB[20] and RDX/GAP[18] combustion because these are representative of AP propellants and non-AP propellants, respectively. RDX/GAP/BTTN[44] has been modeled as well. Liau's model has also been adapted for RDX/GAP[45] and HMX/GAP.[39]

2.2.4 Summary and Relevance

Davidson and others have developed tools for calculating combustion properties of monopropellants and pseudo-propellants. An understanding of monopropellant combustion provides a basis for understanding propellant combustion, since propellants are mixtures of several monopropellant ingredients. For the same reason, monopropellant combustion models can potentially be used in propellant combustion models if ingredient interactions are understood and handled correctly. Pseudo-propellant models can be used to predict ingredient interactions to a certain extent, specifically the interaction of the fine particle sizes with the binder. However, monopropellant models do not lend themselves to calculating all the multi-dimensional complexities of propellant combustion, including particle-size effects. More complex models are needed to capture these effects.

2.3 Non-Aluminized Propellant Combustion

The trends of monopropellant combustion occur in propellant combustion as well, but new complexities are introduced. Propellants are heterogeneous (particles surrounded by binder). There are multiple gas-phase flames instead of a single, premixed flame. The burning surface is uneven, with particles protruding or recessing depending on the pressure and ingredients. Heat feedback to the surface is a three-dimensional problem instead of one-dimensional. The thermal wave, or temperature profile, below the surface changes with time because of the different particle and binder thermal properties.

Figure 2-8 revisits the BDP physical picture, illustrating the flame structure of AP propellants. There are three flames above an AP particle surrounded by HTPB binder—the AP monopropellant flame, the primary diffusion flame, and the final diffusion flame.

If the binder is energetic, such as GAP, or if very fine AP particles are mixed with the inert binder, there is also a fourth flame, a binder premixed flame. Decomposition products from the AP particle and binder diffuse together and react in the primary diffusion flame. The products of the AP monopropellant flame react further with HTPB products in the final diffusion flame. The impact of these flames varies with particle size and pressure.

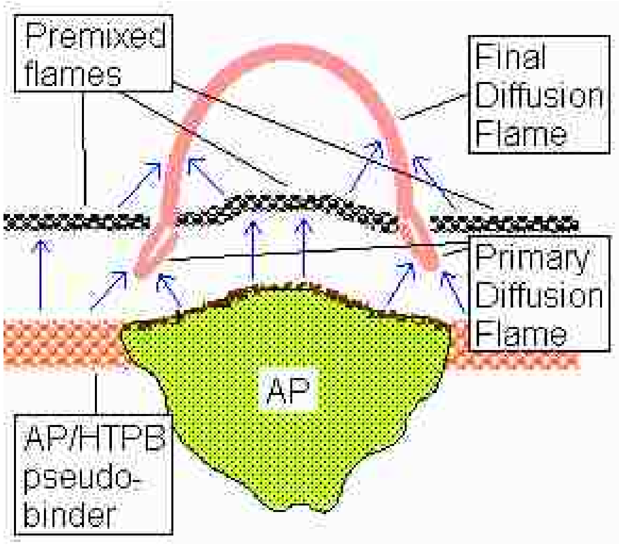

Figure 2-8: Flame structure above a burning AP particle and surrounding HTPB binder.[2]

The strong primary diffusion flame is unique to AP propellant combustion because it is driven primarily by the chlorine-containing species. Relative to the other flames, it is very hot (2500-2800 K)[46] and very close to the surface, and therefore drives the burning rate. In AP propellants, diffusion increases the temperature and surface proximity of the flame at the particle edge (primary diffusion flame).[46] In non-AP propellants, diffusion seems to have the opposite effect, resulting in a diffusion zone that is cooler than the monopropellant flame.[46] The result is that AP propellants burn faster than pure AP while non-AP propellants tend to burn slower than their pure ingredients.

2.3.1 Burning Rate Dependencies

Several factors influence the burning rate, including changes to the composition and combustion conditions. Although the general effect of pressure has already been discussed in the monopropellant combustion section, there are more complex effects discussed in this section that are related to particle-size effects.

2.3.1.1 Effects of Different Oxidizer Ingredients

There are many different types of propellant ingredients, including oxidizers, binders, and curatives that help solidify the binder, and catalysts that increase the burning rate. The focus of this section is on the different types of oxidizers, specifically AP versus non-AP oxidizers, and how they interact differently with the binder, thus affecting the burning rates in different ways.

Heterogeneity causes propellant burning rates to vary greatly from monopropellant rates, due in part to stoichiometry. The stoichiometric AP/HTPB mass ratio is ~90/10. Lower ratios are fuel rich and higher ratios (pure AP) are fuel lean due to the high oxygen content of AP. Pure HMX is fuel rich due to its relatively low oxygen content. Adding HTPB makes it even more fuel rich. Figure 2-9 shows burning rates for AP and HMX monopropellants as well as AP/HTPB and HMX/HTPB propellants. AP burning rates increase and HMX burning rates decrease when combined with HTPB, due to stoichiometry and diffusion effects.

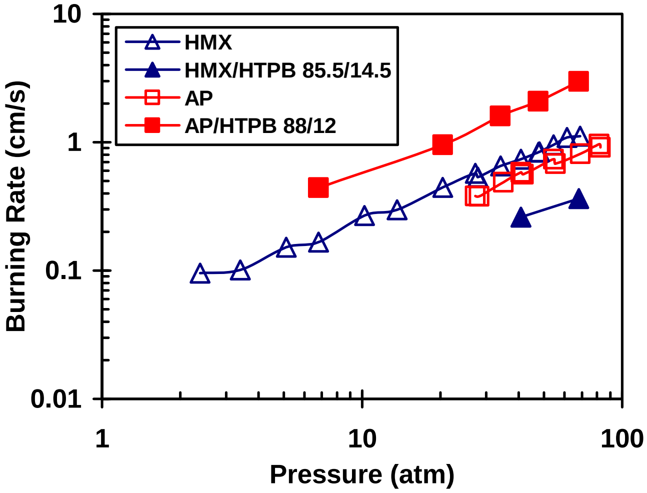

Figure 2-9: Burning rate versus pressure for HMX, AP, HMX/HTPB and AP/HTPB.[23,47,48]

Non-AP propellant burning rates also decrease when combined with energetic binders. Figure 2-10 shows how mixing RDX and GAP decreases the burning rate below monopropellant rates, with a minimum near 60% RDX.

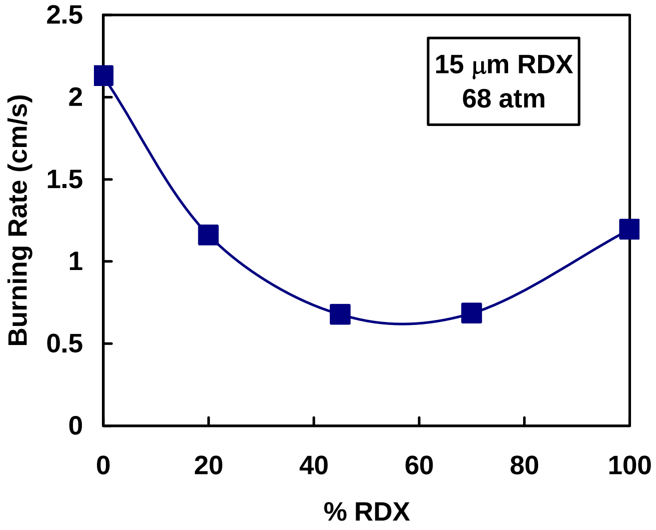

Figure 2-10: Measured RDX/GAP burning rates at 68 atm.[24]

2.3.1.2 Particle-Size Effects

Burning rate changes with particle size. Fine particles behave as though mixed homogeneously with the binder, producing a premixed particle/binder flame if the particles are small enough. Medium-sized and large particles produce diffusion flames with the binder. Transient effects also influence the burning rate. When the burning surface reaches a particle, there is a particle ignition delay time, which increases with particle size. Also, the flame structure likely changes as the particle ignites, burns, and burns out, due to the changing diameter of the particle cross-section. Initial combustion of a particle probably begins with a premixed flame due to the very small particle cross-section diameter. Soon after, a diffusion flame appears as the particle cross-section diameter increases. Finally, the diffusion flame likely disappears and there is a premixed flame once again as the particle burns out.[49]

The dependence of burning rate on AP particle size is an important characteristic of AP propellants. A predicted partice-size dependence of an AP/HTPB propellant's burning rate is shown in Figure 2-11.[3] Large particles begin to approach the monopropellant burning rate of AP, whereas increasingly smaller particles increase the burning rate of AP until they reach a premixed flame limit.

The shape of the curve in Figure 2-11 varies with propellant formulation and pressure. Monopropellant and premixed flame limits occur at different particle diameters for different pressures. Understanding the relationship between the premixed flame limit, particle size, and pressure is very important to solid propellant combustion modeling.

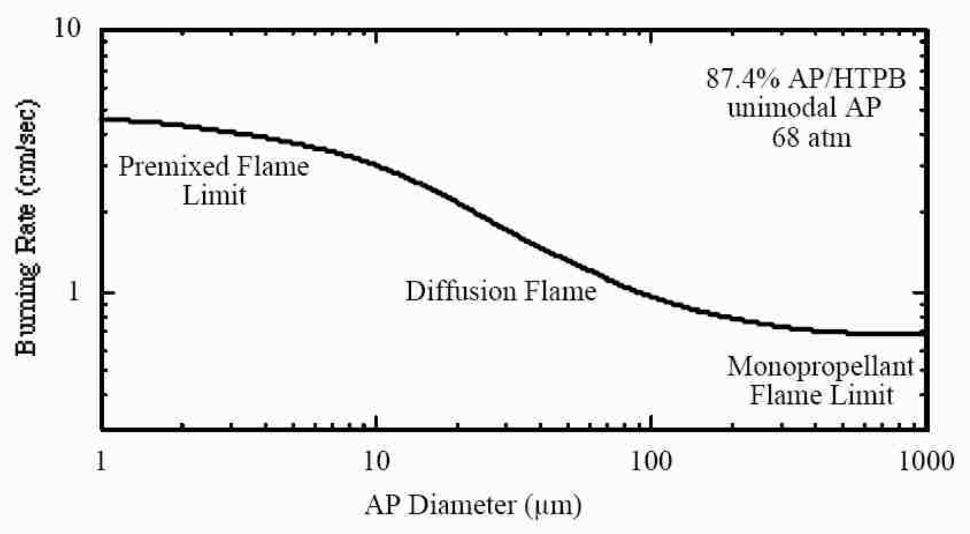

Figure 2-11: Predicted particle-size dependence of AP/HTPB burning rate at 68 atm.

Miller performed a very careful study of AP particle-size effects on burning rate. He measured burning rates while varying the fine AP particle size for a number of multimodal AP/HTPB propellant formulations.[48] A careful study of his data reveals many important trends. Figure 2-12 shows an important set of Miller's data, revealing how the curve in Figure 2-11 changes with pressure. (Please note that Figure 2-12 only captures part of the curve shown in Figure 2-11.)

At the highest pressure (204 atm), the particle-size effect is very evident, indicating a premixed flame limit at an AP diameter of ~2 microns. As pressure decreases, the particle-size effect diminishes and the premixed flame limit is extended to larger AP diameters. At the lowest pressure (6.8 atm), there is no evidence of a particle-size effect, indicating that the entire range of fine AP diameters is burning with a premixed flame.

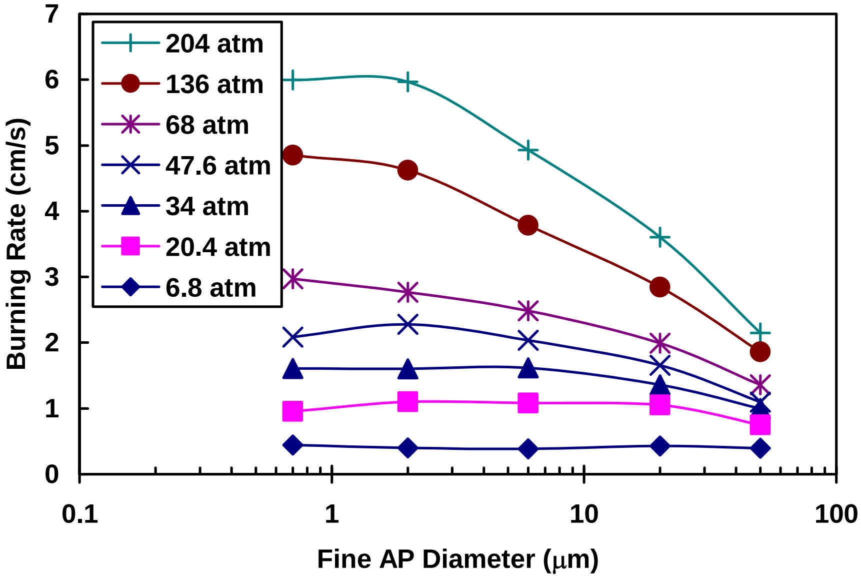

Figure 2-12: Effect of pressure and fine AP particle size on AP/HTPB burning rates (200-micron coarse AP).

Non-AP propellants behave very differently than AP propellants. Figure 2-13 shows particle-size effects for RDX/GAP and AP/HTPB propellants. For RDX/GAP, burning rate increases slightly with increasing particle size. For AP/HTPB, the opposite is true. The difference is attributed to the effects of diffusing oxidizer and binder decomposition products. In AP propellants, diffusion results in the primary diffusion flame, increasing the burning rate, but in non-AP propellants, diffusion results in a colder diffusion zone, decreasing the burning rate. The influence of diffusion is proportional to the particle surface area. As particle size decreases, both the number of particles and the total particle surface area increase. Hence, a decrease in particle size results in an increase in AP propellant burning rates and a decrease in non-AP propellant burning rates.

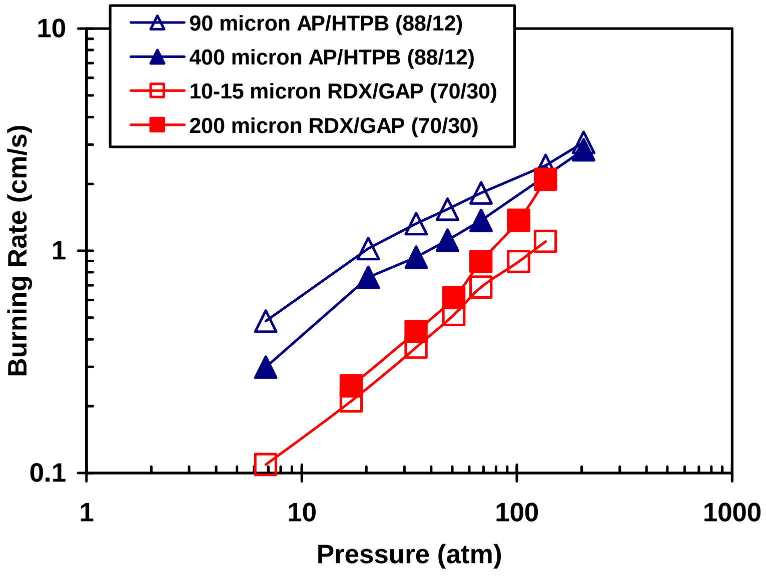

Figure 2-13: AP/HTPB and RDX/GAP burning rates varying particle sizes and pressure.[24,48]

2.3.2 Experimental Studies

Several people have studied propellant combustion by measuring species concentrations, temperatures, and burning rates. A summary of the most relevant work is presented in Table 2-1. The studies presented in this section provide useful data for model validation in the current study. Perhaps the most important are Miller's AP/HTPB burning rate data,[48] which have provided increased understanding of AP propellant combustion and have been used for model validation by many modelers.[50,51,52,53,54,55,56,57]

Many experimentalists have studied the combustion of propellants with GAP binders. The work of Litzinger,[58] Korobeinichev,[59] and Flanagan[24] has proven useful in validating pseudo-propellant combustion models.[18,45,39] The formulation of GAP binder was not always consistent between different researchers. Kubota used a GAP binder consisting of 84.8% GAP, 12% HMDI and 3.2% TMP. Flanagan used a binder containing ~90% GAP, with the remainder being ~9% HMDI, and ~1% HTO, which resulted in higher burning rates than Kubota's measurements due to the higher GAP concentration.

Table 2-1: Summary of propellant combustion experimental studies.

Researcher	Propellant	Data obtained
Miller[48]	AP/HTPB	Burning rate for multimodal mixtures with varied particle sizes.
Litzinger[58]	RDX/GAP, HMX/GAP	Laser-assisted, gas-phase, species and temperature profiles.
Korobeinichev[59]	HMX/GAP	Gas-phase species, temperature profiles.
Kubota[27,60,61]	AP/GAP, HMX/GAP, TAGN/GAP	Burning rate versus pressure, initial temperature, oxidizer fraction, and catalyst content. Temperature profiles for several pressures.
Flanagan[24]	RDX/GAP, TAGN/GAP, RDX/GAP/TMETN, HMX/GAP, AP/GAP	Burning rate versus pressure, oxidizer fraction and particle size.
Oyumi[62,63]	HMX/BAMO/NMMO, HMX/BAMO/AMMO, HMX/AP/BAMO/AMMO, HMX/AN/BAMO/AMMO	Burning rate versus pressure. Temperature profiles.
Egorshev[64]	ADN/GAP	Burning rate versus oxidizer fraction for different binder formulations.
Fong[65]	PETN/RDX/PU, PETN/PU, RDX/PU	Burning rate versus pressure and oxidizer, binder fractions.

2.3.3 Numerical Studies

Various numerical models have been developed to predict the effects of changing formulation and operating conditions on propellant combustion. These models have progressed through various levels of complexity, from 1-D to multi-dimensional models and from global or semi-global gas-phase kinetics to detailed reaction mechanisms. The most prominent of these models are discussed in this section.

2.3.3.1 BDP-Type Models

An early model that laid a framework for future modeling efforts was the BDP model,[2,3] which has been partially discussed in previous sections. The most significant contribution of the BDP model was identifying the significance of the primary diffusion flame in the combustion of AP propellants. The relationship between oxidizer particles and the binder was evaluated statistically to determine the average particle size and the amount of binder surrounding the particle. The surface temperature was averaged over the surface of both the particle and binder. Model predictions were compared with Miller's burning rate data, showing good agreement for temperature sensitivity, surface temperatures and the effect of oxidizer concentration. Predicted particle-size effects were greater than those observed experimentally.

The BDP model has since served as the basis for a number of models, which have been discussed in several reviews.[66,67,68,69,70] In 1982, Cohen developed a model based on the BDP model with added improvements,[71] including separate surface temperatures for the AP particle and binder. He also changed the heat feedback of the diffusion flame to include the binder, affecting the binder regression rate. His model improved burning rate predictions at high pressure and increased the role of the binder in combustion. In 1981, Beckstead developed the SST model[4] with some important differences from the BDP model. The oxidizer and binder were treated as having separate surface temperatures. The burning rate was calculated using a time-averaged approach, treating the particles and binder as though they burned in series. This model worked well for HMX propellants, whereas the original BDP model worked well for AP propellants. The fact that different approaches worked well for different propellant types gave insight into the combustion of AP and non-AP propellants. In 1988, Duterque applied ideas from the SST model to a model for HMX propellants with an energetic binder.[72] In 1993, Ermolin[73] developed an approach for predicting kinetic parameters for global reactions to be used in a BDP-type model. Gusachenko used the time-averaged approach of the SST model in his 1994 model,[74] which was designed for propellants with coarse AP and HTPB-like binders.

2.3.3.2 Models with Detailed Kinetics

Recently, Felt and Gross developed a two-dimensional combustion model,[5,7] using detailed kinetics, that calculates the gas-phase flame structure above an AP particle and surrounding HTPB binder. Figure 2-14 shows a temperature profile calculated for a 400-micron AP particle surrounded by an annulus of 89 microns of binder at 20 atm.

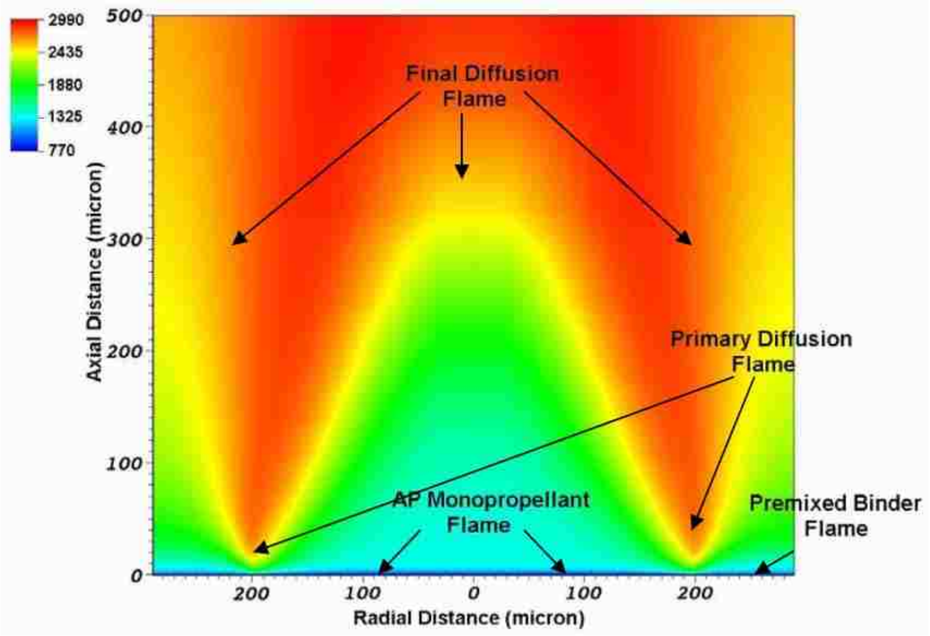

Figure 2-14: Flame structure based on temperature above a 400-micron AP particle surrounded by 89 microns of binder at 20 atm.

Calculations show the existence of the primary diffusion flame close to the surface at the particle/binder interface, validating the ideas of the BDP model. Felt's model is a very powerful tool, capable of determining the effect of varying the AP size, the amount of binder, the pressure, and even the particle and binder ingredients.

Condensed-phase boundary conditions for Felt's model are developed from one-dimensional models of AP[37] and AP/HTPB,[20,75] using PHASE3. These are not coupled dynamically, but the inlet boundary conditions of mass flux, species mass fractions, and surface temperature are calculated from curve fits of calculations performed with the one-dimensional models over a range of gas-phase heat fluxes. The particle was modeled as 100% AP and the binder as a mixture of 77.5% AP and 22.5% HTPB. The binder composition and the binder length of 89 microns were chosen to match the formulation of an 86% AP/14% HTPB propellant.[5] For the model to be applied to a new propellant, a new binder composition and binder thickness would be needed, to be determined based on the new propellant formulation. These numbers are expected to vary with particle size and pressure.

2.3.3.3 Path of Least Time

In 1978, Strahle proposed a model[76] that oversimplified the physics in order to emphasize the packing statistics. He found that there are particle-size, pressure, and packing-density effects on the burning rate due to the statistics alone. He assumed that 1) the path of least time through the propellant determines the burning rate, 2) particles burn out in a spherical geometric pattern at their monopropellant rates beginning at the ignition point, 3) binder combustion is nonlinear, and 4) particle ignition is instantaneous. An important contribution of his work was the idea that the path of least time determines the burning rate. In 1982, Miller also proposed a statistical model[50] based on the same assumption.

In 1987, Kerstein applied his percolation model to solid propellant combustion.[77] He assumed the path of least time is not a straight line and corrected for the excess path length. He concluded that the deviation from linearity is a function of the particle-size distribution. Miller later used a modified percolation theory to model AP propellant combustion.[51,52] Miller's model was empirical in nature, but useful for predicting qualitative burning rate trends.

2.3.3.4 Pseudo-Binder

In the 1990's, several people modeled AP propellant combustion using the idea of a pseudo-binder. This is similar to the idea of a pseudo-propellant, in that the pseudo-binder is assumed to be a homogeneous mixture of fine particles and binder. A propellant with small and large oxidizer particles could therefore be modeled as a mixture of large oxidizer particles and a homogeneous pseudo-propellant binder. Kovalev, in 1991, developed a model based on the idea of a pseudo-binder.[78] In 1992, Rashkovskii developed a similar model which accounted not only for different particle sizes but also for their random distribution throughout the propellant.[79] In 1996, Bilger developed a model[80] defining a unit cell around coarse AP particles, with a certain amount of pseudo-binder apportioned to each large particle.

2.3.3.5 Non-Spherical Particles

Most models assume that oxidizer particles in propellants are spherical. A few people have attempted to model the non-sphericity of particles. Marvasti, in 1992, developed a model[81] that estimated the dimension of the interface between the particles and the binder, allowing for non-spherical interfaces. He found very little effect on the predicted burning rate by modifying the spherical particle assumption.

2.3.3.6 Multi-Dimensional Particle Packs

With advances in computer technology, fewer modeling assumptions are necessary. Recent efforts have been able to integrate two and three dimensional particle packs, focusing on the geometric distribution of the solid phase instead of assuming an average particle size.[8,9,10,11,12] The complex unsteady heat transfer and propellant surface regression through 2-D and 3-D random packs of propellant particles are solved to determine an averaged burning rate. These models typically take a lot of cpu time to generate the particle pack, and to solve the corresponding conservation equations describing the combustion process. To compensate for the large cpu times, the models typically employ simplified, global 2- and 3-step reaction mechanisms to describe the gas-phase heat release.

In 2004, Groult developed a model for AP/HTPB propellant combustion.[82] He used two-step global kinetics with five species and an Arrhenius pyrolysis law for the two ingredients. He also developed a random packing code to simulate 2D heterogeneous particle packs. He implemented a simple surface-tracking method, accounting for the surface heterogeneity. Due to global kinetics, burning rate calculations were lower than expected.

In 2002, Jackson developed a model[53] to describe the combustion of 3D packs representing AP/HTPB propellants generated by his previously developed packing code.[22] He used a two-step model for the gas-phase kinetics and also implemented surface tracking. Jackson's model has been improved since 2002 in several ways. Initially, he ignored the primary diffusion flame, but had poor comparisons with data. In 2004, a third kinetic step was included to account for the primary diffusion flame and agreement with data improved dramatically.[83] The surface-tracking method was improved by the incorporation of a level set method,[13] which reduces the complex surface to a mathematically flat surface to simplify calculations, while still accounting for the heterogeneous nature of the surface.

2.3.4 Summary and Relevance

Several factors influence propellant combustion, including particle sizes, mass fractions, and the choice of ingredients. The efforts of many experimentalists to determine the effects of these factors have helped increase understanding of propellant combustion and have contributed to numerical modeling work. Numerical modelers have used a number of assumptions and approaches. BDP-type models, which use a space-averaging approach, have been successful at predicting AP propellant burning rates. Models that use a time-averaging approach have been more successful at predicting burning rates of non-AP propellants. The assumption of a pseudo-binder for propellants with fine oxidizer particles has worked well for AP propellants and been an important factor in reducing cpu times in multi-dimensional particle packing models. The path of least time assumption has been used successfully to predict qualitative burning rate trends. Models with detailed kinetics, although cpu intensive, have increased understanding of AP-propellant flame structure and helped validate the BDP concept. Several of these ideas are being used in the current study as part of a solid propellant burning rate model, including the time-averaged approach, the path of least time assumption, the pseudo-binder assumption, and the use of multi-dimensional particle packs. Some of these ideas and approaches are also used in the aluminum agglomeration model.

2.4 Aluminum Agglomeration

Extensive overviews of aluminum agglomeration are available from several sources,[84,85,86,87,88] which form a basis for this section. Aluminized propellants typically contain close to 20% aluminum by weight. Nominal particle sizes are typically between 20 and 30 microns, with distributions ranging from very fine (~1 micron) to coarse (over 100 microns). The original size distribution in the propellant is referred to as the “parent” aluminum.

Aluminum oxidation both increases the temperature inside the motor and further reduces H_2O and CO_2 gas species to H_2 and CO, which are more propulsive fluids. These effects combine to increase specific impulse by about 10%. Incomplete aluminum combustion inside the motor, however, decreases the specific impulse efficiency by lessening these effects and creates two-phase flow losses as the gas flow pushes aluminum particles out of the motor.

Another problem with aluminum in rocket motors is slag formation. Slag is formed when molten alumina gets trapped behind the nozzle or at the aft end of the motor. Slag affects performance by adding to the weight of the motor and, if ejected, can affect flight dynamics.

The size of aluminum particles as they flow through the rocket motor is important to both specific impulse efficiency and slag formation, with larger particles being more likely to decrease efficiency and contribute to slag formation. To determine the particle-size distribution in the combustion chamber, it is essential to know as a boundary condition the particle sizes leaving the propellant surface. The main process affecting particle sizes at the surface is agglomeration, through which aluminum particles combine and form larger "agglomerates".

When an aluminum particle reaches the burning surface, it may or may not have begun to melt. It begins or continues to melt as it emerges. Ignition is delayed by the fuel-rich environment and the oxide shell around the particle. During a particle's surface residence time, it possibly sticks to the binder and possibly contacts other melting aluminum particles to form agglomerates. Expansion of the aluminum particle center due to melting may cause the oxide shell to crack, exposing aluminum to oxidizing species such as H_2O and CO_2. When ignition occurs, the aluminum particle or agglomerate balls up into a sphere and leaves the surface.

In 1993, Glotov et al.[89] used high speed photography to capture agglomeration events on the burning surface of an AP/HMX propellant with inert binder. Figure 2-15 shows the steps of agglomeration that occurred. Frames 1 and 2 (0 and 3.5 ms) display a growing conglomerate of aluminum particles. Frame 3 (3.75 ms) shows the ignition of the conglomerate at the top. Frames 4 to 6 (4 to 4.75 ms) show the ignited agglomerate balling up into a sphere and leaving the surface. This is a very large agglomerate, probably due to the presence of HMX in the propellant, but the photographs provide a good visual basis for understanding the process of agglomeration.

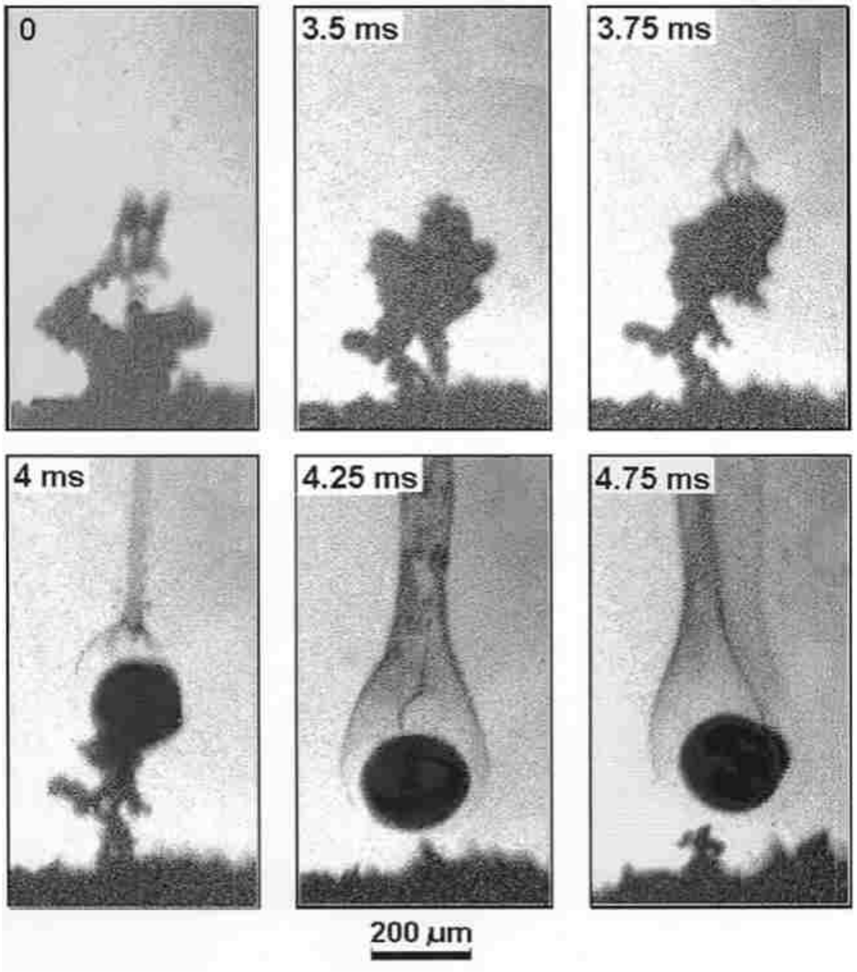

Figure 2-15: Photographs of surface agglomeration events.

Several factors influence agglomeration. These include the burning rate, pressure, ingredient type, ingredient concentrations, and particle-size distributions. Each of these is discussed below.

In general, increasing the propellant burning rate tends to decrease agglomeration, since the hotter flame temperatures that cause the propellant to burn faster also cause aluminum particles to ignite more rapidly, resulting in lower surface residence times and smaller agglomerates. However, modifying the burning rate actually has a more complex effect on agglomeration than might be expected because any modification of the propellant formulation designed to change the burning rate may also affect agglomeration in other ways than through the burning rate. For example, a decrease in AP particle size will cause an increase in burning rate, but will also change the aluminum particle spacing in the propellant matrix. Therefore, it is difficult to attribute a change in agglomeration solely to a change in burning rate. Because of this, burning rate effects on agglomeration can easily be misinterpreted.[87]

In general, agglomerate size decreases with increasing pressure, but the effect is more pronounced at low pressure and very small or nonexistent at high pressures. There are also more complex pressure effects related to the fine AP particle size that are discussed in the following sections.

The type of binder is important because of the surface retention properties of different binders, as well as their effect on flame structure and temperature. Also, propellants that use energetic binders often have lower AP content than those that use inert binders. AP propellants have hotter diffusion flames that are closer to the surface and promote aluminum particle ignition and liftoff. Generally, energetic binders produce larger agglomerates than inert binders due to the AP content in inert-binder propellants.[86]

Increasing the amount of aluminum increases agglomeration since aluminum particles are closer together. The effects of changing the aluminum particle size are more complex. Decreasing the particle size tends to increase a particle’s tendency to agglomerate with other particles, but it also decreases its surface residence time by promoting particle ignition. These are two competing effects, since particles are more likely to agglomerate, but have less time to do it. The burning rate determines which effect is dominant. In lower-burning-rate propellants, decreasing the particle size increases agglomeration, but in higher-burning-rate propellants, decreasing the particle size can decrease agglomeration.[85,86]

“Pockets” are defined as the interstitial spaces between large AP particles where aluminum particles gather.[84,85,86,87] Pockets have been hypothesized to promote agglomeration. In other words, aluminum particles form agglomerates with other particles nearby in the same pocket, so agglomerate size should be proportional to the size of the pocket. Assuming the pocket concept is correct, several factors can affect agglomeration by how they influence pockets. In general, decreasing pocket size decreases agglomeration. Increasing the concentration of the large AP particles forces AP particles closer together, shrinking pockets. Changing the AP size distribution will also change pocket sizes. Pocket size is determined by the coarse AP particle size, but fine AP particles can have an influence if they are large enough or numerous enough to disrupt the spacing of the large AP particles.

2.4.1 Experimental Studies

Agglomeration data are typically collected by one of two methods. One method is to burn small propellant samples and quench the propellant plume at a very close proximity to the surface. The number and size of the collected agglomerates are then measured. Another method is to use high speed photography to look directly at the propellant surface during combustion, and thereby count and measure the agglomerates. Unfortunately, not all researchers use the same method, and those who use the first method often report agglomeration data taken at widely different quench distances. This is significant because agglomerate size depends on the quench distance. Pokhil, in the early 1970's, measured agglomerate sizes while varying the quench distance at two different pressures.[90] His results are shown in Figure 2-16. Although he uses an atypical polyformaldehyde binder, his work still demonstrates the qualitative effect of varying the quench distance. At both pressures, the agglomerate size decreases with increasing pressure. However, the effect is very small at low pressure (1 atm), but more pronounced at moderate pressure (30 atm).

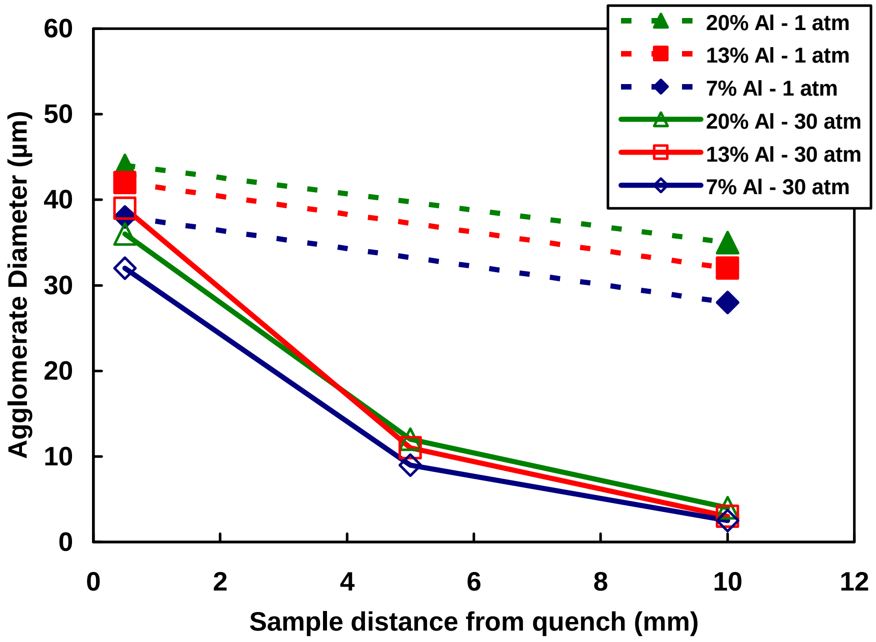

Figure 2-16: Agglomerate size plotted versus sample distance from quench liquid for three aluminum percentages at 1 and 30 atm.

The diversity of experimental procedures and data presentation in the literature, including a significant amount of contradicting data, has made it difficult to determine consistent trends. The widely different quench distances can have a significant effect on the results. There is also significant non-conformity in the type of data reported. Some authors report the fraction of aluminum that agglomerates, others report the agglomerate sizes. In addition, propellant formulations that are tested vary widely between experimentalists. Beckstead, in his overview of aluminum agglomeration,[87] discussed this problem and reported what he found to be the consistent trends from the literature. These include the following:

1. The fraction of aluminum that agglomerates is linearly proportional to the size of the agglomerates.
2. The agglomerate size is linearly proportional to the coarse AP size.
3. At low pressures, agglomeration decreases with increasing pressure, but there is much less effect at the higher pressures typically seen in motors.
4. The coarse to fine AP ratio can have a large effect on agglomeration. The effects of coarse AP size and pressure are greatest at a 90/10 coarse-to-fine AP ratio, but are smaller for smaller ratios or for monomodal AP propellants.
5. The reported effect of fine AP is mixed, but is probably related to the contribution of the primary diffusion flame and its contribution to the ignition of agglomerates.
6. Increasing aluminum concentration leads to increased agglomeration.

Studies relevant to each of these trends are discussed in the following sections.

2.4.1.1 Agglomeration Fraction

Micheli and Schmidt’s work at Aerojet in 1977 is an excellent source of data for typical AP/HTPB propellants.[91] They used a typical propellant with 70% AP, 12% HTPB, and 18% aluminum. They varied several variables, including the AP coarse/fine ratio, AP sizes, aluminum sizes, aluminum concentration, and pressure. Schmidt and Poynter continued the agglomeration work at Aerojet in 1980, adding more propellant types at more pressures.[92]

Liu et al.[93] published data in the 1990’s for AP/RDX/HTPB propellants containing 54% 400 μm AP, 18% 100 μm RDX, 16% 6 μm aluminum, and 12% HTPB. They varied RDX size, aluminum size, fine AP size, AP coarse/fine ratio, and pressure. Data were taken at a very large quench distance of 40 mm.

Babuk et al. published a very systematic set of data in 1999.[94] They formulated a series of propellants containing 24% aluminum, 64% AP, and 12% binder, varying the AP sizes from 1 to 500 μm, including two bimodal mixes. They performed tests at 1 and 6 MPa.

Data from all three investigators, along with linear trendlines, are shown in Figure 2-17. All of the trends show that the fraction of aluminum that agglomerates increases with agglomerate diameter. Differences between investigators are attributed to the differences in propellant formulation and test techniques. There is a lot of scatter in Liu’s data, which may be due to the very large quench distance employed (40 mm), but the main trend is still evident. Babuk’s data show less agglomeration at the higher pressure, which matches Beckstead’s general trends.

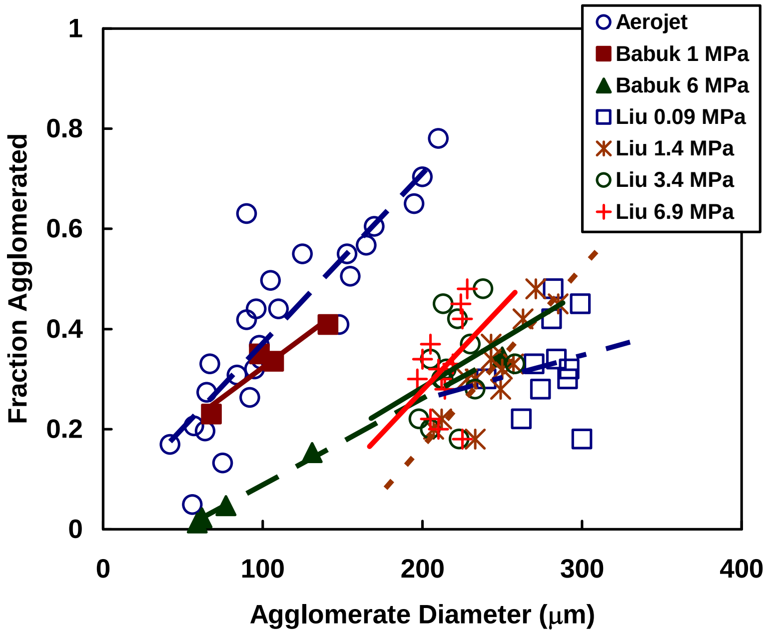

Figure 2-17: Fraction agglomerated versus agglomerate diameter.

2.4.1.2 Coarse AP Diameter

Perhaps the most important and most prevalent trend seen in the literature is that the agglomerate size is linearly proportional to the coarse AP particle size. Several investigators have shown this to be the case.

In 1974, Churchhill et al.[95] performed a study at Lockheed Propulsion Company using a monomodal AP/HTPB propellant containing 69.1% AP, 15.9% Al, and 15% HTPB. This study was performed at two pressures, 200 and 600 psi. They also looked at a propellant containing a CTPB binder, varying the pressure from 15-900 psi. Another very careful experimental study was performed by Grigoryev et al.[96] They tested monomodal AP propellants containing 14 μm aluminum. They varied the AP percentage from 39 to 48, the aluminum percentage from 22 to 44, and the AP sizes from 50 to 360 μm.

Data from Churchhill, Grigoryev, Babuk,[94] and Aerojet[91], with linear trendlines, are shown in Figure 2-18. All data sets exhibit the same general trend, showing an increase in agglomerate size corresponding to a similar increase in AP particle size.

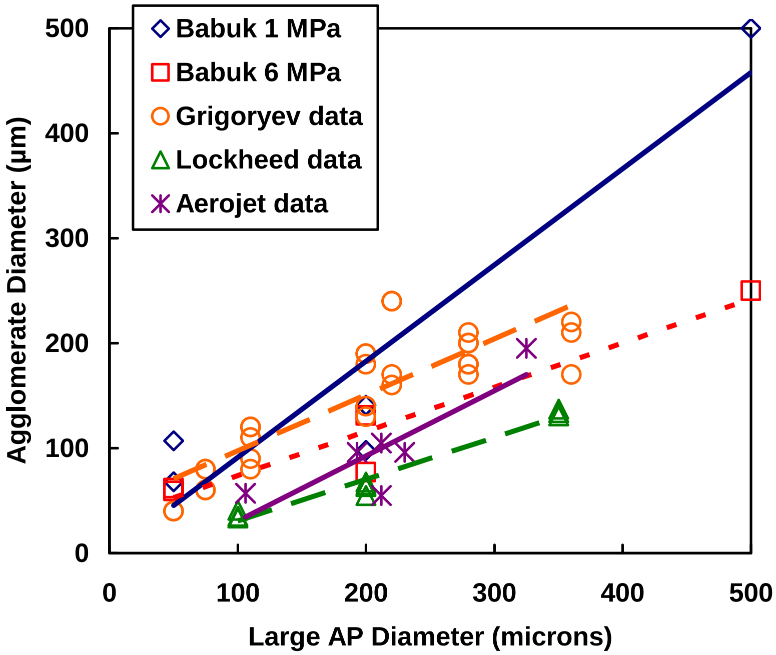

Figure 2-18: Effect of coarse AP diameter on agglomerate diameter.

2.4.1.3 Pressure

Pressure effects on agglomeration can be complex, depending on the propellant formulation, especially the fine AP size. Pressure effects associated with fine AP size are discussed separately.

In 1996, Duterque[97] performed a study at ONERA to determine how to modify the sizes of agglomerates in some common propellants. For one of the propellants, designated as 904118, he measured agglomerate sizes as well as residence times of aluminum particles on the surface. This propellant contained ~60% 200-micron AP, 10% 10-micron AP, 18% 30-micron aluminum, and 12% binder. Pressure was varied between 0.2 and 4 MPa. These results are shown in Table 2-2. Duterque's data verify that residence times and agglomerate sizes increase as pressure decreases. The burning rate also decreases, which may be a contributing factor along with the pressure.

Table 2-2: Measured residence times, agglomerate diameter, and burning rate data for propellant 904118.

Pressure (MPa)	Residence time (ms)	Agglomerate Diameter (μm)	Burning Rate (cm/s)
4.0	2.40	125	0.700
3.0	2.81	138	0.635
1.5	3.54	150	0.500
0.2	4.60	170	0.270

Liu et al.,[93] Babuk et al.,[94] and Churchill et al.[95] all performed studies over a range of pressures. Their data are shown in Figure 2-19 along with Duterque's data. There are large differences in the data between investigators, but the general trend is consistent throughout, which is that agglomerate size increases as pressure decreases, with a larger effect at low pressure. Liu's data, for three different coarse-to-fine ratios (90/10, 70/30, and 60/40), are very high compared to the rest. This is probably due to the RDX content in the propellant. Three of the four propellants from Babuk's work do not show very much change in agglomeration. This is most likely because he did not perform experiments at low enough pressures to capture the full effect. There are slight increases, however, in the agglomerate sizes at 10 atm compared to 60 atm, which matches the expected trend.

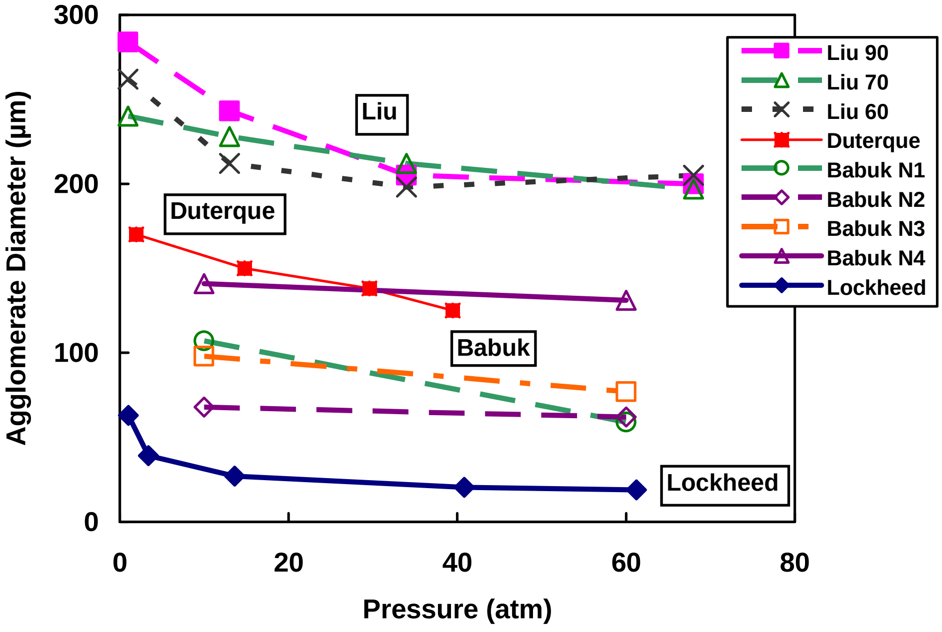

Figure 2-19: Effect of pressure on agglomerate size.

2.4.1.4 Fine AP Diameter

Sambamurthi et al. performed a very careful study of AP/PBAN propellants with bimodal AP size distributions.[98] They used plume quench tests to measure agglomerate size. The coarse AP particle size was 390 microns, aluminum was 30 microns, and fine AP was varied between 17.5 and 196 microns. All of the particle-size distributions were very narrow due to careful screening. For each fine AP size, pressure was varied between 0.1 and 3.1 MPa (1-30 atm) and coarse-to-fine ratio was varied from 60/40 to 100/0.

Figure 2-20 shows Sambamurthi's agglomerate size data versus pressure for four different fine AP sizes. These data display a very clear trend. The agglomerate size stays fairly constant at the lowest pressures, but as pressure increases, the agglomerate size decreases sharply until reaching a new plateau. The dropoff pressure is inversely proportional to the fine AP diameter. Sambamurthi et al. concluded that this is due to the flame structure dependence on both pressure and particle size. For any given particle size, there is a pressure at which the flame will transition from a completely premixed flame to a diffusion flame. For smaller particles, this transition should take place at higher pressures. They concluded from their data that aluminum ignition is initiated by exposure to the AP/binder primary diffusion flame (see Figure 2-8) and that conditions that produce such flames will increase aluminum ignition and decrease agglomeration.

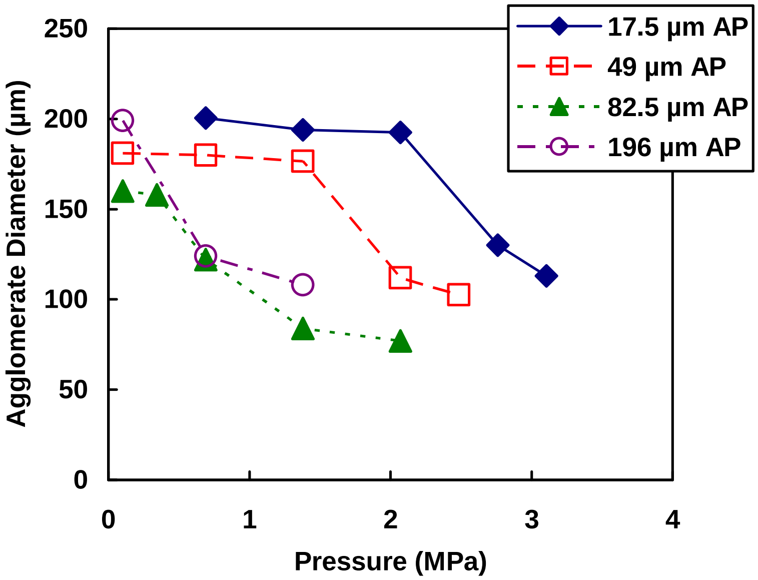

Figure 2-20: Agglomerate size versus pressure for several fine AP sizes.

The data for the 196-micron fine AP size resembles the general pressure trend of the data in Figure 2-19. This is probably because 196 microns is a typical coarse AP size and is not normally considered fine AP. The propellants in Figure 2-19 do not show the same specific trend seen in Figure 2-20, which is probably due to two factors. The fine AP used in those propellants may have been too small to transition to a diffusion flame at the test pressures. Another possibility is that the very narrow AP distributions that were carefully screened by Sambamurthi may be necessary to capture the trends seen in Figure 2-20. A broader fine AP distribution may result in a blending effect, making it difficult to see a sharp drop-off pressure that varies with particle diameter.

The effect of varying the percentage of fine AP is shown in Figure 2-21. These data were taken at a pressure of 1.38 MPa. There is a similar trend to the pressure trend seen in Figure 2-20, in that there is a drop-off point for the agglomerate diameter that varies with fine AP size. The data for 82.5-micron AP drop off immediately, whereas the data for the 49-micron AP stays constant until about 15% fine AP. The data for the 17.5-micron AP is more difficult to understand. It seems to be dropping off at the highest percentage of fine AP, but even greater percentages would need to be tested to verify this.

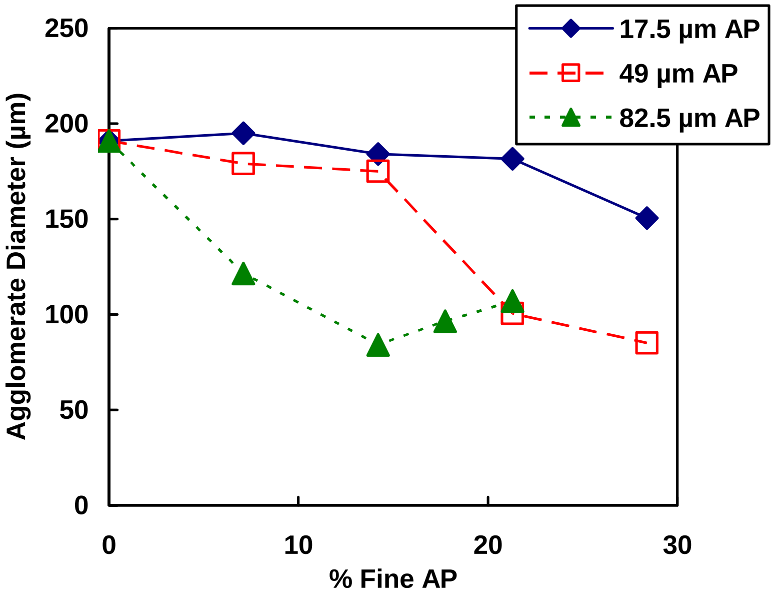

Figure 2-21: Agglomerate size versus % fine AP for several fine AP sizes.

Sambamurthi et al. attributes the trends in Figure 2-21 to the dependence of the pseudo-binder premixed flame on its AP content. As fine AP percentage is increased, the homogeneous mixture of binder and fine AP becomes less fuel rich, resulting in hotter flame temperatures, and the primary diffusion flame of the coarse AP particles is also drawn closer to the surface. The 82.5-micron AP particles may be large enough at 1.38 MPa to produce their own diffusion flame, resulting in a decrease in agglomerate size. The differences between the three fine AP sizes may also be due to their influence on the aluminum particle spacing in the propellant. The 82.5-micron AP size may disrupt the particle spacing at a lower percentage than the 49-micron AP, and that at a lower percentage than the 17.5-micron AP, resulting in different drop-off points.

2.4.1.5 Coarse to Fine AP Ratio

Micheli and Schmidt looked at the effect of the coarse-to-fine AP ratio,[91] which is perhaps the most significant part of their agglomeration work. These data are shown in Figure 2-22 and Figure 2-23. Their data show a maximum agglomerate size at a ratio of ~90/10 for three coarse AP sizes and four pressures. It is significant that there is more agglomeration at the lowest pressure of 200 psi, but at higher pressures there is no effect except at the 90/10 ratio. This may explain why some investigators see a pressure effect at high pressure and some do not. Propellant formulations typically use a 70/30 ratio because it allows the highest packing fraction.[21,87] When agglomeration studies are performed on such propellants, there is usually very little pressure effect seen at high pressures. Based on the results of Figure 2-22, those who do see an effect are probably studying propellants that have an AP coarse-to-fine ratio closer to 90/10.

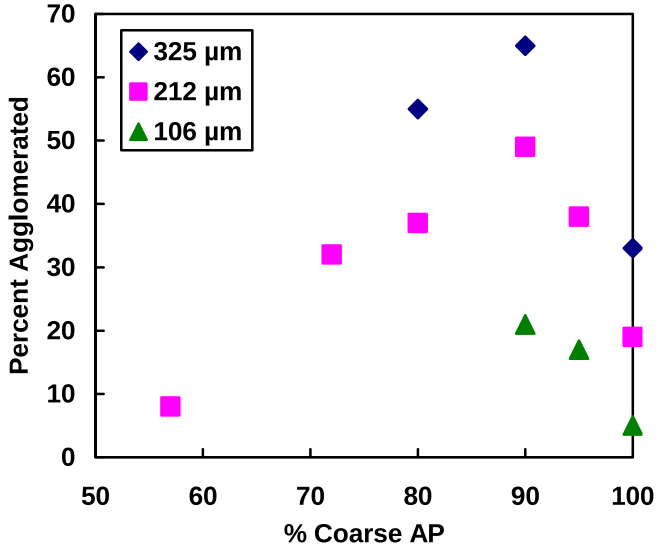

Figure 2-22: Percentage of aluminum that agglomerates as a function of coarse AP percentage for three coarse AP sizes at 200 psi.

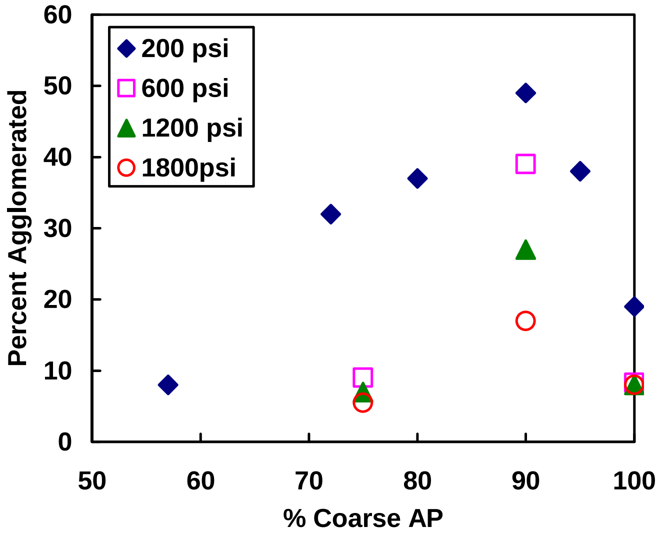

Figure 2-23: Percentage of aluminum that agglomerates plotted versus coarse AP percentage at four pressures for a coarse AP size of 212 microns.

2.4.1.6 Aluminum Fraction

Grigoryev and Zarko[96] investigated the effect of changing the aluminum fraction as part of their agglomeration study. They looked at propellants with 20 and 46% aluminum for several coarse AP sizes. These data are shown in Figure 2-24. The data show a significant increase in agglomeration for the propellant with 46% aluminum. This is a rather intuitive effect. The greater the amount of aluminum, the closer the aluminum particles are to each other, and the more likely they are to agglomerate. However, 46% is an extremely high percentage for aluminum, so it is hard to tell from these data whether a small change in aluminum content, typical of what a propellant chemist might consider, would have a significant effect.

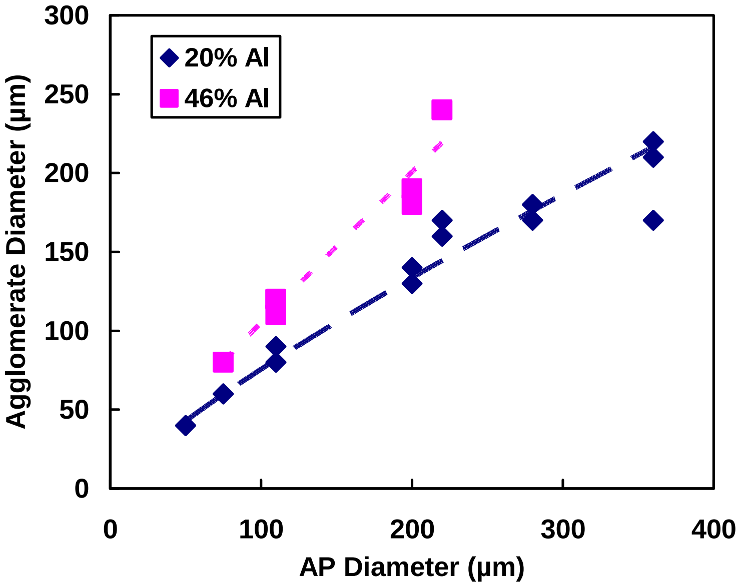

Figure 2-24: Agglomerate size data plotted versus coarse AP size for two aluminum fractions.

2.4.2 Numerical Studies

2.4.2.1 Pocket Models

There have been a number of agglomeration models over the years that were based on the pocket concept, the idea that the aluminum within a pocket between large AP particles will agglomerate. Some of the first were developed by Beckstead[99] and Cohen[100,101] in the late 1970's and early 1980's. Both introduced empirical correlations relating the fraction of aluminum that agglomerates to the coarse AP and aluminum mean particle sizes and the fine to coarse AP mass ratio. Cohen's correlation tries also to account for the effects of intermediate AP particle sizes.

Cohen also developed an analytical model[101] to calculate pocket volumes. He assumed that all melted aluminum particles within a pocket would agglomerate. He determined whether particles would melt by calculating a critical melting diameter. All aluminum particles below the critical diameter were assumed to melt by the time they reached the burning surface and all particles larger than the critical diameter were assumed to reach the surface unmelted and leave the surface unagglomerated. He also included temperature and encapsulation criteria. That is, for an AP particle to establish an effective pocket, it must burn with a hot enough flame to ignite the aluminum. It must also be larger than the aluminum particle being ignited.

There have been several other analytical models based on the idea of pockets.[102,103,104,105] These models are essentially the same but differ somewhat in the criteria for agglomeration. All predict that agglomeration will decrease with an increase in burning rate, AP mass fraction, fine AP particle size, or fine to coarse AP mass ratio, and with a decrease in the coarse AP particle size. Other authors suggest empirical correlations for the critical agglomeration diameter to better match data.[106,107,108]

In 2000, an important study was performed at ONERA by Trubert[109], varying pressure and mass fractions and size distributions of AP and aluminum to verify their effects on aluminum agglomeration. Perhaps his most important conclusion is the validation of the "pocket model". He showed that agglomeration can be reduced by changing the AP and aluminum particle-size distributions to create smaller pockets.

2.4.2.2 Models Based on Random Packing

One very recent model[110] is being developed by Jackson using Rocpack to simulate propellants containing aluminum. By fully simulating the particle packing, the actual spacing of aluminum particles throughout a computer-generated propellant sample can be analyzed to predict agglomeration. This allows a more thorough analysis than previous models and the prediction of agglomerate size distributions rather than just mean agglomerate sizes. The general idea of Jackson's model is that agglomeration is controlled by a separation distance, not necessarily a "pocket". All aluminum particles within a specified distance of each other are assumed to agglomerate. The main problem with Jackson's model is that he has to recalibrate it for every new data set, so it is still an empirical model. He ignored pockets, claiming that they do not control agglomeration.

Another recent study that uses a three-dimensional particle packing model is that of Srinivas and Chakravarthy in 2007.[111] Burning rate is an input to the model, which determines the rate of numerical surface regression for the particle pack. They track the aluminum particles as they move with the regressing surface and form conglomerates, or filigrees, of aluminum. They developed criteria, based on the literature, for the presence of diffusion flamelets attached to AP particles, which act as ignition sources to the aluminum. They also incorporate a one-dimensional heat transfer model to calculate ignition delay times for the filigrees. In this way, they keep track of the formation and ignition of individual agglomerates and calculate the number and size of the agglomerates. Their model calculations successfully predicted the qualitative trends of Sambamurthi's agglomeration data, and also agreed reasonably well quantitatively. Similarities between their model and the current study suggest a high probability of success for the current study.

2.4.3 Summary and Relevance

Aluminum agglomeration experimental studies help increase understanding of the processes that affect aluminum combustion and slag formation in rocket motors. They also contribute to the development of numerical models. Several important numerical modeling ideas are presented, including the ideas of pockets, separation distance, and the use of random particle packing. These form the basis of the approach used in the current study to develop a solid propellant aluminum agglomeration model. The work of Srinivas and Chakravarthy[111] is very similar to the current study, with significant differences in the determination of the presence of AP/binder diffusion flamelets and ignition delay time. Their ideas have not been used in the current study because their work was only recently published. However, there are similar ideas used, but only coincidentally.

2.5 Overall Summary and Objectives

Numerical modeling of solid propellant combustion, including burning rate modeling and aluminum agglomeration modeling, has improved dramatically along with computer technology. Several important tools and approaches have been developed for monopropellant, pseudo-propellant, and propellant combustion modeling. Models have increased in complexity, moving from one to multiple dimensions in the solid and gas phases and incorporating more detailed chemical kinetics. Despite such advances, there is still a great need for further advancement. Current modeling work typically includes multiple dimensions and great detail in one part of the combustion model, whether it is the solid phase-geometry or the gas-phase calculations, but not in all parts. The main objective of the current study is to develop both a burning rate and an agglomeration model that incorporate greater detail in both the solid and gas phases, using a three-dimensional solid-phase model and a two-dimensional diffusion flame model, in order to accurately calculate particle-size effects and other important effects. One-dimensional models of pseudo-propellant combustion, specifically RDX/GAP and AP/HTPB, have also been developed and updated to be used as important tools in the overall modeling work.

3 One-Dimensional RDX/GAP Pseudo-Propellant Model

Energetic binders have attracted interest for use in advanced solid propellants.[112] Azides such as GAP and BAMO have a positive heat of formation and decompose exothermically in the condensed phase during combustion, resulting in high burning rates.[113,114,115,116,117,118,119] GAP has been found to be thermally stable and insensitive.[112] Nitramines such as RDX and HMX have high energy content and a high specific impulse. The products of nitramine combustion contain fewer pollutants when compared with AP and are also smokeless. Nitramine/azide-based composite propellants are thus among the most promising candidates for use as advanced solid propellants.

Experimental studies have analyzed the decomposition and combustion of propellants with nitramines as oxidizer and azides as binder. In particular, studies have analyzed RDX/GAP,[120,121,122] RDX/BAMO,[123] HMX/GAP,[60,61] and HMX/BAMO.[62,63] Although azides have high burning rates, they are fuel rich and burn with a carbonaceous residue. Considering the slightly fuel-rich content of nitramines, the azide/nitramine propellant would also be fuel rich.

Monopropellant premixed combustion of RDX and GAP has been modeled in the past.[15,16,17,28,124,125] Modeling of RDX/GAP pseudo-propellants has been done by Liau et al.[45,126] and Puduppakkam.[18] The current study employs different kinetics than previous models in both the gas and condensed phases. The current study is an extension of the work done by Davidson[15,16] and Puduppakkam.[17,18,125] The majority of the work presented in this chapter has been published previously.[127]

3.1 Experimental Observations

The research on RDX/GAP pseudo-propellants is ongoing and has been very promising, but the literature is not vast. Hence, experimental observations for monopropellant RDX and GAP in the literature are discussed along with the pseudo-propellant studies to get a better understanding of the topic. The experimental studies in the literature have included determining decomposition products at the surface, decomposition pathways, burning rate as a function of pressure and initial temperature, and the effect of varying the percentages of RDX and GAP.

The first step in the decomposition of monopropellant GAP is the exothermic dissociation of N_2, with an activation energy of approximately 40 kcal/mol.[114,117,118] There is a considerable scatter in the experimental data of decomposition products following the initial step. Some of the reasons for the data scatter include differences in heating rates, structure of the GAP, molecular weight, curing agent, pressure and laser power in the experiments. The consensus on the decomposition products would be that a carbonaceous residue forms due to the fuel-rich character of GAP.[113,114,116,118] The exact nature of the residue depends on the experimental conditions, ranging from soot to large fragments of the parent GAP. HCN, NH_3, CO and CH_2O are the major products of decomposition in most studies.[116,117] Pressure does not appear to have an appreciable effect on the decomposition products.[115]

Monopropellant RDX melts at around 478 K, followed by endothermic decomposition and evaporation. It has been observed to predominantly evaporate, while decomposition has been determined to play a minor role. Decomposition occurs through two parallel paths, one producing NO_2 and the other producing N_2O. The major products of decomposition include HCN, CH_2O, NO_2 and N_2O.[130]

An 80% RDX/20% GAP pseudo-propellant produces mostly the same products as the monopropellants.[121] A few products, such as CO_2, were observed for the pseudo-propellant that were not observed for the monopropellants, but their concentrations were low.[121] A simple calculation was made that weighted the mass fraction of the products from monopropellant decomposition studies of RDX and GAP according to the composition (80% RDX/20% GAP) and summed them up. This was done to determine the extent of chemical interaction between the RDX and GAP in the condensed phase. The result was close to the experimental data of the pseudo-propellant, as shown in Figure 3-1, implying that the chemical interaction between the RDX and the GAP in the condensed phase is minor. There is no calculated CO_2 because it is not included in the condensed-phase mechanism, but is accounted for in the gas phase. With increasing GAP content in the pseudo-propellant, the system becomes more fuel rich and this has resulted in a carbonaceous residue for compositions below 80% RDX.[128]

Extensive experimental studies have measured the burning rate of monopropellant RDX and GAP as a function of pressure and initial temperature.[113,114,115,118] The monopropellant burning rate of GAP has been observed to be very dependent on the amount of curing agent.[113,115] The monopropellant pressure exponents of GAP and RDX were reported to be in the range of ~0.45[113,114] and ~0.8[15] respectively. The monopropellant temperature sensitivities of RDX and GAP differ significantly, with GAP having a σ_p of 0.006-0.01,[60,113,115] while that of RDX is approximately ~0.001.

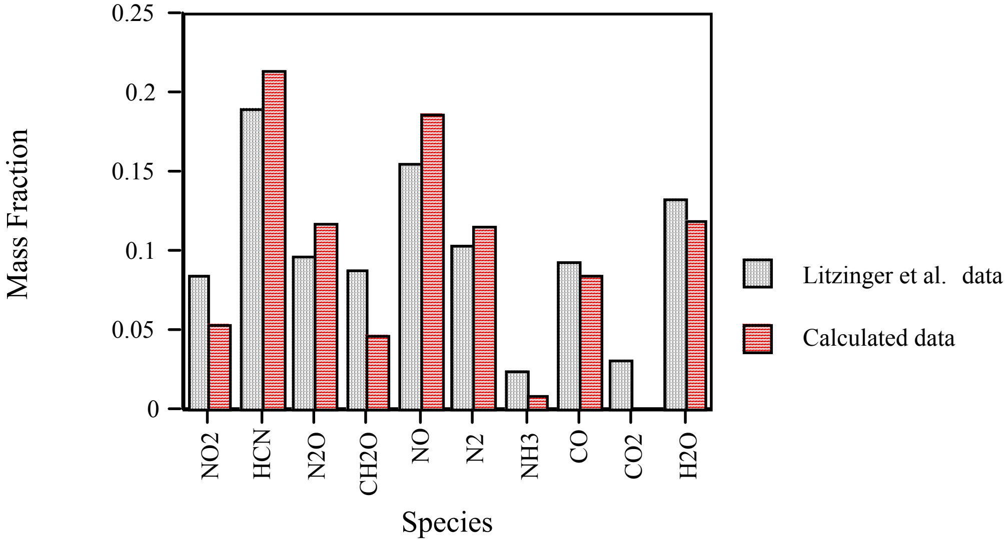

Figure 3-1: Surface decomposition products for an 80% RDX/20% GAP pseudo-propellant at 1 atm.

There are limited data available on the burning rates of azide/nitramine pseudo-propellants. Flanagan et al.[120] have published data for different compositions of RDX/GAP pseudo-propellant at various pressures, while Kubota et al.[60] have published data for HMX/GAP at different compositions. The pseudo-propellants have been found to have a lower burning rate than either the nitramine or the azide.[60,120] The pressure exponent of HMX/GAP pseudo-propellant has been observed to be dependent on the HMX content, with a value of ~ 0.8.[60] Temperature sensitivity data are not available for the RDX/GAP system. The value for HMX/GAP[60] has been determined to be 0.002 K^{-1}. Dark zones have also been observed during the laser-assisted combustion of RDX/GAP pseudo-propellants at low pressures.[121]

3.2 Numerical Model

PHASE3, the numerical model of Davidson,[15] was used in this study. It is a steady state, three-phase, one-dimensional premixed combustion model. The model divides the burning propellant into three regions (see Figure 2-3): 1) the solid, non-reacting region, 2) the condensed-phase decomposition region and 3) the gas-phase region. Region 1 involves only the integration of the energy equation without any source terms. Region 2 involves the energy and species equations and is solved as a system of initial boundary value problems. Since the condensed-phase kinetics are not as well understood as those in the gas phase, global reactions are used. In Davidson's original RDX model, the interface between region 1 and region 2 was the melting temperature of RDX. GAP does not change phase and hence does not have an exact interface like RDX. In the modeling of monopropellant GAP, the interface was taken as an arbitrary temperature where significant decomposition had not started, usually close to the initial temperature.[125] Since the melting temperature of RDX is relatively high, an analysis was made to determine the effect of choosing that temperature as the interface for monopropellant GAP. The burning rate was not affected, implying that decomposition of monopropellant GAP was insignificant at temperatures lower than the melting temperature of RDX. Hence, the melt temperature of RDX has been used in the current study as the interface between regions 1 and 2 for monopropellant RDX and GAP, and for the mixture.

For the RDX/GAP mixture, the interface between regions 2 and 3 is not clearly defined due to GAP. While RDX is expected to predominantly undergo endothermic evaporation, GAP is expected to decompose exothermically. While RDX exists as a liquid in region 2, GAP exists as a solid. In actuality, the gases from RDX and GAP will probably exist as bubbles, the number density of which will increase with distance along region 2. The number density keeps increasing until this region of bubbles in solid and liquid eventually becomes a region of solid and liquid in the gas phase. So, there is no clearly defined separation in actuality between regions 2 and 3, but a location needs to be chosen for modeling purposes.

For GAP monopropellant, the interface was defined by Puduppakkam as the location where 99.9999% of the condensed-phase material has decomposed to gases.[17] For RDX monopropellant, Davidson defined the interface as the location where all the RDX has evaporated.[15] These approaches have also been used for the monopropellants in this study. The approach used for monopropellant RDX was initially used in the current study for the RDX/GAP mixture as well. With this approach, it was found that the predicted surface void fraction (at the interface between regions 2 and 3) increases with increasing GAP content from ~0.33 for 100% RDX/0% GAP to ~0.99 for 45% RDX/55% GAP. As GAP content increases above 55%, the surface void fraction continues to increase towards a value of ~1. However, for the composition of 20% RDX/80% GAP, the approach used for monopropellant RDX resulted in much higher burning rates than those measured experimentally. Hence, the approach used for monopropellant GAP (specifying the surface void fraction) has been used for the composition of 20% RDX/80% GAP.

To determine what surface void fraction to specify for 20% RDX/80% GAP, a void-fraction range was used and burning rates were calculated. This was also done for monopropellant GAP to verify that the void fraction should be 99.9999%. These results are presented in Figure 3-2. There is a large effect on the burning rate for both monopropellant GAP and 20% RDX. When this was discovered, the surface void fraction was varied for other compositions as well, but there was no significant burning rate effect at compositions of more than 20% RDX.

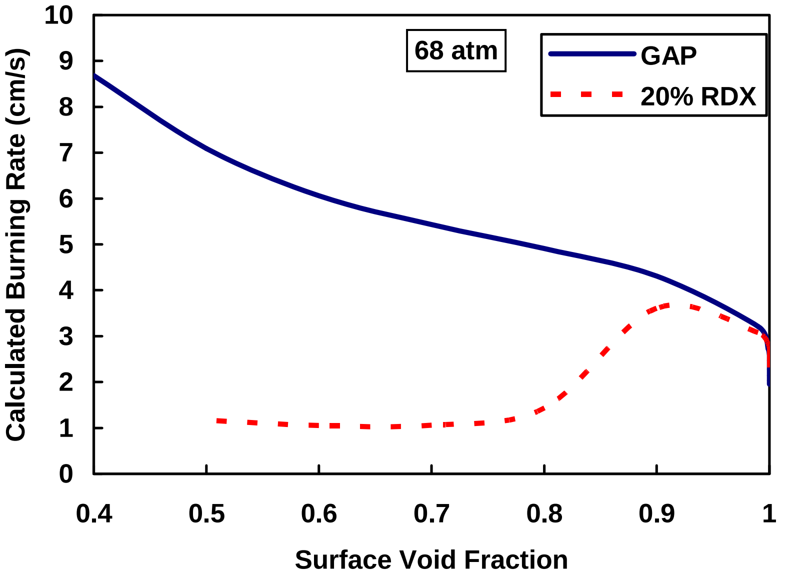

Figure 3-2: Predicted effect of varying surface void fraction on burning rate for monopropellant GAP and 20% RDX/80% GAP at 68 atm.

The burning rate increases dramatically for monopropellant GAP as surface void fraction decreases. For 20% RDX/80% GAP, the burning rate first increases and then decreases and finally levels out as surface void fraction decreases. For monopropellant GAP, a surface void fraction of 99.9999% appeared to be necessary to match experimental burning rate data, so this value was left the same. For 20% RDX/80% GAP, a surface void fraction lower than ~0.75 appeared to be necessary to match the data. A value of 0.6 has been used in the current study.

The effect of varying the surface void fraction is related to the condensed-phase reaction mechanism. When the surface condition is reached in PHASE3, the remaining amount of each condensed-phase species instantly undergoes decomposition to gas-phase species through a designated reaction from the condensed-phase mechanism. Therefore, a change in the surface void fraction affects the burning rate by forcing the condensed-phase species to decompose through a different mechanistic pathway. It is probable that the same change in burning rate can be obtained by modifying the condensed-phase mechanism directly while leaving the surface void fraction alone. However, modification to the condensed-phase mechanism was considered unnecessary since the desired result had already been obtained via modifications to the surface void fraction.

The temperature and species mass fluxes calculated in region 2 serve as boundary conditions for the gas phase (region 3). Temperature and species profiles are calculated in region 3 using a modified version of PREMIX.[30] The burning rate is determined by iterating until matching the heat fluxes from regions 2 and 3.

Although this is a one-dimensional, premixed combustion model, it is expected to simulate the combustion of the composite propellant. Parr et al. have shown that nitramines do not have strong diffusion flames with either energetic or non-energetic binders.[128] Moreover, the experimental data used for comparison use RDX particle sizes of less than 15 μm,[120] which would result in nearly premixed combustion anyway. A premixed model should be able to simulate these conditions well.

3.3 RDX/GAP Condensed-Phase Model

Modeling the chemical kinetics of the condensed phase is the weakest link in most models with detailed kinetics. Gas-phase chemistry is relatively well understood and the kinetic mechanisms have hundreds of elementary reactions. On the other hand, it is much more difficult to obtain experimental data on condensed-phase chemistry, and consequently it is represented by global kinetic mechanisms. More often than not, one or more of the kinetic parameters used for these global reactions are fitted to reproduce experimental burning rates. This may be justified since the species coming from the condensed phase and the surface temperature are boundary conditions in the model for the well understood gas phase, and they can be measured. Thus, if the species concentrations and exothermicity of the condensed phase match the experimental data, the global mechanism achieves its purpose. However, combining two ingredients such as RDX and GAP complicates this process. This is a disadvantage that will exist for some time until the condensed-phase kinetics can be characterized more readily.

As explained previously, the experimental data on RDX/GAP pseudo-propellants indicate that there is little chemical interaction between the RDX and the GAP in the condensed phase. Hence, the approach used in this study was to combine the condensed-phase kinetic mechanisms of the monopropellant RDX and GAP to give the kinetic mechanism for the mixture. Although the model does not consider chemical interaction between RDX and GAP in the condensed phase, the model inherently handles the thermal interaction caused by the RDX and GAP reactions.

The uncured GAP in this model was taken to be a tri-ol with 21 monomer units and to have the structure shown in Figure 3-3.[125] The molecular weight of the structure is

2171 g/mol. A molecular weight of close to 2000 was chosen in the modeling since most of the experiments used GAP with molecular weights in that range.[113,115,118] GAP is usually cured with HMDI. In this model, a formulation of 89.6% GAP/10.4% HMDI was taken as the cured GAP. This particular combination was chosen because the ratio of the NCO units in the isocyanate to the OH units in GAP would be one.

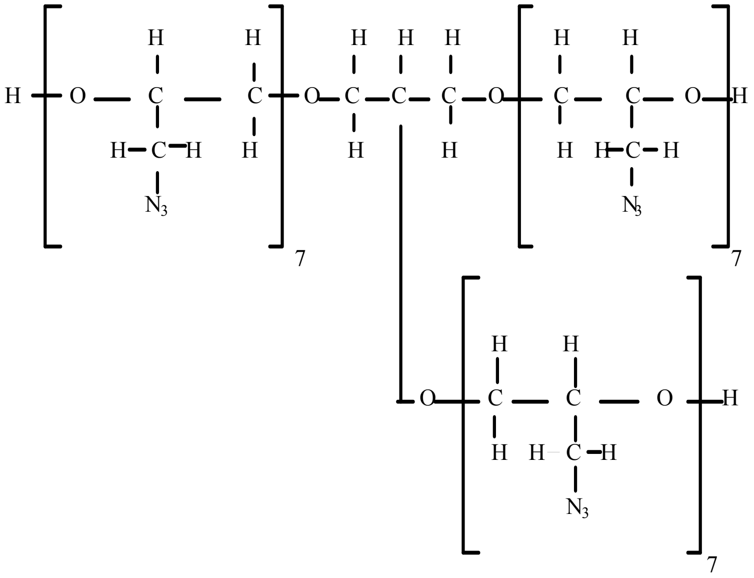

Figure 3-3: Structure of GAP tri-ol considered in study.

The reactions used in the condensed phase for the decomposition of the RDX/GAP mixture are shown in Equations (3-1) to (3-6). The first two reactions have been used in GAP monopropellant combustion modeling,[17] while the final four have been used in RDX monopropellant combustion modeling.[15] Maksimov's vapor pressure correlation[129] is used for the evaporation of RDX in the model. Activation energies are in units of cal/mole.

$$C_{78}H_{131}O_{27}N_{66}(\text{GAP}) \Rightarrow C_{78}H_{131}O_{27}N_{24} + 21\,N_2 \qquad k = 0.1\times10^{16}\exp(\frac{-40000}{RT}) \quad \textbf{(3-1)}$$

$$C_{78}H_{131}O_{27}N_{24} \Rightarrow 21\,C(s) + 10\,H_2 + 18\,HCN + 3\,NH_3 + 13\,CO + 4\,CH_2O + 7\,H_2O$$

$$+12\,CH_4 + 3\,CNO + 3\,CH_2 + 2\,C_2H_4 \qquad k = 0.2\times10^{12}\exp(\frac{-30000}{RT}) \quad \textbf{(3-2)}$$

$$\text{RDX(l)} \Rightarrow 3\,CH_2O + 3\,N_2O \qquad k = 4.88\times10^{11}\exp(\frac{-36000}{RT}) \quad \textbf{(3-3)}$$

$$\text{RDX(l)} \Rightarrow 3\,H_2CN + 3\,NO_2 \qquad k = 1.3\times10^{15}\exp(\frac{-45000}{RT}) \quad \textbf{(3-4)}$$

$$CH_2O + NO_2 \Rightarrow NO + CO + H_2O \qquad k = 802\times T^{2.77}\exp(\frac{-13730}{RT}) \quad \textbf{(3-5)}$$

$$\text{RDX(l)} \Rightarrow \text{RDX(g)} \qquad P_v = 2.66\times10^{13}\exp(\frac{-22500}{RT}) \quad \textbf{(3-6)}$$

Two parameters have been modified—the pre-exponential of Equation (3-4) and the temperature exponent of Equation (3-5)—from the values used by Davidson. Davidson originally divided the pre-exponential of Equation (3-4) in half in order to make the calculated N_2O to NO_2 ratio at the propellant surface agree more closely with Brill's measurements.[130] Presently, however, agreement with Brill's data is improved if the pre-exponential of Equation (3-4) is restored from $6.5\text{x}10^{14}$ to its original value of $1.3\text{x}10^{15}$. This is shown in Figure 3-4. The temperature exponent of Equation (3-5) was reported as 2.77 by Thynell,[131] but Davidson used 2.27 while referencing Thynell. Since there was no explanation given for using a value of 2.27, this was assumed to be a mistake and has been restored to 2.77.

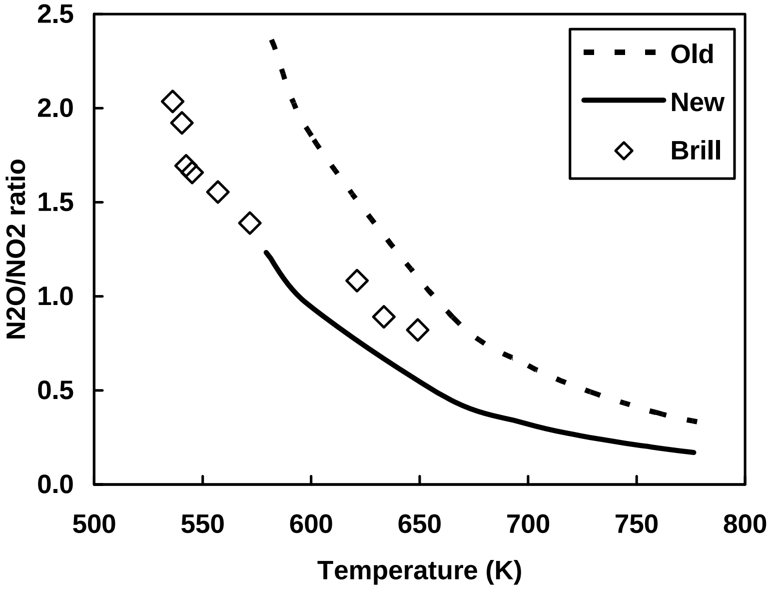

Figure 3-4: RDX surface N2O/NO2 ratio as a function of surface temperature.

3.4 Comprehensive Gas-Phase Mechanism

To be consistent, and in an effort to establish a comprehensive gas-phase kinetic mechanism that can be used for any propellant ingredient,[43] the same gas-phase mechanism has been used for RDX and GAP monopropellants and RDX/GAP pseudo-propellant. This mechanism has been used in previous models with success and was originally developed by Puduppakkam.[19,38,43]

The gas-phase mechanism was assembled from published mechanisms for the combustion of RDX,[132] GRI,[133] NG[35] and ADN.[134] Additional reactions of Lin et al.[135,136,137] involving HCO, HONO, HNOH and HNO were added. The reactions that were redundant from the different mechanisms were listed only once in the detailed mechanism. A few reactions were deleted by Puduppakkam based on the findings of several authors.[38]

The application of Puduppakkam's comprehensive gas-phase mechanism to the RDX monopropellant combustion model, however, resulted in a significant increase (~20%) in the calculated burning rates. The increase was attributed to the uncertainty in the kinetics describing initial RDX decomposition in the gas phase, in agreement with the conclusions of Prasad et al.[29] Theoretical calculations of kinetic parameters for unimolecular decomposition reactions of H_2CNNO_2 in the gas phase, as reported by Chakraborty and Lin,[138] have since been discovered. Three H_2CNNO_2 reactions from Chakraborty and Lin have been added to the mechanism, replacing seven previous reactions, as shown in Table 3-1. This resulted in lower RDX burning rate predictions that are within ~5% of experimental data. The burning rate calculations for both versions of the mechanism, before and after the changes in Table 3-1 were made, are shown in Figure 3-5. The overall gas-phase mechanism, not including chlorine species or reactions, presently consists of 83 species and 530 reactions (Appendix A).

Table 3-1: Modifications to gas-phase H_2CNNO_2 reactions.

Added Reactions	**A**	**b**	**E**	**Reference**
$H_2CNNO_2(+M)=H_2CN+NO_2(+M)$	2.46E+15	0	3.42E+04	138
Fall-off Parameters	2.35E+56	-13.3	2.46E+04	
$H_2CNNO_2(+M)=HONO+HCN(+M)$	6.21E+12	0	3.25E+04	138
Fall-off Parameters	2.87E+39	-9.37	1.78E+04	
$H_2CNNO_2(+M)=CH_2O+N_2O(+M)$	4.52E+11	0	3.84E+04	138
Fall-off Parameters	1.38E+04	0	1.21E+04	
Deleted Reactions	**A**	**b**	**E**	**Reference**
$H_2CNNO_2(+M)=H_2CN+NO_2(+M)$	1.00E+16	0	3.10E+04	139
Fall-off Parameters	7.69E+16	0	2.60E+04	
$H_2CNNO_2+H_2O=CH_2O+N_2O+H_2O$	1.00E+11	0	2.00E+03	139
$H_2CNNO_2+NO_2=CH_2O+N_2O+NO_2$	1.00E+11	0	2.00E+03	124
$H_2CNNO_2+N_2O=CH_2O+N_2O+N_2O$	1.00E+11	0	2.00E+03	124
$H_2CNNO_2+H=H_2CN+HONO$	1.00E+12	0	5.00E+03	139
$H_2CNNO_2+OH=HCN+NO_2+H_2O$	1.00E+13	0	3.00E+03	139
$H_2CNNO_2+OH=CH_2O+N_2O+OH$	1.00E+13	0	0.00E+00	139

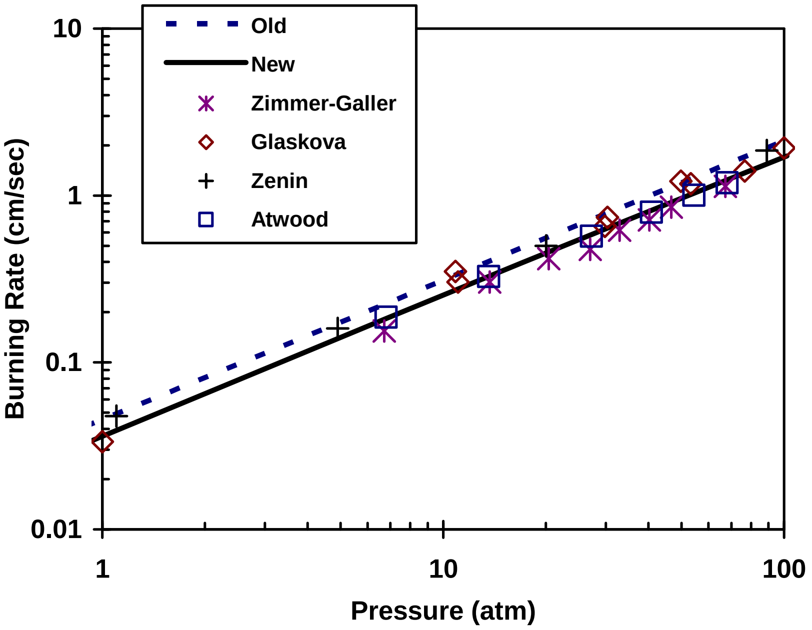

Figure 3-5: RDX burning rate calculations compared with data for two versions of the comprehensive gas-phase mechanism.[23,31,32,33]

3.5 Thermophysical Properties

Most of the thermophysical properties of RDX and GAP are the same values used by Davidson[15] and Puduppakkam.[125] However, the values of heat capacity and thermal conductivity used currently in the model for RDX are based on the measurements of Parr and Hanson-Parr,[140] whose data are more recent and more accurate than those originally used by Davidson, especially in the case of the thermal conductivity, which was previously only estimated. The difference between the model calculations that were based on the previous values and those that were based on Parr's data is insignificant. Most of these properties, with the exception of RDX heat capacity, do not vary with temperature in the model, due to two reasons. First, a relatively small temperature range occurs in the condensed phase. Second, no temperature dependence was reported in the literature.

Table 3-2: Thermophysical properties of RDX and GAP.

Property	Literature values[15,125,140]	Model values
Heat of formation of RDX (kcal/mol)	14.7	14.7
Heat of formation of GAP (kcal/g)	0.28, 0.229, 0.061, 0.33	0.118
Density of RDX (g/cm^3)	1.82,1.81, 1.75	1.81
Density of GAP (g/cm^3)	1.3,1.28,1.27	1.27
Thermal conductivity of RDX (cal/cm-sec-K)	4.06×10^{-4}, 1.75×10^{-4}, 3×10^{-4}, 5×10^{-4}, 7.6×10^{-4}, 6.65×10^{-4}	6.65×10^{-4}
Thermal conductivity of GAP (cal/cm-sec-K)	3.5×10^{-4}, 5.76×10^{-4}	5.76×10^{-4}
Heat capacity of RDX (cal/g-K)	0.0389+0.000703T, 0.269, 0.3, 0.35, 0.45, 0.00473+0.000843T	0.00473+0.000843T
Heat capacity of GAP (cal/g-K)	0.45, 0.385	0.45

3.6 Results and Discussion

The predicted burning rates of several compositions of RDX/GAP are shown in Figure 3-6. The burning rates of the mixture are lower than those of the pure ingredients, with the minimum near 60% RDX. There are several contributing factors. Combustion is driven by the heat feedback from the gas-phase and the heat release from the condensed-phase. RDX combustion is controlled mostly by the heat feedback from the gas phase while GAP is controlled mostly by the condensed-phase heat release. Addition of RDX to pure GAP results in a lower condensed-phase heat release and a lower burning rate. Addition of GAP to pure RDX results in a more fuel rich gas phase and an increase in inert species, N_2 and C(s), from GAP decomposition. These factors lower the flame temperature and the heat feedback to the surface, resulting in a lower burning rate.

The calculated pressure exponents, shown in Table 3-3, indicate a strong dependence on formulation. For 100% GAP and 45% RDX/55% GAP, the pressure exponent (slope in Figure 3-6) decreases as pressure increases. Although experimental data are limited, the calculated pressure exponents closely match the available data.

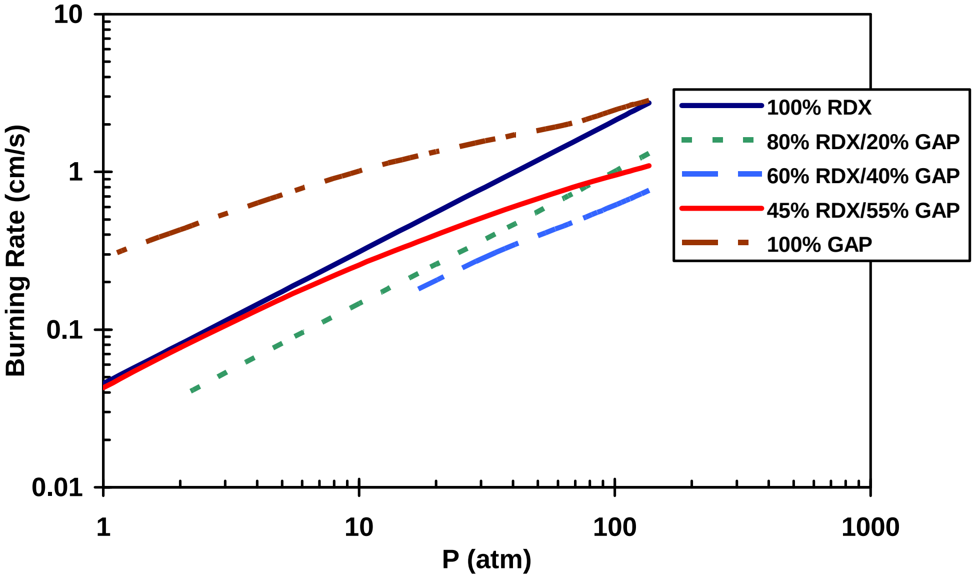

Figure 3-6: Calculated RDX/GAP burning rates as a function of pressure.

Table 3-3: Calculated and measured RDX/GAP pressure exponents.

% RDX	Calculated	Measured Value
100%	0.8	0.8 (Ref. 15)
80%	0.8	-----
60%	0.7	-----
45%	0.5 – 0.8	-----
0%	0.4 – 0.6	0.45 (Ref. 113, 114)

The calculated burning rate is a strong function of the composition, as shown in Figure 3-7 and Figure 3-8. The predicted values match the experimental trend of Flanagan et al.[120] for the compositions and pressures considered. The data and the model indicate a decrease in RDX/GAP burning rates below those of pure RDX or pure GAP, with a minimum near ~60% RDX. This phenomenon is related to the heat flux from the gas and condensed phases, discussed later in this section. Calculated burning rates for monopropellant RDX and GAP match experimental data closely. Calculated rates for monopropellant GAP match the data well at high pressures, but are significantly high at 17 and 6.8 atm. Calculated rates are significantly lower than experimental rates for 20, 45, and 70% RDX, possibly due to a few different factors. The high pressures may invalidate the premixed flame assumption for the ~15 micron RDX particle size, resulting in measured burning rates that are higher than the calculations. Another possibility is that there is significant chemical interaction between RDX and GAP in the condensed phase, which has not been accounted for. However, there is no evidence of this in the literature, so further changes have not been made to the condensed-phase mechanism.

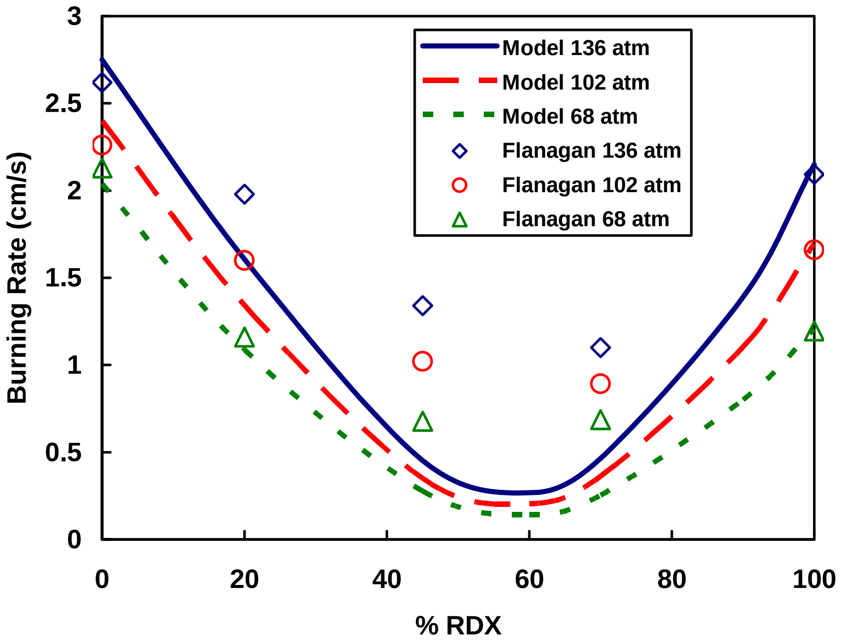

Figure 3-7: Predicted RDX/GAP burning rates as a function of RDX percentage at high pressures.

It would be beneficial if there were more experimental studies done to compare against the model calculations in addition to Flanagan's data. To determine if a premixed flame assumption is valid at pressures as high as 136 atm, experimental studies should be done with RDX particle sizes smaller than 15 microns. Particle size should be decreased until the burning rate no longer decreases, having reached the premixed flame limit.

Figure 3-8 shows the burning rate calculations compared with experimental data at lower pressures. Due to the fuel-rich nature of the RDX/GAP mixture, some of the compositions did not sustain combustion at low pressures. Flanagan did not report burning rates at 6.8 atm for 20% RDX and at 17 and 34 atm for 45% RDX, which may be related. However, with numerical modeling, it is possible to calculate a burning rate at those conditions, even though the propellant sample may self extinguish in reality.

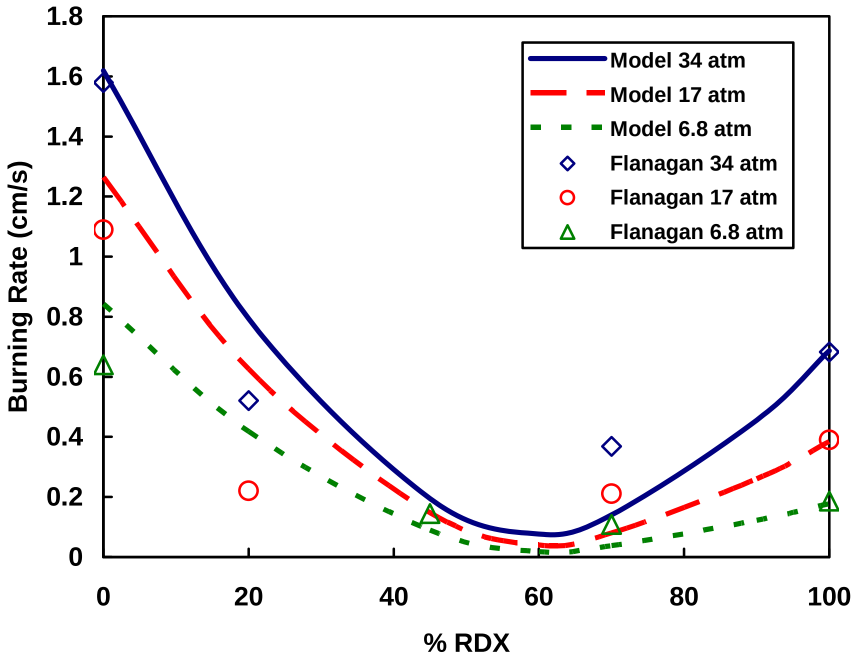

Figure 3-8: Predicted RDX/GAP burning rates as a function of RDX percentage at low pressures.

It is interesting to note that calculations are higher than the experimental data for 20% RDX at these low pressures, whereas they are consistently too low at other compositions and pressures. The high calculated rates at 20% RDX are probably related to the high rates for monopropellant GAP.

The heat feedback from the gas phase to the surface is shown in Figure 3-9. The heat feedback decreases sharply between 100% and 60% RDX. This is similar to the sharp decrease in the burning rate over the same range of compositions, showing that combustion is driven by the gas phase over that range. The low heat feedback for compositions of high GAP content is due to the exothermic condensed phase.

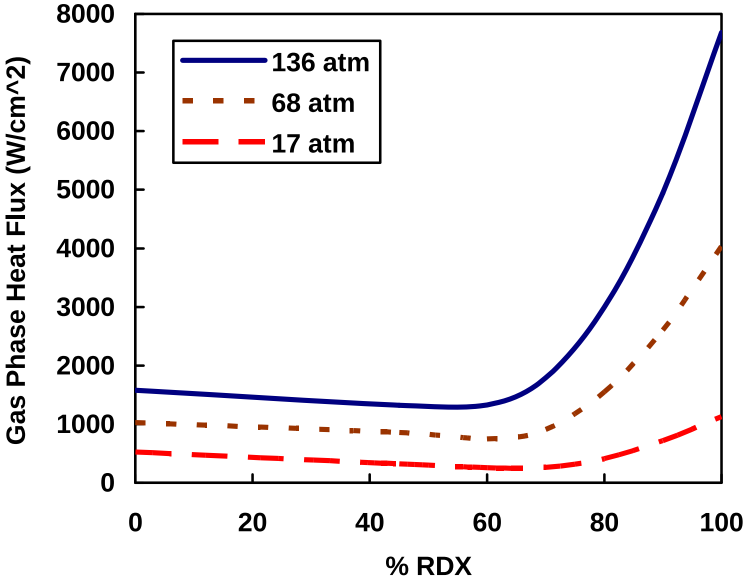

Figure 3-9: Calculated RDX/GAP gas-phase heat flux to the surface as a function of RDX percentage at 17, 68, and 136 atm.

The condensed-phase heat release is shown in Figure 3-10. GAP decomposition in the condensed phase is very exothermic (115 cal/g) compared to RDX, which is endothermic (-70 cal/g at 68 atm). RDX/GAP can be either endothermic (high RDX content) or exothermic (high GAP content) in the condensed phase. The condensed-phase heat release becomes significantly less exothermic between 0% and 60% RDX. This is similar to the significant decrease in burning rate over the same range of compositions, showing that combustion is driven by the condensed phase over that range.

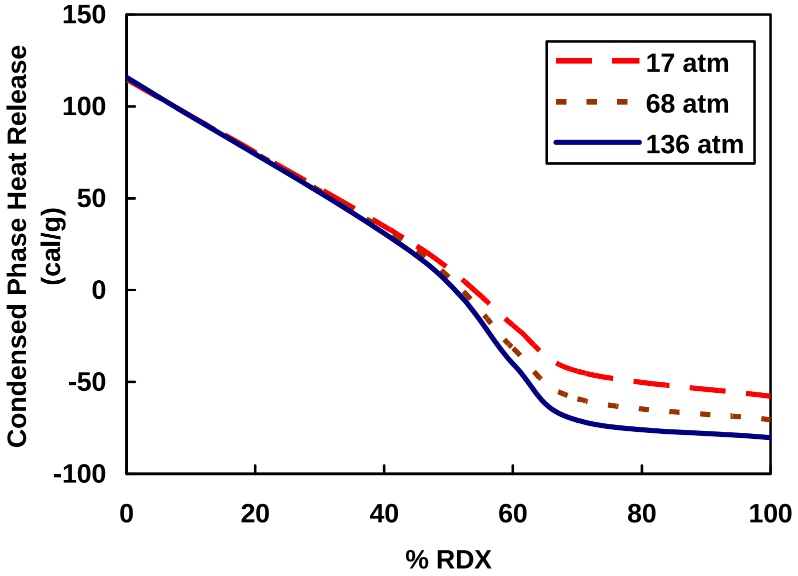

Figure 3-10: RDX/GAP condensed-phase heat release as a function of RDX percentage at 17, 68, and 136 atm.

Temperature sensitivity predictions are shown in Figure 3-11. The temperature sensitivity increases with increasing GAP content. The value for monopropellant GAP (~0.01) is about an order of magnitude higher than the value for monopropellant RDX (~0.001). GAP temperature sensitivity is predicted to decrease with increasing pressure while RDX temperature sensitivity does not vary with pressure. The calculations were made over an initial temperature range of 298 ± 50 K. Kubota et al.[60] reported a temperature sensitivity of ~ 0.002 K^{-1} for an 80% HMX/20% GAP pseudo-propellant (similar to RDX/GAP) and the model prediction for an 80% RDX/20% GAP pseudo-propellant is close to that value.

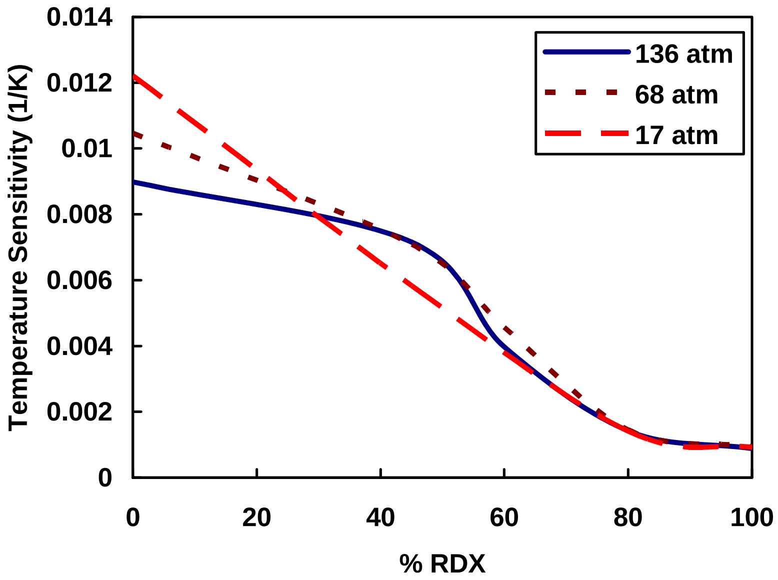

Figure 3-11: Predicted RDX/GAP temperature sensitivity as a function of RDX percentage at 17, 68, and 136 atm.

Litzinger et al. observed a dark zone during laser-assisted deflagration of an 80% RDX/20% GAP pseudo-propellant at 1 atm.[121] Laser-assisted combustion is a two-dimensional phenomenon since the laser flux intensity is a function of radius.[15,141] However, by allowing the flame cross-sectional area to expand as a function of distance from the propellant surface, the one-dimensional model can be made to approximate the observed two-dimensional characteristics.[15,141] Due to a minimal amount of data for the RDX/GAP pseudo-propellant, the expansion of the flame cross-sectional area has been taken to be 2.7 between 0.13 cm and 0.5 cm from the surface, which was calculated for the RDX monopropellant.[15,141] The predicted temperature profile for the 80% RDX/20% GAP pseudo-propellant at 1 atm with a laser flux of 100 W/cm^2 is compared with the experimental data of Litzinger et al.[121] in Figure 3-12. The predicted dark zone length of ~ 0.3 cm and dark zone temperature of ~ 1400 K match the experimental data well. The predicted burning rate of 0.09 cm/sec was close to the experimental value of 0.08 cm/sec.

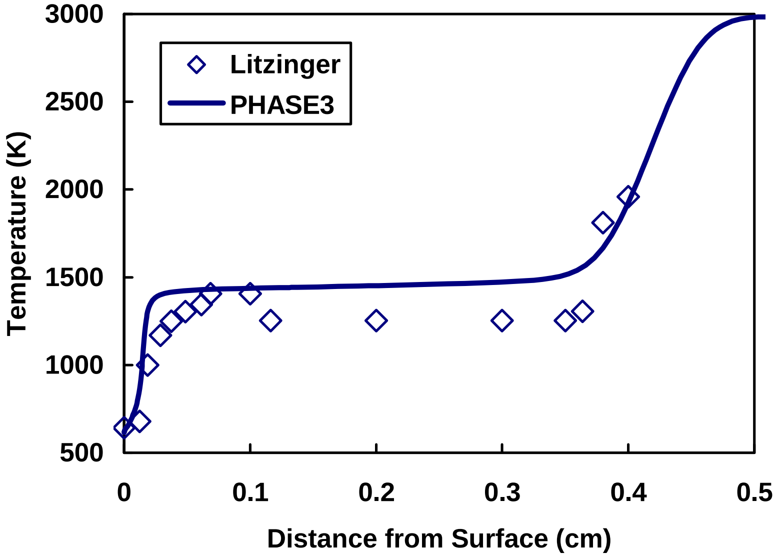

Figure 3-12: Calculated temperature profile for an 80% RDX/20% GAP pseudo-propellant at 1 atm with 100 W/cm^2 laser flux.

The adiabatic flame temperature calculated by PHASE3, using the comprehensive gas-phase mechanism, is shown in Figure 3-13 as a function of RDX percentage. It can be seen that the flame temperature increases with increasing RDX content. This trend has also been reported for RDX propellants with other binders.[142]

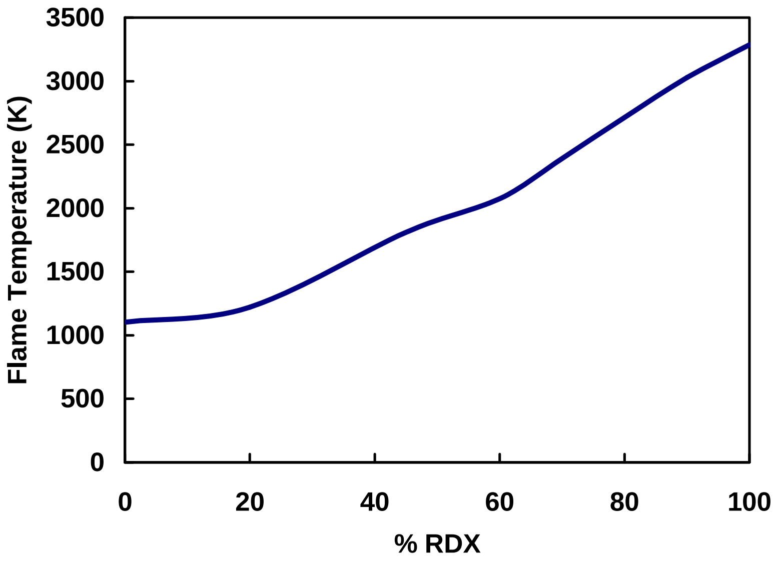

Figure 3-13: RDX/GAP flame temperature as a function of RDX percentage at 68 atm.

3.7 Summary and Conclusions

A one-dimensional model has been developed that simulates the combustion of different formulations of RDX/GAP pseudo-propellants. The burning rate has been determined to be strongly dependent on the formulation, with a minimum burning rate at a formulation of ~60% RDX/40% GAP. Combustion is driven by the gas phase for compositions between 100% and 60% RDX and by the condensed phase for compositions between 60% and 0% RDX. Temperature sensitivity increases with GAP content, while the pressure exponent decreases. The heat feedback decreases significantly and the condensed-phase decomposition becomes more exothermic with increasing GAP content. Dark zones have been predicted for laser-assisted combustion of 80% RDX/ 20% GAP at 1 atm. The predicted trends match those that have been observed experimentally, showing that this is a qualitatively valid model.

Improvements to the gas-phase kinetic mechanism have resulted in improved burning rate predictions for 100% RDX. However, calculated RDX/GAP burning rates are predominantly lower than experimental values for compositions between 100% RDX and 100% GAP. The low predictions are possibly due to the breakdown of the premixed flame assumption at high pressures. There may also be chemical interaction between RDX and GAP in the condensed phase that has not been included in the model.

3.8 Future Work

Due to the successful prediction of several important trends, this model is considered useful for qualitative calculations and has been used in the burning rate model discussed in Chapter 5. Further improvement to the model depends largely on the availability and detail of experimental data. Greater understanding of the condensed-phase kinetics is needed, including possible interaction between RDX and GAP. Hence, more experimental studies are needed that measure surface species while varying the percentage of RDX. Given the availability of such data, further work could be done to improve the condensed-phase mechanism. Further work on the comprehensive gas-phase mechanism may also result in improved agreement with experimental results. Application of the gas-phase kinetics to combustion models of more propellant ingredients would expose weaknesses and provide means for improving the comprehensive mechanism. More experimental studies are needed that measure RDX/GAP burning rates. Such studies should carefully control RDX particle sizes to ensure a premixed flame. This would provide means for further model development and validation. Without such studies, improvements to the model will be difficult to achieve.

4 One-Dimensional AP/HTPB Pseudo-Propellant Model

Ammonium perchlorate (AP) has been a major propellant ingredient for decades. AP is the standard ingredient in solid rocket propellants and is used in many applications, including a variety of missiles and space applications. Two reasons for AP's popularity are its stability, resulting in safe munitions, and its ability to control a propellant's burning rate. By varying the AP particle-size distribution it is possible to achieve vastly different overall propellant burning rates. No other known oxidizer has the capacity to control a propellant's burning rate in this way. This unique behavior of AP has not been accurately calculated using detailed numerical models without relying heavily upon empirical studies. Many studies have been performed on AP propellants, but most are concerned with particle-size and diffusion flame effects. Very few have focused on premixed AP/HTPB combustion.

Foster et al.[143] studied the effects of AP particle size on propellant burning rate. In some of the propellants he used monomodal 12 μm AP, which probably burns with a premixed flame at all but the highest pressures. He created AP/HTPB propellants containing 12 μm AP at AP concentrations of 75%, 77.5%, and 80%. The measured burning rates for the 12 μm AP propellants are shown in Figure 4-1. Foster reported that burning rate increased with AP percentage, a typical result for AP propellants. These data are used for model validation in the current study.

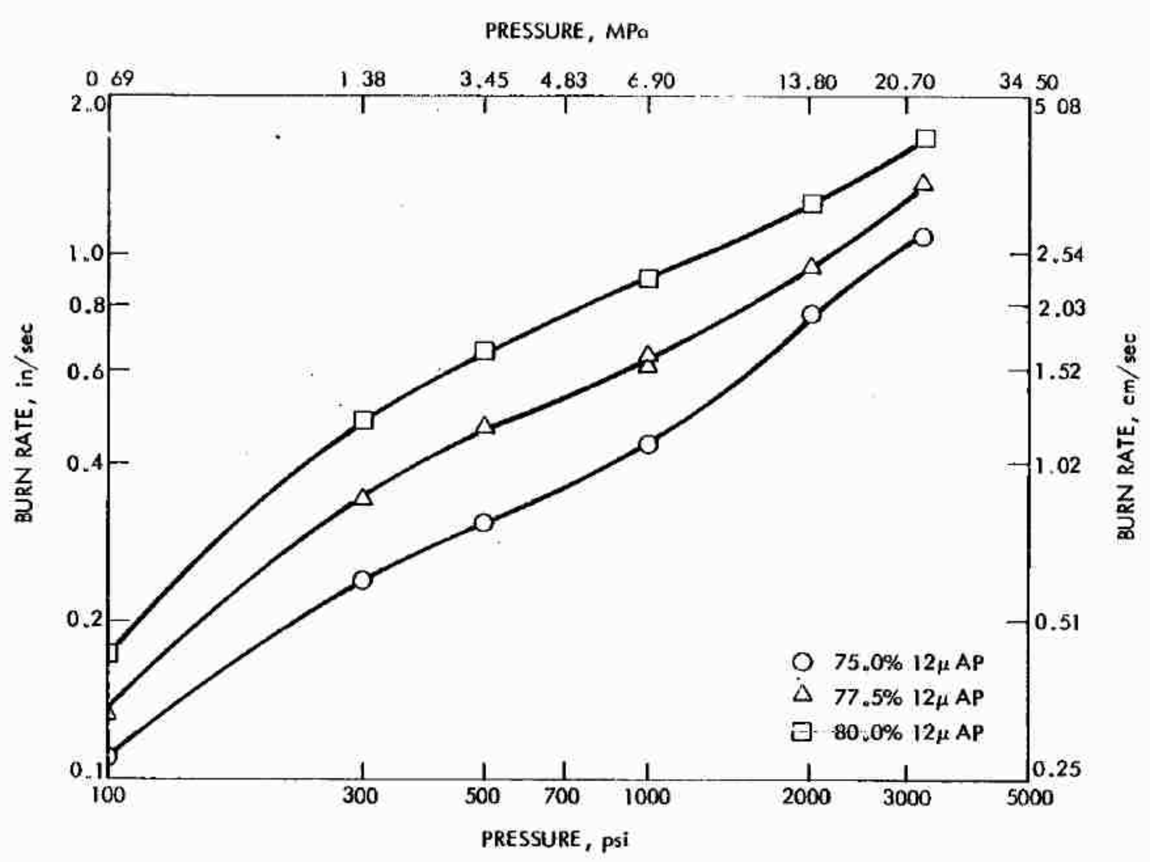

Figure 4-1: Foster's burning rate data for 12 μm AP/HTPB propellants.

Korobeinichev et al.[144,145] studied premixed AP/HTPB combustion by creating a homogeneous composite propellant consisting of 77% AP and 23% polybutadiene binder. Particle sizes were smaller than 50 μm and pressure was ~0.5 atm. They studied the gas flame with a mass spectrometer and reported surface species concentrations, shown in Table 4-1. They also modeled the results using a detailed kinetic mechanism consisting of 49 species and 243 reactions. Model results were reported to be "satisfactory." However, the measured flame temperature was 20% lower than the equilibrium value, and the final oxygen concentration was off by a factor of 2. Nevertheless, their data provide a qualitative understanding of the surface species of AP/HTPB premixed combustion.

Table 4-1: Korobeinichev's measured AP/HTPB surface species concentrations.

Species	H_2O	NH_3	ClOH	C_4H_6	CO_2	HCN	$HClO_4$	O_2	CO	NO_2	C_2H_2	H_2	N_2	NO	other
Wt%	36.9	11.1	7.9	6.7	6.0	5.6	5.3	3.6	3.4	2.5	2.3	1.8	0.7	0.3	5.9

Jeppson also developed a model to describe the premixed combustion of AP/HTPB propellants. AP particles were assumed to be small enough to simulate a homogeneous propellant. The model was based on a detailed gas-phase mechanism consisting of 44 species and 157 reactions. Figure 4-2 shows some of Jeppson's results compared with data from Foster. The model calculations match the experimental data very closely at 6.8 and 20.4 atm, but deviate from the data at higher pressures. There are several possible explanations, but the most likely seems to be that the premixed assumption is no longer valid at high pressure for Foster's 12 μm AP propellants.

The current study is a continuation of Jeppson's modeling work, employing PHASE3. New condensed- and gas-phase kinetic mechanisms have been employed and a wider range of propellant formulations modeled, from 59 to 80% AP. Foster's data are used for model validation, but to be certain that a premixed flame assumption is valid, only the data at 100 and 300 psi have been used. Korobeinichev's surface species data have only been used as a qualitative guide for determining the condensed-phase global mechanism, but have not been used for quantitative comparison with model calculations of surface species due to the uncertainty of the data.

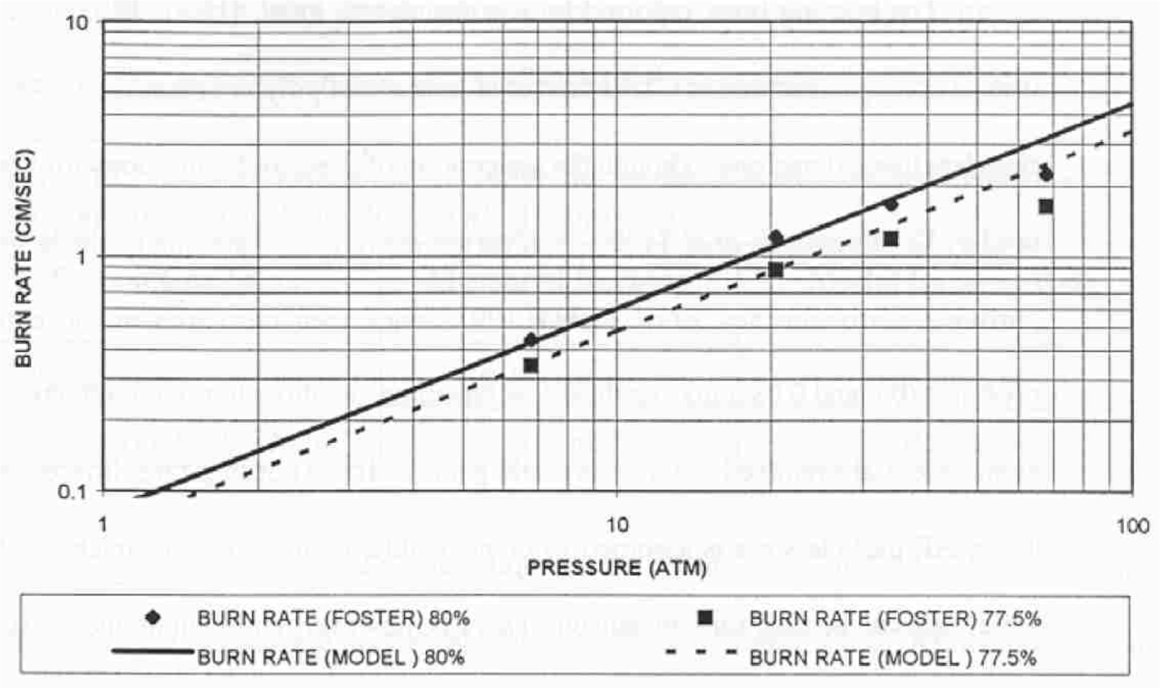

Figure 4-2: Jeppson's premixed AP/HTPB burning rate calculations compared with Foster's burning rate data at 77.5 and 80% AP.

4.1 Methodology to Develop New AP/HTPB Model

As a continuation of Puduppakkam's work to develop a comprehensive gas-phase mechanism, Gross[146,147] added reactions from several sources[37,41,148,149,150,151,152,153] to apply the mechanism to AP and ADN combustion models. The majority of the added reactions were for Cl-containing species and came from Lin,[148] who has performed extensive *ab initio* calculations of kinetic pathways relevant to propellant combustion. Previously, Puduppakkam's comprehensive mechanism had only been used to model the combustion of non-AP monopropellants and pseudo-propellants. The combination of 1) Puduppakkam's comprehensive mechanism, 2) the modifications made to the H_2CNNO_2 reactions for the RDX/GAP model, and 3) the additions by Gross, make up what will be referred to as the universal gas-phase mechanism, which contains 106 species and 611 reactions (Appendix B). The steps taken to incorporate the universal mechanism into Jeppson's AP/HTPB model, and to extend the model to a wider range of compositions than previously modeled by Jeppson, are discussed in this section.

4.1.1 New Condensed-Phase Mechanism #1

Jeppson used a 9-step mechanism in his original model to describe AP/HTPB decomposition in the condensed phase. He included 2 steps describing HTPB decomposition, 3 steps describing interaction between AP and HTPB, and 4 steps describing AP decomposition. He defined the propellant surface, or the interface between the condensed phase and gas phase, as the location where 99.9999% of the condensed-phase material had decomposed to gas-phase species. Any remaining AP and HTPB, although insignificant amounts, were decomposed to gas-phase species via one of the pure AP and pure HTPB decomposition reactions, respectively.

Mike Hawkins, a student at BYU, performed research on Jeppson's condensed-phase mechanism, in conjunction with the universal gas-phase mechanism, in an initial effort to develop a working AP/HTPB model.[154] His work resulted in low burning rate predictions for formulations of 75%, 77.5%, and 80% AP. He achieved the best results using a single global reaction for each AP percentage, but below 80% AP, predictions of the final flame temperature and final species concentrations were poor.

The species coefficients of the condensed-phase reactions for 75%, 77.5%, and 80% AP, that he considered to be his best attempted variations, are presented in Table 4-2. Hawkins sought to maintain reasonable trends in the species coefficients as AP percentage decreased. The coefficients of AP decomposition products ($HClO_4$, ClOH, and NH_3) decrease with AP percentage, and the coefficients of HTPB decomposition products (C_4H_6 and C_2H_2) increase as AP percentage decreases, which is consistent. However, the coefficients of H_2O, H_2, and CO do not show a consistent pattern.

Table 4-2: Best AP/HTPB condensed-phase reactions for 75, 77.5, and 80% AP, as determined by Hawkins.

%AP	Reactants		Products										Kinetic Parameters	
	HTPB	AP	C_4H_6	CO	H_2O	HCN	H_2	CO_2	ClOH	C_2H_2	NH_3	$HClO_4$	A (1/s)	E (cal/mole)
80	1	41	8	4	35	20	30	22	27	4	21	14	$1.40\text{x}10^{11}$	$1.10\text{x}10^{4}$
77.5	1	36	9	5	34	17	23	16	23	6	19	13	$1.40\text{x}10^{11}$	$1.10\text{x}10^{4}$
75	1	31	10	10	34	13	15	9	20	7	18	11	$1.40\text{x}10^{11}$	$1.10\text{x}10^{4}$

Calculated burning rates, using the condensed-phase reactions in Table 4-2 together with the universal gas-phase mechanism, are in good agreement with experimental data. However, he was unable to calculate the correct final flame temperature or final species concentrations below 80% AP, as shown in Figure 4-3. It is evident that as AP percentage decreases, the deviation between PHASE3 and equilibrium calculations increases. There are also some species predicted by PHASE3 that are not predicted in the equilibrium calculations. These include C_2H_2, CH_4, HCN, HNCO, and NH_3. Jeppson noticed a similar deviation in the final flame temperature and species concentrations below 80% AP with his model.[20]

Based on Hawkins research, it was clear that the combination of his proposed condensed-phase mechanism and the universal gas-phase mechanism was insufficient, and further work was needed.

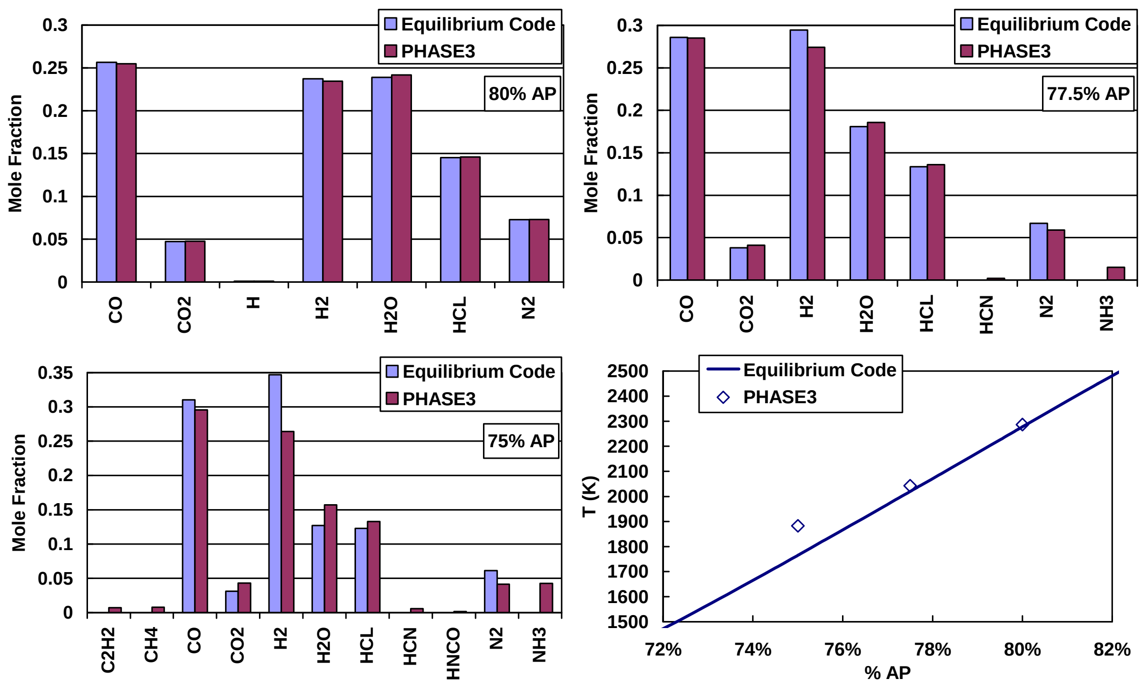

Figure 4-3: Comparison of PHASE3 and equilibrium final flame temperatures and species concentrations for 80%, 77.5%, and 75% AP at 20.4 atm (300 psi).

4.1.2 New Condensed-Phase Mechanism #2

Several new condensed-phase reactions were used in PHASE3 in conjunction with the universal gas-phase mechanism, with the goal to improve trends in the quantities of the products of those reactions while maintaining the accuracy of the burning rate calculations. In addition, three new compositions were modeled—70%, 65%, and 59%. Fifty-nine percent was chosen instead of 60% to match the formulation of the space shuttle propellant. If the fine AP in the shuttle propellant is assumed to be mixed homogeneously with the binder, the resulting pseudo-binder composition is 59% AP/41% binder. The species coefficients of the condensed-phase reactions which gave the best results are presented in Table 4-3. The trends in the product coefficients are a little more consistent than before. For example, the amount of CO increases more steadily from 4 to

6 to 8 as AP decreases from 80% to 77.5% to 75%. H_2O also decreases with AP percentage in a more consistent fashion. Another species, CH_4, which was also included by Jeppson, was added to facilitate balancing the hydrocarbon species.

Table 4-3: Best condensed-phase reactions when combined with the universal gas-phase mechanism for AP/HTPB compositions from 59% to 80% AP.

%AP	Reactants		Products											Kinetic Parameters	
	HTPB	AP	C_4H_6	CO	H_2O	HCN	H_2	CO_2	ClOH	CH_4	C_2H_2	NH_3	$HClO_4$	A (1/s)	E (cal/mole)
80	1	41	8	4	35	20	30	22	27	0	4	21	14	$1.40x10^{11}$	$1.10x10^4$
77.5	1	36	9	6	33	17	23	16	23	1	5	19	13	$1.40x10^{11}$	$1.10x10^4$
75	1	31	10	8	31	13	16	10	19	1	7	18	12	$1.40x10^{11}$	$1.10x10^4$
70	1	24	12	11	27	7	7	3	14	1	8	17	10	$1.40x10^{11}$	$1.10x10^4$
65	1	19	14	12	20	3	5	0	10	1	7	16	9	$1.40x10^{11}$	$1.10x10^4$
59	1	15	16	12	8	0	9	0	6	2	4	15	9	$1.40x10^{11}$	$1.10x10^4$

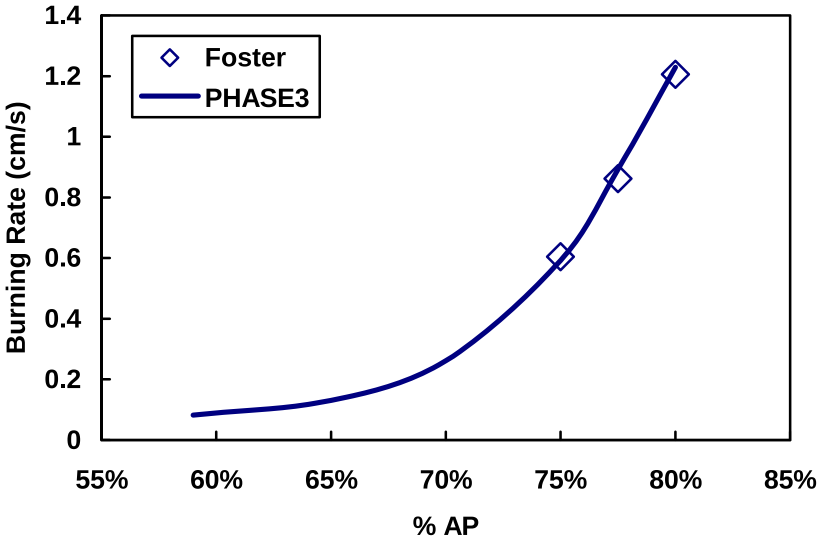

Figure 4-4: Calculated burning rates compared with Foster's data for 59% to 80% AP at 20.4 atm (300 psi).

Calculated burning rates at 300 psi, based on these reactions, are presented in Figure 4-4. The calculations match experimental data very well. Although there are no data with which to compare the model calculations below 75% AP, the trend in the burning rate is consistent with the flame temperature and seems reasonable.

Despite the promising burning rate results, there was no improvement in the calculation of final products or flame temperature. The results for 80%, 77.5%, and 75% remained the same, but for 70%, 65%, and 59%, there were even greater discrepancies in the final species concentrations, as shown in Figure 4-5.

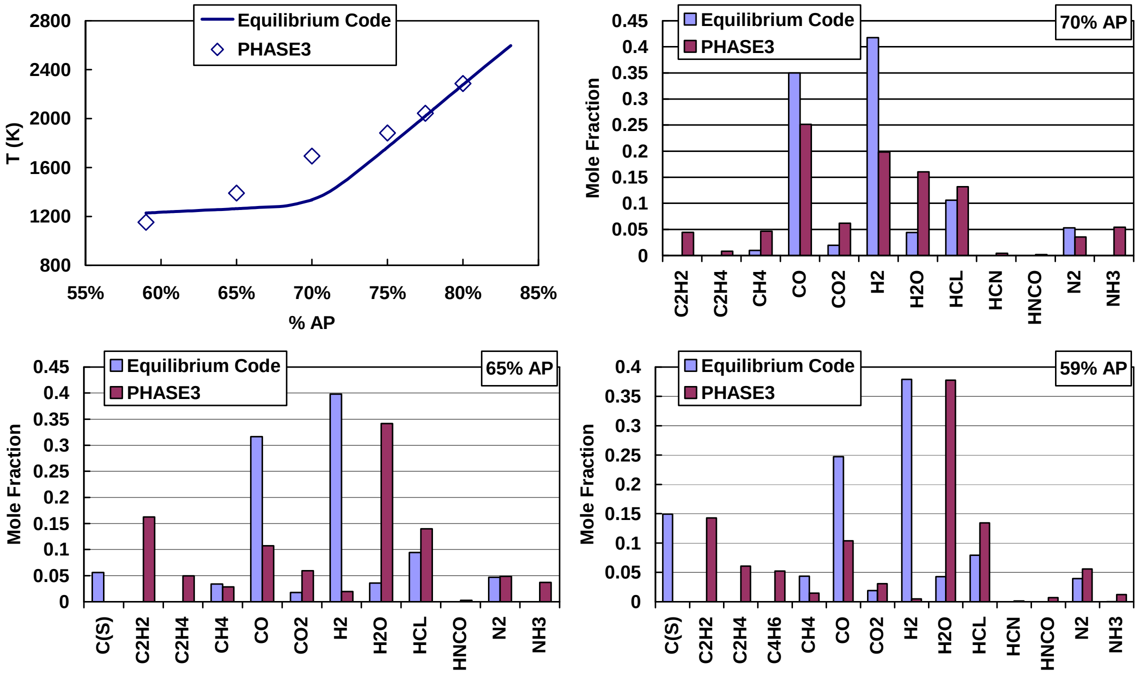

Figure 4-5: Comparison of PHASE3 and equilibrium final flame temperatures and species concentrations for 70%, 65%, and 59% AP at 20.4 atm (300 psi).

As AP percentage decreases, the flame temperature deviates significantly from the flame temperature calculated by Edwards, but then approaches the equilibrium value once again. The improved agreement between PHASE3 and the equilibrium flame temperature at 59% AP, however, is not indicative of a working model. The final species calculations demonstrate how the model gets increasingly less accurate as AP percentage continues to decrease from 70% to 59% AP. There are clearly major deficiencies in the gas-phase universal mechanism. It should be noted that there are no reactions in the universal mechanism for solid carbon, C(S), which begins to appear at compositions below 70% AP in equilibrium calculations. This is one obvious deficiency, but it does not completely account for the inaccuracies at 65% and 59% AP, nor does it account to any extent for the inaccuracies at 70% AP.

4.1.3 Gas-Phase Mechanism Deficiencies

As an initial exploration of the shortcomings of the universal mechanism, a study was performed to investigate the presence of several species in the final products predicted by PHASE3 which were not predicted by equilibrium calculations. These include C_2H_2, C_2H_4, HCN, HNCO, and NH_3. C_4H_6 was ignored in this study because it was less prevalent than the other hydrocarbons, C_2H_2 and C_2H_4. An irreversible elimination reaction was separately introduced into the universal mechanism for each of these species. These reactions are presented in Table 4-4. The pre-exponential parameter for each reaction was optimized with respect to the calculation of final temperature and species concentrations. Calculations of final species concentrations were made at 70% AP and 20.4 atm (300 psi), using each of these reactions one by one. Seventy percent was chosen because the model at 70% was the most inaccurate of the formulations that did not form solid carbon.

Table 4-4: Elimination reactions tested with the universal gas-phase mechanism.

Species	Reaction	A (1/s)	b	E (cal/mole)
C_2H_2	$C_2H_2 \rightarrow C_2H + H$	$1.0\mathrm{x}10^8$	0	0
C_2H_4	$C_2H_4 \rightarrow C_2H_2 + H_2$	$1.0\mathrm{x}10^7$	0	0
HCN	$HCN \rightarrow H + CN$	$1.0\mathrm{x}10^7$	0	0
HNCO	$HNCO \rightarrow NH + CO$	$1.0\mathrm{x}10^6$	0	0
NH_3	$NH_3 \rightarrow NH + H_2$	$1.0\mathrm{x}10^4$	0	0

The elimination reactions for HCN, C_2H_2, and NH_3 all had a positive effect on the final species concentrations, but HCN produced the best results by far. The final products calculated in PHASE3, with the HCN elimination reaction added to the universal mechanism, are presented in Figure 4-6. There is an extraordinary improvement, resulting in almost perfect agreement with equilibrium calculations. There is a corresponding improvement in agreement with the final flame temperature. With the universal mechanism, PHASE3 calculates a flame temperature of 1696 K, which is 27% higher than the equilibrium temperature of 1335 K. With the HCN elimination reaction included, PHASE3 calculates a flame temperature of 1308 K, which is only 2% low. Excellent agreement with equilibrium calculations of flame temperature and final species was also achieved at 75%, 77.5%, and 80% AP. The remarkable improvement indicates that the missing chemistry in the universal mechanism is most likely related to HCN decomposition. However, due to the complexity of the mechanism, which contains 611 reactions and 106 species, it is difficult to pinpoint exactly what is missing.

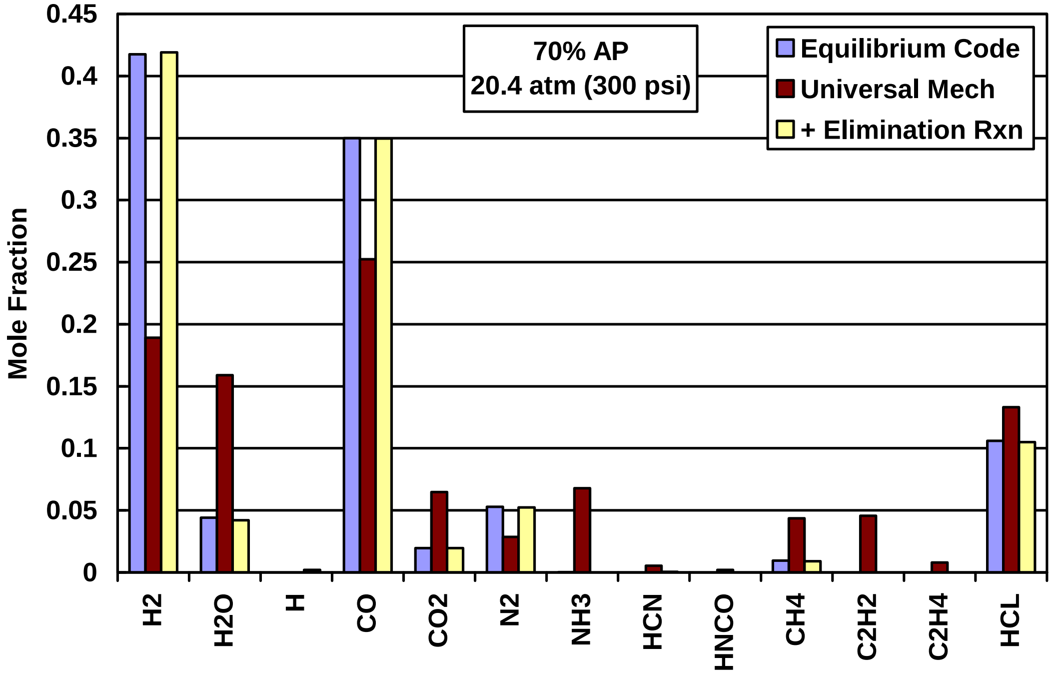

Figure 4-6: Calculated final species concentrations from PHASE3, with and without the HCN elimination reaction, compared with equilibrium calculations.

Since HCN elimination produced the best results, the HCN-containing reactions currently in the universal mechanism were investigated in order to find a more theoretically-based solution to the deficiencies of the universal mechanism. Modifications were made to the pre-exponential Arrhenius parameter of those reactions and the final flame temperature was monitored. The reactions that were investigated were those that eliminated HCN and formed other species whose calculated final concentrations were too low. A sensitivity analysis was also performed with PHASE3 to determine which of these reactions would have a significant impact on the burning rate calculations. The reactions that looked reasonable and were found to be significant are shown in Table 4-5. For each of the reactions, the pre-exponential value was increased and decreased by several orders of magnitude and the flame temperature was calculated. The best calculated flame temperatures for each reaction are included in Table 4-5. Since the calculated flame temperature was originally 1696 K and the target value was 1335 K, there was clearly very little improvement in the model due to these modifications. Hence, the HCN elimination reaction from Table 4-4 was kept in the universal mechanism as a temporary solution to the AP/HTPB model until improved chemical reactions and kinetic parameters for reactions involving HCN can be found. Once it was decided to keep the HCN reaction, a more in-depth investigation was performed to determine the best value of the pre-exponential parameter. It was found that a value of 1.6×10^6 was the lowest possible value that still corrected the calculation of flame temperature and final species concentrations. Therefore, the lower value replaced the previous value of 1.0×10^7 which was reported in Table 4-4.

Table 4-5: HCN reactions of the universal gas-phase mechanism that were modified to improve the final flame temperature and species calculations.

Reaction	Original Kinetic Parameters			Best Flame Temperature (K)
	A (1/s)	b	E (cal/mole)	
HCN = HNC	2.06E14	-1.11	4.37E4	1691
HCN + OH = NH_2 + CO	7.83E-4	4.00	4.00E3	1693
HCN + OH = H_2O + CN	3.90E6	1.83	1.03E4	1693
HCN + O = NH + CO	3.45E3	2.64	4.98E3	1692
HCN + O = NCO + H	1.38E4	2.64	4.98E3	1693

Another concern with the universal mechanism was the absence of any solid carbon reactions, which completely eliminates any possibility of predicting the final products correctly for formulations of less than 70% AP. Two possible approaches were considered that would account for the solid carbon formation. The first possibility was to look for reactions from the literature, especially the online NIST database,[152] and add them to the universal gas-phase mechanism. The second possibility was to include the equilibrium amount of solid carbon in the condensed-phase reaction. Since the solid carbon would not react in the gas phase, the correct amount would be predicted in the final products as well. Due to 1) the extensive amount of research that would be required in attempting the first approach, 2) the significant increase in the complexity of the gas-phase mechanism that would result, and 3) the fact that the second approach has been taken by others in the past,[17,125] it was decided that the solid carbon would be included in the condensed-phase mechanism. This approach is described in the section describing the final condensed-phase mechanism.

4.1.4 Extrapolation of Foster Data

Although there is no experimental burning rate data for premixed AP/HTPB combustion below 75% AP, formulations with as low as 59% AP have still been modeled in the current study. To validate the model at these AP percentages, it was proposed by Beckstead to develop a correlation between Foster's experimental burning rate data and equilibrium flame temperature calculations.[155] In this way, Foster's data could be extrapolated below 75% AP based on flame temperature trends. The 3-parameter function used for the correlation is a combination of a power law pressure correlation, typically used for propellant burning rates, and an Arrhenius flame temperature correlation (Equation (4-1)). Burning rate (r) is in units of cm/s, pressure (P) in atm, and flame temperature (T_f) in Kelvins. The parameter values of b, n and E/R (0.677, 0.833, and 4538) were determined by a least squares fit of Foster's burning rate data with calculated adiabatic flame temperatures at 6.8 and 20.4 atm and at 75%, 77.5%, and 80% AP.

$$r = bP^n \exp(-E/RT_f) \tag{4-1}$$

The calculated rates are presented in Figure 4-7, compared with Foster's burning rate data and the calculated adiabatic flame temperatures. The calculated burning rates clearly follow the trend in the flame temperature, which decreases with AP percentage and levels out somewhat at about 70% AP. The calculated burning rates will be used to validate the AP/HTPB model for formulations below 75% AP.

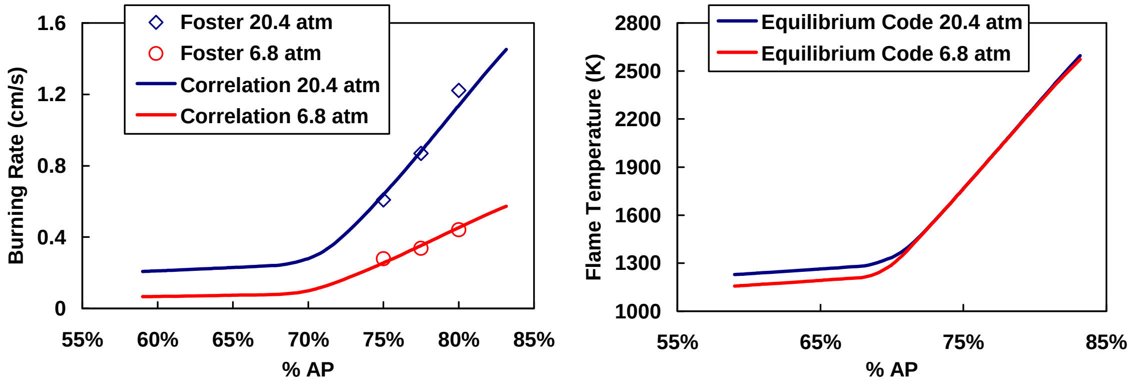

Figure 4-7: Extrapolation of experimental burning rate data using a flame temperature correlation.

4.1.5 Final Condensed-Phase Mechanism

With the addition of the HCN elimination reaction to the universal gas-phase mechanism, the calculated burning rates that resulted from the condensed-phase reactions in Table 4-3 increased significantly due to the presence of HCN as one of the condensed-phase decomposition products. With HCN as a surface species, the addition of an HCN-containing reaction caused an increased gas-phase heat flux back to the surface and thus, an increased burning rate. Therefore, a new set of condensed-phase reactions was needed to reduce the high burning rates back down to the level of the data.

While investigating new condensed-phase reactions, it became clear that slightly different AP percentages should be used to facilitate the establishment of reasonable trends in the condensed-phase mechanisms and to ensure that the percentages of AP and HTPB more closely matched their concentrations in the condensed-phase reactions.

Another important factor was the inclusion of solid carbon, C(S), in the condensed-phase mechanism for formulations of less than 70% AP. Since there were no C(S) reactions in the gas phase, the final mass fraction would be the same as the initial, or surface, mass fraction which resulted from the condensed-phase mechanism. Therefore, the mass fraction of C(S) calculated with the Edwards Equilibrium Code was used to determine the proper numeric coefficient of C(S) in the condensed-phase mechanism at each AP percentage. With the inclusion of solid carbon, the amounts of other species had to be modified to balance the reactions. The initial result was an increase in burning rate for the affected formulations. However, the species coefficients were further adjusted to correct the burning rate and to match the data as closely as possible.

The final condensed-phase mechanisms are shown in Table 4-6. The quantities of each species were doubled from previous values to allow for greater variation in the quantities of the products, which facilitated matching the burning rate data. To be consistent, the pre-exponential factor of each reaction was cut in half, changing from $1.4\text{x}10^{11}$ to $0.7\text{x}10^{11}$. The kinetic parameters were not modified in any other way from the previous versions in Table 4-3.

Table 4-6: Final AP/HTPB condensed-phase mechanism.

%AP	Reactants		Products													
	HTPB	AP	C_4H_6	CO	H_2O	HCN	N_2	H_2	CO_2	ClOH	HCl	CH_4	C_2H_2	NH_3	$HClO_4$	C(S)
79.90	2	82	22	4	88	20	8	12	12	32	4	0	24	46	46	0
77.73	2	72	24	6	78	16	8	14	10	28	4	0	22	40	40	0
75.03	2	62	26	8	68	12	8	16	8	24	4	0	20	34	34	0
71.59	2	52	28	12	37	8	5	30	4	15	2	0	18	34	35	0
65.97	2	40	27	11	25	3	4	39	1	10	1	0	16	29	29	17
59.25	2	30	20	4	0	0	0	69	0	0	0	1	15	30	30	57

Consistent trends have been established in the quantities of product species in the condensed-phase reactions for compositions of 79.90%, 77.73%, and 75.03% AP. However, to more closely match the extrapolated burning rate data, and to include solid carbon, the trends do not continue in exactly the same manner below 75.03%. N_2 has been added as a decomposition product and CH_4 has been removed (except at 59.25% AP) to more closely match the surface species measurements of Korobeinichev. Another species, HCl, has also been added to facilitate the balancing of the reactions. Korobeinichev did not measure HCl directly, but he did not account for 5.9% of the mass leaving the propellant surface, so it may have been present.

Burning rates were calculated using PHASE3 with the condensed-phase mechanism of Table 4-6 and the universal gas-phase mechanism, including the additional HCN elimination reaction. These calculations are compared with Foster's extrapolated burning rate data in Figure 4-8, with very good agreement. The calculated rates at both pressures for 59.25% and 65.97% AP are slightly higher than the extrapolated data. This is mainly due to the inclusion of C(S) in the condensed-phase mechanism, which limits the possible variations of the condensed-phase reactions that can be investigated, and therefore limits the burning rate as well. Several variations of the 59.25% AP reaction were investigated with the intent to lower the burning rate. Unfortunately, the lowest burning rate achieved with this approach was still higher than the desired value of the extrapolated data. The reactions for 65.97% and 71.59% AP could have been modified even more to achieve a lower burning rate, but were left as shown in Table 4-6 to be consistent with the high calculated burning rate at 59.25% AP. High calculated burning rates at 20.4 atm for 75.03%, 77.73%, and 79.90% AP are attributed to the complexity of juggling multiple tasks simultaneously, which include matching experimental burning rates, matching final products and flame temperatures predicted at equilibrium, and establishing consistent trends in the condensed-phase mechanism.

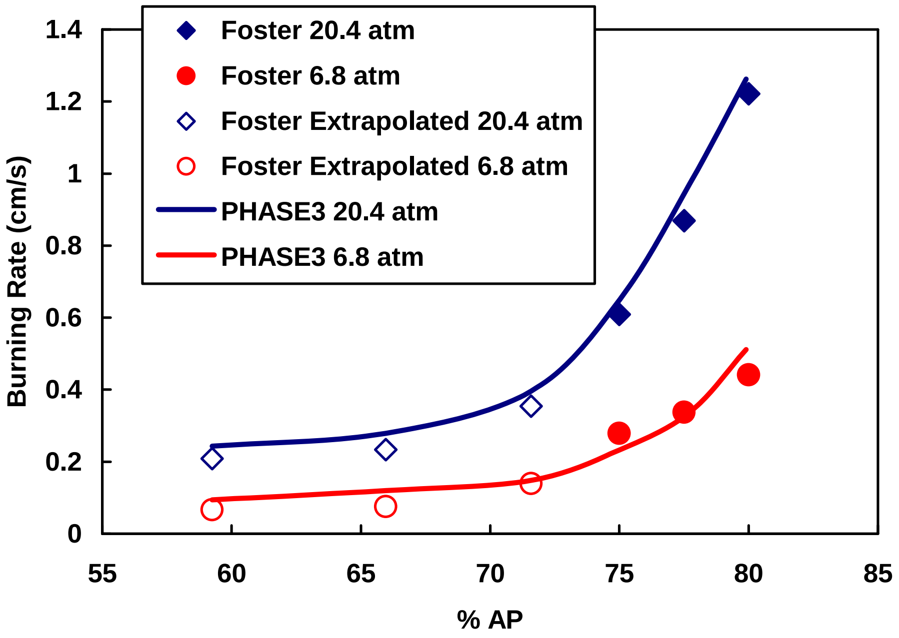

Figure 4-8: Calculated AP/HTPB burning rates as a function of AP percentage compared with Foster's extrapolated data at 6.8 and 20.4 atm (100 and 300 psi).

Flame temperatures calculated with PHASE3, using the universal gas-phase mechanism and the modified universal mechanism, are compared with equilibrium flame temperatures in Figure 4-9. The problems with the universal mechanism are very evident, based on the huge deviation in flame temperature from the equilibrium values. However, with the HCN elimination reaction included in the mechanism, the agreement is excellent.

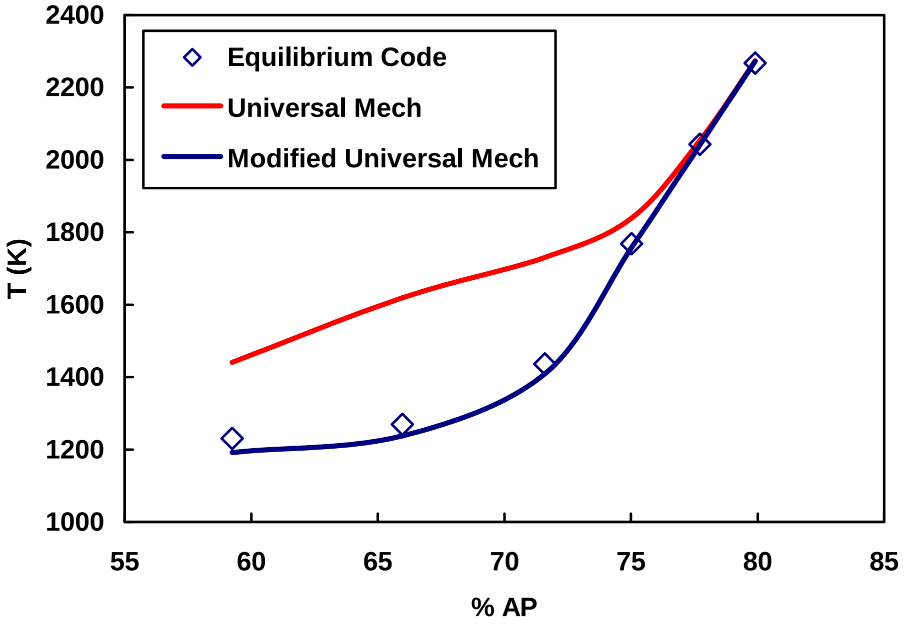

Figure 4-9: Improvements in the flame temperature calculation with the addition of the HCN elimination reaction in the universal mechanism.

The agreement in the final products also improves dramatically along with the flame temperature. The composition that previously resulted in the worst agreement with final products and flame temperature was 59% AP, partly due to the solid carbon, but also due to the inherent problems in the gas-phase mechanism. The final species concentrations were calculated with PHASE3 for 59.25% AP at 20.4 atm with the new condensed-phase mechanism and with the modified universal gas-phase mechanism. The results are presented in Figure 4-10 and are very comparable to those of Figure 4-6, calculated for the 70% AP, 20.4 atm, non-carbon containing condition. In both cases, there is a dramatic improvement in the final species concentrations. The improved agreement also occurs for all the AP percentages that were modeled.

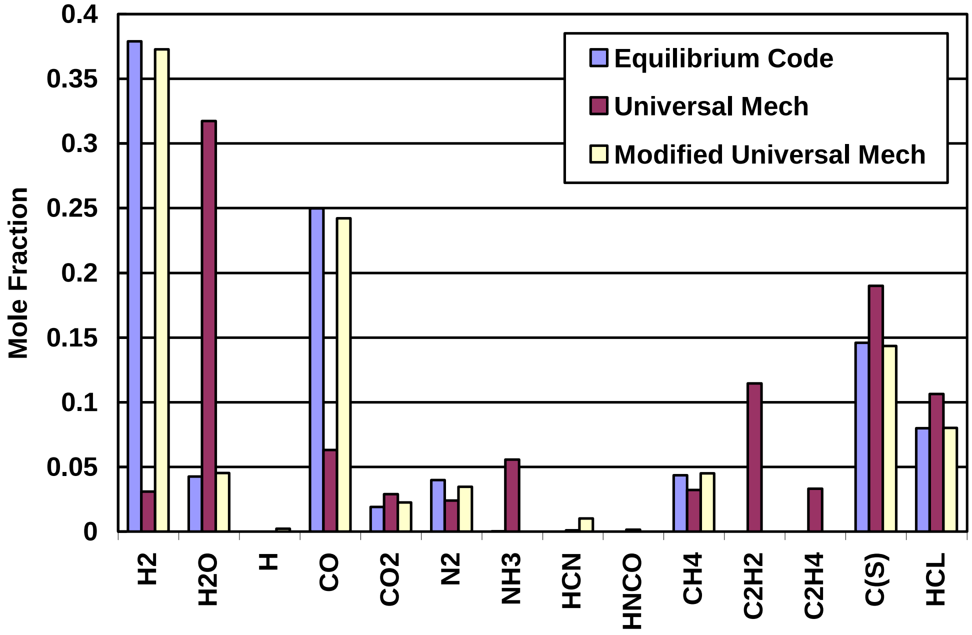

Figure 4-10: Improvement in final species concentrations for 59.25% AP at 20.4 atm with the modified universal mechanism.

4.1.6 Addition of Inert Aluminum

For the purpose of modeling aluminum agglomeration in the shuttle propellant, inert aluminum was added as both a condensed- and a gas-phase species to the AP/HTPB model at 59.25% AP. This was done to simulate the pseudo-binder in the shuttle propellant, which is assumed to contain all of the fine AP and all of the aluminum. The resulting pseudo-binder composition is 40.87% AP, 27.87% binder, and 31.26% aluminum, which is an AP/binder ratio of 59.45/40.55, very close to 59.25%. The binder in the shuttle propellant is PBAN, not HTPB, but the chemical formulations of the two binders are very similar, so the AP/HTPB model is assumed to be adequate. The aluminum is treated as an inert because it burns mostly far from the propellant surface and the goal of this study is to model its effects as an inert heat sink in the condensed phase, and near the surface in the gas phase.

During combustion, aluminum is in a solid or liquid state in the condensed phase and near the surface in the gas phase. Although aluminum was added to the model as both a condensed- and a gas-phase species, it was assigned the properties of solid and liquid aluminum, depending on the temperature, in both phases, in order to keep the model as realistic as possible. Solid and liquid aluminum properties, including the heat of fusion, were taken from the JANAF tables[156] and converted into a form compatible with the CHEMKIN subroutines used in PHASE3 (Appendix C).

The addition of inert aluminum into the gas phase made it so the calculated flame temperature and final products at equilibrium could no longer be corrected with the addition of the HCN elimination reaction. It is not fully understood why this is the case. One possibility is that the inert aluminum acts as a strong enough heat sink so that there is not sufficient energy remaining in the gas phase to reach equilibrium via the HCN reaction. However, since the purpose of adding aluminum to the AP/HTPB model is to study the near-surface phenomena, the poor agreement with final products and flame temperature at equilibrium is not considered a significant drawback.

4.2 Results and Discussion

Having determined the final condensed- and gas-phase mechanisms for the AP/HTPB model, combustion characteristics were calculated at compositions ranging from 59.25% to 79.90% AP and at pressures ranging from 1 to 136 atm. The shuttle pseudo-binder formulation containing inert aluminum was also modeled over the same pressure range. Since flame temperature and final species results have already been presented in Figure 4-9 and Figure 4-10 to a large degree, these are not repeated here.

Calculated burning rates are presented in Figure 4-11. The results are fairly consistent, with burning rate increasing with pressure and AP percentage. As expected, the presence of inert aluminum results in a lower burning rate due to its behavior as a heat sink and also because its presence displaces some reactive AP and HTPB.

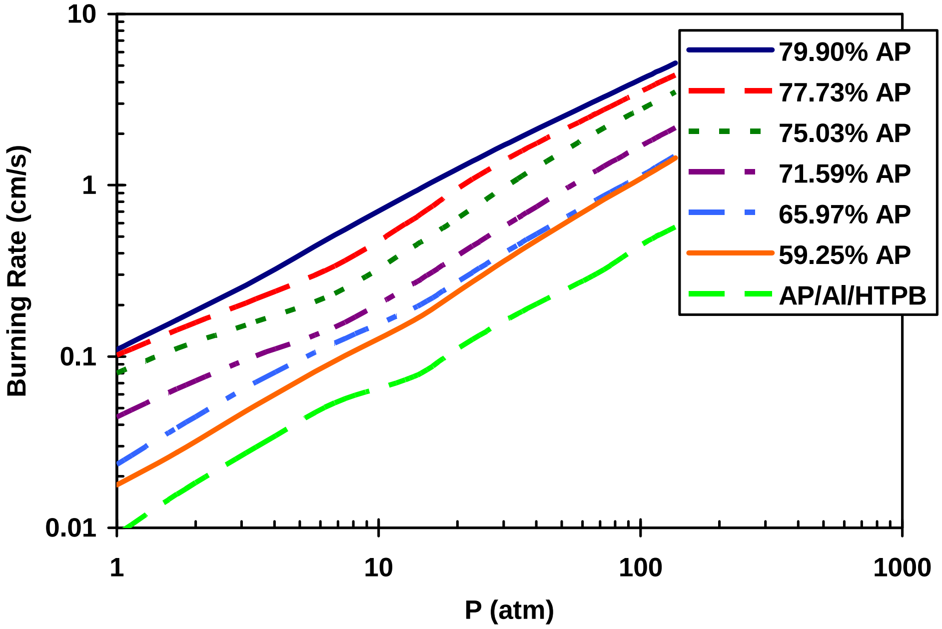

Figure 4-11: Calculated AP/HTPB and AP/Al/HTPB burning rates from 1 to 136 atm.

The condensed-phase heat release as a function of AP percentage at 20.4 atm is presented in Figure 4-12. The condensed phase is endothermic for all AP percentages. There is no significant variation with pressure, so only one pressure is shown. These results are very closely related to the condensed-phase mechanism (Table 4-6). There are very consistent trends in the mechanism from 75.03% to 79.90% AP, and the condensed-phase heat release shows a corresponding linear trend over that range. However, the modifications that were made to the mechanism at the lower AP percentages, for the purpose of matching experimental burning rates and including solid carbon as a condensed-phase species, resulted in a sharp increase in the endothermic nature of the condensed phase. The inert aluminum seems to act as a diluting agent, displacing some of the reactive material and creating a less endothermic condensed phase.

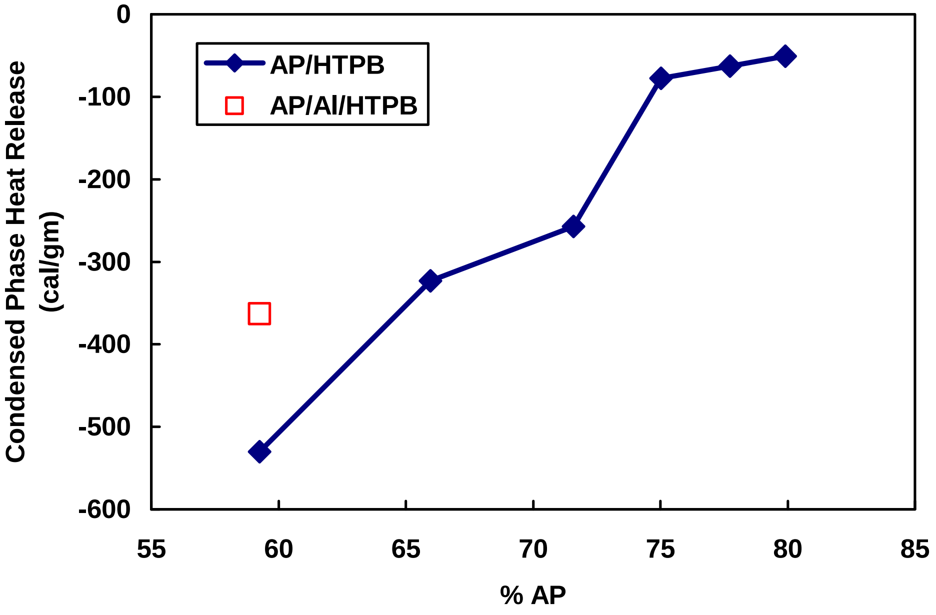

Figure 4-12: Calculated condensed-phase heat release versus AP percentage at 20.4 atm.

The gas-phase heat fluxes to the surface are presented in Figure 4-13. The trends look very similar to the burning rates in Figure 4-11, with some slight differences. The gas-phase heat fluxes for 71.59% AP are very close to the values at 75.03%, just as the values at 59.25% are close to those at 65.97%. Above ~6 atm, the gas-phase heat fluxes at 59.25% AP are actually higher than those at 65.97%. This is not true of the burning rates, which depend on both the gas and condensed-phase heat fluxes. The condensed-phase reaction for 71.59% AP is much more endothermic than the 75.03% reaction (see Figure 4-12). The same is true of the 59.25% reaction in comparison with the 65.97% reaction. A more endothermic condensed phase forces the gas phase to experience more of the initial exothermic decomposition steps, resulting in a higher gas-phase heat flux to the surface.

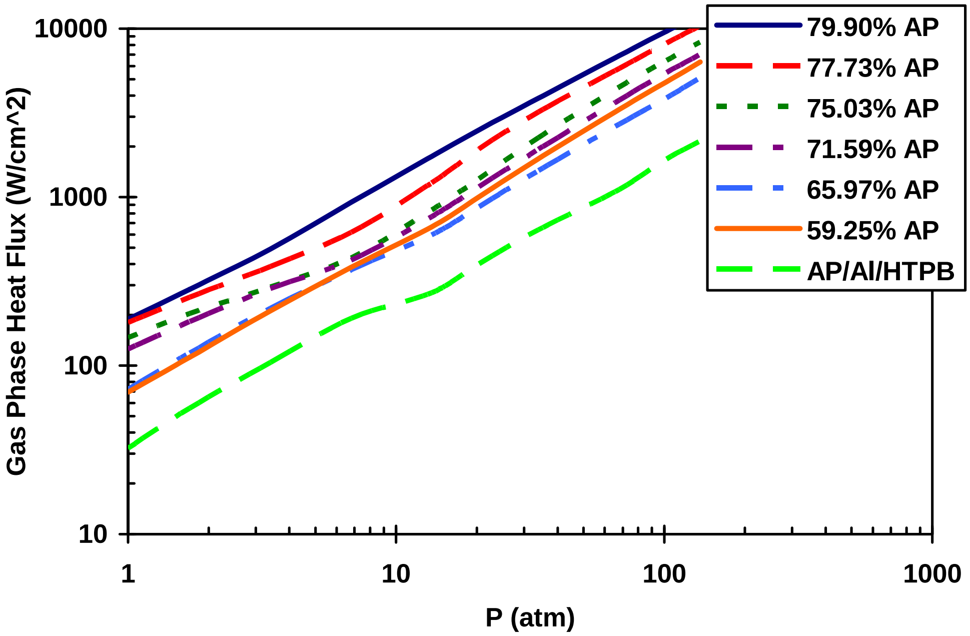

Figure 4-13: Calculated gas-phase heat flux of AP/HTPB and AP/Al/HTPB from 1 to 136 atm.

Calculated surface temperatures are shown in Figure 4-14. These results seem consistent with expectations, which are that the surface temperature increases with pressure and AP percentage, as does the burning rate. However, the results are somewhat dependent on the temperature at which reactions are allowed to begin in the condensed-phase model. This parameter was originally set to 800 K, which was the value used for monopropellant AP.[146,147] This essentially forces the surface temperature to be greater than 800 K. This has more of an effect at low pressure, when the surface temperature approaches 800 K and might drop below that if reactions were allowed to start at a lower temperature in the condensed phase.

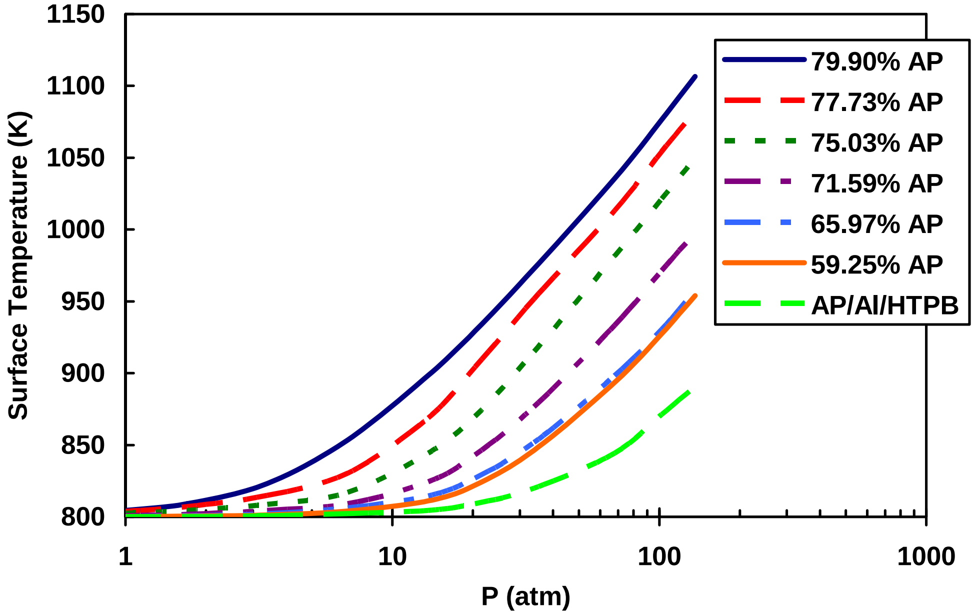

Figure 4-14: Calculated AP/Al/HTPB surface temperatures as a function of pressure, with condensed-phase reactions beginning at 800 K.

To investigate the effect of this parameter on model calculations, it was decreased to a value of 298 K and calculations were repeated at all pressures and compositions. The length of the condensed-phase region and the surface temperature varied significantly as this parameter was varied, but the surface species concentrations did not change due to the global nature of the condensed-phase mechanism. Hence, there was also no significant effect on burning rate, final flame temperature, final species concentrations, or gas-phase heat flux to the surface. The calculated surface temperatures, with reactions starting at 298 K in the condensed phase, are presented in Figure 4-15.

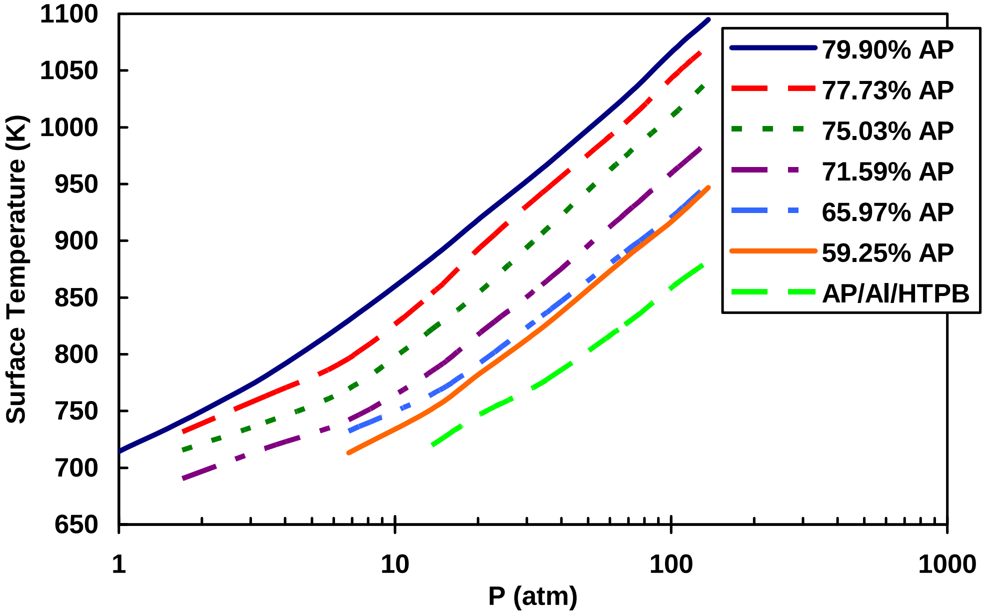

Figure 4-15: Calculated AP/Al/HTPB surface temperatures as a function of pressure, with condensed-phase reactions beginning at 298 K.

The results seem more reasonable than before, matching the burning rate trend shown in Figure 4-11 more closely now that the artificial limit on the surface temperature was removed. There was also an unexpected result, which was that some of the cases at lower pressures did not converge. This appears to be related to the surface temperature itself, or perhaps to the burning rate, since the cases stopped converging at surface temperatures below ~700 K and at burning rates below ~0.1 cm/s. This is significant since it is possible that in reality these propellant formulations would self-extinguish at low pressures. However, the lack of convergence of some of the cases was not investigated further since the combustion characteristics could be calculated at the low pressures with no significant difference in the results by simply increasing the temperature at which reactions begin back up to ~800 K.

4.3 Summary and Conclusions

A one-dimensional model has been developed for AP/HTPB premixed combustion. Formulations ranging from 59.25% to 79.90% AP have been modeled over a pressure range of 1 to 136 atm (14.7 to 2000 psi). Major modifications have been made to Jeppson's original AP/HTPB model[20] in both the gas- and condensed-phase kinetic mechanisms. The universal mechanism is now used in the gas phase. Separate, one-step, condensed-phase mechanisms, based loosely on Korobeinichev's surface species data, have been developed for each AP percentage considered. The universal gas-phase mechanism has been improved with the addition of an HCN-elimination reaction, which dramatically improves the prediction of flame temperature and final species concentrations for all formulations and pressures. This reaction is a temporary fix, which will be removed when more theoretically-based kinetics can be found that result in the same improvement in model calculations. Solid carbon is predicted by the Edwards Equilibrium Code at formulations below 70% AP. Due to the current absence of any reactions in the universal gas-phase mechanism that would produce it, it is included in the condensed-phase model, and exists throughout the gas phase without reacting. Foster's experimental burning rate data have been extrapolated to a wider range of AP percentages by means of a flame temperature correlation proposed by Beckstead, and have been used for model validation.

Combustion characteristics have been calculated varying formulation and pressure. Agreement between calculated burning rates and experimental data is excellent, although data are only available at low pressure for a small range of AP percentages. Agreement between model calculations and equilibrium code calculations of flame temperature and final species concentrations is excellent for all formulations and pressures considered. Calculations show consistent trends in burning rate, gas-phase heat flux, and surface temperature, each of which increases with pressure and AP percentage. Condensed-phase heat release calculations do not vary with pressure, but show an increase in the endothermic nature of the condensed phase as AP percentage decreases.

As part of the agglomeration modeling work, inert aluminum was added to the AP/HTPB model for 59.25% AP. The AP/HTPB ratio was kept approximately the same as the shuttle propellant, resulting in an aluminum percentage of 31.26%. The presence of inert aluminum resulted in lower burning rates, gas-phase heat fluxes, and surface temperatures over the entire range of pressures. These results have been used to develop correlations that serve as condensed-phase boundary conditions in the diffusion flame model (Appendix D), which is discussed in the chapter on agglomeration.

4.4 Future Work

Deficiencies in the universal gas-phase mechanism indicate a need for further research and development of the model. The research of Lin,[148] who has performed extensive *ab initio* calculations of kinetic pathways relative to propellant combustion, has been valuable in the development of the expanded gas-phase mechanism. Clearly, more calculations of this type are needed to complete the mechanism. As more calculated kinetic parameters become available from Lin and others who perform similar work, the HCN elimination reaction can be removed and replaced with more theoretically based reactions and kinetics. Gas-phase kinetics are also needed that describe the formation of solid carbon. If solid carbon, C(S), could be removed from the condensed phase, then more reasonable trends could be established in the condensed-phase mechanism below 70% AP. There also appears to be a need for more reactions in the gas-phase mechanism that describe the initial decomposition of AP and HTPB. This is evident due to the high number of final products that have been included in the condensed-phase mechanism, such as H_2, H_2O, CO, and CO_2, which ideally should be produced in the gas phase.

There is still a great deal of uncertainty in the condensed-phase model. The mechanism is based loosely on the surface species measurements of Korobeinichev, but there are obvious problems with his data. If more experimental studies were to be performed measuring surface species of AP/HTPB premixed combustion over a wide range of formulations and pressures, the data would provide an extremely valuable resource for further development of the model. More burning rate data are needed as well, at a wider range of formulations, expanding on Foster's work. In such a study, more care should be taken to ensure the validity of a premixed flame assumption, using the smallest possible AP particle size so that valid data could be obtained at even higher pressures.

5 RDX/GAP Propellant Burning Rate Model

To investigate particle-size effects in a typical non-AP propellant, a multi-dimensional burning rate model has been developed to describe RDX/GAP propellants. One of the goals of this study has been to improve upon past efforts by incorporating greater detail in modeling both the solid and gas phases, rather than just focusing on one phase, which has typically been the case in past modeling work. To accomplish this, the details of the solid-phase geometry have been modeled using PARPACK,[14] a three-dimensional particle-packing model. In addition, the one-dimensional, detailed gas-phase kinetic models of RDX and GAP monopropellant combustion and RDX/GAP pseudo-propellant combustion, described in Chapter 3, have been used to calculate monopropellant and pseudo-propellant burning rates as needed.

Contractual constraints dictated that the burning rate model finish running in twenty minutes or less. Therefore, to reduce cpu times as much as possible, a simplified approach has been developed. The general approach is explained here. First, a particle pack is generated with PARPACK, which is the most cpu intensive step in the model. Second, the monopropellant and pseudo-propellant burning rates are calculated with PHASE3. This step is almost instantaneous because the PHASE3 calculated burning rates have been organized into a look-up table. Third, the path of least time through the pack, as determined by the model algorithm, is found. The path starts at the top of the pack and travels downward, passing through, or around, particles in the pack. The path burns at the burning rate of the ingredient through which it is moving, so portions of the path burn faster depending on the relative rates of the ingredients. This step is also very fast compared to the first step. The final step is the calculation of the overall burning rate, which is done by dividing the pack height by the total burning time of the path. These steps, and the development of the algorithms involved, are described in detail in this chapter. The modeling approach used in this study is intended to be applied to propellants whose ingredients have been modeled as monopropellants and pseudo-propellants and which do not burn with a significant diffusion flame.

The data of Flanagan et al.[120] have been used for model validation. They obtained burning rate data for two monomodal RDX/GAP propellants containing 10-15 and 200 μm RDX, respectively. They used RDX concentrations of 20%, 45%, and 70%, and they varied pressure from 6.8 to 136 atm.

Due to funding issues, the research presented in this chapter was cut short. However, the initial research and findings are presented, as well as suggestions for future model development. Much of the work presented in this chapter has been published previously.[157]

5.1 Solid-Phase Model

PARPACK is a Monte Carlo particle-packing computer code that builds cylindrical, multi-modal packs of randomly-generated spherical particles. It has been described in detail in Chapter 2. Particle sizes, as well as the overall pack dimensions, are inputs to PARPACK, and therefore, must be known beforehand. The methodology used in the current study to generate particle-size distributions, and to determine the optimal pack dimensions, is discussed in this section.

5.1.1 Particle-Size Distributions

A three-parameter probability density function of the lognormal distribution, Equation (5-1), has been used to describe particle-size distributions. This is similar to what has been done in past models.[158]

$$f(x;\sigma,\theta,m)=\frac{1}{(x-\theta)\sigma\sqrt{2\pi}}\exp\left\{-\frac{1}{2\sigma^2}\left[\ln\left(\frac{x-\theta}{m}\right)\right]^2\right\} \qquad \textbf{(5-1)}$$

The three parameters are σ, θ and m; the shape, location, and scale parameters, respectively. More specifically, σ is the standard deviation of the natural logarithm of x, and m is the mean value of x. For particle-size distributions, the function becomes Equation (5-2), with f, D, and D_m as the mass fraction, the particle diameter, and the mean value of the particle diameter, respectively.

$$f(D;\sigma,\theta,D_m)=\frac{1}{(D-\theta)\sigma\sqrt{2\pi}}\exp\left\{-\frac{1}{2\sigma^2}\left[\ln\left(\frac{D-\theta}{D_m}\right)\right]^2\right\} \qquad \textbf{(5-2)}$$

Parameter values can be obtained by fitting Equation (5-2) to available particle-size distribution data or by estimation, if only nominal (mean) particle sizes are available. If experimental data are cumulative, Equation (5-2) can be integrated to fit the data. Examples of a differential fit and a cumulative fit are shown in Figure 5-1.

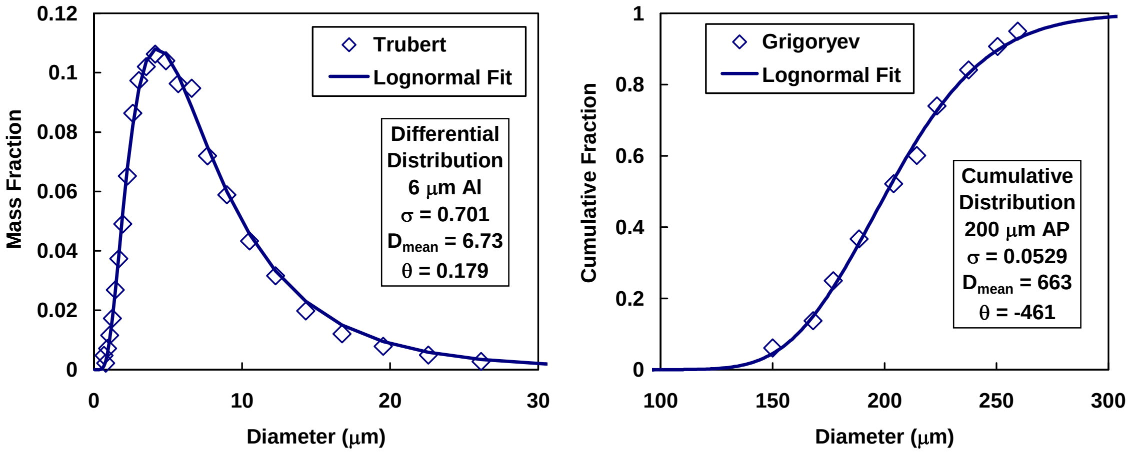

Figure 5-1: Differential and cumulative lognormal fits of experimental particle-size data.[96,109]

Once parameter values are obtained, the distribution can be divided into any number of discrete sizes. There are multiple discretization options. One option is to divide the cumulative distribution into segments of equal mass fraction and calculate an average diameter for each segment. Another option, the opposite of the first, is to divide the differential distribution into segments of equal diameter range and calculate an average mass fraction for each segment. There may also be other discretization methods worth considering. The first option has been used in this study because PARPACK can produce errors when particle sizes have very small mass fractions.[159]

Flanagan et al. reported nominal sizes of 10-15 and 200 μm RDX, but they did not report detailed size-distribution data, so the parameters of Equation (5-2) had to be estimated for these nominal sizes in the current study. In order to estimate the parameters, distribution data from other sources were sought. Miller has reported detailed size-distribution data for AP nominal sizes from 0.7 to 400 μm.[160] Values of the parameter σ were calculated by fitting Miller's data with Equation (5-2) while keeping θ equal to zero and D_m equal to the nominal AP diameter. It was necessary to fix the value of θ at zero because allowing it to vary forced the value of D_m to deviate from the nominal AP diameter. Equation (5-3) was regressed from the calculated σ values in order to correlate σ with the nominal AP diameter. Thus, when no size-distribution data are available for a given nominal size, the distribution can be estimated with Equation (5-2) by setting θ equal to zero, setting D_m equal to the nominal diameter, and calculating σ from Equation (5-3).

$$\sigma(D_n) = -0.102\ln(D_n) + 0.792 \tag{5-3}$$

In the current study, the size distribution for Flanagan's 10-15 μm RDX nominal size has been calculated using Equations (5-2) and (5-3), while assuming a 12.5 μm nominal size. The distribution for the 200 μm size was initially calculated using the same approach, but it was found that the corresponding particle pack generated by PARPACK did not achieve a high enough volume fraction to simulate an RDX/GAP propellant containing 70% RDX by weight. Thus, a different distribution has been used for the 200 μm size. The parameters used for this distribution were obtained by fitting the size-distribution data of the 200 μm AP in the shuttle propellant. Due to the broad nature of these data, it was necessary to use a combination of two distribution functions to fit the data accurately. Both the 12.5 and 200 μm distributions have been discretized into twenty sizes of equal mass fraction. The differential distributions and the discretized, cumulative distributions, along with the corresponding parameter values from Equation (5-2), are shown in Figure 5-2.

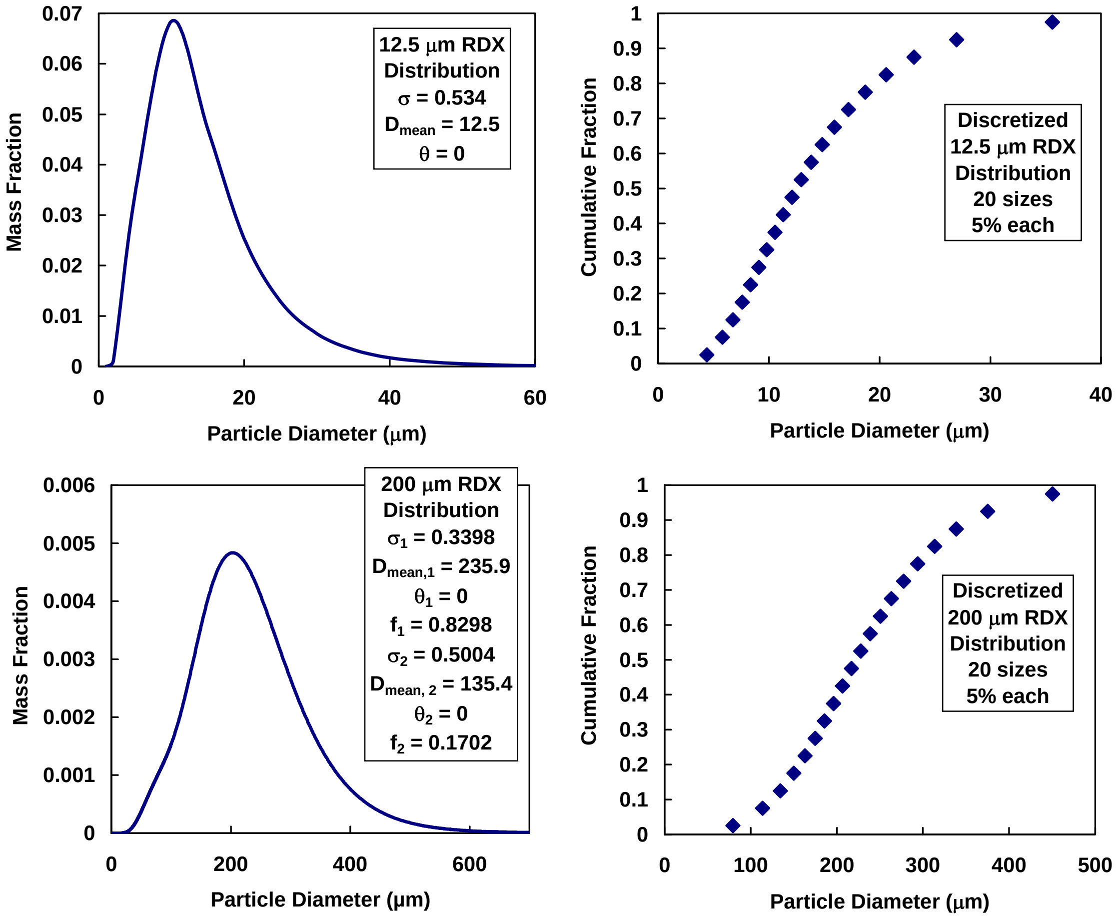

Figure 5-2: Calculated particle-size distributions for Flanagan's 10-15 and 200 μm RDX nominal sizes.

5.1.2 Homogenization

Homogenization of fine particles into the binder is an approach that has been used by modelers in the past, as was discussed in Chapter 2, and it is also used in this study. The purpose of homogenization in this model is twofold. First, it allows the model to simulate the dependence of the flame structure on particle size and pressure. Second, homogenized particles can be left out of the particle pack, reducing required cpu times for generating packs. For modeling purposes, it is necessary to define a homogenization cutoff diameter. Miller's burning rate data[48] (Figure 2-12) show that the burning rate reaches an asymptote for small particles, which varies with pressure. It is concluded that the asymptote corresponds to the transition from a diffusion flame situation to a purely premixed flame environment, representing homogenization of the fine AP and binder. The AP particle diameter and the pressure at this condition represent the homogeneous cutoff diameter. Particles smaller than the cutoff diameter are assumed to be homogenized into the binder, burning by a premixed flame. Sambamurthi's agglomerate data,[98] plotted as size versus fine AP size and pressure (Figure 2-20 and Figure 2-21), show a similar inverse-s shape, and are observed to increase as pressure decreases. These data are interpreted as representing the same phenomena as exhibited by Miller's burning rate data, i.e. a homogeneous cutoff distance. To model this pressure dependence, cutoff diameters at several pressures have been estimated from Miller's burning rate data and Sambamurthi's agglomerate size data. The resulting correlation is shown in Equation (5-4). D_h (homogenization cutoff diameter) is in units of microns and P (pressure) is in atm. The derived pressure correlation and the estimated values of the cutoff diameter are shown in Figure 5-3.

$$D_h(P) = 150\exp\left(-0.06P\right) + 2 \tag{5-4}$$

The correlation (Equation (5-4)) predicts a larger cutoff diameter at low pressure than the estimations from the data. This discrepancy is based on the numerical results of Gross,[7] who predicted a premixed flame for a 400 μm AP particle at 1 atm, which indicates that the homogenization cutoff diameter should be ~400 μm at that pressure. Since Sambamurthi's agglomerate size data and Gross' numerical calculations do not agree, the correlation was left as shown in Figure 5-3, partly between the two.

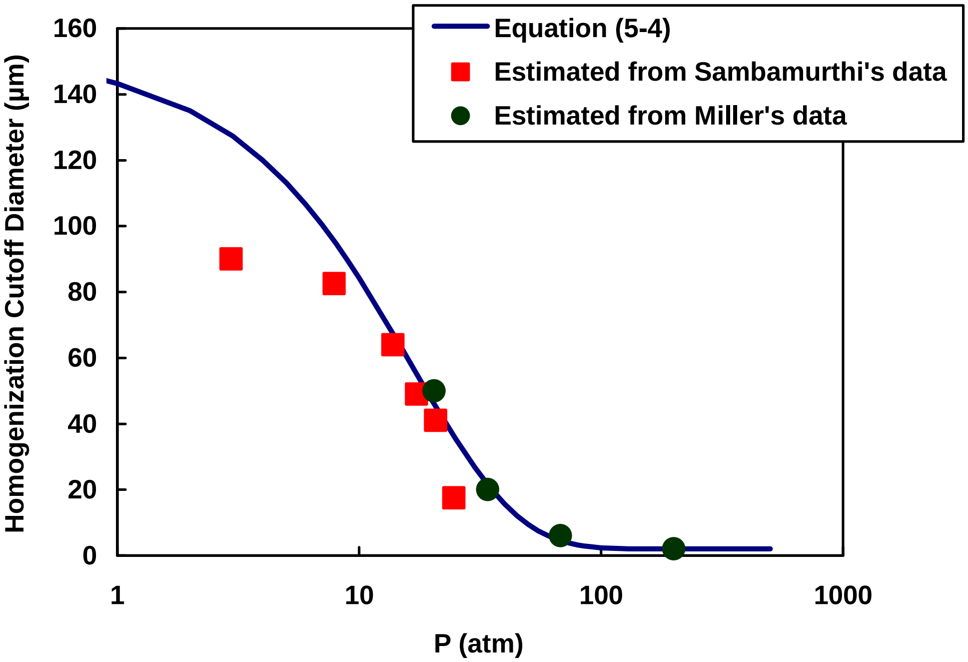

Figure 5-3: Estimated pressure dependence of the homogenization cutoff diameter.

The effect of homogenization on the 12.5 µm RDX particle-size distribution is that about half of the distribution is homogenized at a pressure of ~45 atm and essentially all is homogenized at pressures less than ~20 atm. Lower pressures are required in order for part of the 200 µm distribution to be homogenized. One of the purposes of homogenization is to eliminate the fine particles from the pack and reduce cpu times. However, in the case of the 12.5 µm distribution, this probably would result in unrealistic packing of the remaining particles, since particle spacing would not be influenced by the eliminated particles. To maintain accurate particle packing, a minimum diameter of 2 µm has been used, meaning that homogenized particles that are smaller than 2 µm are left out of the pack, while particles larger than 2 µm are included in the pack. The homogenized particles that are included, however, are ignored by the burning rate algorithm. Thus, the homogenized particles are allowed to influence the particle spacing, but not allowed to influence the burning rate calculation directly.

5.1.3 Pack Height and Diameter

In simulating three-dimensional random particle packs with broad particle-size distributions, a very large number of particles have to be included to obtain good pack statistics.[14] For example, if there are two particle sizes in a pack, and the larger is one hundred times larger than the smaller, then the volume ratio of the two particle sizes is a factor of $100^3 = 10^6$. Therefore, for equal volume quantities of the two sizes, one million small particles would have to be included for every one large particle. Since thousands of large particles should be included, the problem normally requires very large cpu times.

To minimize the required cpu time, a study was performed to determine how much the pack size can be reduced without increasing the variability in the burning rate calculation. This study was performed on two of Flanagan's propellant formulations. The first is the 70% RDX/GAP propellant, containing 12.5 μm RDX, and the second is the 70% RDX/GAP propellant, containing 200 μm RDX. The particle-size distributions used are those shown in Figure 5-2. After a basic burning rate algorithm was developed, several packs of different configurations were generated, and burning rates were calculated at 68 atm to evaluate the effect of pack configuration. The effects of varying the pack height and the pack diameter were examined. While varying the pack height, a pack diameter of 20 nominal particle-size diameters was used, resulting in 250 and 4000 μm pack diameters for the 12.5 and 200 μm nominal sizes, respectively. Once pack heights were chosen for the two formulations, these heights were used while varying the pack diameter. This study was performed for monomodal packs since Flanagan's propellants were all monomodal. However, if the model were to be applied to multimodal propellants in the future, a similar study would be needed for the multimodal packs.

Figure 5-4 shows the results of varying the pack height for both formulations. For each pack height, five packs were generated and burning rates were calculated for five different paths through each pack. Thus, 25 burning rate calculations were made for each pack height. Multiple burning paths through each pack were found by randomly choosing a different starting particle for each path.

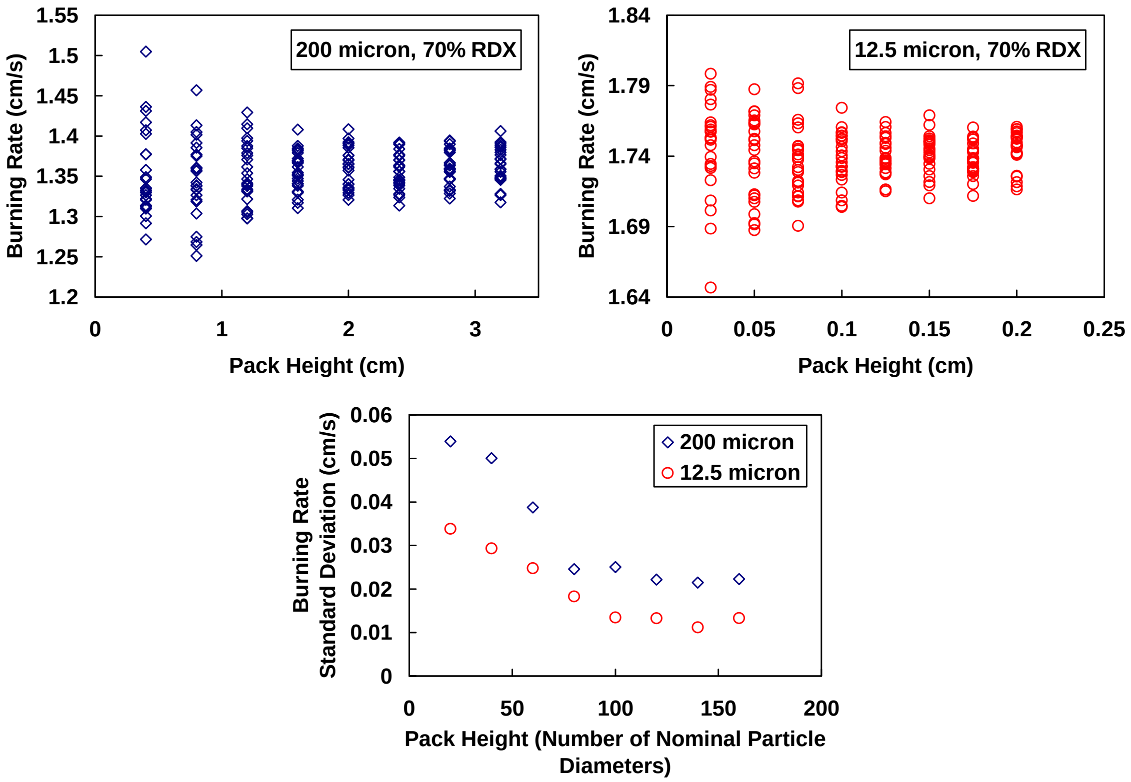

Figure 5-4: Parametric study to determine the optimal pack height for monomodal packs in conjunction with the burning rate model.

There is a clear decrease in burning rate variability as pack height increases. However, the pack heights for the two different formulations are very different in magnitude. In order to compare the pack heights for both formulations to each other, the heights were expressed in terms of an equivalent number of nominal particle-size diameters, rather than in units of cm, in the plot of the standard deviations. In this plot, the standard deviation for both formulations appears to reach a minimum at a pack height of about 120 nominal particle diameters. Therefore this height was chosen as the optimal height for both packs, corresponding to pack heights of 0.15 and 2.4 cm for the 12.5 and 200 micron particle sizes, respectively. Burning rates calculated for packs with heights greater than or equal to the optimal height are within 3% of the average, which seems reasonable considering that there is typically at least that amount of variability in experimental measurements. If the five burning rates calculated for each pack are averaged into one rate for each pack, the burning rate variability decreases to ±1%. Therefore, in the final model calculations, the average of the five calculated burning rates is used.

Having chosen pack heights for both propellant formulations, the pack diameter was also varied in a similar fashion. Since the path of least time is an approximately vertical path through the pack, it was anticipated that there would not be a significant effect of varying the diameter. Pack diameters were varied from 5 to 40 nominal particle diameters for both formulations. There was no significant change found in the standard deviation of the calculated burning rates. Thus, it seemed that a very small diameter could be used. However, the developers of PARPACK have indicated that the pack diameter should be at least 20 times the smallest particle diameter, within the distribution, to avoid edge effects.[159] Therefore, a pack diameter of 10 nominal particle diameters was chosen for both formulations because it met this requirement.

Having chosen an optimal pack height and diameter, one pack was generated for each of the six formulations that were to be modeled. Relevant pack details for each formulation are presented in Table 5-1. It should be noted that the initial pack heights and diameters are the optimal values, but the final heights and diameters are larger. This is due to the volume expansion that each pack undergoes to match the specified propellant formulation. Thus, the packs with 20% RDX are the largest because they had to be expanded the most to achieve a lower particle volume fraction.

Table 5-1: Details of final packs generated for the burning rate model.

Nominal Particle Diameter (microns)	12.5	12.5	12.5	200	200	200
% RDX	20	45	70	20	45	70
CPU Time (min)	16.6	20.0	15.5	15.0	15.1	10.4
Initial Pack Height (cm)	0.15	0.15	0.15	2.4	2.4	2.4
Initial Pack Diameter (cm)	0.0125	0.0125	0.0125	0.2	0.2	0.2
Final Pack Height (cm)	0.246	0.183	0.153	3.93	2.91	2.44
Final Pack Diameter (cm)	0.0205	0.0152	0.0127	0.327	0.242	0.203
Number of Particles	38,252	38,047	37,944	24,539	24,401	24,732

5.2 Path of Least Time

The shape and composition of a propellant's surface at one time during the burning process can be very different from another time. Different particles will have burned to different extents. Some particles would have just started to burn. Others would have burned halfway. Still others would have almost completely burned out. The heterogeneous nature of the propellant surface suggests that the burning rate will be different at different positions on the propellant surface. It is possible that one part of the propellant will burn faster than another and perhaps even undercut a section of the propellant. The modeling approach used in this study allows for variable burning rates through different parts of a propellant. It is designed to search for the fastest burning path, or the path of least time.

The nature of the path of least time probably varies with propellant formulation and pressure. Monopropellant GAP burns faster than monopropellant RDX, but if some RDX is homogenized into the binder, the burning rate of the pseudo-binder may be lower than that of monopropellant RDX. Thus, it is likely that the path of least time would travel mostly through the binder unless there is a high percentage of fine RDX in the propellant, in which case, the path would travel more through the coarse RDX particles.

As an initial investigation into the nature of the path of least time, two different path-finding algorithms have been developed. The first is designed to travel mostly through the binder and the second mostly through the particles. Both approaches are similar to Strahle's approach,[76] in which he assumed that the oxidizer particles burn as monopropellants. In the current study, it has been assumed that the binder burns either as a monopropellant or a pseudo-propellant, depending on whether there is homogenized RDX. The pseudo-binder assumption may result in lower burning rates for the mixture, which would be consistent with the data. These assumptions are also significant because the diffusion flames between RDX particles and GAP binder are considered insignificant and have not been accounted for in the model.

The first approach is illustrated in Figure 5-5 in two dimensions, although the actual model functions in three dimensions. A particle near the top of the pack is chosen as the starting point. After a starting particle is chosen, the path "grows" in increments of two particles per step. The first and second steps are shown in Figure 5-5. Beginning at the starting particle's north pole, multiple paths are generated which travel through or around the particle to its equator. The paths that go around the particle are considered to be in the binder, close to the surface of the particle. From the equator, the paths drop straight down through the binder. Eventually, they will hit either another particle or the bottom of the pack. The paths that hit other particles are allowed to split into even more paths. The new paths continue in the same way, dropping through the binder until reaching more particles below those particles, making a total of 16 possible paths, including 3 particles each. In three dimensions, there are actually 32 paths rather than 16, but half have been left out to simplify the illustration.

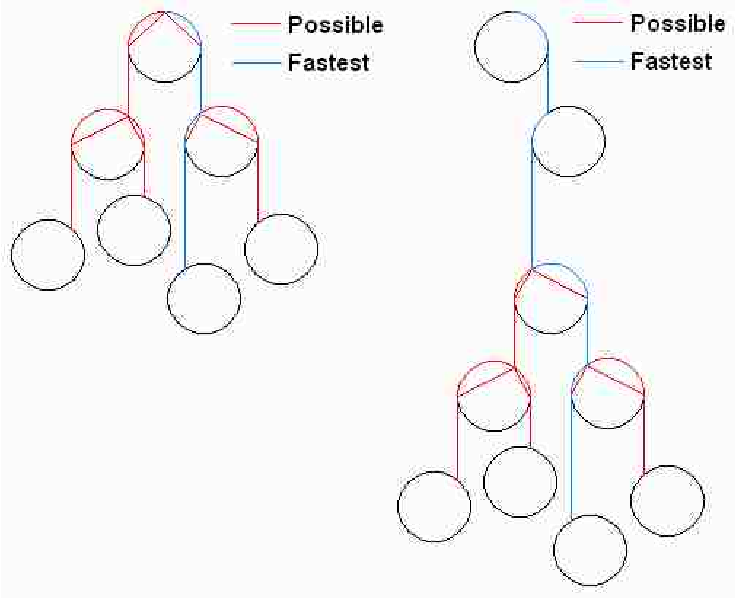

Figure 5-5: Illustration of the first two steps of the binder-preferred path-finding algorithm used in the burning rate model.

After the paths are generated, their burning rates are calculated (the burning rate calculation is explained in the following section). The rates are then compared and the path with the highest rate is chosen. The remaining paths are eliminated and the endpoint of the fastest path becomes the new starting point for the next step of the algorithm. New paths are generated from the new starting point, and the fastest is chosen, and so on. It is possible that there is a faster path, since an eliminated path that starts slow may become the fastest in the end, but the path found by the algorithm is considered to be at least close to the fastest path.

The second approach is similar to the first, in that multiple paths are generated and the fastest is chosen at each step. The difference is that it prefers particles over binder. The algorithm, analogous to Strahle's approach,[76] is designed to build the path by searching for the closest particles below the starting particle. Then, the closest particles below those particles are found. At this point, the burning rates of the multiple paths are compared and the fastest is chosen. The path then continues to grow in the same manner. The basic idea is illustrated in Figure 5-6, with only one path shown to simplify the illustration. Although Figure 5-6 is shown horizontally, it is meant to describe a vertical path.

The path segments through each particle, and those through the binder between the particles, are linear segments designed to minimize the binder path length. The points where the path enters and exits a particle are determined by drawing a line between particle centers, as indicated by the dashed lines in Figure 5-6. The points where this line intersects each particle's surface are calculated and are used as the entrance and exit points.

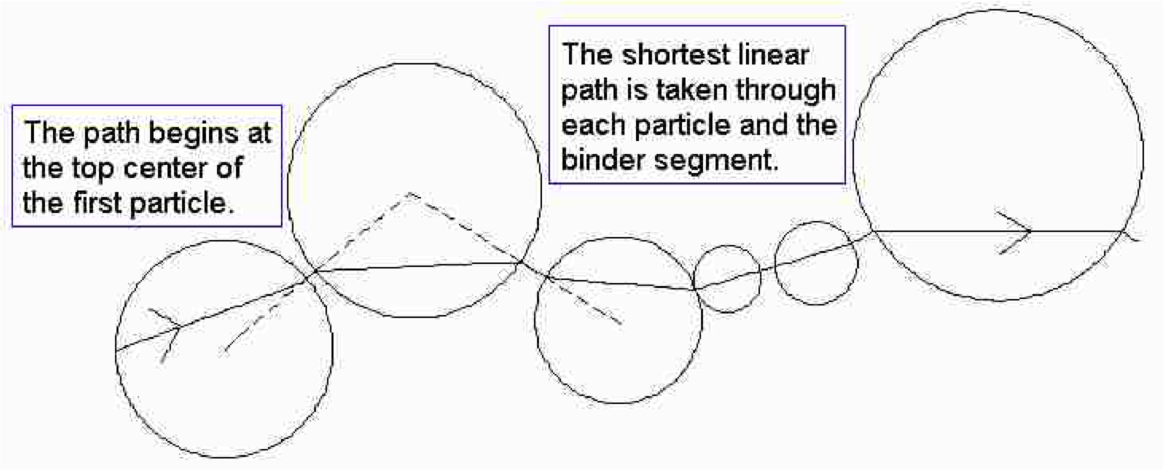

Figure 5-6: Illustration of the oxidizer-preferred path-finding algorithm used in the burning rate model.

A variation of each of the two methods described above has also been used. Instead of choosing the path with the highest burning rate, the "best" path is chosen randomly from the multiple paths generated at each step. Thus, instead of a path of least time, a random path is found, resulting in an average burning rate, rather than the fastest burning rate through the pack. The results of the "fastest" and "random" versions of each path-finding approach are presented in this chapter.

5.3 Burning Rate Calculation

After each step in the path-finding algorithm, the burning rates of the multiple paths are calculated. After the entire path is determined, the final burning rate is calculated. Whether the burning rate is being calculated for one section of the path, or for the complete path, the same calculation is used. This calculation is described in this section. A path is made up of line segments or curves through the pack. Some are inside particles, some follow the binder. The burning times of particle path segments are calculated from PHASE3 burning rates for monopropellant RDX by dividing the length of the path segment by the burning rate. The burning times of binder path segments or curves are calculated from PHASE3 burning rates for monopropellant GAP or pseudo-propellant RDX/GAP, depending on the amount, if any, of homogenized RDX. The path burning rate is calculated by dividing the vertical distance of the path, or section of the path, by the sum of the burning times of all the path segments. If there are particle path segments, then ignition delay times for each particle are included in the sum. For the ignition delay time, Beckstead[4] used a linear regression analysis of Shannon's AP data[161] using burning rate as a correlating parameter. These calculations are shown in Equations (5-5) to (5-7). H_p, r, and t are the pack height, overall burning rate and overall burning time, respectively. $L_{o,i}$ and $L_{b,i}$ are the lengths of the i^{th} oxidizer and binder path segments, respectively. D_i is the i^{th} particle diameter in cm, $t_{ign,i}$ is the ignition delay time of the i^{th} particle, and r_o and r_b are the oxidizer and pseudo-binder burning rates, respectively.

$$r = \frac{H_p}{t} \tag{5-5}$$

$$t = \sum_i \left(\frac{L_{o,i}}{r_o} + \frac{L_{b,i}}{r_b} + t_{ign,i} \right) \tag{5-6}$$

$$t_{ign,i} = \frac{4.321}{cm^{0.7}} \frac{D_i^{1.7}}{r_o} \tag{5-7}$$

5.4 Results and Discussion

Burning rates have been calculated, using both path-finding approaches, as well as their "random" variations, for 200-micron and 12.5-micron RDX/GAP propellants containing 20%, 45%, and 70% RDX. Pressure has been varied from 6.8 to 136 atm. Model calculations have been compared with Flanagan's data.

The results for 20% RDX are presented in Figure 5-7. For the 200-micron particle size, the binder-preferred algorithm (method 1) matches the data more closely. This seems reasonable, since there are relatively few particles at 20% RDX, so the path should mostly follow the binder. Neither approach matches the data at low pressure, however, indicating that the ideas of both approaches may need to be combined. The poor agreement may also be related to the high GAP burning rates predicted by the monopropellant GAP model at low pressures. For the 12.5 micron particle size, the results of all the approaches converge at low pressure. There are also slope breaks as pressure decreases. These effects are produced by homogenization, which has an increasing influence on the 12.5 micron particle-size distribution as pressure decreases. At pressures below ~20 atm, the entire distribution is homogenized, so the burning rate is calculated from the RDX/GAP pseudo-propellant model, which is independent of the path-finding algorithm. The slope breaks are somewhat structured due to the small number of pressures at which calculations have been performed. Including more pressures woud likely result in a smoother curve. The poor agreement at low pressure suggests that the pseudo-propellant model predicts burning rates that are too high for a formulation of 20% RDX. At high pressures, the particle-preferred path-finding approach (method 2) agrees better with the data. It is interesting that one method is better for 200-micron particles, while the other is better for a size of 12.5 microns. This may be because, for equal volumes of particles, there are greater numbers of the smaller size, so the particle-preferred approach is better for smaller sizes.

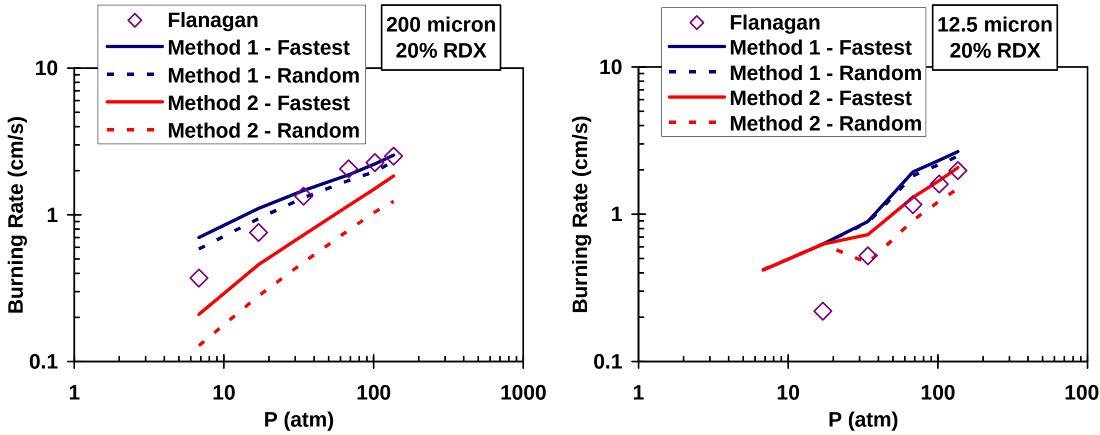

Figure 5-7: Calculated burning rates compared with data for RDX/GAP propellants containing 20% RDX.

The results for 45% RDX are presented in Figure 5-8. For the 200-micron RDX, the binder-preferred approach matches the data more closely at high pressure, but the particle-preferred approach matches the data better at low pressure. For the 12.5-micron size, the particle-preferred method matches the data more closely. The "random" version of this method appears to work better at high pressure for this formulation.

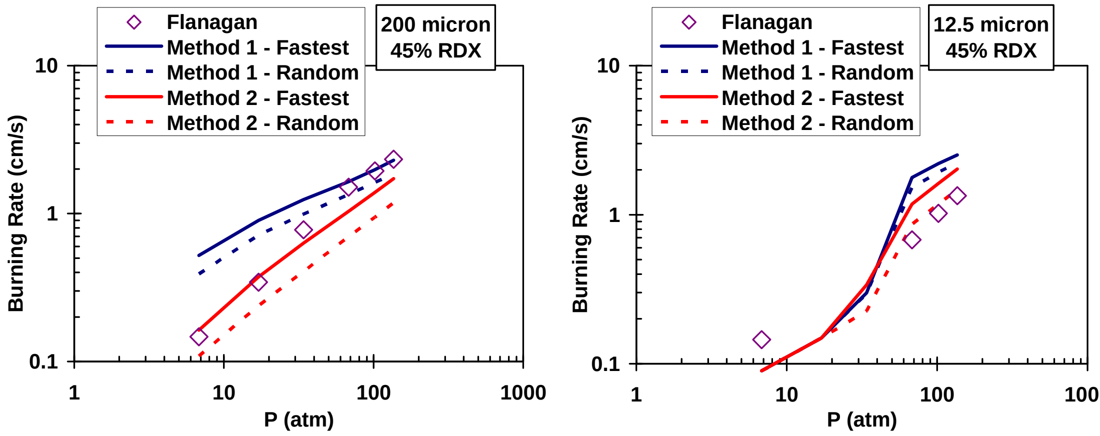

Figure 5-8: Calculated burning rates compared with data for RDX/GAP propellants containing 45% RDX.

The results for 70% RDX are presented in Figure 5-9. The particle-preferred approach matches the data more closely, probably due to the high concentration of RDX particles. The “random” approach works best for the 12.5-micron size at high pressure. Low burning rate predictions at low pressure are due to the low calculated rates of the pseudo-propellant model.

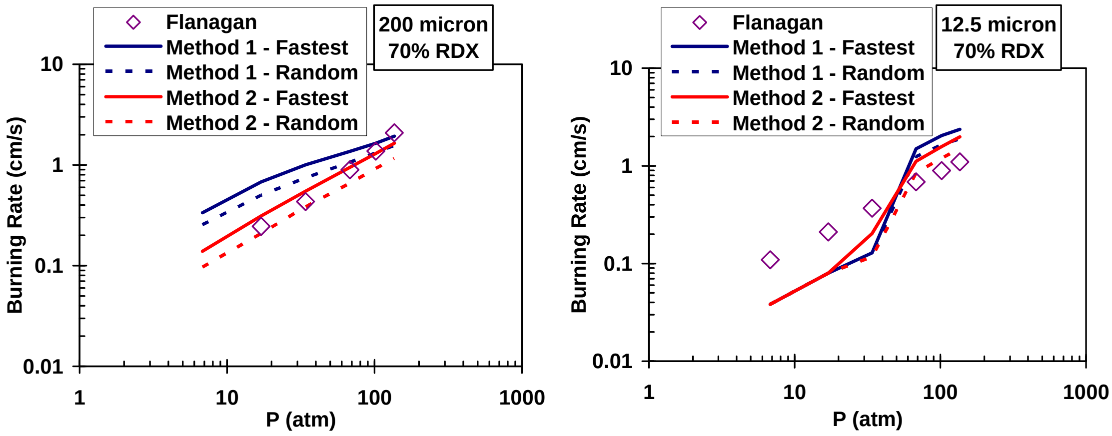

Figure 5-9: Calculated burning rates compared with data for RDX/GAP propellants containing 70% RDX.

Based on the results of Figure 5-7 to Figure 5-9, none of the approaches seems to be sufficient for modeling the entire range of formulations and pressures. Different approaches appear to work better, depending on the particle size, RDX percentage, and the pressure. The model appears to be too simple to capture all of the effects of particle size and pressure, regardless of whether the path of least time is found or whether an average path is found. It may be possible to develop a more sophisticated algorithm that incorporates the ideas of all the approaches. However, the fact that many of the calculated burning rates are higher than the data, suggests that diffusion flames may not be insignificant in RDX/GAP propellants. RDX/GAP diffusion flames do not burn very hot like AP/HTPB flames, but they may have a significant effect in the opposite way, by creating a relatively cooler flame and lowering the burning rate.

5.5 Summary and Conclusions

A heterogeneous propellant combustion model is being developed at BYU. This model combines the geometric modeling capability of PARPACK with the combustion modeling capability of PHASE3 to predict burning rates for solid propellants. The approach of the model is to determine a characteristic burning path through each particle pack and to calculate the burning rate of that path. Two different path-finding approaches have been used, one that prefers a path that travels through the binder, and another that prefers oxidizer particles. Both a path of least time and an average path have been determined for each formulation and pressure, and for each of the two path-finding approaches. Efforts to validate the model have been made by comparing results with Flanagan's data for RDX/GAP propellants. These comparisons show that the model has promise but needs to be developed further. Different approaches work better depending on formulation and pressure. The path-finding algorithms are currently very simple. More research is needed to determine a more appropriate path-finding algorithm, or to develop a different approach.

5.6 Future Work

There are several aspects of the model that require research and development. The RDX/GAP pseudo-propellant combustion model works well for monopropellant RDX and GAP, but may be inaccurate for RDX/GAP mixtures. Unfortunately, there are no experimental data specifically for premixed RDX/GAP combustion, so experiments would need to be designed that would ensure premixed combustion. The path-finding algorithm is very simplified and needs further development. It may be found that the path of least time approach is not effective and a completely new approach may need to be developed. Modeling of diffusion flames in RDX/GAP propellants may be another possible approach. Felt’s diffusion flame model, although developed for AP/HTPB combustion, has the capability to model any propellant ingredient. If his model could be adapted for RDX/GAP combustion, it could be used to calculate the effects of particle-size and pressure on the gas-phase flame, and thereby, on the burning rate. It would also be helpful to this modeling work if more experimental data could be obtained for a greater number of RDX particle sizes, rather than just 12.5 and 200 microns.

6 Aluminum Agglomeration Model

To investigate the effects of varying particle-size distributions and pressure on aluminum agglomeration, an agglomeration model for AP propellants has been developed. PARPACK[14] has been used to simulate the geometrical packing of the propellant, similar to the burning rate model. Initially, three basic agglomeration models were developed to explore separately the ideas of pockets, separation distance, and aluminum ignition. Calculations of agglomerate size in these initial models were based solely on the spacing of aluminum and AP particles in the packs generated by PARPACK. The results of the preliminary models have been published previously.[162] Based partly on the results of these initial models, a final model has been developed which adds increased sophistication by incorporating Felt's two-dimensional diffusion flame model as a means of predicting ignition of aluminum particles. In addition, the surface is numerically regressed through the particle pack to simulate a burning propellant and calculations are performed at each new surface location on the particles that have been "exposed" by the regressing surface. The experimental data of Sambamurthi et al.,[98] Grigoryev et al.,[96] and Micheli and Schmidt[91] have been used for model validation.

6.1 Solid-Phase Geometry

The geometric packing has been modeled in a similar way to the burning rate model discussed in Chapter 5. PARPACK has been used to generate particle packs simulating propellants, using Equation (5-2) to generate particle-size distributions. The main difference between the agglomeration and burning rate models is in the size and shape of the packs that have been generated. For the burning rate model, the packs needed to be very tall to improve the statistics of the burning rate calculations. For the agglomeration model, however, shorter packs with larger diameters have been used to include more coarse AP particles, which have been postulated to influence aluminum agglomeration. For each pack, the value of the pack height and diameter has been set equal to ~7.5 times the average coarse AP diameter. Specific details of particle-size distributions and pack sizes are presented along with model results in later sections of this chapter.

Most of the propellants investigated in this study are multimodal, which resulted in a significant increase in the cpu time required to generate a particle pack. Depending on the pack formulation, cpu times varied from several minutes to several days. An important factor in determining the required cpu time is the ratio of the largest to the smallest particle diameter. For larger ratios, a greater number of small particles have to be included. The ratio of largest to smallest diameter is typically much larger in multimodal packs. Due to the larger cpu times, it was necessary to use a slightly different homogenization approach than was used in the burning rate model. In the burning rate model, a minimum particle size of 2 μm was used for determining what homogenized particles to include in the pack. To reduce cpu times, a minimum size of 6 μm has been used in the agglomeration model. This is also important because of the estimated pressure dependence of the homogenization cutoff diameter (Equation (5-4)). If the cutoff diameter is smaller than the minimum particle size, then the calculated pressure effect may be inconsistent. Equation (5-4) has been modified to match the minimum size of 6 microns, resulting in Equation (6-1). The new pressure correlation always homogenizes particles smaller than 6 microns, reflecting their absence from the packs.

$$D_h(P) = 160\exp\left(-0.07P\right) + 6 \tag{6-1}$$

6.2 Preliminary Models

Three basic agglomeration models—a "Pocket Model", a "Separation Distance Model" and an "Ignition Model"—were developed to explore various ideas from the literature. Each of the algorithms is described in this section. A basic illustration of each is presented in Figure 6-1.

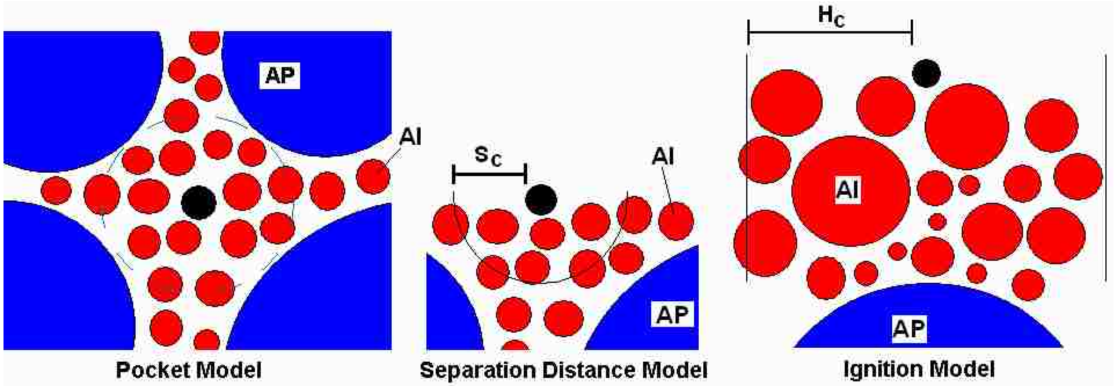

Figure 6-1: Illustration of three preliminary agglomeration models.

6.2.1 Pocket Model

The main idea behind the Pocket Model is that aluminum particles gather in the pockets between coarse AP particles during the propellant mixing process. The resulting proximity of aluminum particles inside pockets causes them to form agglomerates during the combustion process. To model this concept within the framework of particle packs, a method of locating pockets has been developed. It has been assumed that the aluminum particles farthest from the coarse AP particles are at or near the center of pockets. These particles are assumed to be "pocket centers" (black particle in illustration). A spherical pocket around each pocket center is assumed, with a pocket radius equal to the sum of the radius of the pocket center particle and the distance from the pocket center to the closest coarse AP particle. All aluminum particles inside model-defined pockets are assumed to combine and form an agglomerate. Depending on the configuration of coarse AP particles, some model-defined pockets may overlap. In these cases, overlapping pockets are combined to form even larger agglomerates.

6.2.2 Separation Distance Model

The Separation Distance Model is based on the idea that aluminum particles that are close to each other will agglomerate. In the illustration, the black particle represents the highest aluminum particle in the pack, which is where the algorithm begins. The algorithm used in this study is the most basic version used by Jackson et al.[110] For any two aluminum spheres (i,j) with diameters $r_{p,i}$, $r_{p,j}$ and whose centers are located at (x_i, y_i, z_i), (x_j, y_j, z_j), respectively, the separation distance $S_{i,j}$ is defined in Equation (6-2).

$$S_{i,j} = \sqrt{(x_i - x_j)^2 + (y_i - y_j)^2 + (z_i - z_j)^2} - r_{p,i} - r_{p,j} \tag{6-2}$$

If $S_{i,j}$ is less than the critical separation distance S_c, a free parameter in the model, the two spheres will agglomerate unless both have already agglomerated with other particles. Separate agglomerates must not be combined or the final result would be one giant agglomerate consisting of all aluminum particles in the pack. According to Jackson, this approach combines several effects, including surface residence time and sintering of neighboring aluminum particles, into one length scale, S_c. The model also allows for the existence of filigree bridges of aluminum between pockets.[110] Jackson found it necessary to calibrate S_c for each experimental data set, indicating that his model is not predictive. An investigation of this model is worthwhile, however, to determine if it would be beneficial to use a critical separation distance in conjunction with another concept, such as a pocket or ignition model.

6.2.3 Ignition Model

The Ignition Model is based on the idea that non-homogenized AP particles and the surrounding binder produce a hot diffusion flame at the particle/binder edge which acts as an ignition source for the aluminum particles. It is assumed in the model that aluminum particles combine with each other until ignition occurs; that proximity to coarse AP particles results in ignition; and that ignition causes aluminum particles and agglomerates to lift off the surface. A horizontal separation distance between aluminum particles is used to determine if they combine into an agglomerate. For two aluminum spheres with radii $r_{p,i}$, $r_{p,j}$ and whose centers are located at (x_i, y_i, z_i), (x_j, y_j, z_j), respectively, the horizontal separation distance $H_{i,j}$ is defined in Equation (6-3).

$$H_{i,j} = \sqrt{(x_i - x_j)^2 + (y_i - y_j)^2} - r_{p,i} - r_{p,j} \quad \textbf{(6-3)}$$

If $H_{i,j}$ is less than the critical horizontal separation distance H_c, a free parameter in the model, then the two aluminum spheres will agglomerate unless there is an AP particle between them or unless both aluminum particles have already agglomerated with other particles. Separate agglomerates must not be combined, just as in the Separation Distance Model.

6.2.4 Calculation of Mean Agglomerate Size and Agglomeration Fraction

To determine the final agglomerate size distribution, the volumes of the particles in each agglomerate are summed, and an agglomerate diameter is back-calculated from the agglomerate volume, assuming a spherical agglomerate. The agglomeration fraction and weight mean agglomerate diameter are calculated using an agglomeration cutoff diameter, D_{cut}, also used by Jackson in his model.[110] The value of this parameter is based on experimental methods for measuring agglomerate sizes. Often, experimentalists do not measure agglomerates smaller than ~49 microns[98] because smaller sizes are too small to screen. The value of D_{cut} can vary, however, depending on the experimental method used.

The final aluminum distribution is split at D_{cut} into agglomerates and unagglomerated aluminum. The agglomeration fraction, f_{agg}, is the mass fraction of the distribution larger than D_{cut}, as shown in Equation (6-4), and the weight mean agglomerate diameter, D_{agg}, is the weight mean diameter of everything larger than D_{cut}, as shown in Equation (6-5). N is the total number of particles and N_{agg} is the total number of agglomerates in the final aluminum distribution. $D_{agg,i}$ is the diameter of each agglomerate i, and D_j is the diameter of each particle j in the final aluminum distribution.

$$f_{agg} = \frac{\sum_{i=1}^{N_{agg}} D_{agg,i}^3}{\sum_{j=1}^{N} D_j^3} \qquad \textbf{(6-4)}$$

$$D_{agg} = \frac{\sum_{i=1}^{N_{agg}} D_{agg,i}^4}{\sum_{i=1}^{N_{agg}} D_{agg,i}^3} \qquad \textbf{(6-5)}$$

6.2.5 Results of Preliminary Models

Agglomerate sizes calculated by the three models have been compared with the data of Grigoryev et al.[96] and Sambamurthi et al.[98] The data of Grigoryev et al. show an increase in agglomerate size as coarse AP size and aluminum concentration increase. They also varied the pressure but saw no effect on the agglomerate size. The data of Sambamurthi show the effects on agglomerate size of varying the pressure, the coarse-to-fine AP ratio, and the fine AP size.

6.2.5.1 Grigoryev

Grigoryev et al.[96] studied agglomeration in aluminized AP propellants with monomodal AP distributions. The aluminum size was 14 microns for all formulations. The binder type was not specified. They varied AP size from 50 to 280 microns for 48/22/30 and 37/42/21 AP/Al/binder mass ratios. The pressure was varied from 1 to 40 atm.

For each of the three preliminary models, only average particle sizes were included in the packs, rather than full particle-size distributions. Homogenization was not used, so no pressure dependence is included in the models for this comparison. This seems reasonable because Grioryev et al. saw no pressure effect, which may be due to the relatively high binder concentrations in their propellants. The agglomeration cutoff diameter D_{cut} was set equal to 15 microns because Grigoryev reported that agglomerates larger than 15 microns in diameter were reliably recorded and measured. In the Separation Distance Model, the critical separation distance S_c was arbitrarily set equal to 10 microns. In the Ignition Model, the critical horizontal separation distance H_c was arbitrarily set equal to 10 microns. Particle packs generated for this comparison varied in diameter from 375 to 2100 microns, depending on the coarse AP diameter. Pack height was set equal to pack diameter for all packs.

Figure 6-2 shows how the calculated and measured agglomerate diameters increase as AP diameter and aluminum concentration increase. The success of all three models in calculating these qualitative trends is encouraging since, experimentally, these are two of the most consistently observed trends.

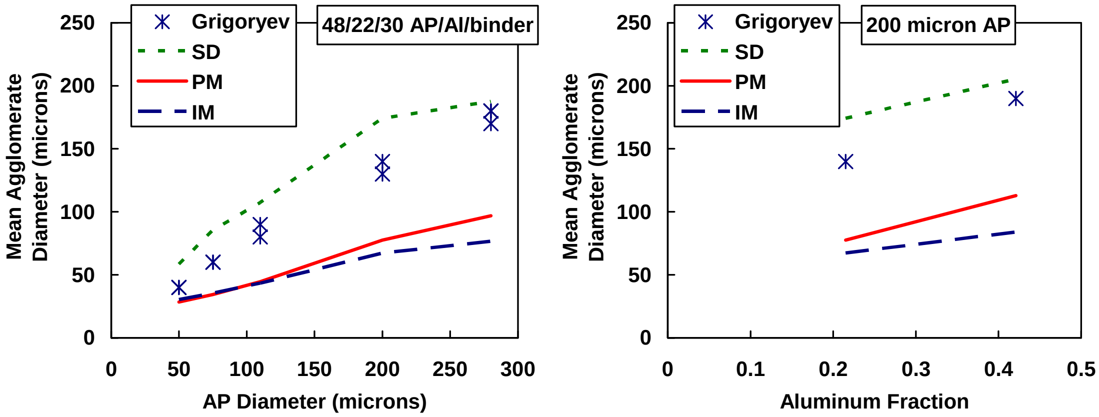

Figure 6-2: Preliminary calculations of agglomerate diameter varying coarse AP diameter and aluminum concentration, compared with the data of Grigoryev et al.

As AP size increases, so does the size of the pockets between AP particles, allowing more aluminum particles to gather in close proximity to each other, resulting in larger agglomerates. Larger AP particles are also less numerous than smaller AP particles (assuming equal mass fractions). Therefore, as AP size increases there are fewer AP particles separating the aluminum particles and fewer aluminum ignition sources. The effect of aluminum concentration is very straightforward. An increase in aluminum concentration forces aluminum particles closer together, which increases their tendency to combine with each other to form agglomerates.

The Separation Distance Model predicts very large agglomerates compared with the relatively small agglomerates predicted by the Ignition and Pocket models. It should be noted that the model parameters have not been calibrated to the experimental data, since the goal with the preliminary models is to explore their qualitative validity. It is possible, however, to calibrate each model by modifying the critical separation distances S_c and H_c in the Separation Distance Model and the Ignition Model, and by modifying the number of model-defined pockets that are allowed to combine in the Pocket Model.

6.2.5.2 Sambamurthi

Sambamurthi et al.[98] studied AP/Al/PBAN propellants with bimodal AP size distributions. All formulations contained 71% AP, 18% Al and 11% PBAN, with 390-micron coarse AP and 30-micron aluminum particles. Fine AP size was varied from 17.5 to 196 microns, coarse-to-fine ratios from 100/0 to 60/40, and pressure from 1 to 30 atm.

Homogenization has been included in the models for comparison with the data of Sambamurthi et al. Only average particle sizes were included in the packs, rather than full particle-size distributions. The agglomeration cutoff diameter D_{cut} was set equal to 49 microns, as used by Sambamurthi et al. In the Separation Distance Model, the critical separation distance S_c was arbitrarily set equal to 10 microns. In the Ignition Model, the critical horizontal separation distance H_c was arbitrarily set equal to 10 microns. Pack diameters and pack heights were approximately 2925 microns.

Figure 6-3 compares experimental and calculated values of agglomerate diameter varying coarse to fine AP ratio for three fine AP sizes at 13.6 atm.

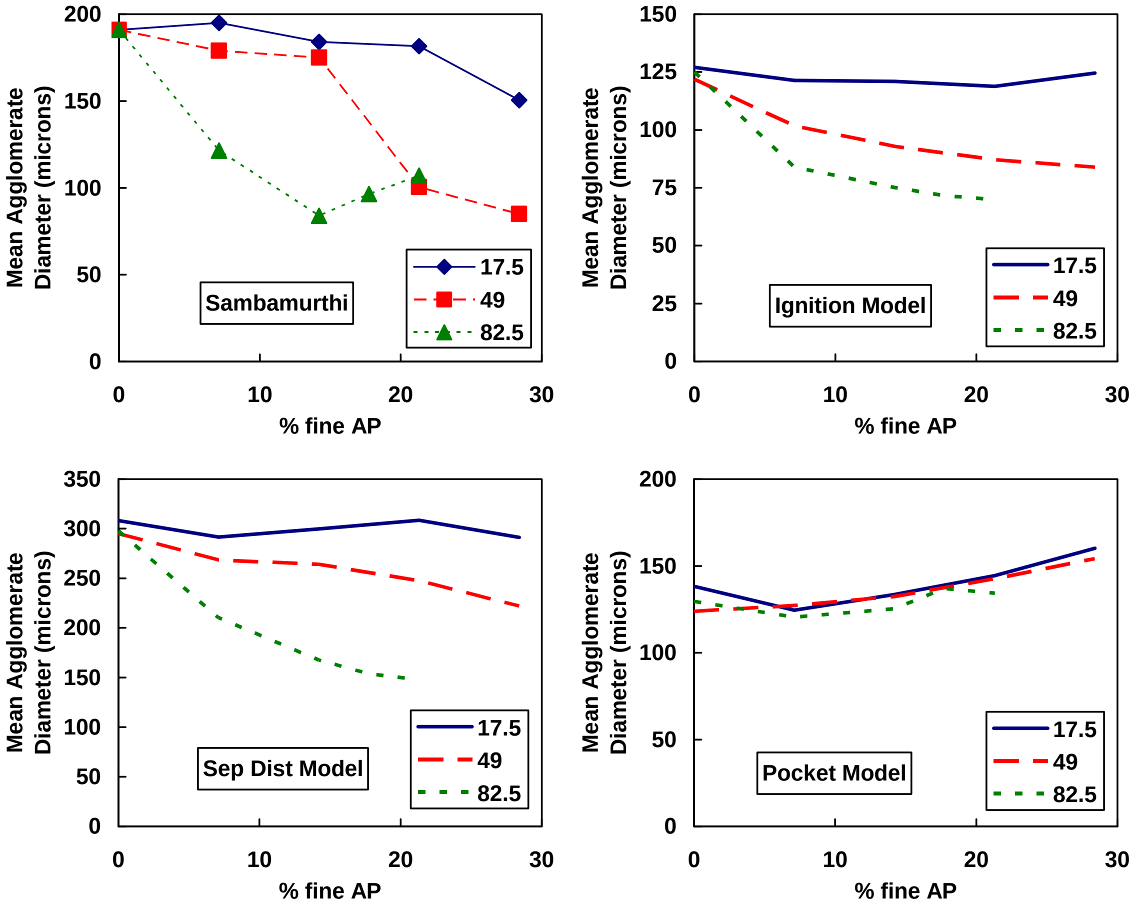

Figure 6-3: Preliminary calculations of agglomerate diameter varying coarse to fine ratio for three different fine AP sizes, compared with the data of Sambamurthi et al.

The general experimental trend is that agglomerate size decreases as the size and concentration of the fine AP increase. The two smaller AP sizes probably mix homogeneously with the binder and burn with a premixed flame. Thus, greater concentrations of fine AP result in hotter binder flames that reduce the surface residence time of aluminum particles. The largest of the three fine AP sizes, 82.5 microns, probably produces a diffusion flame that acts as a direct ignition source for the aluminum particles, which has an even greater reducing effect on the agglomerate size than the higher premixed binder flame temperatures produced by the smaller fine AP sizes. There may also be a geometric effect of the different AP diameters. That is, the 82.5 micron particles probably have a greater effect on particle spacing than the 49 and 17.5 micron AP, which fit more easily into the crevices between coarse AP particles.

The models are only somewhat successful in matching the experimentally observed trends. The Ignition Model and Separation Distance Model both calculate a decrease in agglomerate size with increasing fine AP fraction for the 49 and 82.5 micron AP sizes, consistent with experimental data. They also calculate a decrease in agglomerate size with increasing fine AP size. However, neither model predicts the reverse s-shaped curve seen experimentally for the 49 micron fine AP or the increase in agglomerate size for the 82.5 micron fine AP. The Pocket Model is unable to calculate any of the correct trends. This is likely because the model is only based on the coarse AP particles (390 microns) and does not account for the fine or intermediate sizes directly. To be viable, the Pocket Model would have to be improved to account for the influence of the smaller AP sizes on particle spacing, binder flame temperature, and flame structure.

Figure 6-4 compares experimental and calculated agglomerate sizes varying pressure and fine AP size. The coarse to fine AP ratio is 80/20 for all formulations.

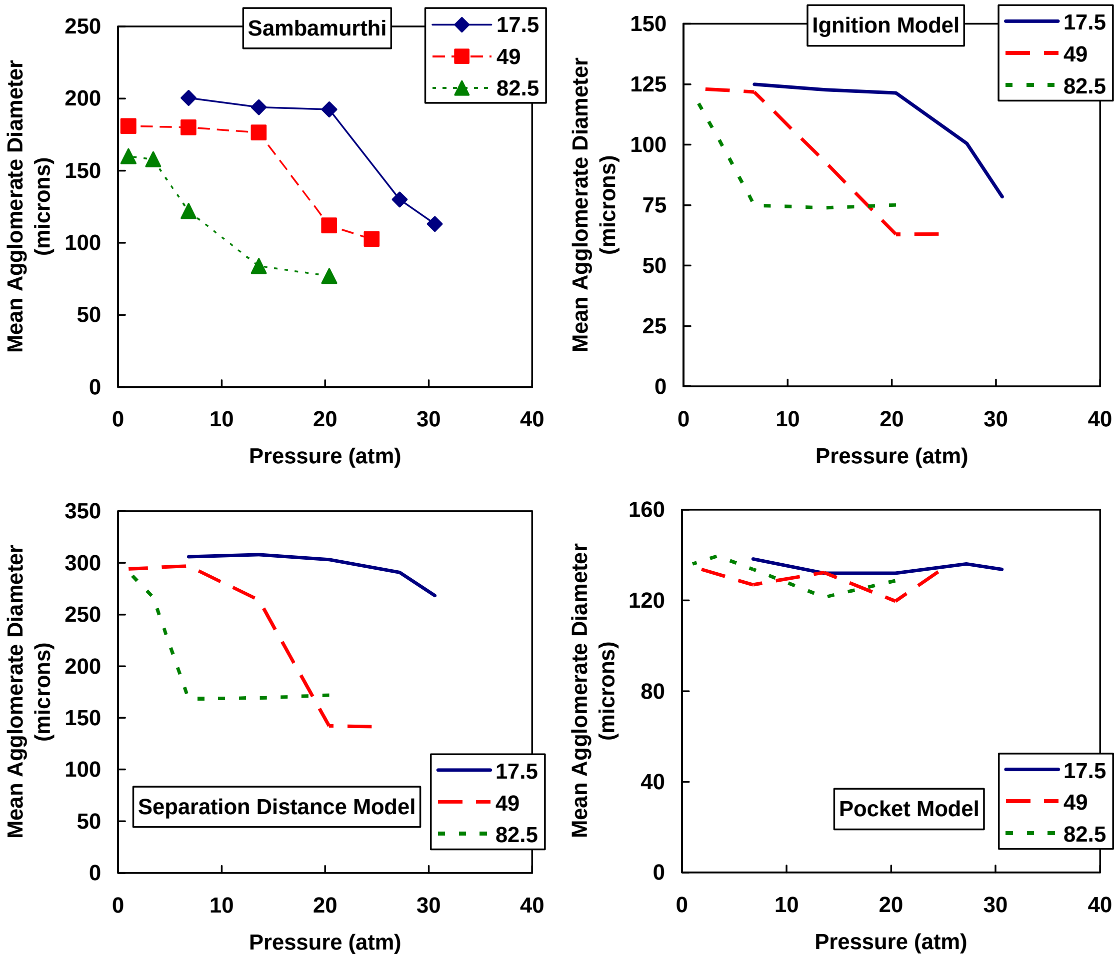

Figure 6-4: Preliminary calculations of agglomerate diameter varying pressure for three different fine AP sizes, compared with the data of Sambamurthi et al.

The experimentally observed trend is that agglomerate size decreases as pressure increases. This is probably due to the increase in burning rate and the changing flame structure. As pressure increases, the premixed flame above a particle and the surrounding binder moves closer to the surface and transitions into a diffusion flame, which acts as a strong ignition source for aluminum particles, resulting in smaller agglomerates. The transition pressure at which agglomerate size begins to decrease is inversely proportional to the fine AP size. This seems consistent because for a smaller AP diameter, a higher pressure is required to achieve a diffusion flame.

Both the Ignition and Separation Distance models show a decrease in agglomerate size as pressure increases. They also show an increase in transition pressure with decreasing fine AP size. The effects are successfully predicted because pressure-dependent homogenization is included in the models (Equation (6-1)). The Pocket Model is once again unable to reproduce the correct trend because it does not account for fine AP particles.

Figure 6-5 compares experimental and calculated agglomerate sizes varying fine AP size at a pressure of 13.6 atm and an 80/20 coarse to fine AP ratio. Experimental data show a reduction in agglomerate size between 49 and 82.5 micron AP. The 17.5 and 49 micron AP particles are apparently small enough at 13.6 atm to burn with the binder in a premixed flame, while the 82.5 and 196 micron particles produce a diffusion flame, reducing the agglomerate size significantly. There may also be a geometric effect. It is possible that 82.5 and 196 micron particles are large enough to create their own pockets, which are smaller than the pockets of the 390 micron particles, resulting in smaller agglomerates.

The Separation Distance Model and the Ignition Model are both successful in matching the experimentally observed trend in Figure 6-5, showing a sharp decrease in agglomerate size between 49 and 82.5 micron fine AP, and an increase between 82.5 and 196 micron AP. The Pocket Model again fails to calculate the correct trend.

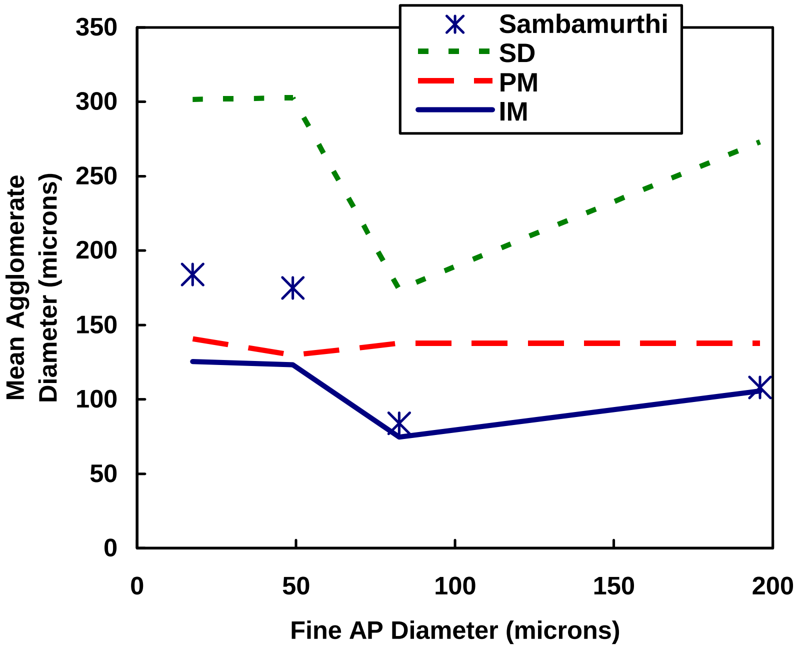

Figure 6-5: Preliminary calculations of agglomerate diameter varying fine AP size, compared with experimental data of Sambamurthi et al.

6.2.6 Conclusions Based on Preliminary Models

Of the three agglomeration models, the Separation Distance Model and the Ignition Model look the most promising, while the Pocket Model does not appear to be viable without extensive revision. Table 6-1 summarizes the results of each model for the five trends that have been investigated in this study.

Table 6-1: Summary of preliminary agglomeration modeling results.

Effect	Coarse AP Size	Al Fraction	Pressure	C/F Ratio	Fine AP Size
Pocket Model	Good	Good	Poor	Poor	Poor
Sep. Dist. Model	Good	Good	Good	Okay	Good
Ignition Model	Good	Good	Good	Okay	Good

Based on the success of the Separation Distance Model and the Ignition Model in predicting these trends, pressure-dependent homogenization and a separation distance parameter both appear to be important. Thus, both have been used in the final model.

To improve the ignition criteria in the final model, Felt's two-dimensional diffusion flame model[5,7] has been used to determine gas-phase temperature profiles for several different AP particle sizes and pressures. This should provide a more accurate determination of what AP sizes and pressures promote aluminum particle ignition.

The particle-size distributions were very simplified in the preliminary model calculations, with only one average particle size used to represent each distribution. Broad particle-size distributions have been used in the final model to more accurately match real propellant formulations.

6.3 Final Model

Based on the preliminary results, several elements of the initial models have been used in the final version of the model. Other elements have also been added. Pressure-dependent homogenization has been included using Equation (6-1). Broad particle-size distributions have been used, rather than just using one average size to represent an entire distribution. Distributions have been discretized into 20 sizes in each case. A critical separation distance parameter S_c has been used to determine whether aluminum particles will combine. The surface is regressed in increments determined by a step size parameter L_s. At each new surface location, a series of calculations are performed to determine if aluminum particles combine with other aluminum particles and if the particles or conglomerates ignite and lift off the surface. Criteria for ignition have been determined using Felt's two-dimensional diffusion flame model in conjunction with PHASE3 and PARPACK. Model calculations and the development of ignition criteria are discussed in detail in this section.

6.3.1 Surface Regression

In the final model, the surface is numerically regressed to mimic a burning propellant. A flat, smooth surface has been assumed due to the complexity of modeling a rough surface. Beginning at the top of the particle pack, the surface is regressed in step sizes equal to L_s. At each new surface location, the horizontal cross-section of the pack is analyzed and individual AP particle cross-sections are calculated. The AP cross-sections are treated in the surface calculations, rather than the entire spherical particle since, realistically, only the particle cross-sections are relevant to the combustion process at any given surface location. The aluminum particles, however, are treated as spheres, since they do not vaporize at the propellant surface, but rather maintain their solid or liquid state until they ignite and lift off the surface. At each new surface location, the following calculations are performed by the model.

1. Each aluminum particle that has been fully exposed by the regressing surface is made to descend with the surface. These particles are not allowed to move horizontally, but only to descend vertically until settling on the surface or on other exposed aluminum particles.
2. The distance between each pair of exposed aluminum particles, whether partially or fully exposed, is calculated and, if less than the critical separation distance S_c, the pair are labeled as part of the same

agglomerate. If one or both of the particles has agglomerated with another particle, then all of the particles are combined into one agglomerate.

3. The distance between each exposed aluminum particle and nearby AP particles is calculated and compared with ignition criteria to determine if the aluminum particle would ignite. If the aluminum particle is found to ignite, then any other aluminum particles that have agglomerated with it are also considered to ignite, and all the ignited particles are removed from further calculations.
4. The size of each ignited agglomerate is calculated. Agglomerates are assumed to be spherical and to contain the entire volume of all the particles within them. Thus, agglomerate diameters are back calculated from their total volumes.

After the surface has regressed through the entire pack and all agglomerates have been determined, the weight mean agglomerate diameter and the agglomerated fraction of aluminum are calculated using Equations (6-4) and (6-5). The final size distribution, including agglomerated and unagglomerated aluminum, is also calculated by the model, although experimental studies usually only report a mean agglomerate size.

6.3.2 Determination of Ignition Criteria

The ignition criteria distinguish the agglomeration model of the current study from any previous agglomeration modeling work. Pressure-dependent homogenization has an effect on aluminum ignition in the model because only non-homogenized AP particles are allowed to act as ignition sources. To determine if non-homogenized AP particles would ignite the aluminum, Felt's diffusion flame model has been used to calculate the temperature profile above burning AP particles and surrounding binder. This has been done for several AP particle sizes and pressures. For each case, an aluminum ignition isotherm of 2200 K has been calculated from the temperature profile and the results have been compiled in the agglomeration model in the form of a lookup table. The calculation of the isotherms and preliminary calculations needed to run Felt's model are discussed in this section.

6.3.2.1 Binder Composition and Binder Allocation

In order to use the diffusion flame model as a predictor of aluminum ignition, several changes had to be made to the propellant and binder formulations previously assumed. Two important parameters, other than AP size and pressure, that need to be specified in the diffusion flame model, are a binder thickness and composition. Previously, these parameters were chosen based on the overall formulation of an 86% AP/14% HTPB propellant.[5] This resulted in a binder thickness that decreased with particle size and a binder composition of 77.5% AP/22.5% HTPB. However, it is probably not necessary to maintain the overall propellant formulation when performing micro-scale modeling. Instead, it would be better to study the propellant at the micro-scale to determine the proper parameter values. This has been done in the current study by generating particle packs and analyzing pack cross-sections in order to determine the amount of binder to allocate to each particle. In addition, to simulate the combustion of an aluminum-containing propellant, the shuttle propellant formulation has been used rather than the previous non-aluminized propellant from Ref. 5. The pseudo-binder composition has been determined from the overall shuttle propellant formulation, and the binder thickness has been determined by analyzing particle packs corresponding to the shuttle propellant.

The shuttle propellant contains 70% AP, 16% 44-micron aluminum, and 14% PBAN. The AP distribution is bimodal, containing 200- and 20-micron sizes at a 70/30 coarse to fine ratio. The pseudo-binder composition of the shuttle propellant was calculated by assuming that all of the 20-micron AP and 44-micron aluminum was homogenized into the binder. This resulted in a binder composition of 40.9% AP, 31.3% aluminum, and 27.9% PBAN. This composition has been modeled in PHASE3 and surface temperatures, burning rates, and surface species mass fractions have been correlated with gas-phase heat flux. These correlations make up the condensed-phase binder boundary condition in the diffusion flame model. It should be noted that the aluminum is treated as an inert. In this way, the effect of aluminum on the gas-phase temperature profile can be calculated before it ignites.

Based on the pressure dependence of homogenization, the binder formulation is allowed to vary with pressure. However, the premixed AP/HTPB model, discussed in Chapter 4, is not robust enough to model a wide range of AP percentages. Hence, the binder composition has not been varied with pressure in the diffusion flame model. This is one aspect of the agglomeration model that needs to be improved in the future when the AP/HTPB premixed combustion model has been further developed.

The binder thickness as a function of pressure and AP size was calculated by analyzing cross-sections of a particle pack matching the shuttle propellant formulation. The pack height and diameter were ~1500 microns, 7.5 times the average coarse AP diameter (200 microns). The particle-size distribution parameters used are shown in Table 6-2. Each distribution was modeled using a combination of two lognormal distributions. Parameters were obtained by fitting detailed distribution data provided by ATK Launch Systems.[159]

Table 6-2: Particle-size distribution parameters used to model the shuttle propellant.

Nominal Size	σ_1	$D_{m,1}$	θ_1	f_1	σ_2	$D_{m,2}$	θ_2	f_2
200-micron AP	0.340	236	0	0.830	0.500	135	0	0.170
20-micron AP	1.01	17.6	0	0.985	0.258	3.12	0	0.0146
44-micron Al	0.709	40.0	0	0.936	1.28	25.3	0	0.0644

A cross-section of the particle pack simulating the shuttle propellant formulation is shown in Figure 6-6 (top left). The gray- and blue-colored particles are the coarse and fine AP, respectively. The red-colored particles are aluminum. Some of the larger particles fall outside the cylindrical boundary of the pack. This is due to the method of particle placement used in PARPACK, which allows larger particles to fall partially outside the cylinder in order to avoid edge effects. Only the portions of the particles within the cylinder are treated in the agglomeration model. It can also be seen that there is a wide range of particle sizes. This is due, in part, to the broad AP particle-size distributions, but it is also due to the fact that these are two-dimensional cross-sections of particles. Depending on the position of a cross-section in a particle, its size can vary dramatically.

An analysis of several cross-sections of the shuttle pack has been performed to determine how the pseudo-binder should be allocated to each particle. The pseudo-binder includes the aluminum, homogenized AP, and binder (void space). Depending on the pressure, there is a different homogenization cutoff diameter and a different amount of pseudo-binder in the cross-section of the pack. To illustrate the effect of homogenization on the pack cross-section, homogenized cross-sections at 68, 34, and 13.6 atm are presented in Figure 6-6, along with the complete (non-homogenized) cross-section.

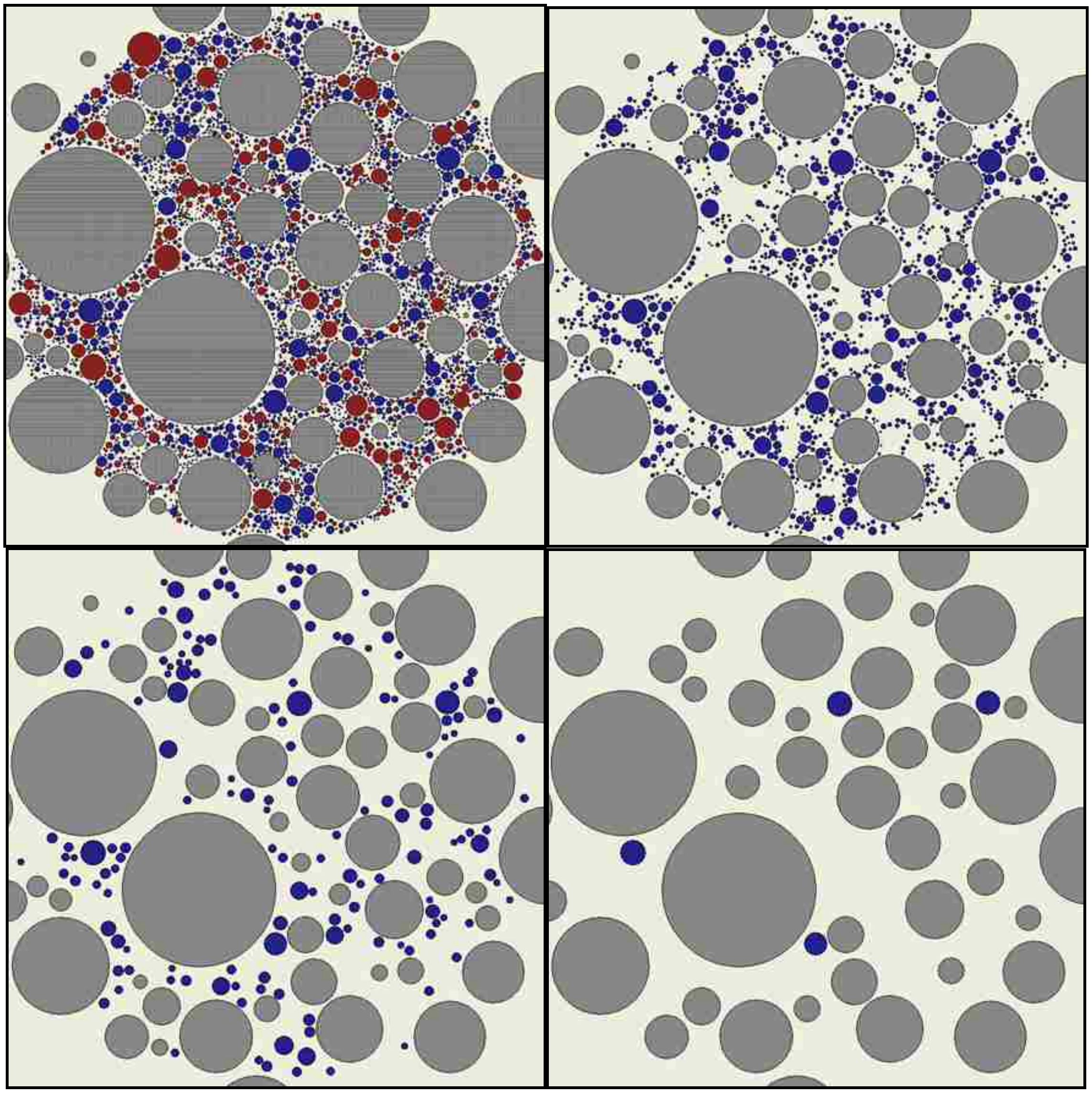

Figure 6-6: Effect of pressure-dependent homogenization on the composition of a pack cross-section. Top left: no homogenization. Top right: 68 atm. Bottom left: 34 atm. Bottom right: 13.6 atm.

While the actual composition of the pack cross-section does not vary with pressure, the flame structure above each particle does vary. As pressure decreases, so does the number of particles that produce a diffusion flame, which is the effect illustrated in Figure 6-6. In addition, the amount of pseudo-binder in the cross-section increases as pressure decreases. Thus, the amount of pseudo-binder allocated to each non-homogenized AP particle would be expected to increase as pressure decreases. The amount of binder allocated to each particle has been calculated in the model by scanning around each non-homogenized AP particle to determine the area of pseudo-binder directly around it. The scan initiates from the center of the particle, as shown in Figure 6-7. There are actually hundreds or thousands of scanning vectors used in the model, depending on the particle size, but there are only 16 shown to simplify the illustration.

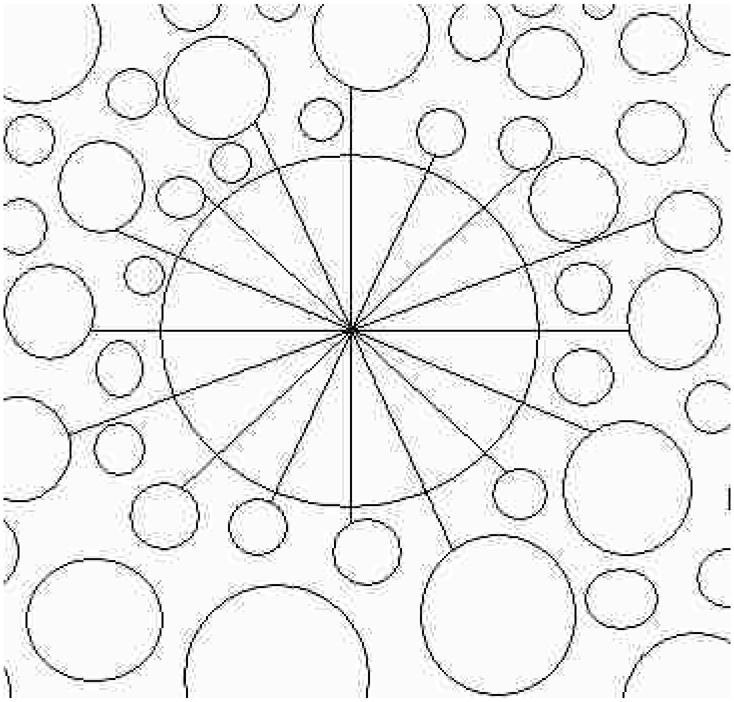

Figure 6-7: Illustration of scanning method used to determine binder allocation.

A pseudo-binder area is calculated for each scanning vector, treating the vector as a “pizza slice” of binder at the edge of the particle. The vector areas are summed to obtain a total pseudo-binder area for each particle. The areas for each particle are then summed to obtain a total pseudo-binder area. With this approach, pseudo-binder areas of different particles overlap, so the total calculated pseudo-binder area is greater than the actual pseudo-binder area in the pack cross-section. Therefore, the total area, as well as the area associated with each particle, is reduced with a correction factor to match the actual area. After the area is corrected, a binder thickness is back calculated for each particle by assuming that the binder forms a larger circle around the particle cross-section and by subtracting the radius of the particle cross section from the larger radius of the surrounding binder. These calculations are shown in Equations (6-6) to (6-8). A_b is the total pseudo-binder area, $A_{b,i}$ is the pseudo-binder area of the i^{th} particle, $T_{b,i}$ is the binder thickness of the i^{th} particle, $r_{p,i}$ is the radius of the i^{th} particle cross-section, $L_{i,j}$ is the length of the j^{th} scanning vector of the i^{th} particle, N_i is the number of scanning vectors of the i^{th} particle, and F is the correction factor. The correction factor F is calculated by subtracting the actual area of the pack cross-section from the calculated area and iterating with a root-finding subroutine to find the value of F.

$$A_b = \sum_i A_{b,i} \tag{6-6}$$

$$A_{b,i} = \sum_j \frac{\pi(r_{p,i} + FL_{i,j})^2 - \pi r_{p,i}{}^2}{N_i} \tag{6-7}$$

$$T_{b,i} = \sqrt{\frac{\pi r_{p,i}{}^2 + A_{b,i}}{\pi}} - r_{p,i} \tag{6-8}$$

These calculations were performed on several pack cross-sections at several pressures. The results for some of the pressures are presented in Figure 6-8. The results have been averaged into 10-micron bins of particle cross-section radius to reduce the number of points and to see trends more clearly. There does not appear to be any dependence of the binder thickness on particle size, but the binder thickness does decrease with increasing pressure. Therefore, binder thickness in the diffusion flame model follows the same trends.

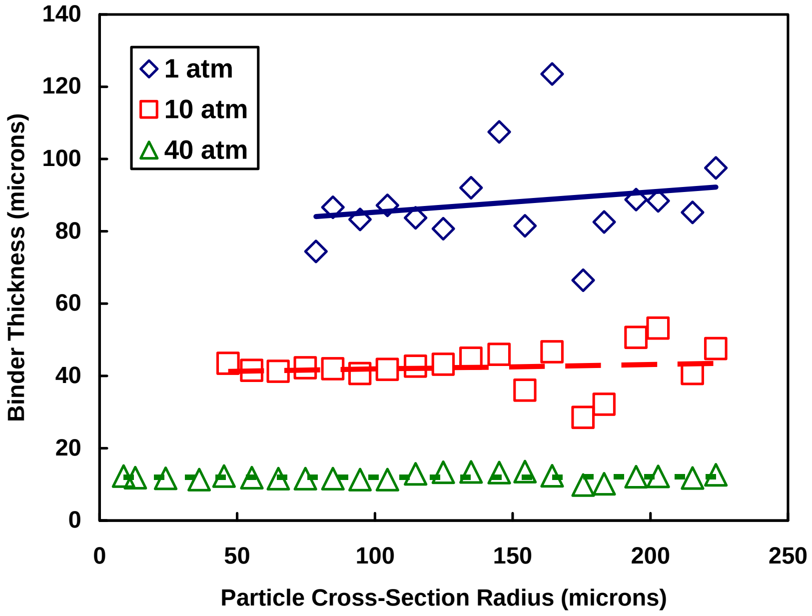

Figure 6-8: Calculated binder thicknesses as a function of particle cross-section radius at several pressures.

Based on the results of these calculations, several values of binder thickness have been chosen at different pressures to be used in the diffusion flame model. These are presented in Figure 6-9. The calculated pressure dependence of the binder thickness is very similar to that of the homogenization cutoff diameter, which is reasonable since homogenization was involved in the calculations.

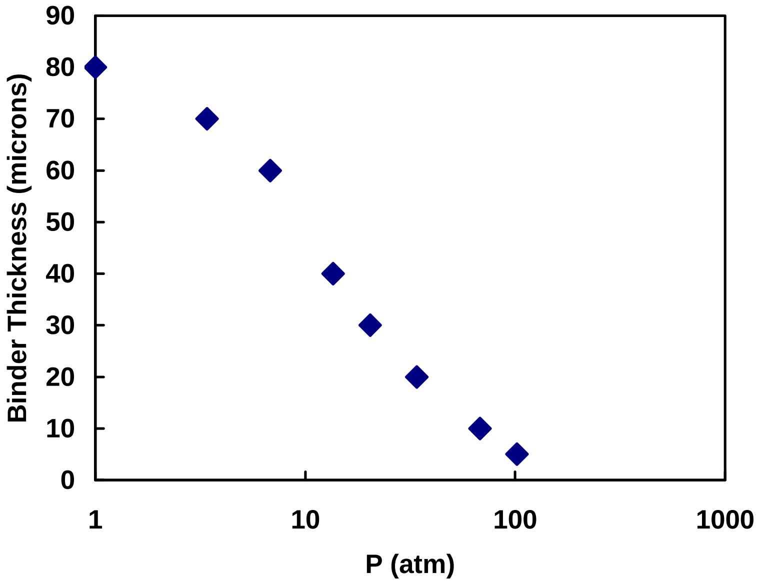

Figure 6-9: Binder thicknesses and pressures used in the diffusion flame model.

6.3.2.2 Diffusion Flame Calculations

Using the binder composition and binder thicknesses presented in the previous section, the diffusion flame model has been used to calculate the temperature profile above a burning AP particle and the surrounding binder for several AP diameters and pressures. Particle diameter has been varied from 7 to 400 microns and pressure has been varied from 1 to 102 atm. The combinations that were run and those that were considered homogenized are indicated in Table 6-3. Some did not converge to a solution (shown in red). The results of those that did converge (shown in blue) have been compiled into a lookup table which has been used in the agglomeration model for ignition criteria.

Because of the large number of cases, only some of the results have been presented. The calculated temperature profiles for 200-micron AP, at pressures from 1 to 34 atm, are shown in Figure 6-10.

Table 6-3: Diameters and pressures used in diffusion flame calculations.

		Pressure (atm)							
		1	3.4	6.8	13.6	20.4	34	68	102
AP Diameter (µm)	7	🟫	🟫	🟫	🟫	🟫	🟫	🟦	🟦
	10	🟫	🟫	🟫	🟫	🟫	🟫	🟦	🟦
	20	🟫	🟫	🟫	🟫	🟫	🟦	🟦	🟦
	30	🟫	🟫	🟫	🟫	🟦	🟦	🟦	🟦
	50	🟫	🟫	🟫	🟦	🟥	🟦	🟦	🟦
	100	🟦	🟦	🟦	🟦	🟦	🟥	🟦	🟦
	200	🟦	🟦	🟦	🟦	🟦	🟦	🟥	🟥
	400	🟦	🟦	🟦	🟦	🟦	🟦	🟥	🟥

blue = converged, red = did not converge, tan = homogenized

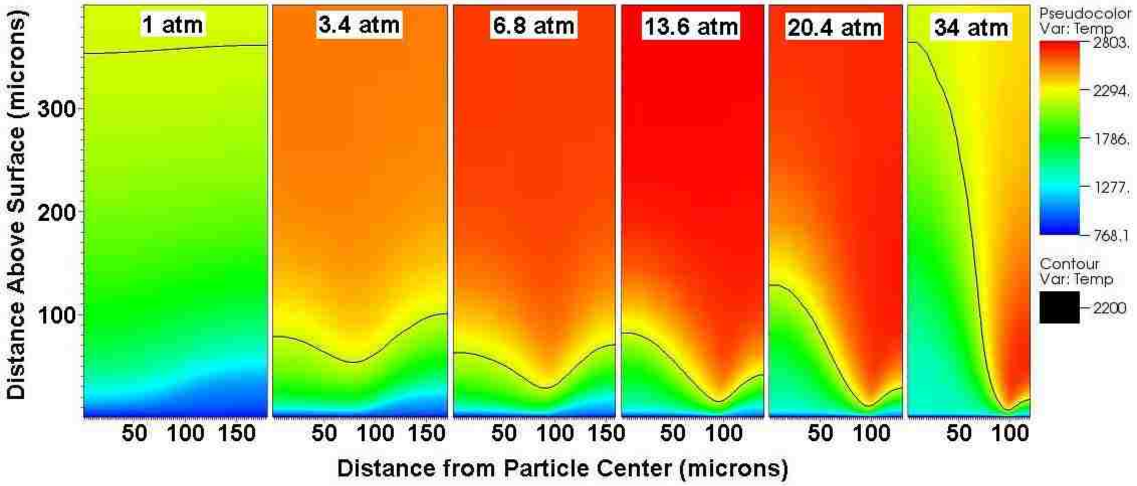

Figure 6-10: Diffusion flame calculations for 200-micron AP from 1 to 34 atm.

It should be noted that the calculations are performed on the particle radius, and the adjacent pseudo-binder, since the model uses an axis of symmetry. Thus, the first 100 microns along the x-axis correspond to the AP particle and beyond that is the AP/HTPB pseudo-binder. The 2200 K isotherm is included in each case, and is very important to the agglomeration model, since it is assumed to control aluminum ignition. If an aluminum particle is positioned above the surface so that the ignition isotherm passes through it, then it is assumed to ignite. The isotherm position, as a function of AP diameter and pressure, is stored in the form of a lookup table in the agglomeration model.

There is a very apparent pressure trend in the position of the isotherm. As pressure increases above 1 atm, the isotherm approaches the surface, with the closest proximity being near the particle edge due to diffusion. There is an interesting effect above the AP particle, which is that the isotherm approaches the surface as pressure increases from 1 to 6.8 atm, but then it moves away from the surface from 6.8 to 34 atm, and probably moves even farther away at pressures above 34 atm. This is due to the changing velocity in the gas phase. At low pressure, there is a high gas-phase velocity due to pressure alone. As pressure increases, the gas velocity decreases due to pressure, but eventually increases due to the increasing mass flux from the burning propellant.

The effect of varying the particle size at 13.6 atm is shown in Figure 6-11. The isotherm in the region above the particle moves closer to the surface as particle size decreases, but the opposite is true in the region above the binder. This seems to be related to the size of the diffusion zone, where temperatures are hottest, relative to the particle size and the binder thickness. For the 400-micron particle, the diffusion zone covers the entire length of binder (40 microns), but does not affect the entire particle. Thus, the temperature is hotter above the binder. As particle size decreases, however, the hot diffusion zone shifts from the region above the binder to the region above the particle.

This appears to be caused by the fact that the particle size varies while the binder thickness does not (at constant pressure). Thus, as particle size decreases, the binder is affected less by the hot diffusion flame and the temperature above the fuel rich binder cools significantly. These results are also related to the overall concentration of AP, which decreases with particle size. Thus, for the smallest size of 50 microns, the high-temperature region is smaller and relatively cooler.

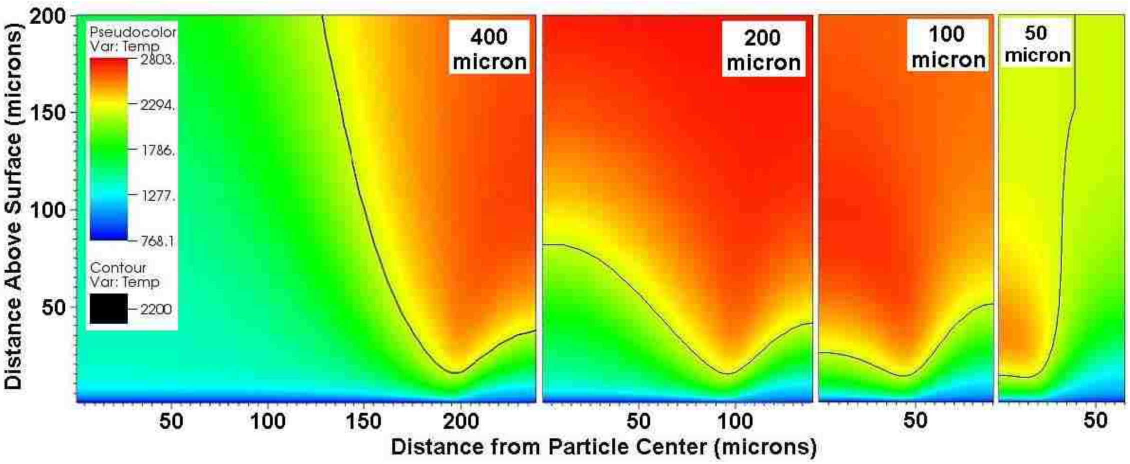

Figure 6-11: Diffusion flame calculations at 13.6 atm from 50 to 400 micron AP particles.

6.3.3 Results and Discussion

Agglomerate diameter and the fraction of agglomerated aluminum have been calculated for several propellant formulations, simulating the experimental work of Grigoryev et al.,[96] Sambamurthi et al.,[98] and Micheli and Schmidt.[91] Variations of the shuttle propellant have also been modeled due to its similarity to the propellants of Micheli and Schmidt. For all calculations the value of S_c, the critical separation distance, has been set equal to 1 micron. In this way, the model allows very little lateral movement of aluminum particles during their surface residence time, consistent with the experimental observations of Glotov et al.[89] (Figure 2-15) and the modeling approach taken by Srinivas and Chakravarthy.[111] The surface regression step size, L_s, has been set equal to 15 μm, a typical aluminum particle radius, for all calculations.

6.3.3.1 Grigoryev

Grigoryev et al.[96] explored the effects on agglomeration of varying the AP particle size and the aluminum concentration. AP diameter was varied from 50 to 280 μm and aluminum concentrations of 22% and 42% were used. The aluminum size was 14 μm for all formulations. They also varied the pressure from 1 to 40 atm, but, contrary to most other researchers,[90,93,95] found no significant pressure effect at 1 atm. Because of the disagreement with most other researchers, the 1 atm data has not been considered here.

Particle-size distribution data were reported and lognormal parameters have been calculated by fitting Equation (5-2) to the data. Distribution parameters are presented in Table 6-4. Due to large cpu times required to generate a particle pack containing 280-μm AP, this formulation has not been modeled.

Table 6-4: Particle-size distribution parameters used to model Grigoryev propellants.

Nominal Size	σ_1	$D_{m,1}$	θ_1	f_1	σ_2	$D_{m,2}$	θ_2	f_2
50-micron AP	0.302	56.3	0	0.825	0.665	7.18	0	0.175
75-micron AP	0.243	82.5	0	0.806	0.0957	43.4	0	0.194
110-micron AP	0.263	109	0	0.500	0.263	109	0	0.500
200-micron AP	0.173	201	0	0.500	0.173	201	0	0.500
14-micron Al	0.199	17.6	0	0.391	0.542	9.69	0	0.458

The agglomeration cutoff diameter D_{cut} was set equal to 15 microns because Grigoryev reported that agglomerates larger than 15 microns in diameter were reliably recorded and measured. Particle packs generated for this comparison varied in diameter from ~375 to ~1500 microns, 7.5 times larger than the average AP particle diameter. Pack height was equal to pack diameter for all packs.

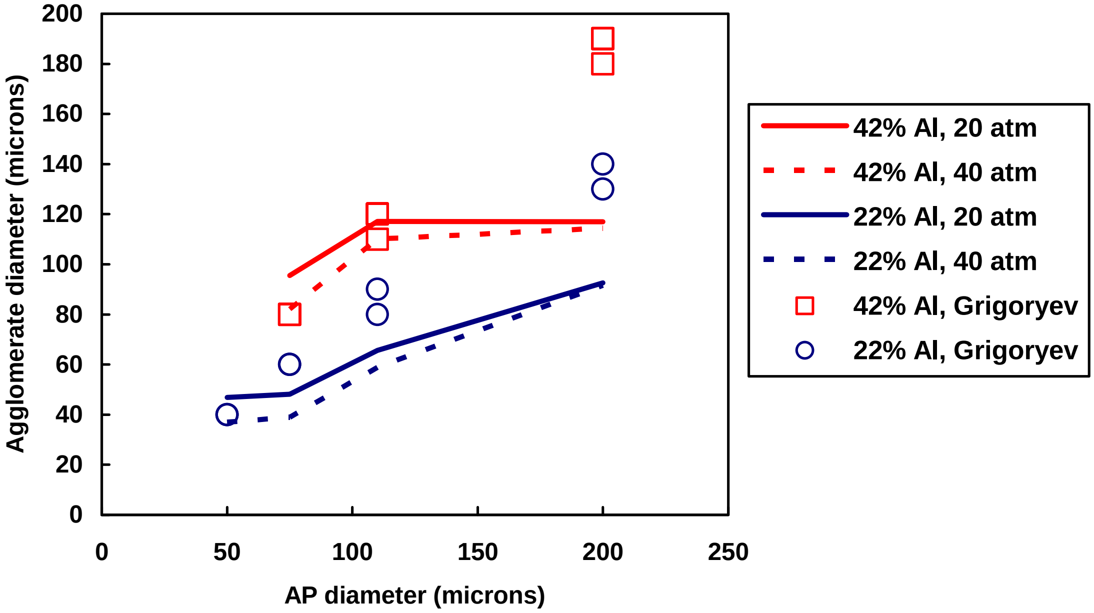

Figure 6-12: Calculated agglomerate diameters compared with Grigoryev's data, varying AP diameter and aluminum concentration.

Calculated agglomerate sizes at 20 and 40 atm are compared with the data in Figure 6-12. The test pressure is not indicated, since no pressure effect was measured by Grigoryev et al. There is only a slight pressure effect predicted by the model, which is fairly consistent with the lack of pressure effect in the data. The general trends are captured by the model, with agglomerate diameter increasing as AP diameter and aluminum concentration increase. However, there is only a slight increase between the

110 and 200 micron AP sizes for the 42% aluminum concentration. The quantitative disagreement between the model and the data may be due to the relatively high binder concentrations, and one very high aluminum concentration, used by Grigoryev et al.

6.3.3.2 Sambamurthi

Sambamurthi et al.[98] studied AP/Al/PBAN propellants with bimodal AP size distributions. Formulations contained 71% AP, 18% aluminum, and 11% PBAN, with 390 μm coarse AP and 30 μm aluminum particles. Fine AP size was varied from 17.5 to 196 μm, coarse-to-fine ratios from 100/0 to 60/40, and pressure from 1 to 30 atm. The 196 μm fine AP size has not been modeled because it is typically a coarse particle size.

Detailed particle-size distribution data were not available, but the diameter range of each distribution was reported. Lognormal parameters for Equation (5-2) were estimated and these are presented in Table 6-5. The agglomeration cutoff diameter D_{cut} was set equal to 49 microns, the same cutoff used by Sambamurthi et al. experimentally. Pack heights and diameters were ~2925 microns, 7.5 times the coarse AP diameter.

Table 6-5: Particle-size distribution parameters used to model Sambamurthi propellants.

Nominal Size	σ_1	$D_{m,1}$	θ_1
17.5-micron AP	0.35	17.5	0
49-micron AP	0.04	49	0
82.5-micron AP	0.04	82.5	0
390-micron AP	0.04	390	0
30-micron Al	0.3	30	0

It was necessary to modify the pack formulations slightly because PARPACK was unable to generate packs of 89% solids, which is the composition of Sambamurthi's propellants. Therefore, packs of 85% solids were generated while maintaining the ratios of coarse to fine AP and AP to aluminum. The lower solids loading, as well as the estimation of particle-size distributions, was expected to possibly distort the calculated results quantitatively, but hopefully not qualitatively.

The calculated pressure trend for three fine AP diameters is compared with Sambamurthi's data in Figure 6-13. Calculations at 1 atm are not included because the model predicted very large agglomerates (300 to 600 microns). The calculations at higher pressures are shown and the trends appear to agree reasonably well with the data.

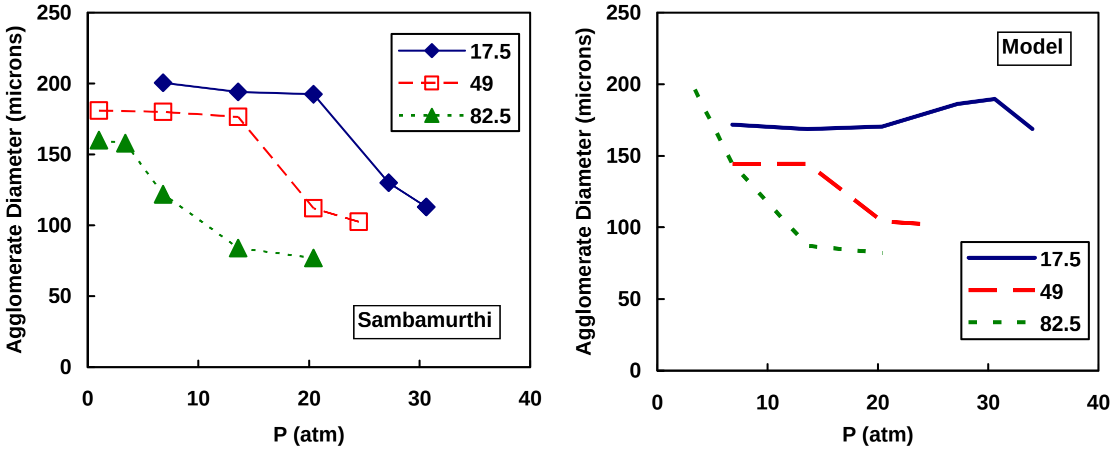

Figure 6-13: Calculated agglomerate sizes compared with Sambamurthi's data, varying pressure and fine AP size.

For all the fine AP sizes, the agglomerate size decreases as pressure increases. The calculated pressure, at which the agglomerate size begins to decrease, varies with fine AP size, just as it does with the data. For the 17.5 micron size, it was necessary to extend the model calculations to higher pressures to achieve the same decrease in agglomerate diameter. This may be an indication that the pressure dependence of homogenization assumed in the model needs to be modified slightly.

For the 17.5-micron AP size, there is a slight increase in the calculated agglomerate size as pressure increases from 15 to 30 atm. This differs from the observed experimental trend and indicates a possible deficiency in the model. The increase in agglomerate size may be due to the calculated position of the ignition isotherm above the AP particle at high pressures (Figure 6-10). The isotherm above the AP particle approaches the propellant surface as pressure increases from 1 to 6.8 atm, but above 6.8 atm, it moves away due to the high mass flux from the burning AP particle. Therefore, while there are more ignition sources at high pressure, there is also a tendency towards larger agglomerates based on the position of the isotherm. The latter effect is evident for the 17.5 micron AP size from 15 to 30 atm. An approach that might eliminate this effect in the model would be to allow the high mass flux from the coarse AP particles to cause aluminum particles to lift off the surface before igniting, which would result in smaller agglomerates and be more consistent with experimental observations.

The calculated effect of varying the coarse-to-fine AP ratio, for 3 different fine AP sizes, is shown in Figure 6-14. The model is successful in predicting the correct trends to a degree. The model predicts a decrease in agglomerate size as the fine AP size increases, which is consistent with the data. The calculations for the 82.5 micron fine AP size match the data fairly well. For the 17.5 micron size, there is only a slight variation in agglomerate size with changing fine AP concentration, which is also consistent.

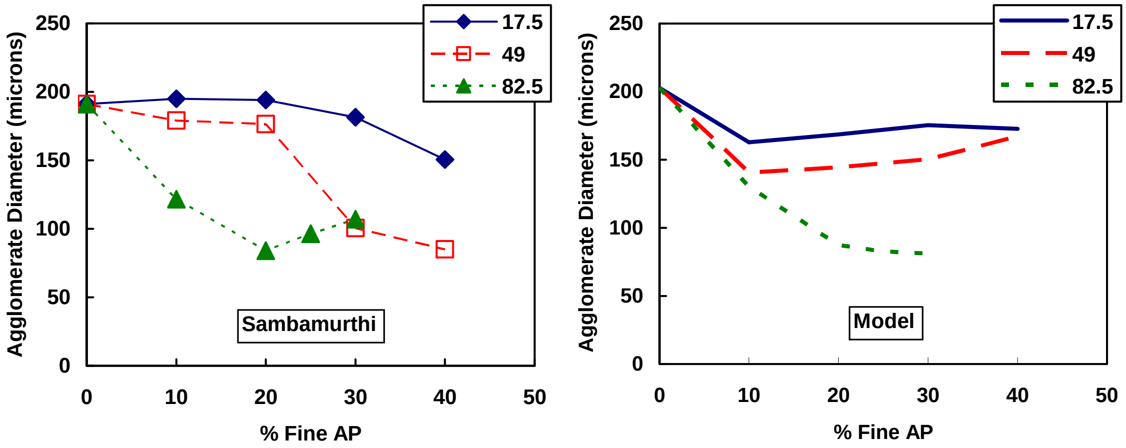

Figure 6-14: Calculated agglomerate sizes compared with Sambamurthi's data, varying fine AP percentage and fine AP diameter.

There are some discrepancies between the model calculations and the data. The calculated agglomerate size at 0% fine AP is relatively larger than at higher fine AP concentrations. This is probably because the particle pack for this formulation was generated with an 82% solids loading, rather than 85%, which was used for all other formulations. The lower AP concentration likely resulted in fewer ignition sources for the aluminum particles and therefore, larger agglomerates. There is also a sharp decrease in the measured agglomerate diameter for the 49-micron fine AP size, between 20 and 30% fine AP, which is not captured by the model. One possible explanation is that the varying pseudo-binder composition, as fine AP concentration is varied, has not been accounted for in the model. At higher fine AP concentrations, the pseudo-binder would have a higher AP concentration and would produce a hotter flame, resulting in smaller calculated agglomerates, which would be more consistent with the data. The pressure dependence of the pseudo-binder composition has not been accounted for either. In reality, the binder composition probably contains higher AP concentrations at lower pressures, when more AP is homogenized. Varying the binder composition with pressure in the model would likely have a significant effect on the position of the ignition isotherm, which would probably be relatively farther from the propellant surface at high pressure, and closer at low pressure. The approach of varying the binder concentration was considered, but has not been included due to the limitations of the premixed AP/HTPB model. As the premixed model is developed further, this approach will become more feasible.

6.3.3.3 Micheli and Schmidt

Micheli and Schmidt[91] studied AP/HTPB propellants containing 70% AP, 12% HTPB, and 18% aluminum. They used a 6-micron fine AP diameter and varied the coarse AP diameter from 106 to 325 microns. The aluminum diameter was 25 microns. In addition to the coarse AP size, they also varied the AP coarse/fine ratio from 57/43 to 100/0 and the pressure from 13.6 to 122.5 atm. Distribution data were not provided, so lognormal parameters have been estimated and are presented in Table 6-6.

Table 6-6: Estimated Micheli and Schmidt distribution parameters.

Nominal Size	σ_1	$D_{m,1}$	θ_1
6-micron AP	0.6	6	0
106-micron AP	0.08	106	0
212-micron AP	0.075	212	0
23-micron Al	0.4	23	0

The agglomeration cutoff diameter D_{cut} was set equal to 45 microns, consistent with the experiment. Pack heights and diameters ranged from ~795 to ~1590 microns, depending on the coarse AP size. The 325 micron size has not been modeled due to the excessive cpu time required to generate a corresponding particle pack. The coarse to fine AP ratio has been varied from 70/30 to 90/10 in the model. PARPACK was unable to achieve 88% solids loading for ratios larger than 90/10, so these formulations have not been modeled. Pressure was varied from 13.6 to 81.7 atm. The pressure of 122.5 atm has not been modeled since it lies outside the range of the diffusion flame lookup table.

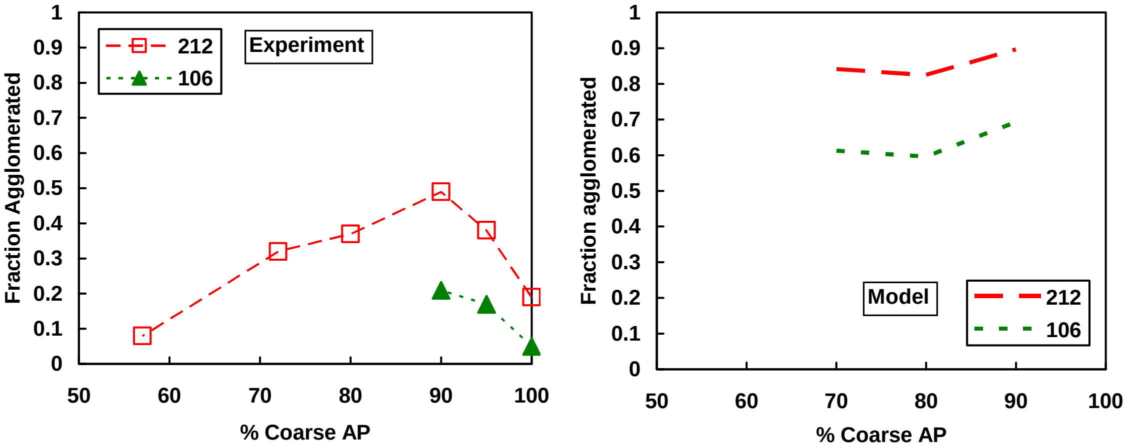

Figure 6-15: Calculated agglomerate sizes compared with the data of Micheli and Schmidt, varying coarse to fine AP ratio and coarse AP size.

The calculated agglomerated fractions of aluminum, varying coarse to fine AP ratio and coarse AP size, are compared with the data in Figure 6-15. The calculated agglomerated fraction increases with coarse AP size and is greatest at a ratio of 90/10, which is consistent with the data. However, the calculated agglomerated fractions are significantly higher than the measured values. This may be due to some fundamental differences between the experiment and the model. In the experimental study, agglomerated fractions were measured after quenching the gas-phase plume a short distance from the propellant surface, whereas in the model the values are calculated at the immediate surface. As reported by Pokhil, agglomerate size decreases as the quench distance increases, due to oxidation reactions, so the measured values may be smaller than what they would have been if measured at the immediate propellant surface.

Another discrepancy is that there is a slight increase in the calculated fraction between 80/20 and 70/30 coarse to fine AP ratios, which contradicts the data. A possible explanation for this difference is that the varying pseudo-binder composition, as fine AP concentration changes, has not been accounted for in the model. A similar discrepancy was found between the calculated agglomerate sizes and the data of Sambamurthi et al. If the varying binder composition were accounted for, the higher AP concentration in the binder at a coarse to fine ratio of 70/30 would likely result in smaller calculated agglomerated fractions, which would be more consistent with the data.

Another limitation is that PARPACK was unable to generate packs with sufficiently high volume fractions at coarse to fine AP ratios greater than 90/10. Thus, it is not known if the model would predict the correct trends between ratios of 90/10 and 100/0. However, this is a limitation of the particle-packing model, and not related to the agglomeration model directly.

The calculated agglomerated fractions, varying coarse to fine AP ratio and pressure, are compared with the data in Figure 6-16. Again, the highest agglomerated fraction is calculated at a 90/10 ratio, which is consistent with the data. However, the calculated fractions increase from 13.6 to 40.8 atm, but then decrease from 40.8 to 81.7

atm, which is inconsistent with the data. A similar discrepancy was found between the model and the data of Sambamurthi et al. for the 17.5 micron fine AP size between 15 and 30 atm. This effect is probably due to the position of the ignition isotherm high above the coarse AP particle at high pressures, as explained in the previous section. Another possibility is that more diffusion flame calculations need to be performed, since 40.8 and 81.7 atm are not included in the lookup table. Thus, the model is forced to interpolate, using the results calculated at 34, 68, and 102 atm. If diffusion flame calculations were performed at 40 and 80 atm, the model might agree more with the data.

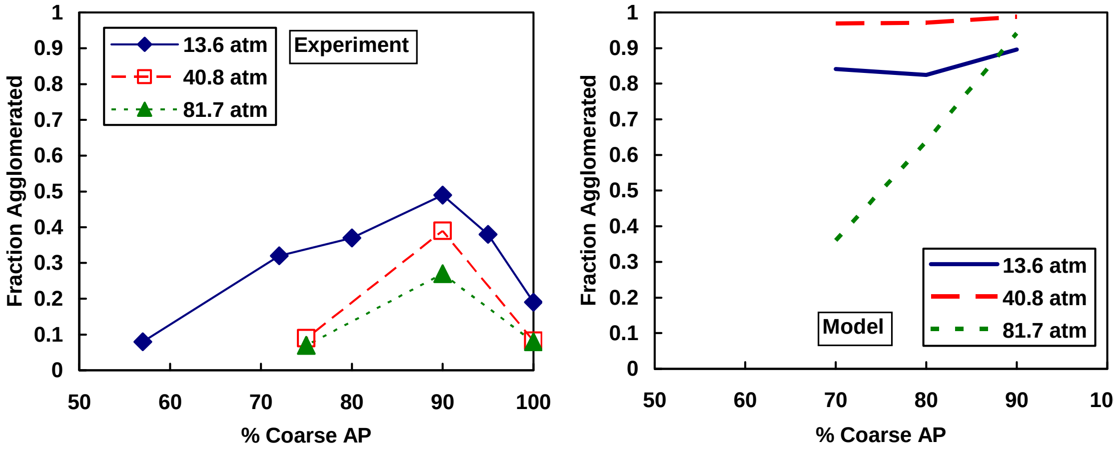

Figure 6-16: Calculated agglomerated fractions compared with the data of Micheli and Schmidt, varying coarse to fine AP ratio and pressure.

Agglomerate diameters and agglomerated fractions were calculated for every formulation and pressure. Fractions have been plotted versus diameter in Figure 6-17, showing calculated fractions increasing with diameter, matching the experimental trend.

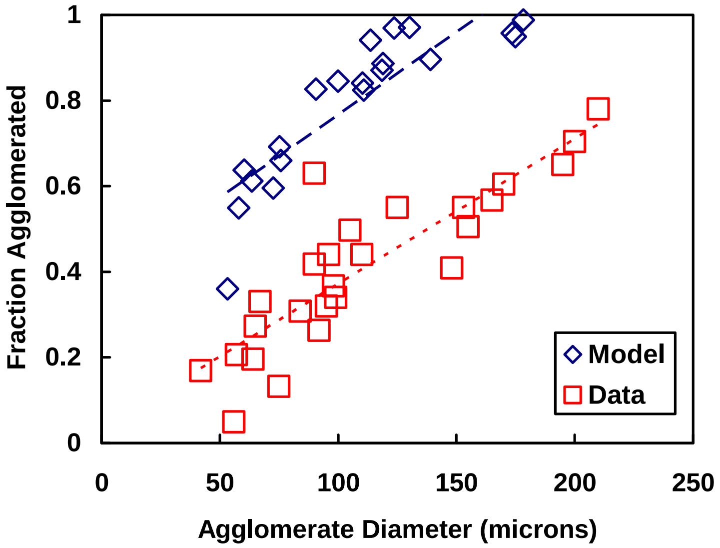

Figure 6-17: Calculated agglomerated fractions versus agglomerate diameters for Micheli and Schmidt propellants.

6.3.3.4 Shuttle

Due to similarities between the shuttle propellant and the propellants studied by Micheli and Schmidt, shuttle propellant agglomeration has also been modeled. The shuttle propellant contains 70% AP, 16% 44-micron aluminum, and 14% PBAN. The AP distribution is bimodal, containing 200- and 20-micron sizes at a 70/30 coarse to fine ratio. To explore the trends discussed in the previous section, the coarse AP size has been varied from 100 to 300 microns, the coarse to fine AP ratio from 70/30 to 90/10, and the pressure from 13.6 to 81.7 atm. The particle-size distribution parameters used in the model are presented in Table 6-7. The agglomeration cutoff diameter D_{cut} was set at 45 microns. Pack heights and diameters ranged from ~750 to ~2250 microns.

Table 6-7: Particle-size distribution parameters used to model the shuttle propellant.

Nominal Size	σ_1	$D_{m,1}$	θ_1	f_1	σ_2	$D_{m,2}$	θ_2	f_2
20-micron AP	1.01	17.6	0	0.985	0.258	3.12	0	0.0146
100-micron AP	0.340	118	0	0.830	0.500	67.7	0	0.170
200-micron AP	0.340	236	0	0.830	0.500	135	0	0.170
300-micron AP	0.340	354	0	0.830	0.500	203	0	0.170
44-micron Al	0.709	40.0	0	0.936	1.28	25.3	0	0.0644

The calculated agglomerated fraction versus coarse to fine AP ratio is plotted for three coarse AP sizes at 13.6 atm (Figure 6-18) and for three pressures for the 200-micron coarse AP size (Figure 6-19), showing results similar to those of the previous section.

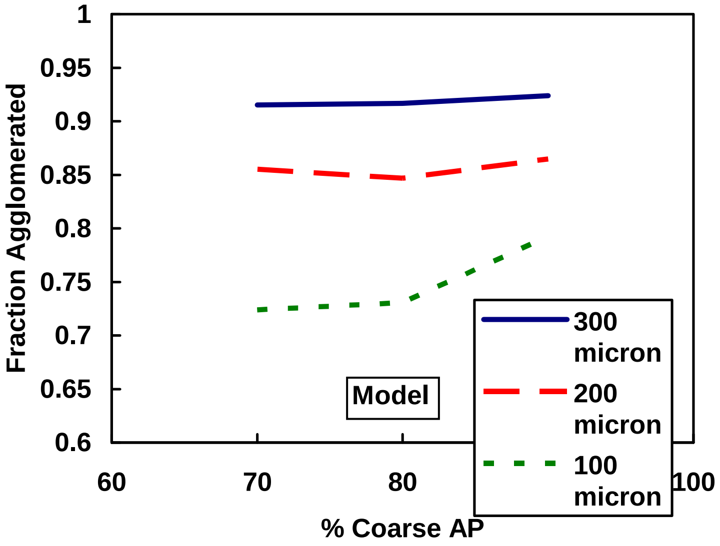

Figure 6-18: Calculated agglomerated fraction for the shuttle propellant, varying coarse to fine AP ratio for 3 coarse AP diameters.

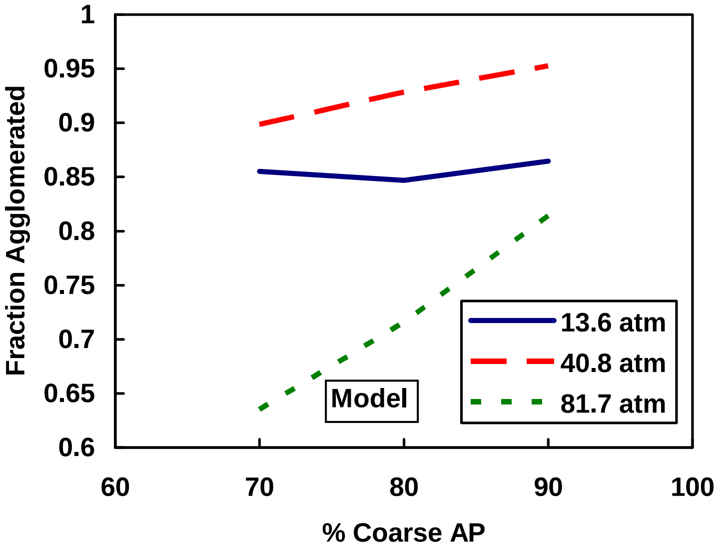

Figure 6-19: Calculated agglomerated fraction for variations of the shuttle propellant, varying coarse to fine AP ratio for 3 pressures.

The calculated agglomerated fraction increases with coarse AP size, with the largest fraction at a coarse to fine ratio of 90/10, which is consistent. This is most apparent for the 100-micron AP at a pressure of 40.8 atm. However, the inconsistencies of the previous section, with pressure and coarse to fine ratio, are also apparent.

To explore the pressure trend more carefully, the agglomerate diameter has been calculated at several pressures for the shuttle propellant (Figure 6-20). The agglomerate size follows the experimentally observed trend for the most part, except at 40.8 atm, where the model predicts a larger agglomerate than at 34 atm. It seems likely that this is due to faulty interpolation in the diffusion flame lookup table, since 40.8 atm was not modeled. To improve the accuracy of the model and avoid extensive interpolation or extrapolation, diffusion flame calculations should be performed at more pressures (and possibly more particle sizes).

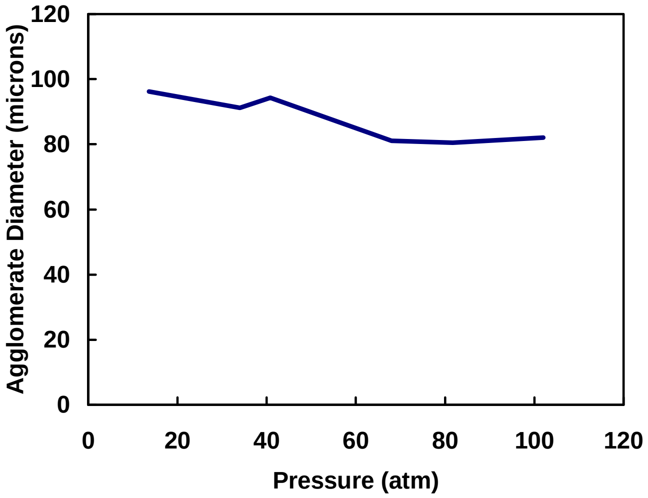

Figure 6-20: Calculated agglomerate size versus pressure for the shuttle propellant.

For all the shuttle propellant calculations, the agglomerated fraction has been plotted versus the agglomerate diameter in Figure 6-21. The calculated trend matches the experimentally observed trend reasonably well.

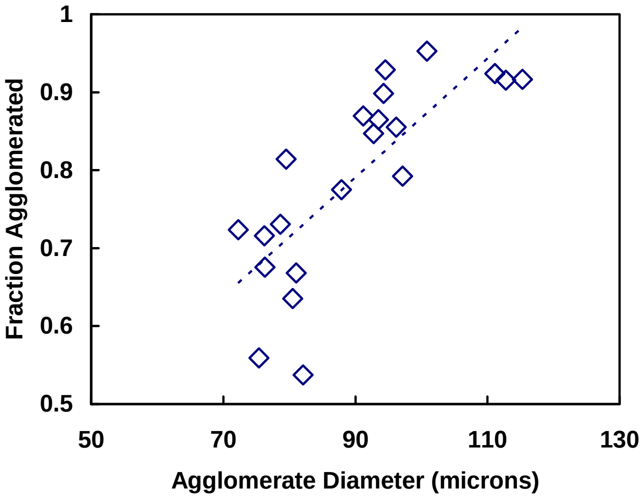

Figure 6-21: Calculated agglomerated fraction versus agglomerate diameter for the shuttle propellant variations.

6.3.4 Summary and Conclusions

A solid propellant aluminum agglomeration model has been developed based on the approaches and results of three preliminary models—a Pocket Model, a Separation Distance Model, and an Ignition Model. A critical separation distance parameter, a surface regression step size parameter, and pressure dependent homogenization of AP particles have been used in the final version of the model. A three-dimensional particle pack is first generated matching the propellant composition as closely as possible. The surface is then regressed numerically, with calculations performed at each surface location on the exposed aluminum particles, based on their proximity to each other and to non-homogenized AP particles. Surface calculations determine if aluminum particles combine, and if the particles or agglomerates ignite and lift off the surface.

Aluminum particle ignition criteria have been developed based on diffusion flame calculations in the gas phase above AP particles and surrounding binder. Binder thickness, one of the inputs to the diffusion flame model, has been calculated as a function of pressure and particle size by analyzing cross-sections of particle packs of the shuttle propellant. Binder composition, another input to the diffusion flame model, has been calculated by assuming the fine AP and aluminum are homogenized with the binder. Parametric diffusion flame calculations have been performed at several pressures and particle sizes and the position of aluminum ignition isotherms in the gas phase have been compiled into a lookup table that is used in the agglomeration model. In general, the position of the isotherm moves closer to the surface as pressure increases. However, for large AP particles, the isotherm moves away from the surface in the region above the particle at high pressures, due to the high mass burning rate of the AP particle.

The propellants studied by Grigoryev et al.,[96] Sambamurthi et al.,[98] and Micheli and Schmidt,[91] as well as the shuttle propellant, have been modeled and results have been compared to their data. Several trends have been captured successfully by the model, but there have been some inconsistencies in the calculation of the effects of pressure and coarse to fine AP ratio. The general results are summarized in Table 6-8.

Table 6-8: Agglomeration model results.

Effect	Coarse AP Diameter	Agglomerated Fraction vs Diameter	Aluminum Concentration	Fine AP Diameter	Coarse to Fine AP ratio	Pressure
Result	Good	Good	Good	Good	Okay	Okay

There are discrepancies between the model calculations and data at low pressure (~1 atm). The inconsistencies are probably due to the position and shape of the ignition isotherm, as predicted by the diffusion flame model. At 1 atm, the isotherm is relatively far from the surface compared to other pressures, resulting in very large calculated agglomerate sizes. However, the data do not show an equivalent increase in agglomerate size at 1 atm. One possible explanation is that aluminum particles have higher surface residence times at low pressure, which leads to the melting of the aluminum core and the subsequent cracking of the oxide shell. The exposure of the aluminum core reduces the ignition temperature, which would result in smaller agglomerates. It may be possible to model this by making the ignition temperature in the model proportional to the pressure.

There are also some inconsistencies at medium to high pressures in the model. At 40.8 atm, some of the calculations show larger agglomerates than at 34 atm, which is inconsistent with the data. There may be two reasons for this effect. First, the calculated isotherm position moves away from propellant surface at high pressure in the region over large AP particles, which can result in larger calculated agglomerates at high pressure. It may be possible to counter this effect by allowing the high mass flux from the AP particle at high pressure to cause unignited aluminum particles to lift off the surface. Second, there may not be a sufficient number of pressures in the diffusion flame lookup table, which forces the model to interpolate between 34 and 68 atm.

The effect of varying the coarse to fine AP ratio is captured in part by the model. Larger agglomerates are predicted at a ratio of 90/10, which is consistent. However, as the ratio decreases, the calculated agglomerate sizes do not decrease as much as the data. This is probably because the model does not account for the effect of an increasing concentration of fine AP in the pseudo-binder. If this effect were modeled, there would likely be smaller agglomerates predicted as the coarse to fine AP ratio decreased, which would be more consistent with the data.

6.3.5 Future Work

Several things have been identified that can be done to further develop the model. These are summarized below.

1. The surface residence time of aluminum particles should be accounted for, possibly by varying the aluminum particle ignition temperature with pressure. This seems to be more important at very low pressures (1 atm).
2. The high mass flux of coarse AP particles at high pressure should be accounted for by allowing unignited aluminum particles to lift off the

surface. A correlation would need to be developed between mass flux and aluminum particle diameter.

3. The pressure dependence of homogenization may need to be varied slightly to better match the pressure trend in the data of Sambamurthi et al. In addition, the effect of homogenization on the pseudo-binder composition should be accounted for in the model. This would ideally be handled in the diffusion flame model. However, that model depends on the premixed AP/HTPB combustion model, which is still quite limited. Hence, this effect may have to be estimated until the premixed model can be further developed.
4. More pressures and particle sizes should be included in the diffusion flame calculations, which provide the ignition criteria for the lookup table in the model. This would eliminate inconsistencies due to interpolation or extrapolation.
5. For scenarios where the propellant is completely homogenized, ignition criteria should be developed using the premixed AP/HTPB model. Inert aluminum should be added at different AP concentrations and the temperature profile should be calculated at several pressures to develop a lookup table for ignition criteria.
6. Cross-sections of each propellant formulation should be analyzed to determine binder thicknesses, which probably vary with formulation. This information could be used to expand the diffusion flame calculations to include more binder thicknesses.

7 Conclusions

A solid propellant burning rate model has been developed to investigate particle-size and pressure effects in RDX/GAP propellants. Work was also performed to develop a detailed gas-phase kinetic model for RDX/GAP, which was used as a submodel in the burning rate model. A solid propellant aluminum agglomeration model has been developed to investigate the effects of particle size and pressure on agglomerate sizes. A detailed gas-phase kinetic model for AP/HTPB has been developed, which was crucial to the development of the agglomeration model. The following sections outline the results obtained for each of these studies and give recommendations for future development of each of the models.

7.1 RDX/GAP Pseudo-Propellant Model

7.1.1 Summary

A one-dimensional premixed combustion model has been developed for RDX/GAP pseudo-propellants. PHASE3, a numerical tool developed by Davidson to model monopropellant combustion, has been used along with a comprehensive gas-phase mechanism developed previously by Puduppakkam. The condensed-phase mechanisms of Davidson’s RDX model and Puduppakkam’s GAP model have been combined to form the RDX/GAP condensed-phase mechanism. Slight modifications have been made to the kinetics in the condensed and gas phases to improve the calculations of monopropellant RDX burning rates and surface species concentrations. Several compositions between 0% RDX/100% GAP and 100% RDX/0% GAP have been modeled. The propellant surface, or the boundary between the condensed and gas phases, is determined by an evaporation model for compositions between 45% and 100% RDX. For compositions containing less than 45% RDX, the surface void fraction is specified.

The burning rate has been determined to be strongly dependent on the formulation, with a minimum burning rate at a formulation of ~60% RDX/40% GAP. Combustion is driven by the gas phase for compositions between 100% and 60% RDX and by the condensed phase for compositions between 60% and 0% RDX. Temperature sensitivity is calculated to increase with GAP content, while the pressure exponent decreases. The heat feedback decreases significantly and the condensed-phase decomposition becomes more exothermic with increasing GAP content. Dark zones have been predicted for laser-assisted combustion of 80% RDX/ 20% GAP at 1 atm. The predicted trends match those that have been observed experimentally, showing that this is a qualitatively valid model.

Calculated RDX/GAP burning rates are predominantly lower than experimental values. The low predictions are possibly due to the breakdown of the premixed flame assumption at high pressures. Another possibility is that there is chemical interaction between RDX and GAP in the condensed phase that has not been included in the model.

7.1.2 Future Work

Further improvement to the model depends largely on the availability and detail of experimental data. Greater understanding of the condensed-phase kinetics is needed, including possible interaction between RDX and GAP. Hence, more experimental studies are needed that measure surface species while varying RDX percentage. Given the availability of such data, further work could be done to improve the condensed-phase mechanism. Further work on the comprehensive gas-phase mechanism may also result in improved agreement with experimental results. Application of the gas-phase kinetics to combustion models of more propellant ingredients would expose weaknesses and provide means for improving the comprehensive mechanism. More experimental studies are needed that measure RDX/GAP burning rates. Such studies should carefully control RDX particle sizes to ensure a premixed flame. This would provide means for further development and validation of the model and kinetic mechanisms. Without further experimental work, improvements to the model will be difficult to achieve.

7.2 AP/HTPB Pseudo-Propellant Model

7.2.1 Summary

A one-dimensional model has been developed for AP/HTPB premixed combustion, based on Jeppson's original AP/HTPB model. Formulations ranging from 59.25% to 79.90% AP have been modeled over a pressure range of 1 to 136 atm (14.7 to 2000 psi). Major modifications have been made in both the gas and condensed-phase kinetic mechanisms. The universal mechanism developed by Gross is used in the gas phase. An HCN-elimination reaction has been added to the universal gas-phase mechanism, which dramatically improves the prediction of flame temperature and final species concentrations for all formulations and pressures considered. This reaction is a temporary fix, which will be removed when more theoretically-based kinetics can be found that result in the same improvement in model calculations. Separate, one-step, condensed-phase mechanisms, based loosely on Korobeinichev's surface species data, have been developed for each AP percentage considered. Solid carbon is predicted by the Edwards Equilibrium Code at formulations below 70% AP. Due to the absence of any reactions in the gas-phase mechanism that would produce carbon, it is included in the condensed-phase model, and exists throughout the gas phase without reacting. Foster's experimental burning rate data have been extrapolated to a wider range of AP percentages by means of a flame temperature correlation proposed by Beckstead, and have been used for model validation.

Combustion characteristics have been calculated varying formulation and pressure. Agreement between calculated burning rates and experimental data is excellent, although data are only available at low pressure for a small range of AP percentages. Agreement between model calculations and equilibrium code calculations of flame temperature and final species concentrations is excellent for all formulations and pressures considered. Calculations show consistent trends in burning rate, gas-phase heat flux, and surface temperature, each of which increases with pressure and AP percentage. Condensed-phase heat release calculations do not vary with pressure, but show an increase in the endothermic nature of the condensed phase as AP percentage decreases.

As part of the agglomeration modeling work, inert aluminum was added to the AP/HTPB model for 59.25% AP. The AP/HTPB ratio was kept approximately the same as the space shuttle propellant, resulting in an aluminum percentage of 31.26%. The presence of inert aluminum resulted in lower burning rates, gas-phase heat fluxes, and surface temperatures over the entire range of pressures. These results have been used to develop correlations that serve as condensed-phase boundary conditions in the diffusion flame model, which is discussed in Chapter 6 on agglomeration.

7.2.2 Future Work

Deficiencies in the universal gas-phase mechanism indicate a need for further research and development of the mechanism. The research of Lin,[148] who has performed extensive *ab initio* calculations of kinetic pathways relative to propellant combustion, has been valuable in the development of the expanded gas-phase mechanism. Clearly, more calculations of this type are needed to improve the capabilities of the mechanism. As more accurate kinetic parameters become available from Lin and others who perform similar work, the HCN elimination reaction can be removed and replaced with more theoretically based reactions and kinetics. Gas-phase kinetics are also needed that describe the formation of solid carbon. If solid carbon, C(S), could be removed from the condensed phase, then more reasonable trends could be established in the condensed-phase mechanism below 70% AP. There also appears to be a need for more reactions in the gas-phase mechanism that describe the initial decomposition of AP and HTPB. This is evident due to the high number of final products that have been included in the condensed-phase mechanism, such as H_2, H_2O, CO, and CO_2, which realistically should be produced in the gas phase.

There is still a great deal of uncertainty in the condensed-phase model. The mechanism is based loosely on the surface species measurements of Korobeinichev, but there are obvious problems with his data, which were taken at very low pressure and very high initial temperature. If more experimental studies were to be performed measuring surface species of AP/HTPB premixed combustion over a wide range of formulations and pressures, the data would provide an extremely valuable resource for further development of the model. More burning rate data are needed as well, over a wider range of formulations, expanding on Foster's work. In such a study, more care should be taken to ensure the validity of a premixed flame assumption, using the smallest possible AP particle size so that valid premixed data could be obtained at even higher pressures.

7.3 Propellant Burning Rate Model

7.3.1 Summary

A heterogeneous propellant combustion model has been developed. This model combines the geometric modeling capability of PARPACK with the combustion modeling capability of PHASE3 to predict burning rates for solid propellants. The approach of the model is to determine a characteristic burning path through each particle pack and to calculate the burning rate of that path. Two different path-finding approaches have been used, one that utilizes a path that travels through the binder, and another that utilizes oxidizer particles. Both a path of least time and an average path have been determined for each formulation and pressure, and for each of the two path-finding approaches. Efforts to validate the model have been made by comparing results with Flanagan's data for RDX/GAP propellants. These comparisons show that the model has promise, but needs to be developed further. Different approaches appear to work better depending on formulation and pressure. The path-finding algorithms are currently very simple and more research is needed to determine a more appropriate path-finding algorithm, or to develop a different approach.

7.3.2 Future Work

There are several aspects of the model that require research and development. The RDX/GAP pseudo-propellant combustion model works well for monopropellant RDX and GAP, but may be inaccurate for RDX/GAP mixtures. Unfortunately, there are no experimental species data specifically for premixed RDX/GAP combustion, so experiments are needed that would ensure premixed combustion. The path-finding algorithm is very simplified and needs further development. It may be found that the path of least time approach is not effective and a completely new approach may need to be developed. Modeling of diffusion flames in RDX/GAP propellants may be another possible approach. Felt's diffusion flame model, although developed for AP/HTPB combustion, has the capability to model any propellant ingredient. If his model could be adapted for RDX/GAP combustion, it could be used to calculate the effects of particle-size and pressure on the gas-phase flame, and thereby, on the burning rate. It would also be helpful to this modeling work if more experimental data could be obtained for a greater number of RDX particle sizes, rather than just 12.5 and 200 microns.

7.4 Aluminum Agglomeration Model

7.4.1 Summary

A solid propellant aluminum agglomeration model has been developed based on the approaches and results of three preliminary models—a Pocket Model, a Separation Distance Model, and an Ignition Model. A critical separation distance parameter, a surface regression step size parameter, and pressure dependent homogenization of AP particles have been used in the final version of the model. A three-dimensional particle pack is first generated matching the propellant composition as closely as possible. The surface is then regressed numerically, with calculations performed at each surface location on the exposed aluminum particles, based on their proximity to each other and to non-homogenized AP particles. The model then determines if they will combine with each other to form an agglomerate, and if the particles or agglomerates will ignite and lift off the surface.

Aluminum particle ignition criteria have been developed based on diffusion flame calculations in the gas phase above AP particles and surrounding binder. Binder thickness, one of the inputs to the diffusion flame model, has been calculated as a function of pressure and particle size by analyzing cross-sections of particle packs of the shuttle propellant. Binder composition, another input to the diffusion flame model, has been calculated by assuming the fine AP and aluminum are homogenized with the binder. Parametric diffusion flame calculations have been performed at several pressures and particle sizes and the position of aluminum ignition isotherms in the gas phase have been compiled into a lookup table that is used in the agglomeration model. In general, the position of the isotherm moves closer to the surface as pressure increases. However, for large AP particles, the isotherm moves away from the surface in the region above the particle at high pressures, due to the high mass burning rate of the AP particle at the high pressures.

The propellants studied by Grigoryev et al.,[96] Sambamurthi et al.,[98] and Micheli and Schmidt,[91] as well as the shuttle propellant, have been modeled and results have been compared to their data. Several trends have been captured successfully by the model, including the effects of varying the coarse AP diameter, the fine AP diameter, and the aluminum concentration. However, there have been some inconsistencies in the calculation of the effects of pressure and coarse to fine AP ratio.

There are discrepancies between the model calculations and data at low pressure (~1 atm). The inconsistencies are probably due to the position and shape of the ignition isotherm, as predicted by the diffusion flame model. At 1 atm, the isotherm is relatively far from the surface compared to other pressures, resulting in very large calculated agglomerate sizes. However, the data do not show an equivalent increase in agglomerate size at 1 atm. One possible explanation is that aluminum particles have higher surface residence times at low pressure, which leads to the melting of the aluminum core and the subsequent cracking of the oxide shell. The exposure of the aluminum core reduces the ignition temperature, which would result in smaller agglomerates. It may be possible to model this by making the ignition temperature in the model proportional to the pressure.

There are also some inconsistencies at medium to high pressures in the model. At 40.8 atm, some of the calculations show larger agglomerates than at 34 atm, which is inconsistent with the data. There may be two reasons for this effect. First, the calculated isotherm position moves away from propellant surface at high pressure in the region over large AP particles, which can result in larger calculated agglomerates at high pressure. It may be possible to counter this effect by allowing the high mass flux from the AP particle at high pressure to cause unignited aluminum particles to lift off the surface. Second, there may not be a sufficient number of pressures in the diffusion flame lookup table, which forces the model to interpolate between 34 and 68 atm.

The effect of varying the coarse to fine AP ratio is captured in part by the model. Larger agglomerates are predicted at a ratio of 90/10, which is consistent. However, as the ratio decreases, the calculated agglomerate sizes do not decrease as much as the data. This is probably because the model does not account for the effect of an increasing concentration of fine AP in the pseudo-binder. If this effect were modeled, there would likely be smaller agglomerates predicted as the coarse to fine AP ratio decreased, which would be more consistent with the data.

7.4.2 Future Work

Several things have been identified that can be done to further develop the model. These are summarized below.

1. The surface residence time of aluminum particles should be accounted for, possibly by varying the aluminum particle ignition temperature with pressure. This seems to be more important at very low pressures (1 atm).
2. The high mass flux of coarse AP particles at high pressure should be accounted for by allowing unignited aluminum particles to lift off the surface. A correlation would need to be developed between mass flux and aluminum particle diameter.

3. The pressure dependence of homogenization may need to be varied slightly to better match the pressure trend in the data of Sambamurthi et al. In addition, the effect of homogenization on the pseudo-binder composition should be accounted for in the model. This would ideally be handled in the diffusion flame model. However, that model depends on the premixed AP/HTPB combustion model, which is still quite limited. Hence, this effect may have to be estimated until the premixed model can be further developed.
4. More pressures and particle sizes should be included in the diffusion flame calculations, which provide the ignition criteria for the lookup table in the model. This would eliminate inconsistencies due to interpolation or extrapolation.
5. For scenarios where the propellant is completely homogenized, ignition criteria should be developed using the premixed AP/HTPB model. Inert aluminum should be added at different AP concentrations and the temperature profile should be calculated at several pressures to develop a lookup table for ignition criteria.
6. Cross-sections of each propellant formulation should be analyzed to determine binder thicknesses, which probably vary with formulation. This information could be used to expand the diffusion flame calculations to include more binder thicknesses.

8 References

1. Data provided by R. Bennett from ATK Thiokol, Brigham City, Utah, 2004.

2. Beckstead, M.W., Derr, R.L. and Price, C.F. "A Model of Composite Solid-Propellant Combustion Based on Multiple Flames," *AIAA Journal*, Vol. 8, No. 12, Dec. 1970, pp. 2200-2207.

3. Beckstead, M. W., "Combustion Calculations for Composite Solid Propellants*," 13th JANNAF Combustion Meeting*, Vol. II, CPIA No. 281, 1976, pp. 299-312.

4. Beckstead, M. W., "A Model for Solid Propellant Combustion", *18th Symposium (International) on Combustion*, 1981, pp. 175-185.

5. Felt, S. A. and Beckstead, M. W., "A Model of the AP/HTPB Diffusion Flame", *40th JANNAF Combustion Meeting*, 2005.

6. Felt, S. A., "Two-Dimensional Modeling of AP Composite Propellant Flame Structure with Detailed Kinetics", Ph.D. Dissertation, *Brigham Young University*, Provo, UT, 2004.

7. Gross, M. L., Felt, S. A. and Beckstead, M. W., "Two-dimensional Modeling of AP Composite Propellants with Detailed Kinetics: Particle Size Effects", *AIAA 2006-4925*.

8. Buckmaster, J., Jackson, T. L. and Yao, J., "An Elementary Discussion of Propellant Flame Geometry," *Combustion and Flame*, Vol. 117, 1999, pp. 541-552.

9. Kochevets, S., Buckmaster, J. and Jackson, T. L., "Random Propellant Packs and the Flames they Support," *36th AIAA/ASME/SAE/ASEE Joint Propulsion Conference*, 2000, AIAA 2000-3461.

10. Hegab, A., Jackson, T. L., Buckmaster, J. and Stewart, D. S., "The Burning of Periodic Sandwich Propellants," *36th AIAA/ASME/SAE/ASEE Joint Propulsion Conference*, 2000, AIAA 2000-3459.

11. Jackson, T. L., Buckmaster, J., Campbell, M., Kochevets, S. and Massa, L., "The Burning of 3D Random-pack Heterogeneous Propellants," *37th AIAA/ASME/SAE/ASEE Joint Propulsion Conference*, 2001, AIAA 2001-3952.

12. Massa, L., Jackson, T. L. and Short, M., "Numerical Solution of Three-dimensional Heterogeneous Solid Propellants," *Combustion Theory and Modeling*, Vol. 7, 2003, pp. 579-602.

13. Wang, X., Jackson, T. L. and Massa, L., "Numerical Simulation of Heterogeneous Propellant Combustion by a Level Set Method," *Combustion Theory and Modeling*, Vol. 8, 2004, pp. 227-254.

14. Davis, I. L. and Carter, R. G., "Random Particle Packing by Reduced Dimension Algorithms," *Journal of Applied Physics*, Vol. 67, No. 2, 1990, pp. 1022-1029.

15. Davidson, J. E. and Beckstead, M. W., "Improvements to Steady-State Combustion Modeling of Cyclotrimethylenetrinitramine", *J. of Propulsion and Power*, Vol. 13, No. 3, 1997, pp. 375-383.

16. Davidson, J. E. and Beckstead, M. W., "A Mechanism and Model for GAP Combustion", *33rd JANNAF Combustion Meeting*, CPIA #653, Vol. II, 1996, pp. 91-100.

17. Puduppakkam, K. V. and Beckstead, M. W., "Combustion Modeling of Glycidyl Azide Polymer with Detailed Kinetics", *Combustion Sci. & Tech*, Vol. 177, 2005, pp. 1661-1697.

18. Puduppakkam, K. V. and Beckstead, M. W., "RDX/GAP Pseudo-Propellant Combustion Modeling", *38th JANNAF Combustion Meeting*, CPIA #712, Vol. I, 2002, pp. 143-156.

19. Beckstead, M. W. and Puduppakkam, K. V., "Combustion Modeling of Nitrate Esters with Detailed Kinetics", *40th JANNAF Combustion Meeting*, 2005.

20. Jeppson, M. B., Beckstead, M. W. and Jing, Q., "A Kinetic Model for the Premixed Combustion of a Fine AP/HTPB Composite Propellant", *AIAA 36th Aerospace Sciences Meeting*, AIAA 98-0447, 1998.

21. McGeary, R. K., "Mechanical Packing of Spherical Particles," *Journal of the American Ceramic Society*, Vol. 44, No. 10, 1961, pp. 513-522.

22. Knott, G. M., Jackson, T. L. and Buckmaster, J., "Random Packing of Heterogeneous Propellants," *AIAA Journal*, Vol. 39, No. 4, Apr. 2001, pp. 678-686.

23. Atwood, A. I., Boggs, T. L., Curran, P. O., Parr, T. P., Hanson-Parr, D. M., Price, C. F., and Wiknich, J., "Burning Rate of Solid Propellant Ingredients, Part 1: Pressure and Initial Temperature Effects," *J. of Propulsion and Power*, 1999, Vol. 15, No. 6, pp 740-747.

24. Flanagan, J., Woolery, D., Kistner, R., "Fundamental Studies of Azide Decomposition and Combustion Mechanisms", *Rockwell Report*, AFAL-TR-87-107, Canoga Park, CA, Jan. 1988.

25. Zenin, A. A., Puchkov, V. M. and Finjakov, S. V, "Characteristics of HMX Combustion Waves at Various Pressures and Initial Temperatures", *Combustion, Explosion, and Shock Waves*, Vol. 34, No. 2, 1998, pp. 170-176.

26. Boggs, T. L., Price, C. F., Zurn, D. E., Derr, R. L. and Dibble, E. J., "The Self-Deflagration of Cyclotetramethylenetetranitramine (HMX)", *13th AIAA Propulsion Conference*, AIAA-1977-859, 1977.

27. Kubota, N. and Aoki, I., "Burning Rate Characterization of GAP/HMX Energetic Composite Materials", *Propellants, Explosives, Pyrotechnics*, Vol. 25, 2000, pp. 168-171.

28. Liau, Y.-C. and Yang, V., "Analysis of RDX Monopropellant Combustion with Two-Phase Subsurface Reactions", *Journal of Propulsion and Power*, Vol. 11, No. 4, 1995, pp. 729-739.

29. Prasad, K., Yetter, R. A. and Smooke, M. D., "An Eigenvalue Method for Computing the Burning Rates of RDX Propellants", *Combustion, Science & Technology*, Vol. 124, 1997, pp. 35-82.

30. Kee, R. J., Rupley, F. M. and Miller, J. A., "A Fortran Program for Modeling Steady, Laminar, One-Dimensional, Premixed Flames", *Sandia Report*, SAND85-8240, Livermore, CA, Aug. 1989.

31. Zimmer-Galler, R., "Correlations Between Deflagration Characteristics and Surface Properties of Nitramine-Based Propellants," *AIAA J.*, Vol. 6, No. 11, 1968, pp. 2107-2110.

32. Glaskova, A. P., Rozantsev, E. G., Boblev, V. K. and Skripko, L. A., "Effect of the Chemical Structure of the Inhibitor on the Combustion of RDX," *Combustion, Explosion & Shock Waves*, No. 4, 1970, pp. 584-585.

33. Zenin, A., "HMX and RDX: Combustion Mechanism and Influence on Modern Double Base Propellant Combustion," *Journal of Propulsion and Power*, Vol. 11. No. 4, 1995, pp. 752-758.

34. Homan, B. E., Miller, M. S. and Vanderhoff, J. A., "Absorption Diagnostics and Modeling Investigations of RDX Flame Structure," *Comb. and Flame*, 2000, Vol. 120, pp. 301-317.

35. Miller, M. S. and Anderson, W. R., "Energetic-Material Combustion Modeling with Elementary Gas-Phase Reactions: a Practical Approach", Chapter 2.12, *Solid Propellant Chemistry, Combustion, and Motor Interior Ballistics*, Vol. 185, 2000, pp. 501-531.

36. Davidson, J. E. and Beckstead, M. W., "A Three-Phase Model of HMX Combustion", *26th Symposium (International) on Combustion*, The Combustion Institute, 1996, pp. 1989-1996.

37. Jing, Q., Beckstead, M. W. and Jeppson, M. B., "Influence of AP Solid Phase Decomposition on Temperature Profile and Sensitivity", *AIAA 36th Aerospace Sciences Meeting*, AIAA 98-0448, 1998.

38. Beckstead, M. W. and Puduppakkam, K. V., "Combustion Modeling of Butanetriol Trinitrate with Detailed Kinetics", *40th JANNAF Combustion Meeting*, 2005.

39. Kim, E. S., Yang, V. and Liau, Y.-C., "Modeling of HMX/GAP Pseudo-Propellant Combustion", *Combustion and Flame*, Vol. 131, 2002, pp. 227-245.

40. Kim, E. S., "Modeling and Simulation of Laser-Induced Ignition of RDX Monopropellant and Steady-State Combustion of HMX/GAP Pseudo Propellant," Ph.D. Thesis, The Pennsylvania State University, University Park, PA, 2000.

41. Liau, Y.C., Yang, V., Lin, M.C., and Park, J., "Analysis of Ammonium Dinitramide (ADN) Combustion with Detailed Chemistry," *35th JANNAF Combustion Meeting*, CPIA No. 685, 1998, pp.13-30.

42. Prasad, K., Yetter, R. A. and Smooke, M. D., "An Eigenvalue Method for Computing the Burning Rates of HMX Propellants", *Combustion & Flame*, Vol. 115, 1998, pp. 406-416.

43. Beckstead, M. W., Puduppakkam, K. V., and Yang, V., "Modeling and Simulation of Combustion of Solid Propellant Ingredients Using Detailed Chemical Kinetics", AIAA-2004-4036, *40th AIAA/ASME/SAE/ASEE Joint Propulsion Conference*, July 11-14, 2004.

44. Puduppakkam, K. V. and Beckstead, M. W., "Combustion Modeling of RDX/GAP/BTTN Pseudo-Propellant", *39th JANNAF Combustion Meeting*, 2003.

45. Liau, Y.-C., Yang, V. and Thynell, S. T., “Modeling of RDX/GAP Propellant Combustion with Detailed Chemical Kinetics”, *Solid Propellant Chemistry, Combustion, and Motor Interior Ballistics*, AIAA Progress in Astronautics and Aeronautics, Chapter 2.11, 2000, pp. 477-500.

46. Beckstead, M. W., “Overview of Combustion Mechanisms and Flame Structures with Implications for Advanced Solid Propellants”, *J. of Propulsion and Power*, Vol. 16, No. 1, 2000, pp. 1-8.

47. Cohen, N. S., “Combustion of Nitramine Propellants,” Publ. 261, Vol. 1, Chemical Propulsion Information Agency, Laurel, MD, 1974, pp. 267-284.

48. Miller, R. R., “Effects of Particle Size on Reduced Smoke Propellant Ballistics”, AIAA Paper 82-1096, *AIAA/SAE/ASME 18th Joint Propulsion Conference*, June 21-23, 1982.

49. Beckstead, M.W., "Solid Propellant Combustion Mechanisms and Flame Structure", *Pure & Appl. Chem*, 1993, Vol. 65, No. 2, pp.297-307.

50. Miller, R. R., “A Framework for a Totally Statistical Composite Propellant Combustion Model”, *19th JANNAF Combustion Meeting*, Vol II, CPIA #366, Oct. 1982, pp. 81-92.

51. Miller, R. R. and Freeman, J. M., “A Semi-Empirical Model for Plateau Propellant Burn Rates: Effects of AP Size Distribution”, *36th JANNAF Combustion Meeting*, CPIA #691, Vol. III, 1999, pp. 355-370.

52. Freeman, J. M., Tzeng, D. D. and Miller, R. R., “A Semi-Empirical Model for Propellant Burn Rates”, *37th AIAA/ASME/SAE/ASEE Joint Propulsion Conference*, AIAA 2001-3939.

53. Jackson, T. L. and Buckmaster, J., “Heterogeneous Propellant Combustion”, AIAA Journal, Vol. 40, No. 6, June 2002, pp. 1122-1130.

54. Renie J. P. and Osborn, J. R., "An Implicit Flame Interaction Combustion Model", *15th JANNAF Combustion Meeting*, 1979, Vol. II, CPIA #297.

55. Glick R. L. and Condon, J. A., "Statistical Combustion Modeling - The Effect of Additives", *14th JANNAF Combustion Meeting*, 1977, CPIA #292, pp. 341-378.

56. Renie J. P., Condon, J. A. and Osborn J. R., "Oxidizer Size Distribution Effects on Propellant Combustion", *AIAA Journal*, 1979, Vol. 17, No. 8, pp. 877-883.

57. Cohen, N. S., Price C. F. and Strand L. D., "Analytical Model of the Combustion of Multicomponent Solid Propellants", *AIAA-77-927*, 1977.

58. Tang, C. –J., Lee, Y. and Litzinger, T. A., "The Chemical and Thermal Processes of GAP/Nitramine Pseudo-Propellants under CO2 Laser Heating", *34th JANNAF Combustion Meeting*, CPIA #662, Vol. II, 1997.

59. Paletsky, A. A., Korobeinichev, O. P., Tereshchenko, A. G., Volkov, E. N. and Polyakov, P. D., "Flame Structure of HMX/GAP Propellant at High Pressure", *Proceedings of the Combustion Institute*, 30, 2005, pp. 2105-2112.

60. Kubota, N., Sonobe, T., Yamamoto, A. and Shimizu, H., "Burning Rate Characteristics of GAP Propellants", *Journal of Propulsion*, Vol. 6, No. 6, 1989, pp. 686-689.

61. Kubota, N. and Sonobe, T., "Burning Rate Catalysis of Azide/Nitramine Propellants", 23rd Symposium (International) on Combustion, The Combustion Institute, 1990, pp. 1331-1337.

62. Oyumi, Y., Inokami, K., Yamazaki, K. and Matsumoto, K., "Burning Rate Augmentation of BAMO Based Propellants", *Propellants, Explosives, Pyrotechnics*, Vol. 19, 1994, pp. 180-186.

63. Kimura, E. and Oyumi, Y., "Effects of Copolymerization Ratio of BAMO/NMMO and Catalyst Sensitivity and Burning Rate of HMX Propellant", *Propellants, Explosives, Pyrotechnics*, Vol. 20, 1995, pp. 215-221.

64. Egorshev, V. Y., Sinditskii, V. P., Levshenkov, A. I. and Berezin, M. V., "Physical and Chemical Processes Governing the Combustion of Binary Compositions of Ammonium Dinitramide with Glycidylazidepolymer", *ISICP Conference*, Santiago, Chile, 2005.

65. Fong, C. W. and Smith, R. F., "The Effect of Binder, Particle Size and Catalyst on the Burning Rates of PETN and RDX Composite Propellants", *Combust. Sci. and Tech.*, 1988, Vol. 57, pp. 1-15.

66. Beckstead, M.W. "An Overview of Combustion Mechanisms and Flame Structures for Advanced Solid Propellants," 36th *AIAA Joint Propulsion Conference*, Huntsville, AL, AIAA-2000-3325, 2000.

67. Kishore, K., "Comprehensive View of the Combustion Models of Composite Solid Propellants," *AIAA Journal*, Vol. 17, No. 11, 1979, pp. 1216-1224.

68. Cohen, N.S. “Review of Composite Propellant Burn Rate Modeling,” *AIAA Journal*, Vol. 18, No. 3, 1980, pp. 277-293.

69. Cohen, N.S. and Flanagan, D.A. “Mechanisms and Models of Solid-Propellant Burn Rate Temperature Sensitivity: A Review,” *AIAA Journal*, Vol. 23, No. 10, 1985, pp. 1538-1547.

70. Strunin, V.A. and Manelis, G.B. “Analysis of Elementary Models for the Steady-State Combustion of Solid Propellants,” *Journal of Propulsion and Power*, Vol. 11, No. 4, 1995, pp. 666-676.

71. Cohen, N. S. and Strand, L. D., “An Improved Model for the Combustion of AP Composite Propellants”, *AIAA Journal*, Vol. 20, No. 12, Dec. 1982, pp. 1739-1746.

72. Duterque, J. and Lengelle, G., “Combustion Mechanisms of Nitramine Based Propellants with Additives”, *24th AIAA/ASME/SAE/ASEE Joint Propulsion Conference*, AIAA-88-3253.

73. Ermolin, N.E., “Kinetic Parameters of Overall Gas-Phase Reactions for Propellants Based on Ammonium Perchlorate and Polybutadiene Binder,” *Combustion, Explosion, and Shock Waves*, Vol. 29, No. 4, 1993, pp. 97-104.

74. Gusachenko, L. K, “Version of a Combustion Relay Model for a Mixture of Components Which Do Not Burn Spontaneously”, *Combustion, Explosion, and Shock Waves*, 1994, Vol. 30, No. 3, pp. 33-35.

75. Jeppson, M.B., “A Kinetics model for the Premixed Combustion of a Fine AP/HTPB Composite Propellant,” M.S. Thesis, Department of Chemical Engineering, Brigham Young University, Provo, UT, 1998.

76. Strahle, W. C., “Some Statistical Considerations in the Burning of Composite Solid Propellants”, *AIAA Journal*, 1978, Vol. 16, No. 8, pp. 843-847.

77. Kerstein, A. R., “Percolation Model of Polydisperse Composite Solid Propellant Combustion”, *Combustion and Flame*, Vol. 69, 1987, pp. 95-112.

78. Kovalev, O. B., “Approximate Structural Calculation of Combustion Wave for Composite Condensed Systems”, *Flame Structure*, 1991, Vol. 1, Nauka, Novosibirsk, pp. 254-257.

79. Rashkovskii, S. A., “Statistical Model for Combustion of a Condensed Heterogeneous Mixture”, *Combustion, Explosion & Shock Waves*, 1992, Vol. 28, No. 6, pp. 17-24.

80. Bilger, R. W., Jia, X., Li, J. D. and Nguyen, T. T., "Theoretical and Experimental Study of Composite Propellant Combustion", *Combust. Sci. Tech.*, 1996, Vol. 115, pp. 1-39.

81. Marvasti, M. A. and Strahle, W. C., "Burning Rate Prediction of Composite Solid Propellants Using Fractal Geometry", *Combust. Sci. and Tech.*, 1992, Vol. 83, pp. 291-304.

82. Groult, S. and Bizot, A., "Numerical Simulation of Heterogeneous AP/HTPB Propellant Combustion", *40th AIAA/ASME/SAE/ASEE Joint Propulsion Conference*, AIAA 2004-4039.

83. Massa L., Jackson, T. L., Buckmaster, J. and Campbell, M., "Three-Dimensional Heterogeneous Propellant Combustion", *Proc. Comb. Inst.*, 29, 2975-83.

84. Zarko, V. E. and Gusachenko, L. K., "Simulation of Energetic Materials Combustion," *Report*, Russion Academy of Sciences, Novosibirsk Inst of Chemical Kinetics and Combustion, 2000.

85. Cohen, N., "Overview of Aluminum Behavior in Solid Propellant Combustion as a Foundation for Stability Calculations", *MURI Program Report*, Feb. 1999.

86. Price, E. W. and Sigman, R. K., "Combustion of Aluminized Solid Propellants", *36th JANNAF Combustion Meeting*, CPIA #691, Vol. I, 1999, pp. 227-248.

87. Beckstead, M. W., "An Overview of Aluminum Agglomeration Effects", *JANNAF Journal of Propulsion and Energetics*, Vol. 1, No. 1, 2008.

88. Fry, R. S. and Ruttenberg, E. C., "Aluminum and Aluminum Oxide Particulate Behavior in Solid Rocket Motors", *32nd JANNAF Combustion Meeting*, CPIA # 631, 1995.

89. Glotov, O. G., Zarko, V. E., Karasev, V. V. and Beckstead, M. W., "Condensed Combustion Products of Metalized Propellants of Variable Formulation", *AIAA-98-0449*, 1998.

90. Pokhil, P.F., Belyayev, A.F., Frolov, Y.V., Logachev, V.S., and Korotkov, A.I., "Combustion of Powdered Metals in Active Media," Nauka, FTDMT-24-551-73 (English translation) (1972).

91. Micheli, P.L. and Schmidt W.G., "Behavior of Aluminum in Solid Rocket Motors," *AFRPL-TR-77-29*, 1, Aerojet Solid Propulsion Co. (1977).

92. Schmidt, W.G. and Poynter, R.C., "Zirconium/Aluminum Combustion," *Aerojet Report*, AFRPL-TR-80-8, Aerojet Solid Propulsion Co. (1980).

93. Liu, T.K., Perng, H.C., Luh, S.P., and Liu, F., "Aluminum Agglomeration in AP/RDX/Al/HTPB Propellant Combustion," *J. Propulsion & Power*, 8, (6), 1177-1184 (1992).

94. Babuk, V.A., Vasilyev and Malakhov, M.S., "Condensed Combustion Products at the Burning Surface of Aluminized Solid Propellant," *J. Propulsion & Power*, 15, (6), 783-793 (1999).

95. Churchill, H., Fleming, R.W., and Cohen, N.S., "Aluminum Behavior in Solid Propellant Combustion," *Lockheed Report*, AFRPL-TR-74-13, Lockheed Propulsion Company (1974).

96. Grigoryev, V. G., Zarko, V. E. and Kutsenogii, K. P., "Experimental Investigation of the Agglomeration of the Aluminum Particles of Burning Condensed Systems", *Combustion, Explosion & Shock Waves*, 1981, Vol. 17, No. 3, pp. 3-10.

97. Duterque, J., "Experimental Studies of Aluminum Agglomeration in Solid Rocket Motors", *4th International Symposium on Special Topics in Chemical Propulsion*, 1996, Vol. 12, No. 5.

98. Sambamurthi, J. K., Price, E. W. and Sigman, R. K., "Aluminum Agglomeration in Solid Propellant Combustion", *AIAA Journal*, 1984, Vol. 22, No. 8., pp. 1132-1138.

99. Beckstead, M. W., "A Model for Solid Propellant Combustion", *14th JANNAF Combustion Meeting*, CPIA # 292, Vol. I, Dec. 1977, pp. 281-306.

100. Cohen, N. S. and Strand, L. D., "A Model for the Burning Rates of Composite Propellants", *17th JANNAF Combustion Meeting*, CPIA #329, Vol. I, Nov. 1980, pp. 53-97.

101. Cohen, N. S., "A Pocket Model for Aluminum Agglomeration in Composite Propellants", *AIAA Journal*, 1983, Vol. 21, No. 5, pp. 720-725.

102. Grigoryev, V.G., Kutsenogii, K.P., and Zarko, V.A., "Model of Aluminum Agglomeration During Combustion of Composite Propellants," *Combustion, Explosion & Shock Waves*, 17, (4), pp. 9-17 (1981).

103. Leiji, J. and Shuffen Lo, "A Sponge Model for Aluminum Agglomeration in Composite Propellant", *39th Congress of the International Astronautical Federation, Bangalore, India*, 1988.

104. Kovalev, O. B., Petrov, A. P. and Fol'ts, A. V., "Simulating Aluminum Powder Aggregation in Mixed Condensed-System Combustion", *Combustion, Explosion & Shock Waves*, 1987, Vol. 23, No.2, pp. 17-20.

105. Luh, S. P., Liu, T. K. and Perng, H. C., "Pocket Model Application to the Combustion of AP/RDX/Al/HTPB Propellants", *AIAA 95-3110*, 31st Joint Populsion Conf., 1995.

106. Hermsen, R. W., "Aluminum Combustion Efficiency in Solid Rocket Motors", *AIAA 81-0038*, 1981.

107. Liu, T., Perng, H., Luh, S. and Liu, F., "Aluminum Agglomeration in an AP/RDX/Al/HTPB Propellant Combustion", *AIAA 91-1870*, 1991.

108. Salita, M., "Survey of Recent Al2O3 Droplet Size Data in Solid Rocket Chambers, Nozzles and Plumes", *31st JANNAF Combustion Meeting*, CPIA # 620, Vol. I, 1994, pp. 1-18.

109. Trubert, J. F., "Agglomeration and Combustion of Aluminum Particles in Solid Rocket Motors", *Proceedings of the Space Solid Propulsion Workshop*, Rome, Italy, 21-24 November 2000, Paper 44.

110. Jackson, T.L., Najjar, F. and Buckmaster, J., "An Aluminum Injection Model Based on Random Packs for Solid Propellant Rocket Motor Simulations", *40th AIAA/ASME/SAE/ASEE Joint Propulsion Conference*, 2004, AIAA Paper 2004-4042.

111. Srinivas, V., and Chakravarthy, S. R., "Computer Model of Aluminum Agglomeration on Burning Surface of Composite Solid Propellant," *Journal of Propulsion and Power*, Vol. 23, No. 4, 2007, pp. 728-736.

112. Frankel, M. B., Grant, L. R., and Flanagan, J. E., "Historical Development of Glycidyl Azide Polymer", *Journal of Propulsion and Power*, Vol. 8, No.3, 1992, pp. 560-563.

113. Zenin, A. A. and Finjakov, S. V., "Physics of GAP combustion", *38th Aerospace Sciences Meeting*, AIAA 2000-1032, 2000.

114. Kubota, N. and Sonobe, T., "Combustion of GAP Propellants", *Combustion and Detonation Phenomena, 19th International Annual Conference of ICT*, Germany, 1988, pp.2-1 to 2-12.

115. Flanagan, J., Woolery, D. and Kistner, R., "Fundamental Studies of Azide Decomposition and Combustion", *AFRPL-TR-86-094*, Dec.1986.

116. Tang, C. -J., Lee, Y., and Litzinger, T. A., “Simultaneous Temperature and Species Measurements of the Glycidyl Azide Polymer (GAP) Propellant During Laser-Induced Decomposition”, *Combustion and Flame*, Vol. 117, 1999, pp. 244-256.

117. Arisawa, H., and Brill, T. B., “Thermal Decomposition of Energetic Materials 71: Structure-Decomposition and Kinetic Relationships in Flash of Glycidyl Azide Polymer (GAP)”, *Combustion and Flame*, Vol. 112, 1998, pp. 533-544.

118. Korobeinichev, O. P., Kuibida, L. V., Shmakov, A. G. and Paletsky, A. A., “GAP Decomposition and Combustion Chemistry Studied by Molecular Beam Mass-Spectrometry”, *37th AIAA Aerospace Sciences Meeting*, AIAA-99-0596, 1999.

119. Miyazaki, T. and Kubota, N., “Energetics of BAMO”, *Propellants, Explosives, Pyrotechnics*, Vol. 17, 1992, pp. 5-9.

120. Flanagan, J. E., Woolery, D. O. and Kistner, R. L., "Combustion Characteristics of GAP/RDX Gumstocks", *24th JANNAF Combustion Meeting*, CPIA # 476, Vol. 3, 1987, pp. 29-38.

121. Litzinger, T. A., Lee, Y. and Tang, C. -J., "An Experimental Study of Nitramine/Azide Propellant Combustion", *Solid Propellant Chemistry, Combustion, and Motor Interior Ballistics*, AIAA Progress in Astronautics and Aeronautics, Chapter 2.4, 2000, pp. 355-379.

122. Brill, T. B. and Roos, B. D., "Chemistry of GAP/RDX Propellant Upon Flash Pyrolysis", *37th JANNAF Combustion Meeting*, CPIA # 701, Vol. 1, 2000, pp. 373-382.

123. Lee, Y. J., Kudva, G., Tang, C.J. and Litzinger, T. A., "Thermal Decomposition of BAMO and RDX/BAMO Pseudo-Propellants", *33rd JANNAF Combustion Meeting*, CPIA # 653, Vol. 2. 1996, pp. 79-90.

124. Prasad, K., Yetter, R. and Smooke, M., "An Eigenvalue Method for Computing the Burning Rates of RDX Propellants", *32nd JANNAF Combustion Meeting*, CPIA# 638, Vol. 1, 1995, pp. 69-84.

125. Puduppakkam, K. V. and Beckstead, M. W., "Glycidyl Azide Polymer Combustion Modeling", *37th AIAA/ASME/SAE/ASEE Joint Propulsion Conference*, AIAA2001-3429, 2001.

126. Kim, E. S. and Yang, V., "Steady State Combustion of HMX/GAP Pseudo-Propellant", *37th JANNAF Combustion Meeting*, CPIA # 701, Vol. 1, 2000, pp. 403-425.

127. Puduppakkam, K. V., Tanner, M. W. and Beckstead, M. W., “RDX/GAP Pseudo-Propellant Combustion Modeling,” *42nd AIAA/ASME/SAE/ASEE Joint Propulsion Conference*, 2006, AIAA 2006-4926.

128. Parr, T. and Hanson-Parr, D., "RDX/GAP/BTTN Propellant Flame Studies", *Combustion and Flame*, Vol. 127, 2001, pp. 1895-1905.

129. Maksimov, Y. Y., “Boiling Point and Enthalpy of Evaporation of Liquid Hexogen and Octogen”, *Russian Journal of Physical Chemistry*, Vol. 66, 1992, pp. 280-281.

130. Brill, T. B., “Multiphase Chemistry Considerations at the Surface of Burning Nitramine Monopropellants”, *Journal of Propulsion and Power*, Vol. 11, No. 4, 1995, pp. 740-751.

131. Thynell, S., Gongwer, P. E. and Brill, T. B., “Modeling of Thermal Response of Filament Used in T-Jump Experiment”, *31st JANNAF Combustion Meeting*, Vol. 2, Chemical Propulsion Information Agency, 1994, pp. 221-232.

132. Yetter, R. A., Dryer, F. L., Allen, M. T. and Gatto, J. L., “Development of Gas-Phase Reaction Mechanism for Nitramine Combustion”, *Journal of Propulsion and Power*, Vol. 11, No. 4, 1995, pp. 683-697.

133. Frenklach, M., Bowman, T., Smith, G. and Gardiner, B., “GRI-MECH 3.0”, Downloaded from http://euler.me.berkeley.edu/gri_mech/

134. Park, J., Chakraborty, D. and Lin, M. C., “Thermal Decomposition of Gaseous Ammonium Dinitramide at Low Pressure: Kinetic Modeling of Product Formation with Ab Initio MO/cVRRKM Calculations”, *27th International Symposium on Combustion*, Vol. 2, 1998, pp. 2351-2357.

135. Xu, Z. F. and Lin, M. C., “A Computational Study of the Kinetics and Mechanism for the Reaction of HCO with HNO”, *International Journal of Chemical Kinetics*, Vol. 36, 2004, pp. 205-215.

136. Xu, Z. F. and Lin, M. C., “Computational Study on the Kinetics and Mechanisms for the Reactions of HCO with HONO and HNOH”, *International Journal of Chemical Kinetics*, Vol. 36, 2004, pp. 178-187.

137. Xu, Z. F., Hsu, C.-H. and Lin, M. C. "Ab initio kinetics of the reaction of HCO with NO: Abstraction vs association/elimination mechanism", *Journal of Chemical Physics*, accepted.

138. Chakraborty, D. and Lin, M. C., “Gas Phase Chemical Kinetics of [C,H,N,O]-Systems Relevant to the Combustion of Nitramines in Their Early Stages”, *J. Propulsion and Power*, 23 Dec 1998.

139. Melius, C. F., “Thermochemical Modeling: II. Application to Ignition and Combustion of Energetic Materials”, *Chemistry and Physics of Energetic Materials*, Kluwer, Dordrecht, The Netherlands, 1990, pp. 51-78.

140. Parr, T. P. and Hanson-Parr, D. M., “Thermal Properties Measurements of Solid Rocket Propellant Oxidizers and Binder Materials as a Function of Temperature”, *34th JANNAF Combustion Meeting*, CPIA #662, Vol. 2, 1997, pp. 379-404.

141. Davidson, J. E., "Combustion Modeling of RDX, HMX and GAP with Detailed Kinetics", *Ph. D. Dissertation*, Brigham Young University, 1996, pp. 63-71.

142. Kubota, N., "Survey of Rocket Propellants and Their Combustion Characteristics", Fundamentals of Solid-Propellant Combustion, *Progress in Astronautics and Aeronautics*, Vol. 90, 1984, pp. 20-26.

143. Foster, R.L., Condon, J.A., and Miller, R.R., “Low Exponent Technology,” *Hercules Report*, AFRPL-TR-81-95, Hercules Inc., Air Force Rocket Propulsion Laboratory, Edwards AFB, CA, 1982.

144. Korobeinichev, O.P., Ermolin, N.E., Chernov, A.A., and Emel’yanov, I.D., “Flame Structure, Kinetics and Mechanism of Chemical Reactions in Flames of Mixed Composition Based on Ammonium Perchlorate and Polybutadiene Rubber,” *Combustion, Explosion, and Shock Waves*, Vol. 28, No. 4, 1992, pp. 53-59.

145. Korobeinichev, O.P., Chernov, A.A., Emel’yanov, I.D., Ermolin, N.E., and Trofimycheva, T.V. “Investigation of the Kinetics and the Chemical Reaction Mechanism in the Flame of a Mixed Compound, Based on Ammonium Perchlorate and Polybutadiene Rubber,” *Combustion, Explosion, and Shock Waves*, Vol. 26, 1990, pp.292-300.

146. Gross, M. L., Shurtz, R. C., Hawkins, M. G., Beckstead, M. W. and Hecker, W. C., “Development of an Updated Model for Monopropellant AP Combustion: Methodology and Results,” *41st JANNAF Combustion Meeting*, December, 2006.

147. Gross, M. L., “Two-Dimensional Modeling of AP/HTPB Utilizing a Vorticity Formulation and One-Dimensional Modeling of AP and ADN,” *Ph. D. Dissertation*, Brigham Young University, 2007.

148. Lin, M. C., “M. C. Lin’s Chemical Kinetics Research Group,” Oct. 2002. [http://mc2.chem.emory.edu/]

149. Ermolin, N.E., Korobeinichev, O.P., Tereshchenko, A.G., and Fomin, V.M., "Kinetic Calculations and Mechanism Definitions for Reactions in an Ammonium Perchlorate Flame," *Combustion, Explosion, and Shock Waves*, Vol. 18, 1982, pp. 180-188.

150. Ermolin, N.E., "Model for Chemical Reaction Kinetics in Perchloric Acid – Ammonia Flames," *Combustion, Explosion, and Shock Waves*, Vol. 31, No. 5, 1995, pp. 555-565.

151. International Union of Pure and Applied Chemistry, "IUPAC Subcommittee for Gas Kinetic Data Evaluation," June 2006. [http://www.iupac-kinetic.ch.cam.ac.uk/]

152. National Institute of Standards and Technology, Standard Reference Database 17, Version 7.0, Release 1.4, 2000. [http://kinetics.nist.gov/]

153. Korobeinichev, O.P., Bolshova, T.A. and Paletsky, A.A., "Modeling the Chemical Reaction of Ammonium Dinitramide (ADN) in a Flame," *Combustion and Flame*, Vol. 126, 2001, pp. 1516-1523.

154. Personal communication with Mike Hawkins, an undergraduate student working as a research assistant at Brigham Young University in the Chemical Engineering Department, 2007.

155. Personal communication with Professor Merrill Beckstead, Brigham Young University, Chemical Engineering, 2008.

156. JANAF Thermochemical Tables, 3rd Edition, *Journal of Physical and Chemical Reference Data*, Vol. 14, 1985.

157. Tanner, M. W., Beckstead, M. W., Gross, M. L. and Davis, I. L., "Heterogeneous Propellant Combustion Modeling Using a Particle Packing Model," *40th JANNAF Combustion Meeting*, 2005.

158. Nickerson, G. R., Culick, F. E. C. and Dang, A. L., "The Solid Propellant Rocket Motor Performance Computer Program (SPP) Version 6.0", *Air Force Astronautics Laboratory*, User's Manual, Vol. VI, Dec. 1987.

159. Personal communication with Lee Davis and Michael Webb at ATK, Brigham City, Utah, 2006.

160. Miller, R. R., Donohue, M. T., Yount, R. A. and Martin, J. R., "Control of Solids Distribution in HTPB Propellants", *Hercules Report*, AFRPL-TR-78-14, Cumberland, MD, Apr. 1978.

161. Shannon, L. J. and Peterson, E. E., *AIAA J.*, Vol. 2, No. 1, Jan. 1964, pp. 168-169.

162. Tanner, M. W., Beckstead, M. W., Davis, I. L. and Webb, M., "Numerical Modeling of Aluminum Agglomeration in Solid Propellants Using a Three-Dimensional Particle-Packing Model," *41st JANNAF Combustion Meeting*, 2006.

Appendix A. Comprehensive Gas-Phase Mechanism

The following is the comprehensive gas-phase mechanism used in the RDX/GAP combustion model, including Pudupppakkam's comprehensive mechanism with modifications to the H_2CNNO_2 decomposition reactions, as outlined in Chapter 3.

```
CHEMKIN INTERPRETER OUTPUT: CHEMKIN-II Version 3.1 Feb. 1993
                             DOUBLE PRECISION

                         --------------------
                         ELEMENTS     ATOMIC
                         CONSIDERED   WEIGHT
                         --------------------
                          1. AR      39.9480
                          2. C       12.0112
                          3. H       1.00797
                          4. N       14.0067
                          5. O       15.9994
                         --------------------
--------------------------------------------------------------------------------
                        C
                      P H
                      H A
                      A R
SPECIES               S G MOLECULAR TEMPERATURE   ELEMENT COUNT
CONSIDERED            E E WEIGHT      LOW  HIGH   AR C  H  N  O
--------------------------------------------------------------------------------
  1. AR               G 0  39.94800  300.0 5000.0  1  0  0  0  0
  2. H2               G 0   2.01594  300.0 5000.0  0  0  2  0  0
  3. O2               G 0  31.99880  300.0 5000.0  0  0  0  0  2
  4. H2O              G 0  18.01534  300.0 5000.0  0  0  2  0  1
  5. O                G 0  15.99940  300.0 5000.0  0  0  0  0  1
  6. HNOH             G 0  32.02204  300.0 4000.0  0  0  2  1  1
  7. H                G 0   1.00797  300.0 5000.0  0  0  1  0  0
  8. OH               G 0  17.00737  300.0 5000.0  0  0  1  0  1
  9. HO2              G 0  33.00677  200.0 3500.0  0  0  1  0  2
 10. H2O2             G 0  34.01474  300.0 5000.0  0  0  2  0  2
 11. CH2O             G 0  30.02649  300.0 5000.0  0  1  2  0  1
 12. HCO              G 0  29.01852  300.0 5000.0  0  1  1  0  1
 13. CO               G 0  28.01055  300.0 5000.0  0  1  0  0  1
 14. CO2              G 0  44.00995  300.0 5000.0  0  1  0  0  2
 15. N                G 0  14.00670  200.0 6000.0  0  0  0  1  0
 16. N2               G 0  28.01340  300.0 5000.0  0  0  0  2  0
 17. NO               G 0  30.00610  200.0 6000.0  0  0  0  1  1
 18. NO2              G 0  46.00550  200.0 6000.0  0  0  0  1  2
 19. NH               G 0  15.01467  200.0 6000.0  0  0  1  1  0
 20. NH2              G 0  16.02264  200.0 6000.0  0  0  2  1  0
 21. NH3              G 0  17.03061  200.0 6000.0  0  0  3  1  0
 22. NNH              G 0  29.02137  200.0 6000.0  0  0  1  2  0
 23. HNO              G 0  31.01407  200.0 6000.0  0  0  1  1  1
```

```
 24. HONO             G 0  47.01347  300.0 5000.0  0  0  1  1  2
 25. HCN              G 0  27.02582  200.0 6000.0  0  1  1  1  0
 26. N2O              G 0  44.01280  200.0 6000.0  0  0  0  2  1
 27. CN               G 0  26.01785  200.0 6000.0  0  1  0  1  0
 28. C2N2             G 0  52.03570  300.0 5000.0  0  2  0  2  0
 29. NCN              G 0  40.02455  300.0 4000.0  0  1  0  2  0
 30. NCO              G 0  42.01725  200.0 6000.0  0  1  0  1  1
 31. CNO              G 0  42.01725  300.0 4000.0  0  1  0  1  1
 32. HNCO             G 0  43.02522  300.0 5000.0  0  1  1  1  1
 33. HOCN             G 0  43.02522  300.0 5000.0  0  1  1  1  1
 34. HCNO             G 0  43.02522  300.0 5000.0  0  1  1  1  1
 35. NO3              G 0  62.00490  300.0 5000.0  0  0  0  1  3
 36. HNO3             G 0  63.01287  300.0 5000.0  0  0  1  1  3
 37. H2CN             G 0  28.03379  300.0 4000.0  0  1  2  1  0
 38. H2CNH            G 0  29.04176  300.0 4000.0  0  1  3  1  0
 39. H2CNO            G 0  44.03319  300.0 4000.0  0  1  2  1  1
 40. H2CNNO           G 0  58.03989  300.0 4000.0  0  1  2  2  1
 41. H2CNNO2          G 0  74.03929  300.0 4000.0  0  1  2  2  2
 42. RDX              G 0 222.11787  300.0 4000.0  0  3  6  6  6
 43. RDXR             G 0 176.11237  300.0 4000.0  0  3  6  5  4
 44. RDXRO            G 0 176.11237  300.0 4000.0  0  3  6  5  4
 45. HNC              G 0  27.02582  300.0 5000.0  0  1  1  1  0
 46. H2COHNNO2        G 0  91.04666  300.0 4000.0  0  1  3  2  3
 47. C                G 0  12.01115  300.0 5000.0  0  1  0  0  0
 48. CH               G 0  13.01912  300.0 5000.0  0  1  1  0  0
 49. CH2              G 0  14.02709  250.0 4000.0  0  1  2  0  0
 50. CH2(S)           G 0  14.02709  300.0 4000.0  0  1  2  0  0
 51. CH3              G 0  15.03506  300.0 5000.0  0  1  3  0  0
 52. CH4              G 0  16.04303  300.0 5000.0  0  1  4  0  0
 53. CH2OH            G 0  31.03446  250.0 4000.0  0  1  3  0  1
 54. CH3O             G 0  31.03446  300.0 3000.0  0  1  3  0  1
 55. CH3OH            G 0  32.04243  300.0 5000.0  0  1  4  0  1
 56. C2H3             G 0  27.04621  300.0 5000.0  0  2  3  0  0
 57. C2H2             G 0  26.03824  300.0 5000.0  0  2  2  0  0
 58. C2H              G 0  25.03027  300.0 5000.0  0  2  1  0  0
 59. C2H4             G 0  28.05418  300.0 5000.0  0  2  4  0  0
 60. C2H5             G 0  29.06215  300.0 5000.0  0  2  5  0  0
 61. C2H6             G 0  30.07012  300.0 4000.0  0  2  6  0  0
 62. HCCO             G 0  41.02967  300.0 4000.0  0  2  1  0  1
 63. CH2CO            G 0  42.03764  300.0 5000.0  0  2  2  0  1
 64. HCCOH            G 0  42.03764  300.0 4000.0  0  2  2  0  1
 65. HCNN             G 0  41.03252  300.0 5000.0  0  1  1  2  0
 66. C3H7             G 0  43.08924  300.0 5000.0  0  3  7  0  0
 67. C3H8             G 0  44.09721  300.0 5000.0  0  3  8  0  0
 68. CH2CHO           G 0  43.04561  300.0 5000.0  0  2  3  0  1
 69. CH3CHO           G 0  44.05358  200.0 6000.0  0  2  4  0  1
 70. C(S)             S 0  12.01115  300.0 5000.0  0  1  0  0  0
 71. N2H2             G 0  30.02934  300.0 5000.0  0  0  2  2  0
 72. N2H3             G 0  31.03731  300.0 5000.0  0  0  3  2  0
 73. N2H4             G 0  32.04528  300.0 5000.0  0  0  4  2  0
 74. BTTN             G 0 241.11509  200.0 6000.0  0  4  7  3  9
 75. HOCO             G 0  45.01792  300.0 4000.0  0  1  1  0  2
 76. HNNO             G 0  45.02077  300.0 4000.0  0  0  1  2  1
 77. ADN(G)           G 0 124.05628  300.0 5000.0  0  0  4  4  4
 78. HN3O4            G 0 107.02567  300.0 5000.0  0  0  1  3  4
 79. HNNO2            G 0  61.02017  300.0 5000.0  0  0  1  2  2
 80. H2NNO            G 0  46.02874  300.0 4000.0  0  0  2  2  1
 81. H2NO             G 0  32.02204  300.0 4000.0  0  0  2  1  1
 82. HNNH             G 0  30.02934  300.0 6000.0  0  0  2  2  0
 83. H2NOH            G 0  33.03001  300.0 4000.0  0  0  3  1  1
-------------------------------------------------------------------------------


                                                     (k = A T**b exp(-E/RT))
     REACTIONS CONSIDERED                              A        b        E

  1. H2+M=H+H+M                                     4.57E+19   -1.40   104000.0
        H2               Enhanced by    2.500E+00
        H2O              Enhanced by    1.200E+01
        CO               Enhanced by    1.900E+00
```

```
       CO2              Enhanced by    3.800E+00
 2. O+H2O=OH+OH                                    2.97E+06    2.02    13400.0
 3. O+H2=H+OH                                      5.06E+04    2.67     6290.0
 4. O+O+M=O2+M                                     6.17E+15   -0.50        0.0
       H2               Enhanced by    2.500E+00
       H2O              Enhanced by    1.200E+01
       CO               Enhanced by    1.900E+00
       CO2              Enhanced by    3.800E+00
 5. H+O2=O+OH                                      1.94E+14    0.00    16440.0
 6. H+O2(+M)=HO2(+M)                               4.52E+13    0.00        0.0
    Low pressure limit:  0.67000E+20 -0.14200E+01  0.00000E+00
    TROE centering:      0.10000E+01  0.10000E-89  0.10000E+91
       H2               Enhanced by    2.500E+00
       H2O              Enhanced by    1.200E+01
       CO               Enhanced by    1.900E+00
       CO2              Enhanced by    3.800E+00
 7. H+O+M=OH+M                                     4.72E+18   -1.00        0.0
       H2               Enhanced by    2.500E+00
       H2O              Enhanced by    1.200E+01
       CO               Enhanced by    1.900E+00
       CO2              Enhanced by    3.800E+00
 8. OH+H2=H2O+H                                    2.16E+08    1.51     3430.0
 9. OH+H+M=H2O+M                                   2.21E+22   -2.00        0.0
       H2               Enhanced by    2.500E+00
       H2O              Enhanced by    1.200E+01
       CO               Enhanced by    1.900E+00
       CO2              Enhanced by    3.800E+00
10. HO2+O=O2+OH                                    1.75E+13    0.00     -397.0
11. HO2+H=H2+O2                                    6.62E+13    0.00     2130.0
12. HO2+H=OH+OH                                    1.69E+14    0.00      874.0
13. HO2+OH=H2O+O2                                  1.90E+16   -1.00        0.0
14. HO2+HO2=H2O2+O2                                4.20E+14    0.00    11980.0
    Declared duplicate reaction...
15. HO2+HO2=H2O2+O2                                1.30E+11    0.00    -1629.0
    Declared duplicate reaction...
16. H2O2(+M)=OH+OH(+M)                             2.95E+14    0.00    48460.0
    Low pressure limit:  0.12000E+18  0.00000E+00  0.45500E+05
    TROE centering:      0.50000E+00  0.10000E-89  0.10000E+91
17. H2O2+O=OH+HO2                                  9.64E+06    2.00     3970.0
18. H2O2+H=H2O+OH                                  1.00E+13    0.00     3590.0
19. H2O2+H=HO2+H2                                  4.82E+13    0.00     7950.0
20. H2O2+OH=H2O+HO2                                1.00E+12    0.00        0.0
    Declared duplicate reaction...
21. H2O2+OH=H2O+HO2                                5.80E+14    0.00     9557.0
    Declared duplicate reaction...
22. CH2O+O2=HCO+HO2                                2.05E+13    0.00    38920.0
23. CH2O+O=HCO+OH                                  1.81E+13    0.00     3078.0
24. CH2O+H=HCO+H2                                  1.26E+08    1.62     2163.0
25. CH2O+OH=HCO+H2O                                3.43E+09    1.18     -447.0
26. CH2O+HO2=HCO+H2O2                              1.99E+12    0.00    11660.0
27. HCO+M=H+CO+M                                   1.85E+17   -1.00    17000.0
       H2               Enhanced by    1.890E+00
       H2O              Enhanced by    1.200E+01
       CO               Enhanced by    1.900E+00
       CO2              Enhanced by    3.800E+00
28. HCO+O2=CO+HO2                                  7.58E+12    0.00      406.0
29. HCO+O=CO+OH                                    3.00E+13    0.00        0.0
30. HCO+O=CO2+H                                    3.00E+13    0.00        0.0
31. HCO+H=CO+H2                                    7.23E+13    0.00        0.0
32. HCO+OH=CO+H2O                                  3.00E+13    0.00        0.0
33. HCO+HO2=CO2+OH+H                               3.00E+13    0.00        0.0
34. CO+O(+M)=CO2(+M)                               1.80E+10    0.00     2380.0
    Low pressure limit:  0.13500E+25 -0.27880E+01  0.41910E+04
    TROE centering:      0.10000E+01  0.10000E-89  0.10000E+91
       N2               Enhanced by    1.330E+00
       H2               Enhanced by    2.500E+00
       H2O              Enhanced by    1.200E+01
       CO               Enhanced by    1.900E+00
       CO2              Enhanced by    3.800E+00
35. CO+O2=CO2+O                                    2.53E+12    0.00    47700.0
36. CO+OH=CO2+H                                    1.50E+07    1.30     -765.0
```

```
37. CO+HO2=CO2+OH                                  5.80E+13    0.00    22930.0
38. N+H2=H+NH                                      1.60E+14    0.00    25140.0
39. N+O2=NO+O                                      6.40E+09    1.00     6280.0
40. N+OH=NO+H                                      3.80E+13    0.00        0.0
41. N+HO2=NH+O2                                    1.00E+13    0.00     2000.0
42. N+HO2=NO+OH                                    1.00E+13    0.00     2000.0
43. N+NO=N2+O                                      3.27E+12    0.30        0.0
44. N+NO2=NO+NO                                    4.00E+12    0.00        0.0
45. N+NO2=N2O+O                                    5.00E+12    0.00        0.0
46. N+NO2=N2+O2                                    1.00E+12    0.00        0.0
47. N+HNO=NH+NO                                    1.00E+13    0.00     2000.0
48. N+HNO=N2O+H                                    5.00E+10    0.50     3000.0
49. N+N2O=N2+NO                                    1.00E+13    0.00    19870.0
50. NO+M=N+O+M                                     9.64E+14    0.00   148400.0
       N2              Enhanced by    1.500E+00
       CO2             Enhanced by    2.500E+00
51. NO+O(+M)=NO2(+M)                               1.30E+15   -0.75        0.0
    Low pressure limit:  0.47200E+25 -0.28700E+01  0.15510E+04
    TROE centering:      0.95700E+00  0.10000E-89  0.83320E+04
52. NO+H(+M)=HNO(+M)                               1.52E+15   -0.41        0.0
    Low pressure limit:  0.89600E+20 -0.13200E+01  0.73520E+03
    TROE centering:      0.82000E+00  0.10000E-89  0.10000E+91
53. NO+OH(+M)=HONO(+M)                             1.99E+12   -0.05     -721.0
    Low pressure limit:  0.50800E+24 -0.25100E+01 -0.67560E+02
    TROE centering:      0.62000E+00  0.10000E-89  0.10000E+91
       H2O             Enhanced by    5.000E+00
54. HO2+NO=NO2+OH                                  2.11E+12    0.00     -479.0
55. NO+HCO=HNO+CO                                  7.23E+12    0.00        0.0
56. NO2+O=O2+NO                                    3.91E+12    0.00     -238.0
57. NO2+O(+M)=NO3(+M)                              1.33E+13    0.00        0.0
    Low pressure limit:  0.14900E+29 -0.40800E+01  0.24670E+04
    TROE centering:      0.82600E+00  0.10000E-89  0.31910E+04
58. NO2+H=NO+OH                                    1.32E+14    0.00      361.6
59. NO2+OH(+M)=HNO3(+M)                            2.41E+13    0.00        0.0
    Low pressure limit:  0.64200E+33 -0.54900E+01  0.23500E+04
    TROE centering:      0.83700E+00  0.10000E-89  0.16570E+04
60. NO2+HCO=CO+HONO                                1.24E+23   -3.29     2354.0
61. NO2+HCO=H+CO2+NO                               8.39E+15   -0.75     1927.0
62. NO2+CO=CO2+NO                                  9.03E+13    0.00    33780.0
63. NO2+NO2=NO3+NO                                 9.64E+09    0.73    20920.0
64. NO2+NO2=2NO+O2                                 1.63E+12    0.00    26120.0
65. NH+M=N+H+M                                     2.65E+14    0.00    75510.0
66. NH+O2=HNO+O                                    3.89E+13    0.00    17890.0
67. NH+O2=NO+OH                                    7.60E+10    0.00     1530.0
68. NH+O=NO+H                                      5.50E+13    0.00        0.0
69. NH+O=N+OH                                      3.72E+13    0.00        0.0
70. NH+OH=HNO+H                                    2.00E+13    0.00        0.0
71. NH+OH=N+H2O                                    5.00E+11    0.50     2000.0
72. NH+N=N2+H                                      3.00E+13    0.00        0.0
73. NH+NO=N2O+H                                    2.94E+14   -0.40        0.0
    Declared duplicate reaction...
74. NH+NO=N2O+H                                   -2.16E+13   -0.23        0.0
    Declared duplicate reaction...
75. NH+NO=N2+OH                                    2.16E+13   -0.23        0.0
76. NH+NO2=NO+HNO                                  1.00E+11    0.50     4000.0
77. NH+NO2=N2O+OH                                  1.00E+13    0.00        0.0
78. NH+NH=N2+H+H                                   5.10E+13    0.00        0.0
79. NH2+O2=HNO+OH                                  1.78E+12    0.00    14900.0
80. NH2+O=HNO+H                                    6.63E+14   -0.50        0.0
81. NH2+O=NH+OH                                    6.75E+12    0.00        0.0
82. NH2+H=NH+H2                                    6.92E+13    0.00     3650.0
83. NH2+OH=NH+H2O                                  4.00E+06    2.00     1000.0
84. NH2+N=N2+2H                                    7.20E+13    0.00        0.0
85. NH2+NO=NNH+OH                                  2.80E+13   -0.55        0.0
86. NH2+NO=N2+H2O                                  1.30E+16   -1.25        0.0
    Declared duplicate reaction...
87. NH2+NO=N2+H2O                                 -2.80E+13   -0.55        0.0
    Declared duplicate reaction...
88. NH2+NO=N2O+H2                                  5.00E+13    0.00    24640.0
89. NH2+NO=HNO+NH                                  1.00E+13    0.00    40000.0
90. NH2+NO2=N2O+H2O                                3.28E+18   -2.20        0.0
```

```
 91. NH3+M=NH2+H+M                                 2.20E+16    0.00    93470.0
 92. NH3+O=NH2+OH                                  9.40E+06    1.94     6460.0
 93. NH3+H=NH2+H2                                  6.40E+05    2.39    10170.0
 94. NH3+OH=NH2+H2O                                2.04E+06    2.04      566.0
 95. NH3+HO2=NH2+H2O2                              3.00E+11    0.00    22000.0
 96. NH2+HO2=NH3+O2                                1.00E+13    0.00        0.0
 97. NH2+NH2=NH3+NH                                5.00E+13    0.00    10000.0
 98. NNH+M=N2+H+M                                  1.00E+14    0.00     3000.0
 99. NNH+O=N2O+H                                   1.00E+14    0.00        0.0
100. NNH+H=N2+H2                                   1.00E+14    0.00        0.0
101. NNH+OH=N2+H2O                                 5.00E+13    0.00        0.0
102. NNH+NO=N2+HNO                                 5.00E+13    0.00        0.0
103. NNH+NH=N2+NH2                                 5.00E+13    0.00        0.0
104. NNH+NH2=N2+NH3                                5.00E+13    0.00        0.0
105. HNO+O2=NO+HO2                                 1.00E+13    0.00    25000.0
106. HNO+O=OH+NO                                   1.81E+13    0.00        0.0
107. HNO+H=H2+NO                                   1.81E+13    0.00      993.5
108. HNO+OH=H2O+NO                                 1.00E+13    0.00      993.5
109. HNO+NO=N2O+OH                                 2.00E+12    0.00    26000.0
110. HNO+NO2=HONO+NO                               6.02E+11    0.00     1987.0
111. HNO+NH2=NO+NH3                                2.00E+13    0.00     1000.0
112. HNO+HNO=H2O+N2O                               8.51E+08    0.00     3080.0
113. HONO+O=OH+NO2                                 1.20E+13    0.00     5961.0
114. HONO+H=H2+NO2                                 1.20E+13    0.00     7352.0
115. HONO+OH=H2O+NO2                               1.26E+10    1.00      135.1
116. HCN(+M)=H+CN(+M)                              8.30E+17   -0.93   123800.0
     Low pressure limit:  0.35700E+27 -0.26000E+01  0.12490E+06
     TROE centering:      0.95700E+00  0.10000E-89  0.83320E+04
117. HCN+O=CN+OH                                   2.70E+09    1.58    29200.0
118. HCN+O=NH+CO                                   3.45E+03    2.64     4980.0
119. HCN+O=NCO+H                                   1.38E+04    2.64     4980.0
120. HCN+OH=H2O+CN                                 3.90E+06    1.83    10290.0
121. HCN+OH=H+HOCN                                 5.85E+04    2.40    12500.0
122. HCN+OH=H+HNCO                                 1.98E-03    4.00     1000.0
123. HCN+OH=NH2+CO                                 7.83E-04    4.00     4000.0
124. HCN=HNC                                       2.06E+14   -1.11    43710.0
125. HNC+O=NH+CO                                   2.89E+12    0.00        0.0
126. HNC+O=H+NCO                                   1.60E+01    3.08     -224.0
127. HNC+OH=HNCO+H                                 2.80E+13    0.00     3700.0
128. HNC+OH=CN+H2O                                 1.50E+12    0.00     7680.0
129. HNC+NO2=HNCO+NO                               1.00E+12    0.00    32000.0
130. HNC+CN=C2N2+H                                 1.00E+13    0.00        0.0
131. N2O(+M)=N2+O(+M)                              7.91E+10    0.00    56020.0
     Low pressure limit:  0.91300E+15  0.00000E+00  0.57690E+05
        H2O              Enhanced by    7.500E+00
        NO               Enhanced by    2.000E+00
        CO               Enhanced by    2.000E+00
        CO2              Enhanced by    3.000E+00
        HCN              Enhanced by    3.000E+00
132. N2O+O=O2+N2                                   1.00E+14    0.00    28000.0
133. N2O+O=2NO                                     1.00E+14    0.00    28000.0
134. N2O+H=N2+OH                                   2.53E+10    0.00     4550.0
     Declared duplicate reaction...
135. N2O+H=N2+OH                                   2.23E+14    0.00    16750.0
     Declared duplicate reaction...
136. N2O+OH=HO2+N2                                 2.00E+12    0.00    40000.0
137. N2O+CO=N2+CO2                                 5.01E+13    0.00    44000.0
138. CN+H2=H+HCN                                   5.50E+02    3.18     -223.0
139. CN+O2=NCO+O                                   7.50E+12    0.00     -389.0
140. CN+O=CO+N                                     1.80E+13    0.00        0.0
141. CN+OH=NCO+H                                   4.22E+13    0.00        0.0
142. CN+CH2O=HCN+HCO                               4.22E+13    0.00        0.0
143. CN+HCO=HCN+CO                                 6.02E+13    0.00        0.0
144. CN+CO2=CO+NCO                                 3.67E+06    2.16    26900.0
145. CN+NO=NCO+N                                   9.64E+13    0.00    42120.0
146. CN+NO2=NCO+NO                                 1.59E+13    0.00    -1133.0
147. CN+HNO=HCN+NO                                 1.81E+13    0.00        0.0
148. CN+HONO=HCN+NO2                               1.20E+13    0.00        0.0
149. CN+HCN=H+C2N2                                 1.21E+07    1.71     1530.0
150. CN+N2O=NCN+NO                                 3.85E+03    2.60     3696.0
151. CN+CN(+M)=C2N2(+M)                            5.66E+12    0.00        0.0
```

```
     Low pressure limit:  0.34200E+26 -0.26100E+01  0.00000E+00
     TROE centering:      0.50000E+00  0.10000E-89  0.10000E+91
152. C2N2+O=NCO+CN                                 4.57E+12    0.00     8880.0
153. C2N2+OH=HOCN+CN                               1.86E+11    0.00     2900.0
154. NCN+O2=NO+NCO                                 1.00E+14    0.00        0.0
155. NCN+O=CN+NO                                   1.00E+14    0.00        0.0
156. NCN+H=HCN+N                                   1.00E+14    0.00        0.0
157. NCN+OH=HCN+NO                                 5.00E+13    0.00        0.0
158. NCO+M=N+CO+M                                  3.10E+16   -0.50    48300.0
        N2               Enhanced by    1.500E+00
159. NCO+H2=HNCO+H                                 7.60E+02    3.00     4000.0
160. NCO+O2=NO+CO2                                 2.00E+12    0.00    20000.0
161. NCO+O=CO+NO                                   2.00E+13    0.00        0.0
162. NCO+H=NH+CO                                   5.36E+13    0.00        0.0
163. NCO+OH=NO+CO+H                                1.00E+13    0.00        0.0
164. NCO+OH=NO+HCO                                 5.00E+12    0.00    15000.0
165. NCO+CH2O=HNCO+HCO                             6.02E+12    0.00        0.0
166. NCO+HCO=HNCO+CO                               3.61E+13    0.00        0.0
167. NCO+N=N2+CO                                   2.00E+13    0.00        0.0
168. NCO+NO=N2O+CO                                 6.20E+17   -1.73      763.0
169. NCO+NO=CO2+N2                                 7.80E+17   -1.73      763.0
170. NCO+NO2=CO+2NO                                1.39E+13    0.00        0.0
171. NCO+NO2=CO2+N2O                               4.17E+12    0.00        0.0
172. NCO+HNO=HNCO+NO                               1.81E+13    0.00        0.0
173. NCO+HONO=HNCO+NO2                             3.61E+12    0.00        0.0
174. NCO+N2O=N2+NO+CO                              9.03E+13    0.00    27820.0
175. NCO+CN=NCN+CO                                 1.81E+13    0.00        0.0
176. NCO+NCO=N2+2CO                                1.00E+13    0.00        0.0
177. CNO+O=CO+NO                                   1.00E+13    0.00        0.0
178. CNO+NO2=CO+2NO                                1.00E+13    0.00        0.0
179. CNO+N2O=N2+CO+NO                              1.00E+12    0.00    15000.0
180. HNCO(+M)=NH+CO(+M)                            6.00E+13    0.00    99800.0
     Low pressure limit:  0.21700E+29 -0.31000E+01  0.10190E+06
     TROE centering:      0.93800E+00  0.10000E-89  0.33040E+04
181. HNCO+O2=HNO+CO2                               1.00E+12    0.00    35000.0
182. HNCO+O=CO2+NH                                 9.64E+07    1.41     8524.0
183. HNCO+O=OH+NCO                                 6.67E-04    4.55     1780.0
184. HNCO+O=HNO+CO                                 1.58E+08    1.57    44300.0
185. HNCO+H=NH2+CO                                 2.20E+07    1.70     3800.0
186. HNCO+OH=H2O+NCO                               6.38E+05    2.00     2563.0
187. HNCO+HO2=NCO+H2O2                             3.00E+11    0.00    29000.0
188. HNCO+NH=NH2+NCO                               3.00E+13    0.00    23700.0
189. HNCO+NH2=NH3+NCO                              5.00E+12    0.00     6200.0
190. HNCO+CN=HCN+NCO                               1.51E+13    0.00        0.0
191. HCNO+O=HCO+NO                                 1.00E+12    0.00     9000.0
192. HCNO+OH=HCO+HNO                               1.00E+13    0.00     5000.0
193. HCNO+OH=CNO+H2O                               1.00E+12    0.00     2000.0
194. HCNO+CN=HCN+CNO                               1.00E+12    0.00     2000.0
195. HOCN+O=NCO+OH                                 1.50E+04    2.64     4000.0
196. HOCN+H=HNCO+H                                 2.00E+07    2.00     2000.0
197. HOCN+OH=NCO+H2O                               6.40E+05    2.00     2560.0
198. H2CN+M=HCN+H+M                                5.30E+16    0.00    29000.0
199. H2CN+CH2O=H2CNH+HCO                           1.00E+11    0.00    14000.0
200. H2CN+NO=HCN+HNO                               1.00E+11    0.00     3000.0
201. H2CN+NO2=HCN+HONO                             1.00E+11    0.00     1000.0
202. H2CN+NO2=H2CNO+NO                             1.00E+11    0.00     3000.0
203. H2CN+HNO=H2CNH+NO                             1.00E+11    0.00     4000.0
204. H2CN+HONO=H2CNH+NO2                           1.00E+11    0.00    12000.0
205. H2CN+N2O=H2CNO+N2                             1.00E+11    0.00     3000.0
206. H2CNH+OH=H2CN+H2O                             1.00E+13    0.00        0.0
207. H2CNH+CN=H2CN+HCN                             1.00E+13    0.00        0.0
208. H2CNO+M=HCNO+H                                1.00E+16    0.00    50000.0
209. H2CNO+OH=HCNO+H2O                             1.00E+13    0.00        0.0
210. H2CNO+NO=HCNO+HNO                             1.00E+12    0.00    25000.0
211. H2CNO+NO2=HCNO+HONO                           1.00E+12    0.00     2000.0
212. H2CNO+NO2=CH2O+NO+NO                          1.00E+12    0.00        0.0
213. H2CNO+HNO=H2CN+HONO                           1.00E+12    0.00     2000.0
214. H2CNNO(+M)=H2CN+NO(+M)                        1.00E+16    0.00     2000.0
     Low pressure limit:  0.76900E+17  0.00000E+00  0.15000E+05
215. H2CNNO2(+M)=H2CN+NO2(+M)                      2.46E+15    0.00    34200.0
     Low pressure limit:  0.23500E+57 -0.13260E+02  0.24550E+05
```

```
216. H2CNNO2(+M)=HONO+HCN(+M)                       6.21E+12    0.00    32500.0
     Low pressure limit:  0.28700E+40 -0.93700E+01  0.17800E+05
217. H2CNNO2(+M)=CH2O+N2O(+M)                       4.52E+11    0.00    38400.0
     Low pressure limit:  0.13800E+05  0.00000E+00  0.12100E+05
218. RDX(+M)=RDXR+NO2(+M)                           2.00E+16    0.00    45000.0
     Low pressure limit:  0.15700E+18  0.00000E+00  0.28000E+05
219. RDX+H=RDXR+HONO                                1.00E+13    0.00     5000.0
220. RDX+OH=>2H2CNNO2+H2COHNNO2                     1.00E+13    0.00     5000.0
221. H2COHNNO2=>HCN+NO2+H2O                         1.00E+16    0.00        0.0
222. RDXR(+M)=>RDXRO(+M)                            1.00E+16    0.00    23000.0
     Low pressure limit:  0.76900E+17  0.00000E+00  0.18000E+05
223. RDXRO(+M)=>2H2CNNO2+H2CN(+M)                   1.00E+16    0.00    23000.0
     Low pressure limit:  0.76900E+17  0.00000E+00  0.18000E+05
224. O+CH<=>H+CO                                    5.70E+13    0.00        0.0
225. O+CH2<=>H+HCO                                  8.00E+13    0.00        0.0
226. O+CH2(S)<=>H2+CO                               1.50E+13    0.00        0.0
227. O+CH2(S)<=>H+HCO                               1.50E+13    0.00        0.0
228. O+CH3<=>H+CH2O                                 5.06E+13    0.00        0.0
229. O+CH4<=>OH+CH3                                 1.02E+09    1.50     8600.0
230. O+CH2OH<=>OH+CH2O                              1.00E+13    0.00        0.0
231. O+CH3O<=>OH+CH2O                               1.00E+13    0.00        0.0
232. O+CH3OH<=>OH+CH2OH                             3.88E+05    2.50     3100.0
233. O+CH3OH<=>OH+CH3O                              1.30E+05    2.50     5000.0
234. O+C2H<=>CH+CO                                  5.00E+13    0.00        0.0
235. O+C2H2<=>H+HCCO                                1.35E+07    2.00     1900.0
236. O+C2H2<=>OH+C2H                                4.60E+19   -1.41    28950.0
237. O+C2H2<=>CO+CH2                                6.94E+06    2.00     1900.0
238. O+C2H3<=>H+CH2CO                               3.00E+13    0.00        0.0
239. O+C2H4<=>CH3+HCO                               1.25E+07    1.83      220.0
240. O+C2H5<=>CH3+CH2O                              2.24E+13    0.00        0.0
241. O+C2H6<=>OH+C2H5                               8.98E+07    1.92     5690.0
242. O+HCCO<=>H+2CO                                 1.00E+14    0.00        0.0
243. O+CH2CO<=>OH+HCCO                              1.00E+13    0.00     8000.0
244. O+CH2CO<=>CH2+CO2                              1.75E+12    0.00     1350.0
245. H+2O2<=>HO2+O2                                 2.08E+19   -1.24        0.0
246. 2H+H2<=>2H2                                    9.00E+16   -0.60        0.0
247. 2H+H2O<=>H2+H2O                                6.00E+19   -1.25        0.0
248. 2H+CO2<=>H2+CO2                                5.50E+20   -2.00        0.0
249. H+HO2<=>O+H2O                                  3.97E+12    0.00      671.0
250. H+CH<=>C+H2                                    1.65E+14    0.00        0.0
251. H+CH2(+M)<=>CH3(+M)                            6.00E+14    0.00        0.0
     Low pressure limit:  0.10400E+27 -0.27600E+01  0.16000E+04
     TROE centering:      0.56200E+00  0.91000E+02  0.58360E+04  0.85520E+04
        H2               Enhanced by    2.000E+00
        H2O              Enhanced by    6.000E+00
        CH4              Enhanced by    2.000E+00
        CO               Enhanced by    1.500E+00
        CO2              Enhanced by    2.000E+00
        C2H6             Enhanced by    3.000E+00
        AR               Enhanced by    7.000E-01
252. H+CH2(S)<=>CH+H2                               3.00E+13    0.00        0.0
253. H+CH3(+M)<=>CH4(+M)                            1.39E+16   -0.53      536.0
     Low pressure limit:  0.26200E+34 -0.47600E+01  0.24400E+04
     TROE centering:      0.78300E+00  0.74000E+02  0.29410E+04  0.69640E+04
        H2               Enhanced by    2.000E+00
        H2O              Enhanced by    6.000E+00
        CH4              Enhanced by    3.000E+00
        CO               Enhanced by    1.500E+00
        CO2              Enhanced by    2.000E+00
        C2H6             Enhanced by    3.000E+00
        AR               Enhanced by    7.000E-01
254. H+CH4<=>CH3+H2                                 6.60E+08    1.62    10840.0
255. H+CH2O(+M)<=>CH2OH(+M)                         5.40E+11    0.45     3600.0
     Low pressure limit:  0.12700E+33 -0.48200E+01  0.65300E+04
     TROE centering:      0.71870E+00  0.10300E+03  0.12910E+04  0.41600E+04
        H2               Enhanced by    2.000E+00
        H2O              Enhanced by    6.000E+00
        CH4              Enhanced by    2.000E+00
        CO               Enhanced by    1.500E+00
        CO2              Enhanced by    2.000E+00
        C2H6             Enhanced by    3.000E+00
```

```
256. H+CH2O(+M)<=>CH3O(+M)                          5.40E+11    0.45     2600.0
     Low pressure limit:  0.22000E+31 -0.48000E+01  0.55600E+04
     TROE centering:      0.75800E+00  0.94000E+02  0.15550E+04  0.42000E+04
        H2               Enhanced by    2.000E+00
        H2O              Enhanced by    6.000E+00
        CH4              Enhanced by    2.000E+00
        CO               Enhanced by    1.500E+00
        CO2              Enhanced by    2.000E+00
        C2H6             Enhanced by    3.000E+00
257. H+CH2OH(+M)<=>CH3OH(+M)                        1.06E+12    0.50       86.0
     Low pressure limit:  0.43600E+32 -0.46500E+01  0.50800E+04
     TROE centering:      0.60000E+00  0.10000E+03  0.90000E+05  0.10000E+05
        H2               Enhanced by    2.000E+00
        H2O              Enhanced by    6.000E+00
        CH4              Enhanced by    2.000E+00
        CO               Enhanced by    1.500E+00
        CO2              Enhanced by    2.000E+00
        C2H6             Enhanced by    3.000E+00
258. H+CH2OH<=>H2+CH2O                              2.00E+13    0.00        0.0
259. H+CH2OH<=>OH+CH3                               1.65E+11    0.65     -284.0
260. H+CH2OH<=>CH2(S)+H2O                           3.28E+13   -0.09      610.0
261. H+CH3O(+M)<=>CH3OH(+M)                         2.43E+12    0.52       50.0
     Low pressure limit:  0.46600E+42 -0.74400E+01  0.14080E+05
     TROE centering:      0.70000E+00  0.10000E+03  0.90000E+05  0.10000E+05
        H2               Enhanced by    2.000E+00
        H2O              Enhanced by    6.000E+00
        CH4              Enhanced by    2.000E+00
        CO               Enhanced by    1.500E+00
        CO2              Enhanced by    2.000E+00
        C2H6             Enhanced by    3.000E+00
262. H+CH3O<=>H+CH2OH                               4.15E+07    1.63     1924.0
263. H+CH3O<=>H2+CH2O                               2.00E+13    0.00        0.0
264. H+CH3O<=>OH+CH3                                1.50E+12    0.50     -110.0
265. H+CH3O<=>CH2(S)+H2O                            2.62E+14   -0.23     1070.0
266. H+CH3OH<=>CH2OH+H2                             1.70E+07    2.10     4870.0
267. H+CH3OH<=>CH3O+H2                              4.20E+06    2.10     4870.0
268. H+C2H(+M)<=>C2H2(+M)                           1.00E+17   -1.00        0.0
     Low pressure limit:  0.37500E+34 -0.48000E+01  0.19000E+04
     TROE centering:      0.64640E+00  0.13200E+03  0.13150E+04  0.55660E+04
        H2               Enhanced by    2.000E+00
        H2O              Enhanced by    6.000E+00
        CH4              Enhanced by    2.000E+00
        CO               Enhanced by    1.500E+00
        CO2              Enhanced by    2.000E+00
        C2H6             Enhanced by    3.000E+00
        AR               Enhanced by    7.000E-01
269. H+C2H2(+M)<=>C2H3(+M)                          5.60E+12    0.00     2400.0
     Low pressure limit:  0.38000E+41 -0.72700E+01  0.72200E+04
     TROE centering:      0.75070E+00  0.98500E+02  0.13020E+04  0.41670E+04
        H2               Enhanced by    2.000E+00
        H2O              Enhanced by    6.000E+00
        CH4              Enhanced by    2.000E+00
        CO               Enhanced by    1.500E+00
        CO2              Enhanced by    2.000E+00
        C2H6             Enhanced by    3.000E+00
        AR               Enhanced by    7.000E-01
270. H+C2H3(+M)<=>C2H4(+M)                          6.08E+12    0.27      280.0
     Low pressure limit:  0.14000E+31 -0.38600E+01  0.33200E+04
     TROE centering:      0.78200E+00  0.20750E+03  0.26630E+04  0.60950E+04
        H2               Enhanced by    2.000E+00
        H2O              Enhanced by    6.000E+00
        CH4              Enhanced by    2.000E+00
        CO               Enhanced by    1.500E+00
        CO2              Enhanced by    2.000E+00
        C2H6             Enhanced by    3.000E+00
        AR               Enhanced by    7.000E-01
271. H+C2H3<=>H2+C2H2                               3.00E+13    0.00        0.0
272. H+C2H4(+M)<=>C2H5(+M)                          5.40E+11    0.45     1820.0
     Low pressure limit:  0.60000E+42 -0.76200E+01  0.69700E+04
     TROE centering:      0.97530E+00  0.21000E+03  0.98400E+03  0.43740E+04
        H2               Enhanced by    2.000E+00
```

```
        H2O              Enhanced by    6.000E+00
        CH4              Enhanced by    2.000E+00
        CO               Enhanced by    1.500E+00
        CO2              Enhanced by    2.000E+00
        C2H6             Enhanced by    3.000E+00
        AR               Enhanced by    7.000E-01
273. H+C2H4<=>C2H3+H2                               1.33E+06    2.53    12240.0
274. H+C2H5(+M)<=>C2H6(+M)                          5.21E+17   -0.99     1580.0
     Low pressure limit:  0.19900E+42 -0.70800E+01  0.66850E+04
     TROE centering:      0.84220E+00  0.12500E+03  0.22190E+04  0.68820E+04
        H2               Enhanced by    2.000E+00
        H2O              Enhanced by    6.000E+00
        CH4              Enhanced by    2.000E+00
        CO               Enhanced by    1.500E+00
        CO2              Enhanced by    2.000E+00
        C2H6             Enhanced by    3.000E+00
        AR               Enhanced by    7.000E-01
275. H+C2H5<=>H2+C2H4                               2.00E+12    0.00        0.0
276. H+C2H6<=>C2H5+H2                               1.15E+08    1.90     7530.0
277. H+HCCO<=>CH2(S)+CO                             1.00E+14    0.00        0.0
278. H+CH2CO<=>HCCO+H2                              5.00E+13    0.00     8000.0
279. H+CH2CO<=>CH3+CO                               1.13E+13    0.00     3428.0
280. H+HCCOH<=>H+CH2CO                              1.00E+13    0.00        0.0
281. OH+C<=>H+CO                                    5.00E+13    0.00        0.0
282. OH+CH<=>H+HCO                                  3.00E+13    0.00        0.0
283. OH+CH2<=>H+CH2O                                2.00E+13    0.00        0.0
284. OH+CH2<=>CH+H2O                                1.13E+07    2.00     3000.0
285. OH+CH2(S)<=>H+CH2O                             3.00E+13    0.00        0.0
286. OH+CH3(+M)<=>CH3OH(+M)                         2.79E+18   -1.43     1330.0
     Low pressure limit:  0.40000E+37 -0.59200E+01  0.31400E+04
     TROE centering:      0.41200E+00  0.19500E+03  0.59000E+04  0.63940E+04
        H2               Enhanced by    2.000E+00
        H2O              Enhanced by    6.000E+00
        CH4              Enhanced by    2.000E+00
        CO               Enhanced by    1.500E+00
        CO2              Enhanced by    2.000E+00
        C2H6             Enhanced by    3.000E+00
287. OH+CH3<=>CH2+H2O                               5.60E+07    1.60     5420.0
288. OH+CH3<=>CH2(S)+H2O                            6.44E+17   -1.34     1417.0
289. OH+CH4<=>CH3+H2O                               1.00E+08    1.60     3120.0
290. OH+CH2OH<=>H2O+CH2O                            5.00E+12    0.00        0.0
291. OH+CH3O<=>H2O+CH2O                             5.00E+12    0.00        0.0
292. OH+CH3OH<=>CH2OH+H2O                           1.44E+06    2.00     -840.0
293. OH+CH3OH<=>CH3O+H2O                            6.30E+06    2.00     1500.0
294. OH+C2H<=>H+HCCO                                2.00E+13    0.00        0.0
295. OH+C2H2<=>H+CH2CO                              2.18E-04    4.50    -1000.0
296. OH+C2H2<=>H+HCCOH                              5.04E+05    2.30    13500.0
297. OH+C2H2<=>C2H+H2O                              3.37E+07    2.00    14000.0
298. OH+C2H2<=>CH3+CO                               4.83E-04    4.00    -2000.0
299. OH+C2H3<=>H2O+C2H2                             5.00E+12    0.00        0.0
300. OH+C2H4<=>C2H3+H2O                             3.60E+06    2.00     2500.0
301. OH+C2H6<=>C2H5+H2O                             3.54E+06    2.12      870.0
302. OH+CH2CO<=>HCCO+H2O                            7.50E+12    0.00     2000.0
303. HO2+CH2<=>OH+CH2O                              2.00E+13    0.00        0.0
304. HO2+CH3<=>O2+CH4                               1.00E+12    0.00        0.0
305. HO2+CH3<=>OH+CH3O                              3.78E+13    0.00        0.0
306. C+O2<=>O+CO                                    5.80E+13    0.00      576.0
307. C+CH2<=>H+C2H                                  5.00E+13    0.00        0.0
308. C+CH3<=>H+C2H2                                 5.00E+13    0.00        0.0
309. CH+O2<=>O+HCO                                  6.71E+13    0.00        0.0
310. CH+H2<=>H+CH2                                  1.08E+14    0.00     3110.0
311. CH+H2O<=>H+CH2O                                5.71E+12    0.00     -755.0
312. CH+CH2<=>H+C2H2                                4.00E+13    0.00        0.0
313. CH+CH3<=>H+C2H3                                3.00E+13    0.00        0.0
314. CH+CH4<=>H+C2H4                                6.00E+13    0.00        0.0
315. CH+CO(+M)<=>HCCO(+M)                           5.00E+13    0.00        0.0
     Low pressure limit:  0.26900E+29 -0.37400E+01  0.19360E+04
     TROE centering:      0.57570E+00  0.23700E+03  0.16520E+04  0.50690E+04
        H2               Enhanced by    2.000E+00
        H2O              Enhanced by    6.000E+00
        CH4              Enhanced by    2.000E+00
```

```
        CO               Enhanced by    1.500E+00
        CO2              Enhanced by    2.000E+00
        C2H6             Enhanced by    3.000E+00
        AR               Enhanced by    7.000E-01
316. CH+CO2<=>HCO+CO                                1.90E+14    0.00     15792.0
317. CH+CH2O<=>H+CH2CO                              9.46E+13    0.00      -515.0
318. CH+HCCO<=>CO+C2H2                              5.00E+13    0.00         0.0
319. CH2+O2=>OH+H+CO                                5.00E+12    0.00      1500.0
320. CH2+H2<=>H+CH3                                 5.00E+05    2.00      7230.0
321. 2CH2<=>H2+C2H2                                 1.60E+15    0.00     11944.0
322. CH2+CH3<=>H+C2H4                               4.00E+13    0.00         0.0
323. CH2+CH4<=>2CH3                                 2.46E+06    2.00      8270.0
324. CH2+CO(+M)<=>CH2CO(+M)                         8.10E+11    0.50      4510.0
     Low pressure limit:  0.26900E+34 -0.51100E+01  0.70950E+04
     TROE centering:      0.59070E+00  0.27500E+03  0.12260E+04  0.51850E+04
        H2               Enhanced by    2.000E+00
        H2O              Enhanced by    6.000E+00
        CH4              Enhanced by    2.000E+00
        CO               Enhanced by    1.500E+00
        CO2              Enhanced by    2.000E+00
        C2H6             Enhanced by    3.000E+00
        AR               Enhanced by    7.000E-01
325. CH2+HCCO<=>C2H3+CO                             3.00E+13    0.00         0.0
326. CH2(S)+N2<=>CH2+N2                             1.50E+13    0.00       600.0
327. CH2(S)+AR<=>CH2+AR                             9.00E+12    0.00       600.0
328. CH2(S)+O2<=>H+OH+CO                            2.80E+13    0.00         0.0
329. CH2(S)+O2<=>CO+H2O                             1.20E+13    0.00         0.0
330. CH2(S)+H2<=>CH3+H                              7.00E+13    0.00         0.0
331. CH2(S)+H2O(+M)<=>CH3OH(+M)                     4.82E+17   -1.16      1145.0
     Low pressure limit:  0.18800E+39 -0.63600E+01  0.50400E+04
     TROE centering:      0.60270E+00  0.20800E+03  0.39220E+04  0.10180E+05
        H2               Enhanced by    2.000E+00
        H2O              Enhanced by    6.000E+00
        CH4              Enhanced by    2.000E+00
        CO               Enhanced by    1.500E+00
        CO2              Enhanced by    2.000E+00
        C2H6             Enhanced by    3.000E+00
332. CH2(S)+H2O<=>CH2+H2O                           3.00E+13    0.00         0.0
333. CH2(S)+CH3<=>H+C2H4                            1.20E+13    0.00      -570.0
334. CH2(S)+CH4<=>2CH3                              1.60E+13    0.00      -570.0
335. CH2(S)+CO<=>CH2+CO                             9.00E+12    0.00         0.0
336. CH2(S)+CO2<=>CH2+CO2                           7.00E+12    0.00         0.0
337. CH2(S)+CO2<=>CO+CH2O                           1.40E+13    0.00         0.0
338. CH2(S)+C2H6<=>CH3+C2H5                         4.00E+13    0.00      -550.0
339. CH3+O2<=>O+CH3O                                3.56E+13    0.00     30480.0
340. CH3+O2<=>OH+CH2O                               2.31E+12    0.00     20315.0
341. CH3+H2O2<=>HO2+CH4                             2.45E+04    2.47      5180.0
342. 2CH3(+M)<=>C2H6(+M)                            6.77E+16   -1.18       654.0
     Low pressure limit:  0.34000E+42 -0.70300E+01  0.27620E+04
     TROE centering:      0.61900E+00  0.73200E+02  0.11800E+04  0.99990E+04
        H2               Enhanced by    2.000E+00
        H2O              Enhanced by    6.000E+00
        CH4              Enhanced by    2.000E+00
        CO               Enhanced by    1.500E+00
        CO2              Enhanced by    2.000E+00
        C2H6             Enhanced by    3.000E+00
        AR               Enhanced by    7.000E-01
343. 2CH3<=>H+C2H5                                  6.84E+12    0.10     10600.0
344. CH3+HCO<=>CH4+CO                               2.65E+13    0.00         0.0
345. CH3+CH2O<=>HCO+CH4                             3.32E+03    2.81      5860.0
346. CH3+CH3OH<=>CH2OH+CH4                          3.00E+07    1.50      9940.0
347. CH3+CH3OH<=>CH3O+CH4                           1.00E+07    1.50      9940.0
348. CH3+C2H4<=>C2H3+CH4                            2.27E+05    2.00      9200.0
349. CH3+C2H6<=>C2H5+CH4                            6.14E+06    1.74     10450.0
350. HCO+H2O<=>H+CO+H2O                             1.50E+18   -1.00     17000.0
351. CH2OH+O2<=>HO2+CH2O                            1.80E+13    0.00       900.0
352. CH3O+O2<=>HO2+CH2O                             4.28E-13    7.60     -3530.0
353. C2H+O2<=>HCO+CO                                1.00E+13    0.00      -755.0
354. C2H+H2<=>H+C2H2                                5.68E+10    0.90      1993.0
355. C2H3+O2<=>HCO+CH2O                             4.58E+16   -1.39      1015.0
356. C2H4(+M)<=>H2+C2H2(+M)                         8.00E+12    0.44     86770.0
```

```
     Low pressure limit:  0.15800E+52 -0.93000E+01  0.97800E+05
     TROE centering:      0.73450E+00  0.18000E+03  0.10350E+04  0.54170E+04
        H2               Enhanced by    2.000E+00
        H2O              Enhanced by    6.000E+00
        CH4              Enhanced by    2.000E+00
        CO               Enhanced by    1.500E+00
        CO2              Enhanced by    2.000E+00
        C2H6             Enhanced by    3.000E+00
        AR               Enhanced by    7.000E-01
357. C2H5+O2<=>HO2+C2H4                             8.40E+11    0.00     3875.0
358. HCCO+O2<=>OH+2CO                               3.20E+12    0.00      854.0
359. 2HCCO<=>2CO+C2H2                               1.00E+13    0.00        0.0
360. NNH<=>N2+H                                     3.30E+08    0.00        0.0
361. NNH+O2<=>HO2+N2                                5.00E+12    0.00        0.0
362. NNH+O<=>OH+N2                                  2.50E+13    0.00        0.0
363. NNH+O<=>NH+NO                                  7.00E+13    0.00        0.0
364. NNH+CH3<=>CH4+N2                               2.50E+13    0.00        0.0
365. H2CN+N<=>N2+CH2                                6.00E+13    0.00      400.0
366. C+N2<=>CN+N                                    6.30E+13    0.00    46020.0
367. CH+N2<=>HCN+N                                  3.12E+09    0.88    20130.0
368. CH+N2(+M)<=>HCNN(+M)                           3.10E+12    0.15        0.0
     Low pressure limit:  0.13000E+26 -0.31600E+01  0.74000E+03
     TROE centering:      0.66700E+00  0.23500E+03  0.21170E+04  0.45360E+04
        H2               Enhanced by    2.000E+00
        H2O              Enhanced by    6.000E+00
        CH4              Enhanced by    2.000E+00
        CO               Enhanced by    1.500E+00
        CO2              Enhanced by    2.000E+00
        C2H6             Enhanced by    3.000E+00
        AR               Enhanced by    1.000E+00
369. CH2+N2<=>HCN+NH                                1.00E+13    0.00    74000.0
370. CH2(S)+N2<=>NH+HCN                             1.00E+11    0.00    65000.0
371. C+NO<=>CN+O                                    1.90E+13    0.00        0.0
372. C+NO<=>CO+N                                    2.90E+13    0.00        0.0
373. CH+NO<=>HCN+O                                  4.10E+13    0.00        0.0
374. CH+NO<=>H+NCO                                  1.62E+13    0.00        0.0
375. CH+NO<=>N+HCO                                  2.46E+13    0.00        0.0
376. CH2+NO<=>H+HNCO                                3.10E+17   -1.38     1270.0
377. CH2+NO<=>OH+HCN                                2.90E+14   -0.69      760.0
378. CH2+NO<=>H+HCNO                                3.80E+13   -0.36      580.0
379. CH2(S)+NO<=>H+HNCO                             3.10E+17   -1.38     1270.0
380. CH2(S)+NO<=>OH+HCN                             2.90E+14   -0.69      760.0
381. CH2(S)+NO<=>H+HCNO                             3.80E+13   -0.36      580.0
382. CH3+NO<=>HCN+H2O                               9.60E+13    0.00    28800.0
383. CH3+NO<=>H2CN+OH                               1.00E+12    0.00    21750.0
384. HCNN+O<=>CO+H+N2                               2.20E+13    0.00        0.0
385. HCNN+O<=>HCN+NO                                2.00E+12    0.00        0.0
386. HCNN+O2<=>O+HCO+N2                             1.20E+13    0.00        0.0
387. HCNN+OH<=>H+HCO+N2                             1.20E+13    0.00        0.0
388. HCNN+H<=>CH2+N2                                1.00E+14    0.00        0.0
389. HNCO+OH<=>NH2+CO2                              3.30E+06    1.50     3600.0
390. HCNO+H<=>H+HNCO                                2.10E+15   -0.69     2850.0
391. HCNO+H<=>OH+HCN                                2.70E+11    0.18     2120.0
392. HCNO+H<=>NH2+CO                                1.70E+14   -0.75     2890.0
393. HCCO+NO<=>HCNO+CO                              9.00E+12    0.00        0.0
394. CH3+N<=>H2CN+H                                 6.10E+14   -0.31      290.0
395. CH3+N<=>HCN+H2                                 3.70E+12    0.15      -90.0
396. O+CH3=>H+H2+CO                                 3.37E+13    0.00        0.0
397. O+C2H4<=>H+CH2CHO                              6.70E+06    1.83      220.0
398. O+C2H5<=>H+CH3CHO                              1.10E+14    0.00        0.0
399. OH+CH3=>H2+CH2O                                8.00E+09    0.50    -1755.0
400. CH+H2(+M)<=>CH3(+M)                            1.97E+12    0.43     -370.0
     Low pressure limit:  0.48200E+26 -0.28000E+01  0.59000E+03
     TROE centering:      0.57800E+00  0.12200E+03  0.25350E+04  0.93650E+04
        H2               Enhanced by    2.000E+00
        H2O              Enhanced by    6.000E+00
        CH4              Enhanced by    2.000E+00
        CO               Enhanced by    1.500E+00
        CO2              Enhanced by    2.000E+00
        C2H6             Enhanced by    3.000E+00
        AR               Enhanced by    7.000E-01
```

```
401. CH2+O2=>2H+CO2                                 5.80E+12    0.00     1500.0
402. CH2+O2<=>O+CH2O                                2.40E+12    0.00     1500.0
403. CH2+CH2=>2H+C2H2                               2.00E+14    0.00    10989.0
404. CH2(S)+H2O=>H2+CH2O                            6.82E+10    0.25     -935.0
405. C2H3+O2<=>O+CH2CHO                             3.03E+11    0.29       11.0
406. C2H3+O2<=>HO2+C2H2                             1.34E+06    1.61     -384.0
407. O+CH3CHO<=>OH+CH2CHO                           2.92E+12    0.00     1808.0
408. O+CH3CHO=>OH+CH3+CO                            2.92E+12    0.00     1808.0
409. O2+CH3CHO=>HO2+CH3+CO                          3.01E+13    0.00    39150.0
410. H+CH3CHO<=>CH2CHO+H2                           2.05E+09    1.16     2405.0
411. H+CH3CHO=>CH3+H2+CO                            2.05E+09    1.16     2405.0
412. OH+CH3CHO=>CH3+H2O+CO                          2.34E+10    0.73    -1113.0
413. HO2+CH3CHO=>CH3+H2O2+CO                        3.01E+12    0.00    11923.0
414. CH3+CH3CHO=>CH3+CH4+CO                         2.72E+06    1.77     5920.0
415. H+CH2CO(+M)<=>CH2CHO(+M)                       4.87E+11    0.42    -1755.0
     Low pressure limit:  0.10120E+43 -0.76300E+01  0.38540E+04
     TROE centering:      0.46500E+00  0.20100E+03  0.17730E+04  0.53330E+04
        H2               Enhanced by    2.000E+00
        H2O              Enhanced by    6.000E+00
        CH4              Enhanced by    2.000E+00
        CO               Enhanced by    1.500E+00
        CO2              Enhanced by    2.000E+00
        C2H6             Enhanced by    3.000E+00
        AR               Enhanced by    7.000E-01
416. O+CH2CHO=>H+CH2+CO2                            1.50E+14    0.00        0.0
417. O2+CH2CHO=>OH+CO+CH2O                          1.81E+10    0.00        0.0
418. O2+CH2CHO=>OH+2HCO                             2.35E+10    0.00        0.0
419. H+CH2CHO<=>CH3+HCO                             2.20E+13    0.00        0.0
420. H+CH2CHO<=>CH2CO+H2                            1.10E+13    0.00        0.0
421. OH+CH2CHO<=>H2O+CH2CO                          1.20E+13    0.00        0.0
422. OH+CH2CHO<=>HCO+CH2OH                          3.01E+13    0.00        0.0
423. CH3+C2H5(+M)<=>C3H8(+M)                        9.43E+12    0.00        0.0
     Low pressure limit:  0.27100E+75 -0.16820E+02  0.13065E+05
     TROE centering:      0.15270E+00  0.29100E+03  0.27420E+04  0.77480E+04
        H2               Enhanced by    2.000E+00
        H2O              Enhanced by    6.000E+00
        CH4              Enhanced by    2.000E+00
        CO               Enhanced by    1.500E+00
        CO2              Enhanced by    2.000E+00
        C2H6             Enhanced by    3.000E+00
        AR               Enhanced by    7.000E-01
424. O+C3H8<=>OH+C3H7                               1.93E+05    2.68     3716.0
425. H+C3H8<=>C3H7+H2                               1.32E+06    2.54     6756.0
426. OH+C3H8<=>C3H7+H2O                             3.16E+07    1.80      934.0
427. C3H7+H2O2<=>HO2+C3H8                           3.78E+02    2.72     1500.0
428. CH3+C3H8<=>C3H7+CH4                            9.03E-01    3.65     7154.0
429. CH3+C2H4(+M)<=>C3H7(+M)                        2.55E+06    1.60     5700.0
     Low pressure limit:  0.30000E+64 -0.14600E+02  0.18170E+05
     TROE centering:      0.18940E+00  0.27700E+03  0.87480E+04  0.78910E+04
        H2               Enhanced by    2.000E+00
        H2O              Enhanced by    6.000E+00
        CH4              Enhanced by    2.000E+00
        CO               Enhanced by    1.500E+00
        CO2              Enhanced by    2.000E+00
        C2H6             Enhanced by    3.000E+00
        AR               Enhanced by    7.000E-01
430. O+C3H7<=>C2H5+CH2O                             9.64E+13    0.00        0.0
431. H+C3H7(+M)<=>C3H8(+M)                          3.61E+13    0.00        0.0
     Low pressure limit:  0.44200E+62 -0.13545E+02  0.11357E+05
     TROE centering:      0.31500E+00  0.36900E+03  0.32850E+04  0.66670E+04
        H2               Enhanced by    2.000E+00
        H2O              Enhanced by    6.000E+00
        CH4              Enhanced by    2.000E+00
        CO               Enhanced by    1.500E+00
        CO2              Enhanced by    2.000E+00
        C2H6             Enhanced by    3.000E+00
        AR               Enhanced by    7.000E-01
432. H+C3H7<=>CH3+C2H5                              4.06E+06    2.19      890.0
433. OH+C3H7<=>C2H5+CH2OH                           2.41E+13    0.00        0.0
434. HO2+C3H7<=>O2+C3H8                             2.55E+10    0.26     -943.0
435. HO2+C3H7=>OH+C2H5+CH2O                         2.41E+13    0.00        0.0
```

```
436. CH3+C3H7<=>2C2H5                               1.93E+13   -0.32        0.0
437. H+O2+H2O<=>HO2+H2O                             1.13E+19   -0.76        0.0
438. H+O2+N2<=>HO2+N2                               2.60E+19   -1.24        0.0
439. H+O2+AR<=>HO2+AR                               7.00E+17   -0.80        0.0
440. BTTN=>2NO2+3CH2O+HCO+NO                        5.00E+16    0.00    40000.0
441. BTTN=>3CH2O+NO2+NO+CO+HONO                     5.00E+16    0.00    40000.0
442. N2+M=N+N+M                                     3.71E+21   -1.60   225000.0
443. NO2+NO3=NO+NO2+O2                              1.40E+11    0.00     3180.0
444. H2+O2=2OH                                      1.70E+13    0.00    47780.0
445. N2O+H=N2+OH                                    2.53E+10    0.00     4550.0
     Declared duplicate reaction...
446. N2O+H=N2+OH                                    2.23E+14    0.00    16750.0
     Declared duplicate reaction...
447. NH2+NH=N2H2+H                                  1.50E+15   -0.50        0.0
448. NH2+NH2=N2H2+H2                                5.00E+11    0.00        0.0
449. NH2+NH2=N2H3+H                                 1.79E+13   -0.35    11320.0
450. NH2+NH2+M=N2H4+M                               2.98E+47   -9.44     9680.0
451. N2H4+H=N2H3+H2                                 1.00E+12    0.50     2000.0
452. N2H4+OH=N2H3+H2O                               3.00E+10    0.68     1290.0
453. N2H4+O=N2H3+OH                                 2.00E+13    0.00     1000.0
454. N2H3=N2H2+H                                    1.20E+13    0.00    58000.0
455. N2H3+H=N2H2+H2                                 1.00E+12    0.50     2000.0
456. N2H3+OH=N2H2+H2O                               3.00E+10    0.68     1290.0
457. N2H3+O=N2H2+OH                                 2.00E+13    0.00     1000.0
458. N2H2+M=NNH+H+M                                 5.00E+16    0.00    50000.0
        H2O              Enhanced by    1.500E+01
        O2               Enhanced by    2.000E+00
        N2               Enhanced by    2.000E+00
        H2               Enhanced by    2.000E+00
459. N2H2+H=NNH+H2                                  5.00E+13    0.00     1000.0
460. N2H2+O=NH2+NO                                  1.00E+13    0.00        0.0
461. N2H2+O=NNH+OH                                  2.00E+13    0.00     1000.0
462. N2H2+OH=NNH+H2O                                1.00E+13    0.00     1000.0
463. N2H2+NH=NNH+NH2                                1.00E+13    0.00     1000.0
464. N2H2+NH2=NH3+NNH                               1.00E+13    0.00     1000.0
465. N2O+NO=N2+NO2                                  4.29E+13    0.00    47130.0
466. NO+NO+NO=N2O+NO2                               1.07E+10    0.00    26800.0
467. HOCO+M=OH+CO+M                                 2.19E+23   -1.89    35270.0
468. CH+NO2=HCO+NO                                  1.01E+14    0.00        0.0
469. NNH=N2+H                                       3.00E+08    0.00        0.0
470. HNO+NO+NO=HNNO+NO2                             1.70E+11    0.00     2100.0
471. HNNO+NO=NNH+NO2                                3.20E+12    0.00      270.0
472. HNNO+NO=N2+HONO                                2.60E+11    0.00      810.0
473. HNNO+M=H+N2O+M                                 2.20E+15    0.00    21600.0
474. HNNO+M=N2+OH+M                                 1.00E+15    0.00    25600.0
475. H+HCO(+M)<=>CH2O(+M)                           1.09E+12    0.48     -260.0
     Low pressure limit:  0.13500E+25 -0.25700E+01  0.14250E+04
     TROE centering:      0.78240E+00  0.27100E+03  0.27550E+04  0.65700E+04
        H2               Enhanced by    2.000E+00
        H2O              Enhanced by    6.000E+00
        CO               Enhanced by    1.500E+00
        CO2              Enhanced by    2.000E+00
476. H2+CO(+M)<=>CH2O(+M)                           4.30E+07    1.50    79600.0
     Low pressure limit:  0.50700E+28 -0.34200E+01  0.84350E+05
     TROE centering:      0.93200E+00  0.19700E+03  0.15400E+04  0.10300E+05
        H2               Enhanced by    2.000E+00
        H2O              Enhanced by    6.000E+00
        CO               Enhanced by    1.500E+00
        CO2              Enhanced by    2.000E+00
477. HCO+HCO=CH2O+CO                                3.00E+13    0.00        0.0
478. HCO+HCO=H2+CO+CO                               5.20E+12    0.00        0.0
479. ADN(G)+M=>NH3+HN3O4+M                          3.00E+12    0.00    12040.0
480. HN3O4=HNNO2+NO2                                2.01E+48  -10.90    42214.0
481. HNNO2+M<=>N2O+OH+M                             7.53E+24   -2.90    25150.0
482. HNNO2+M<=>NH+NO2+M                             6.35E+18   -1.10    39397.0
483. HNNO2+NO2<=>HNO+NO+NO2                         3.00E+12    0.00        0.0
484. HNNO2+OH<=>H2O+2NO                             5.00E+12    0.00        0.0
485. HNNO2+OH<=>HNO+HONO                            5.00E+12    0.00        0.0
486. NH2+NO2<=>H2NO+NO                              6.56E+16   -1.50      268.0
487. H2NO+H<=>HNO+H2                                3.00E+07    2.00     2000.0
488. H2NO+H<=>NH2+OH                                5.00E+13    0.00        0.0
```

489.	H2NO+M<=>H2+NO+M	7.83E+27	-4.30	60306.0
490.	H2NO+M<=>HNO+H+M	1.69E+32	-5.00	62312.0
491.	H2NO+M<=>HNOH+M	4.46E+30	-3.80	56888.0
492.	H2NO+NH2<=>HNO+NH3	3.00E+12	0.00	1000.0
493.	H2NO+NO<=>HNO+HNO	2.00E+07	2.00	13000.0
494.	H2NO+NO2<=>HONO+HNO	6.00E+11	0.00	2000.0
495.	H2NO+O<=>HNO+OH	3.00E+07	2.00	2000.0
496.	H2NO+O<=>NH2+O2	4.00E+13	0.00	0.0
497.	HNNH+OH<=>H2O+N2+H	2.50E+12	0.00	0.0
498.	HNNO2+NH2<=>HNNH+HONO	2.50E+12	0.00	0.0
499.	HNNO2+NO<=>HNNO+NO2	2.50E+12	0.00	0.0
500.	HNNO2+NO<=>HONO+N2O	2.50E+12	0.00	0.0
501.	HNOH+M<=>H+HNO+M	1.03E+04	-4.80	59527.0
502.	HONO+H<=>HNO+OH	5.64E+10	0.90	4969.0
503.	HONO+H<=>NO+H2O	8.13E+06	1.90	3846.0
504.	HONO+HONO<=>NO+NO2+H2O	9.69E+10	0.00	14132.0
505.	HONO+NH<=>NH2+NO2	1.00E+13	0.00	0.0
506.	N2H2+NO<=>N2O+NH2	3.00E+12	0.00	0.0
507.	N2H3+M<=>N2H2+H+M	3.50E+16	0.00	46000.0
508.	N2H3+NH<=>N2H2+NH2	2.00E+13	0.00	0.0
509.	N2H3+O<=>NH2+HNO	1.00E+13	0.00	0.0
510.	N2H3+OH<=>NH3+HNO	1.00E+12	0.00	15000.0
511.	N2H4+NH2<=>N2H3+NH3	3.90E+12	0.00	1500.0
512.	N2H4+O<=>N2H2+H2O	8.50E+13	0.00	1200.0
513.	NH2+HO2<=>H2NO+OH	2.50E+13	0.00	0.0
514.	NH3+HNO3<=>H2NO+H2O+NO	2.32E+01	3.50	44926.0
515.	NNH<=>N2+H	1.00E+06	0.00	0.0
516.	NO3+H<=>NO2+OH	6.00E+13	0.00	0.0
517.	NO3+HO2<=>NO2+O2+OH	1.50E+12	0.00	0.0
518.	NO3+O<=>NO2+O2	1.00E+13	0.00	0.0
519.	NO3+OH<=>NO2+HO2	1.00E+13	0.00	0.0
520.	H2NO+OH=HNO+H2O	2.00E+07	2.00	1000.0
521.	NH2+OH+M=H2NOH+M	5.00E+17	0.00	0.0
522.	HNO3+OH=H2O+NO3	1.03E+10	0.00	-1240.0
523.	HCO+HONO=CH2O+NO2	2.39E-03	4.28	4370.0
524.	HCO+HONO=H2O+CO+NO	1.90E-08	6.12	9190.0
525.	HCO+HNOH=HNO+CO+H2	1.71E+03	2.27	-9424.0
526.	HCO+HNOH=CH2O+HNO	3.10E-01	3.52	-854.0
527.	HCO+HNOH=H2NOH+CO	2.15E+03	2.42	-8446.0
528.	HCO+HNO=CH2O+NO	5.83E-01	3.84	115.0
529.	HCO+HNO=CO+H2NO	4.89E+01	3.27	1754.5
530.	HCO+HNO=HNOH+CO	1.31E+13	-0.20	3646.0

NOTE: A units mole-cm-sec-K, E units cal/mole

Appendix B. Universal Gas-Phase Mechanism

The following is the universal gas-phase mechanism used in the AP/HTPB combustion model, including Puduppakkam's modified comprehensive mechanism, the chorine-containing reactions added by Gross, and the HCN-elimination reaction, as outlined in Chapter 4.

```
CHEMKIN INTERPRETER OUTPUT: CHEMKIN-II Version 3.1 Feb. 1993
                             DOUBLE PRECISION

                         --------------------
                         ELEMENTS     ATOMIC
                         CONSIDERED   WEIGHT
                         --------------------
                          1. AR      39.9480
                          2. C       12.0112
                          3. H       1.00797
                          4. N       14.0067
                          5. O       15.9994
                          6. CL      35.4530
                          7. AL      26.9815
                         --------------------
-------------------------------------------------------------------------------
                        C
                      P H
                      H A
                      A R
SPECIES               S G MOLECULAR TEMPERATURE   ELEMENT COUNT
CONSIDERED            E E WEIGHT    LOW    HIGH   AR C  H  N  O  CL AL
-------------------------------------------------------------------------------
  1. AR               G 0  39.94800  300.0 5000.0  1  0  0  0  0  0  0
  2. H2               G 0   2.01594  300.0 5000.0  0  0  2  0  0  0  0
  3. O2               G 0  31.99880  300.0 5000.0  0  0  0  0  2  0  0
  4. H2O              G 0  18.01534  300.0 5000.0  0  0  2  0  1  0  0
  5. O                G 0  15.99940  300.0 5000.0  0  0  0  0  1  0  0
  6. HNOH             G 0  32.02204  300.0 4000.0  0  0  2  1  1  0  0
  7. H                G 0   1.00797  300.0 5000.0  0  0  1  0  0  0  0
  8. OH               G 0  17.00737  300.0 5000.0  0  0  1  0  1  0  0
  9. HO2              G 0  33.00677  200.0 3500.0  0  0  1  0  2  0  0
 10. H2O2             G 0  34.01474  300.0 5000.0  0  0  2  0  2  0  0
 11. CH2O             G 0  30.02649  300.0 5000.0  0  1  2  0  1  0  0
 12. HCO              G 0  29.01852  300.0 5000.0  0  1  1  0  1  0  0
 13. CO               G 0  28.01055  300.0 5000.0  0  1  0  0  1  0  0
 14. CO2              G 0  44.00995  300.0 5000.0  0  1  0  0  2  0  0
 15. N                G 0  14.00670  200.0 6000.0  0  0  0  1  0  0  0
 16. N2               G 0  28.01340  300.0 5000.0  0  0  0  2  0  0  0
 17. NO               G 0  30.00610  200.0 6000.0  0  0  0  1  1  0  0
 18. NO2              G 0  46.00550  200.0 6000.0  0  0  0  1  2  0  0
```

```
19. NH               G 0  15.01467  200.0 6000.0  0  0  1  1  0  0  0
20. NH2              G 0  16.02264  200.0 6000.0  0  0  2  1  0  0  0
21. NH3              G 0  17.03061  200.0 6000.0  0  0  3  1  0  0  0
22. NNH              G 0  29.02137  200.0 6000.0  0  0  1  2  0  0  0
23. HNO              G 0  31.01407  200.0 6000.0  0  0  1  1  1  0  0
24. HONO             G 0  47.01347  300.0 5000.0  0  0  1  1  2  0  0
25. HCN              G 0  27.02582  200.0 6000.0  0  1  1  1  0  0  0
26. N2O              G 0  44.01280  200.0 6000.0  0  0  0  2  1  0  0
27. CN               G 0  26.01785  200.0 6000.0  0  1  0  1  0  0  0
28. C2N2             G 0  52.03570  300.0 5000.0  0  2  0  2  0  0  0
29. NCN              G 0  40.02455  300.0 4000.0  0  1  0  2  0  0  0
30. NCO              G 0  42.01725  200.0 6000.0  0  1  0  1  1  0  0
31. CNO              G 0  42.01725  300.0 4000.0  0  1  0  1  1  0  0
32. HNCO             G 0  43.02522  300.0 5000.0  0  1  1  1  1  0  0
33. HOCN             G 0  43.02522  300.0 5000.0  0  1  1  1  1  0  0
34. HCNO             G 0  43.02522  300.0 5000.0  0  1  1  1  1  0  0
35. NO3              G 0  62.00490  300.0 5000.0  0  0  0  1  3  0  0
36. HNO3             G 0  63.01287  300.0 5000.0  0  0  1  1  3  0  0
37. H2CN             G 0  28.03379  300.0 4000.0  0  1  2  1  0  0  0
38. H2CNH            G 0  29.04176  300.0 4000.0  0  1  3  1  0  0  0
39. H2CNO            G 0  44.03319  300.0 4000.0  0  1  2  1  1  0  0
40. H2CNNO           G 0  58.03989  300.0 4000.0  0  1  2  2  1  0  0
41. H2CNNO2          G 0  74.03929  300.0 4000.0  0  1  2  2  2  0  0
42. RDX              G 0 222.11787  300.0 4000.0  0  3  6  6  6  0  0
43. RDXR             G 0 176.11237  300.0 4000.0  0  3  6  5  4  0  0
44. RDXRO            G 0 176.11237  300.0 4000.0  0  3  6  5  4  0  0
45. HNC              G 0  27.02582  300.0 5000.0  0  1  1  1  0  0  0
46. H2COHNNO2        G 0  91.04666  300.0 4000.0  0  1  3  2  3  0  0
47. C                G 0  12.01115  300.0 5000.0  0  1  0  0  0  0  0
48. CH               G 0  13.01912  300.0 5000.0  0  1  1  0  0  0  0
49. CH2              G 0  14.02709  250.0 4000.0  0  1  2  0  0  0  0
50. CH2(S)           G 0  14.02709  300.0 4000.0  0  1  2  0  0  0  0
51. CH3              G 0  15.03506  300.0 5000.0  0  1  3  0  0  0  0
52. CH4              G 0  16.04303  300.0 5000.0  0  1  4  0  0  0  0
53. CH2OH            G 0  31.03446  250.0 4000.0  0  1  3  0  1  0  0
54. CH3O             G 0  31.03446  300.0 3000.0  0  1  3  0  1  0  0
55. CH3OH            G 0  32.04243  300.0 5000.0  0  1  4  0  1  0  0
56. C2H3             G 0  27.04621  300.0 5000.0  0  2  3  0  0  0  0
57. C2H2             G 0  26.03824  300.0 5000.0  0  2  2  0  0  0  0
58. C2H              G 0  25.03027  300.0 5000.0  0  2  1  0  0  0  0
59. C2H4             G 0  28.05418  300.0 5000.0  0  2  4  0  0  0  0
60. C2H5             G 0  29.06215  300.0 5000.0  0  2  5  0  0  0  0
61. C2H6             G 0  30.07012  300.0 4000.0  0  2  6  0  0  0  0
62. HCCO             G 0  41.02967  300.0 4000.0  0  2  1  0  1  0  0
63. CH2CO            G 0  42.03764  300.0 5000.0  0  2  2  0  1  0  0
64. HCCOH            G 0  42.03764  300.0 4000.0  0  2  2  0  1  0  0
65. HCNN             G 0  41.03252  300.0 5000.0  0  1  1  2  0  0  0
66. C3H7             G 0  43.08924  300.0 5000.0  0  3  7  0  0  0  0
67. C3H8             G 0  44.09721  300.0 5000.0  0  3  8  0  0  0  0
68. CH2CHO           G 0  43.04561  300.0 5000.0  0  2  3  0  1  0  0
69. CH3CHO           G 0  44.05358  200.0 6000.0  0  2  4  0  1  0  0
70. C(S)             S 0  12.01115  300.0 5000.0  0  1  0  0  0  0  0
71. C4H6             G 0  54.09242  300.0 5000.0  0  4  6  0  0  0  0
72. N2H2             G 0  30.02934  300.0 5000.0  0  0  2  2  0  0  0
73. N2H3             G 0  31.03731  300.0 5000.0  0  0  3  2  0  0  0
74. N2H4             G 0  32.04528  300.0 5000.0  0  0  4  2  0  0  0
75. BTTN             G 0 241.11509  200.0 6000.0  0  4  7  3  9  0  0
76. HOCO             G 0  45.01792  300.0 4000.0  0  1  1  0  2  0  0
77. HNNO             G 0  45.02077  300.0 4000.0  0  0  1  2  1  0  0
78. ADN(G)           G 0 124.05628  300.0 5000.0  0  0  4  4  4  0  0
79. HN3O4            G 0 107.02567  300.0 5000.0  0  0  1  3  4  0  0
80. HNNO2            G 0  61.02017  300.0 5000.0  0  0  1  2  2  0  0
81. H2NNO            G 0  46.02874  300.0 4000.0  0  0  2  2  1  0  0
82. H2NO             G 0  32.02204  300.0 4000.0  0  0  2  1  1  0  0
83. HNNH             G 0  30.02934  300.0 6000.0  0  0  2  2  0  0  0
84. H2NOH            G 0  33.03001  300.0 4000.0  0  0  3  1  1  0  0
85. CLO              G 0  51.45240  300.0 5000.0  0  0  0  0  1  1  0
86. CLO2             G 0  67.45180  300.0 5000.0  0  0  0  0  2  1  0
87. CLO3             G 0  83.45120  300.0 4000.0  0  0  0  0  3  1  0
88. CLO4             G 0  99.45060  300.0 4000.0  0  0  0  0  4  1  0
89. CL               G 0  35.45300  300.0 5000.0  0  0  0  0  0  1  0
```

```
 90. CLOH             G 0  52.46037  300.0 5000.0  0  0  1  0  1  1  0
 91. HCL              G 0  36.46097  300.0 5000.0  0  0  1  0  0  1  0
 92. HCLO4            G 0 100.45857  300.0 4000.0  0  0  1  0  4  1  0
 93. NOCL             G 0  65.45910  300.0 5000.0  0  0  0  1  1  1  0
 94. CL2              G 0  70.90600  300.0 5000.0  0  0  0  0  0  2  0
 95. CLOO             G 0  67.45180  300.0 4000.0  0  0  0  0  2  1  0
 96. CL2O             G 0  86.90540  300.0 5000.0  0  0  0  0  1  2  0
 97. HCLO2            G 0  68.45977  300.0 4000.0  0  0  1  0  2  1  0
 98. HCLO3            G 0  84.45917  300.0 4000.0  0  0  1  0  3  1  0
 99. HOOCLO2          G 0 100.45857  300.0 4000.0  0  0  1  0  4  1  0
100. CLNO2            G 0  81.45850  300.0 5000.0  0  0  0  1  2  1  0
101. CLONO2           G 0  97.45790  300.0 5000.0  0  0  0  1  3  1  0
102. CLOCL            G 0  86.90540  300.0 5000.0  0  0  0  0  1  2  0
103. CLOOCL           G 0 102.90480  300.0 5000.0  0  0  0  0  2  2  0
104. CLOCLO           G 0 102.90480  300.0 5000.0  0  0  0  0  2  2  0
105. CLOCLOO          G 0 118.90420  300.0 5000.0  0  0  0  0  3  2  0
106. O3               G 0  47.99820  300.0 5000.0  0  0  0  0  3  0  0
-------------------------------------------------------------------------------


                                                     (k = A T**b exp(-E/RT))
     REACTIONS CONSIDERED                              A        b        E

  1. H2+M=H+H+M                                     4.57E+19   -1.40   104000.0
        H2               Enhanced by    2.500E+00
        H2O              Enhanced by    1.200E+01
        CO               Enhanced by    1.900E+00
        CO2              Enhanced by    3.800E+00
  2. O+H2O=OH+OH                                    2.97E+06    2.02    13400.0
  3. O+H2=H+OH                                      5.06E+04    2.67     6290.0
  4. O+O+M=O2+M                                     6.17E+15   -0.50        0.0
        H2               Enhanced by    2.500E+00
        H2O              Enhanced by    1.200E+01
        CO               Enhanced by    1.900E+00
        CO2              Enhanced by    3.800E+00
  5. H+O2=O+OH                                      1.94E+14    0.00    16440.0
  6. H+O2(+M)=HO2(+M)                               4.52E+13    0.00        0.0
     Low pressure limit:  0.67000E+20 -0.14200E+01  0.00000E+00
     TROE centering:      0.10000E+01  0.10000E-89  0.10000E+91
        H2               Enhanced by    2.500E+00
        H2O              Enhanced by    1.200E+01
        CO               Enhanced by    1.900E+00
        CO2              Enhanced by    3.800E+00
  7. H+O+M=OH+M                                     4.72E+18   -1.00        0.0
        H2               Enhanced by    2.500E+00
        H2O              Enhanced by    1.200E+01
        CO               Enhanced by    1.900E+00
        CO2              Enhanced by    3.800E+00
  8. OH+H2=H2O+H                                    2.16E+08    1.51     3430.0
  9. OH+H+M=H2O+M                                   2.21E+22   -2.00        0.0
        H2               Enhanced by    2.500E+00
        H2O              Enhanced by    1.200E+01
        CO               Enhanced by    1.900E+00
        CO2              Enhanced by    3.800E+00
 10. HO2+O=O2+OH                                    1.75E+13    0.00     -397.0
 11. HO2+H=H2+O2                                    6.62E+13    0.00     2130.0
 12. HO2+H=OH+OH                                    1.69E+14    0.00      874.0
 13. HO2+OH=H2O+O2                                  1.90E+16   -1.00        0.0
 14. HO2+HO2=H2O2+O2                                4.20E+14    0.00    11980.0
     Declared duplicate reaction...
 15. HO2+HO2=H2O2+O2                                1.30E+11    0.00    -1629.0
     Declared duplicate reaction...
 16. H2O2(+M)=OH+OH(+M)                             2.95E+14    0.00    48460.0
     Low pressure limit:  0.12000E+18  0.00000E+00  0.45500E+05
     TROE centering:      0.50000E+00  0.10000E-89  0.10000E+91
 17. H2O2+O=OH+HO2                                  9.64E+06    2.00     3970.0
 18. H2O2+H=H2O+OH                                  1.00E+13    0.00     3590.0
 19. H2O2+H=HO2+H2                                  4.82E+13    0.00     7950.0
 20. H2O2+OH=H2O+HO2                                1.00E+12    0.00        0.0
     Declared duplicate reaction...
```

```
21. H2O2+OH=H2O+HO2                                5.80E+14    0.00      9557.0
    Declared duplicate reaction...
22. CH2O+O2=HCO+HO2                                2.05E+13    0.00     38920.0
23. CH2O+O=HCO+OH                                  1.81E+13    0.00      3078.0
24. CH2O+H=HCO+H2                                  1.26E+08    1.62      2163.0
25. CH2O+OH=HCO+H2O                                3.43E+09    1.18      -447.0
26. CH2O+HO2=HCO+H2O2                              1.99E+12    0.00     11660.0
27. HCO+M=H+CO+M                                   1.85E+17   -1.00     17000.0
       H2               Enhanced by    1.890E+00
       H2O              Enhanced by    1.200E+01
       CO               Enhanced by    1.900E+00
       CO2              Enhanced by    3.800E+00
28. HCO+O2=CO+HO2                                  7.58E+12    0.00       406.0
29. HCO+O=CO+OH                                    3.00E+13    0.00         0.0
30. HCO+O=CO2+H                                    3.00E+13    0.00         0.0
31. HCO+H=CO+H2                                    7.23E+13    0.00         0.0
32. HCO+OH=CO+H2O                                  3.00E+13    0.00         0.0
33. HCO+HO2=CO2+OH+H                               3.00E+13    0.00         0.0
34. CO+O(+M)=CO2(+M)                               1.80E+10    0.00      2380.0
    Low pressure limit:  0.13500E+25 -0.27880E+01  0.41910E+04
    TROE centering:      0.10000E+01  0.10000E-89  0.10000E+91
       N2               Enhanced by    1.330E+00
       H2               Enhanced by    2.500E+00
       H2O              Enhanced by    1.200E+01
       CO               Enhanced by    1.900E+00
       CO2              Enhanced by    3.800E+00
35. CO+O2=CO2+O                                    2.53E+12    0.00     47700.0
36. CO+OH=CO2+H                                    1.50E+07    1.30      -765.0
37. CO+HO2=CO2+OH                                  5.80E+13    0.00     22930.0
38. N+H2=H+NH                                      1.60E+14    0.00     25140.0
39. N+O2=NO+O                                      6.40E+09    1.00      6280.0
40. N+OH=NO+H                                      3.80E+13    0.00         0.0
41. N+HO2=NH+O2                                    1.00E+13    0.00      2000.0
42. N+HO2=NO+OH                                    1.00E+13    0.00      2000.0
43. N+NO=N2+O                                      3.27E+12    0.30         0.0
44. N+NO2=NO+NO                                    4.00E+12    0.00         0.0
45. N+NO2=N2O+O                                    5.00E+12    0.00         0.0
46. N+NO2=N2+O2                                    1.00E+12    0.00         0.0
47. N+HNO=NH+NO                                    1.00E+13    0.00      2000.0
48. N+HNO=N2O+H                                    5.00E+10    0.50      3000.0
49. N+N2O=N2+NO                                    1.00E+13    0.00     19870.0
50. NO+M=N+O+M                                     9.64E+14    0.00    148400.0
       N2               Enhanced by    1.500E+00
       CO2              Enhanced by    2.500E+00
51. NO+O(+M)=NO2(+M)                               1.30E+15   -0.75         0.0
    Low pressure limit:  0.47200E+25 -0.28700E+01  0.15510E+04
    TROE centering:      0.95700E+00  0.10000E-89  0.83320E+04
52. NO+H(+M)=HNO(+M)                               1.52E+15   -0.41         0.0
    Low pressure limit:  0.89600E+20 -0.13200E+01  0.73520E+03
    TROE centering:      0.82000E+00  0.10000E-89  0.10000E+91
53. NO+OH(+M)=HONO(+M)                             1.99E+12   -0.05      -721.0
    Low pressure limit:  0.50800E+24 -0.25100E+01 -0.67560E+02
    TROE centering:      0.62000E+00  0.10000E-89  0.10000E+91
       H2O              Enhanced by    5.000E+00
54. HO2+NO=NO2+OH                                  2.11E+12    0.00      -479.0
55. NO+HCO=HNO+CO                                  7.23E+12    0.00         0.0
56. NO2+O=O2+NO                                    3.91E+12    0.00      -238.0
57. NO2+O(+M)=NO3(+M)                              1.33E+13    0.00         0.0
    Low pressure limit:  0.14900E+29 -0.40800E+01  0.24670E+04
    TROE centering:      0.82600E+00  0.10000E-89  0.31910E+04
58. NO2+H=NO+OH                                    1.32E+14    0.00       361.6
59. NO2+OH(+M)=HNO3(+M)                            2.41E+13    0.00         0.0
    Low pressure limit:  0.64200E+33 -0.54900E+01  0.23500E+04
    TROE centering:      0.83700E+00  0.10000E-89  0.16570E+04
60. NO2+HCO=CO+HONO                                1.24E+23   -3.29      2354.0
61. NO2+HCO=H+CO2+NO                               8.39E+15   -0.75      1927.0
62. NO2+CO=CO2+NO                                  9.03E+13    0.00     33780.0
63. NO2+NO2=NO3+NO                                 9.64E+09    0.73     20920.0
64. NO2+NO2=2NO+O2                                 1.63E+12    0.00     26120.0
65. NH+M=N+H+M                                     2.65E+14    0.00     75510.0
66. NH+O2=HNO+O                                    3.89E+13    0.00     17890.0
```

```
 67. NH+O2=NO+OH                                    7.60E+10    0.00     1530.0
 68. NH+O=NO+H                                      5.50E+13    0.00        0.0
 69. NH+O=N+OH                                      3.72E+13    0.00        0.0
 70. NH+OH=HNO+H                                    2.00E+13    0.00        0.0
 71. NH+OH=N+H2O                                    5.00E+11    0.50     2000.0
 72. NH+N=N2+H                                      3.00E+13    0.00        0.0
 73. NH+NO=N2O+H                                    2.94E+14   -0.40        0.0
     Declared duplicate reaction...
 74. NH+NO=N2O+H                                   -2.16E+13   -0.23        0.0
     Declared duplicate reaction...
 75. NH+NO=N2+OH                                    2.16E+13   -0.23        0.0
 76. NH+NO2=NO+HNO                                  1.00E+11    0.50     4000.0
 77. NH+NO2=N2O+OH                                  1.00E+13    0.00        0.0
 78. NH+NH=N2+H+H                                   5.10E+13    0.00        0.0
 79. NH2+O2=HNO+OH                                  1.78E+12    0.00    14900.0
 80. NH2+O=HNO+H                                    6.63E+14   -0.50        0.0
 81. NH2+O=NH+OH                                    6.75E+12    0.00        0.0
 82. NH2+H=NH+H2                                    6.92E+13    0.00     3650.0
 83. NH2+OH=NH+H2O                                  4.00E+06    2.00     1000.0
 84. NH2+N=N2+2H                                    7.20E+13    0.00        0.0
 85. NH2+NO=NNH+OH                                  2.80E+13   -0.55        0.0
 86. NH2+NO=N2+H2O                                  1.30E+16   -1.25        0.0
     Declared duplicate reaction...
 87. NH2+NO=N2+H2O                                 -2.80E+13   -0.55        0.0
     Declared duplicate reaction...
 88. NH2+NO=N2O+H2                                  5.00E+13    0.00    24640.0
 89. NH2+NO=HNO+NH                                  1.00E+13    0.00    40000.0
 90. NH2+NO2=N2O+H2O                                3.28E+18   -2.20        0.0
 91. NH3+M=NH2+H+M                                  2.20E+16    0.00    93470.0
 92. NH3+O=NH2+OH                                   9.40E+06    1.94     6460.0
 93. NH3+H=NH2+H2                                   6.40E+05    2.39    10170.0
 94. NH3+OH=NH2+H2O                                 2.04E+06    2.04      566.0
 95. NH3+HO2=NH2+H2O2                               3.00E+11    0.00    22000.0
 96. NH2+HO2=NH3+O2                                 1.00E+13    0.00        0.0
 97. NH2+NH2=NH3+NH                                 5.00E+13    0.00    10000.0
 98. NNH+M=N2+H+M                                   1.00E+14    0.00     3000.0
 99. NNH+O=N2O+H                                    1.00E+14    0.00        0.0
100. NNH+H=N2+H2                                    1.00E+14    0.00        0.0
101. NNH+OH=N2+H2O                                  5.00E+13    0.00        0.0
102. NNH+NO=N2+HNO                                  5.00E+13    0.00        0.0
103. NNH+NH=N2+NH2                                  5.00E+13    0.00        0.0
104. NNH+NH2=N2+NH3                                 5.00E+13    0.00        0.0
105. HNO+O2=NO+HO2                                  1.00E+13    0.00    25000.0
106. HNO+O=OH+NO                                    1.81E+13    0.00        0.0
107. HNO+H=H2+NO                                    1.81E+13    0.00      993.5
108. HNO+OH=H2O+NO                                  1.00E+13    0.00      993.5
109. HNO+NO=N2O+OH                                  2.00E+12    0.00    26000.0
110. HNO+NO2=HONO+NO                                6.02E+11    0.00     1987.0
111. HNO+NH2=NO+NH3                                 2.00E+13    0.00     1000.0
112. HNO+HNO=H2O+N2O                                8.51E+08    0.00     3080.0
113. HONO+O=OH+NO2                                  1.20E+13    0.00     5961.0
114. HONO+H=H2+NO2                                  1.20E+13    0.00     7352.0
115. HONO+OH=H2O+NO2                                1.26E+10    1.00      135.1
116. HCN+OH=H+HOCN                                  5.85E+04    2.40    12500.0
117. HCN+OH=H+HNCO                                  1.98E-03    4.00     1000.0
118. HCN+OH=NH2+CO                                  7.83E-04    4.00     4000.0
119. HNC+O=NH+CO                                    2.89E+12    0.00        0.0
120. HNC+O=H+NCO                                    1.60E+01    3.08     -224.0
121. HNC+OH=HNCO+H                                  2.80E+13    0.00     3700.0
122. HNC+OH=CN+H2O                                  1.50E+12    0.00     7680.0
123. HNC+NO2=HNCO+NO                                1.00E+12    0.00    32000.0
124. HNC+CN=C2N2+H                                  1.00E+13    0.00        0.0
125. N2O(+M)=N2+O(+M)                               7.91E+10    0.00    56020.0
     Low pressure limit:  0.91300E+15  0.00000E+00  0.57690E+05
        H2O             Enhanced by    7.500E+00
        NO              Enhanced by    2.000E+00
        CO              Enhanced by    2.000E+00
        CO2             Enhanced by    3.000E+00
        HCN             Enhanced by    3.000E+00
126. N2O+O=O2+N2                                    1.00E+14    0.00    28000.0
127. N2O+O=2NO                                      1.00E+14    0.00    28000.0
```

```
128. N2O+H=N2+OH                                    2.53E+10    0.00      4550.0
     Declared duplicate reaction...
129. N2O+H=N2+OH                                    2.23E+14    0.00     16750.0
     Declared duplicate reaction...
130. N2O+OH=HO2+N2                                  2.00E+12    0.00     40000.0
131. N2O+CO=N2+CO2                                  5.01E+13    0.00     44000.0
132. CN+O2=NCO+O                                    7.50E+12    0.00      -389.0
133. CN+O=CO+N                                      1.80E+13    0.00         0.0
134. CN+OH=NCO+H                                    4.22E+13    0.00         0.0
135. CN+HCO=HCN+CO                                  6.02E+13    0.00         0.0
136. CN+CO2=CO+NCO                                  3.67E+06    2.16     26900.0
137. CN+NO=NCO+N                                    9.64E+13    0.00     42120.0
138. CN+NO2=NCO+NO                                  1.59E+13    0.00     -1133.0
139. CN+HNO=HCN+NO                                  1.81E+13    0.00         0.0
140. CN+HONO=HCN+NO2                                1.20E+13    0.00         0.0
141. CN+N2O=NCN+NO                                  3.85E+03    2.60      3696.0
142. CN+CN(+M)=C2N2(+M)                             5.66E+12    0.00         0.0
     Low pressure limit:  0.34200E+26 -0.26100E+01  0.00000E+00
     TROE centering:      0.50000E+00  0.10000E-89  0.10000E+91
143. C2N2+O=NCO+CN                                  4.57E+12    0.00      8880.0
144. C2N2+OH=HOCN+CN                                1.86E+11    0.00      2900.0
145. NCN+O2=NO+NCO                                  1.00E+14    0.00         0.0
146. NCN+O=CN+NO                                    1.00E+14    0.00         0.0
147. NCN+H=HCN+N                                    1.00E+14    0.00         0.0
148. NCN+OH=HCN+NO                                  5.00E+13    0.00         0.0
149. NCO+M=N+CO+M                                   3.10E+16   -0.50     48300.0
        N2                Enhanced by    1.500E+00
150. NCO+H2=HNCO+H                                  7.60E+02    3.00      4000.0
151. NCO+O2=NO+CO2                                  2.00E+12    0.00     20000.0
152. NCO+O=CO+NO                                    2.00E+13    0.00         0.0
153. NCO+H=NH+CO                                    5.36E+13    0.00         0.0
154. NCO+OH=NO+CO+H                                 1.00E+13    0.00         0.0
155. NCO+OH=NO+HCO                                  5.00E+12    0.00     15000.0
156. NCO+CH2O=HNCO+HCO                              6.02E+12    0.00         0.0
157. NCO+HCO=HNCO+CO                                3.61E+13    0.00         0.0
158. NCO+N=N2+CO                                    2.00E+13    0.00         0.0
159. NCO+NO=N2O+CO                                  6.20E+17   -1.73       763.0
160. NCO+NO=CO2+N2                                  7.80E+17   -1.73       763.0
161. NCO+NO2=CO+2NO                                 1.39E+13    0.00         0.0
162. NCO+NO2=CO2+N2O                                4.17E+12    0.00         0.0
163. NCO+HNO=HNCO+NO                                1.81E+13    0.00         0.0
164. NCO+HONO=HNCO+NO2                              3.61E+12    0.00         0.0
165. NCO+N2O=N2+NO+CO                               9.03E+13    0.00     27820.0
166. NCO+CN=NCN+CO                                  1.81E+13    0.00         0.0
167. NCO+NCO=N2+2CO                                 1.00E+13    0.00         0.0
168. CNO+O=CO+NO                                    1.00E+13    0.00         0.0
169. CNO+NO2=CO+2NO                                 1.00E+13    0.00         0.0
170. CNO+N2O=N2+CO+NO                               1.00E+12    0.00     15000.0
171. HNCO(+M)=NH+CO(+M)                             6.00E+13    0.00     99800.0
     Low pressure limit:  0.21700E+29 -0.31000E+01  0.10190E+06
     TROE centering:      0.93800E+00  0.10000E-89  0.33040E+04
172. HNCO+O2=HNO+CO2                                1.00E+12    0.00     35000.0
173. HNCO+O=CO2+NH                                  9.64E+07    1.41      8524.0
174. HNCO+O=OH+NCO                                  6.67E-04    4.55      1780.0
175. HNCO+O=HNO+CO                                  1.58E+08    1.57     44300.0
176. HNCO+H=NH2+CO                                  2.20E+07    1.70      3800.0
177. HNCO+OH=H2O+NCO                                6.38E+05    2.00      2563.0
178. HNCO+HO2=NCO+H2O2                              3.00E+11    0.00     29000.0
179. HNCO+NH=NH2+NCO                                3.00E+13    0.00     23700.0
180. HNCO+NH2=NH3+NCO                               5.00E+12    0.00      6200.0
181. HNCO+CN=HCN+NCO                                1.51E+13    0.00         0.0
182. HCNO+O=HCO+NO                                  1.00E+12    0.00      9000.0
183. HCNO+OH=HCO+HNO                                1.00E+13    0.00      5000.0
184. HCNO+OH=CNO+H2O                                1.00E+12    0.00      2000.0
185. HCNO+CN=HCN+CNO                                1.00E+12    0.00      2000.0
186. HOCN+O=NCO+OH                                  1.50E+04    2.64      4000.0
187. HOCN+H=HNCO+H                                  2.00E+07    2.00      2000.0
188. HOCN+OH=NCO+H2O                                6.40E+05    2.00      2560.0
189. H2CN+CH2O=H2CNH+HCO                            1.00E+11    0.00     14000.0
190. H2CN+NO=HCN+HNO                                1.00E+11    0.00      3000.0
191. H2CN+NO2=HCN+HONO                              1.00E+11    0.00      1000.0
```

```
192. H2CN+NO2=H2CNO+NO                              1.00E+11    0.00     3000.0
193. H2CN+HNO=H2CNH+NO                              1.00E+11    0.00     4000.0
194. H2CN+HONO=H2CNH+NO2                            1.00E+11    0.00    12000.0
195. H2CN+N2O=H2CNO+N2                              1.00E+11    0.00     3000.0
196. H2CNH+OH=H2CN+H2O                              1.00E+13    0.00        0.0
197. H2CNH+CN=H2CN+HCN                              1.00E+13    0.00        0.0
198. H2CNO+M=HCNO+H                                 1.00E+16    0.00    50000.0
199. H2CNO+OH=HCNO+H2O                              1.00E+13    0.00        0.0
200. H2CNO+NO=HCNO+HNO                              1.00E+12    0.00    25000.0
201. H2CNO+NO2=HCNO+HONO                            1.00E+12    0.00     2000.0
202. H2CNO+NO2=CH2O+NO+NO                           1.00E+12    0.00        0.0
203. H2CNO+HNO=H2CN+HONO                            1.00E+12    0.00     2000.0
204. H2CNNO(+M)=H2CN+NO(+M)                         1.00E+16    0.00     2000.0
     Low pressure limit:  0.76900E+17  0.00000E+00  0.15000E+05
205. H2CNNO2(+M)=H2CN+NO2(+M)                       2.46E+15    0.00    34200.0
     Low pressure limit:  0.23500E+57 -0.13260E+02  0.24550E+05
206. H2CNNO2(+M)=HONO+HCN(+M)                       6.21E+12    0.00    32500.0
     Low pressure limit:  0.28700E+40 -0.93700E+01  0.17800E+05
207. H2CNNO2(+M)=CH2O+N2O(+M)                       4.52E+11    0.00    38400.0
     Low pressure limit:  0.13800E+05  0.00000E+00  0.12100E+05
208. RDX(+M)=RDXR+NO2(+M)                           2.00E+16    0.00    45000.0
     Low pressure limit:  0.15700E+18  0.00000E+00  0.28000E+05
209. RDX+H=RDXR+HONO                                1.00E+13    0.00     5000.0
210. RDX+OH=>2H2CNNO2+H2COHNNO2                     1.00E+13    0.00     5000.0
211. H2COHNNO2=>HCN+NO2+H2O                         1.00E+16    0.00        0.0
212. RDXR(+M)=>RDXRO(+M)                            1.00E+16    0.00    23000.0
     Low pressure limit:  0.76900E+17  0.00000E+00  0.18000E+05
213. RDXRO(+M)=>2H2CNNO2+H2CN(+M)                   1.00E+16    0.00    23000.0
     Low pressure limit:  0.76900E+17  0.00000E+00  0.18000E+05
214. O+CH<=>H+CO                                    5.70E+13    0.00        0.0
215. O+CH2<=>H+HCO                                  8.00E+13    0.00        0.0
216. O+CH2(S)<=>H2+CO                               1.50E+13    0.00        0.0
217. O+CH2(S)<=>H+HCO                               1.50E+13    0.00        0.0
218. O+CH3<=>H+CH2O                                 5.06E+13    0.00        0.0
219. O+CH4<=>OH+CH3                                 1.02E+09    1.50     8600.0
220. O+CH2OH<=>OH+CH2O                              1.00E+13    0.00        0.0
221. O+CH3O<=>OH+CH2O                               1.00E+13    0.00        0.0
222. O+CH3OH<=>OH+CH2OH                             3.88E+05    2.50     3100.0
223. O+CH3OH<=>OH+CH3O                              1.30E+05    2.50     5000.0
224. O+C2H<=>CH+CO                                  5.00E+13    0.00        0.0
225. O+C2H2<=>H+HCCO                                1.35E+07    2.00     1900.0
226. O+C2H2<=>OH+C2H                                4.60E+19   -1.41    28950.0
227. O+C2H2<=>CO+CH2                                6.94E+06    2.00     1900.0
228. O+C2H3<=>H+CH2CO                               3.00E+13    0.00        0.0
229. O+C2H4<=>CH3+HCO                               1.25E+07    1.83      220.0
230. O+C2H5<=>CH3+CH2O                              2.24E+13    0.00        0.0
231. O+C2H6<=>OH+C2H5                               8.98E+07    1.92     5690.0
232. O+HCCO<=>H+2CO                                 1.00E+14    0.00        0.0
233. O+CH2CO<=>OH+HCCO                              1.00E+13    0.00     8000.0
234. O+CH2CO<=>CH2+CO2                              1.75E+12    0.00     1350.0
235. H+2O2<=>HO2+O2                                 2.08E+19   -1.24        0.0
236. 2H+H2<=>2H2                                    9.00E+16   -0.60        0.0
237. 2H+H2O<=>H2+H2O                                6.00E+19   -1.25        0.0
238. 2H+CO2<=>H2+CO2                                5.50E+20   -2.00        0.0
239. H+HO2<=>O+H2O                                  3.97E+12    0.00      671.0
240. H+CH<=>C+H2                                    1.65E+14    0.00        0.0
241. H+CH2(+M)<=>CH3(+M)                            6.00E+14    0.00        0.0
     Low pressure limit:  0.10400E+27 -0.27600E+01  0.16000E+04
     TROE centering:      0.56200E+00  0.91000E+02  0.58360E+04  0.85520E+04
        H2               Enhanced by    2.000E+00
        H2O              Enhanced by    6.000E+00
        CH4              Enhanced by    2.000E+00
        CO               Enhanced by    1.500E+00
        CO2              Enhanced by    2.000E+00
        C2H6             Enhanced by    3.000E+00
        AR               Enhanced by    7.000E-01
242. H+CH2(S)<=>CH+H2                               3.00E+13    0.00        0.0
243. H+CH3(+M)<=>CH4(+M)                            1.39E+16   -0.53      536.0
     Low pressure limit:  0.26200E+34 -0.47600E+01  0.24400E+04
     TROE centering:      0.78300E+00  0.74000E+02  0.29410E+04  0.69640E+04
        H2               Enhanced by    2.000E+00
```

```
        H2O              Enhanced by    6.000E+00
        CH4              Enhanced by    3.000E+00
        CO               Enhanced by    1.500E+00
        CO2              Enhanced by    2.000E+00
        C2H6             Enhanced by    3.000E+00
        AR               Enhanced by    7.000E-01
244. H+CH4<=>CH3+H2                                 6.60E+08    1.62    10840.0
245. H+CH2O(+M)<=>CH2OH(+M)                         5.40E+11    0.45     3600.0
     Low pressure limit:  0.12700E+33 -0.48200E+01  0.65300E+04
     TROE centering:      0.71870E+00  0.10300E+03  0.12910E+04  0.41600E+04
        H2               Enhanced by    2.000E+00
        H2O              Enhanced by    6.000E+00
        CH4              Enhanced by    2.000E+00
        CO               Enhanced by    1.500E+00
        CO2              Enhanced by    2.000E+00
        C2H6             Enhanced by    3.000E+00
246. H+CH2O(+M)<=>CH3O(+M)                          5.40E+11    0.45     2600.0
     Low pressure limit:  0.22000E+31 -0.48000E+01  0.55600E+04
     TROE centering:      0.75800E+00  0.94000E+02  0.15550E+04  0.42000E+04
        H2               Enhanced by    2.000E+00
        H2O              Enhanced by    6.000E+00
        CH4              Enhanced by    2.000E+00
        CO               Enhanced by    1.500E+00
        CO2              Enhanced by    2.000E+00
        C2H6             Enhanced by    3.000E+00
247. H+CH2OH(+M)<=>CH3OH(+M)                        1.06E+12    0.50       86.0
     Low pressure limit:  0.43600E+32 -0.46500E+01  0.50800E+04
     TROE centering:      0.60000E+00  0.10000E+03  0.90000E+05  0.10000E+05
        H2               Enhanced by    2.000E+00
        H2O              Enhanced by    6.000E+00
        CH4              Enhanced by    2.000E+00
        CO               Enhanced by    1.500E+00
        CO2              Enhanced by    2.000E+00
        C2H6             Enhanced by    3.000E+00
248. H+CH2OH<=>H2+CH2O                              2.00E+13    0.00        0.0
249. H+CH2OH<=>OH+CH3                               1.65E+11    0.65     -284.0
250. H+CH2OH<=>CH2(S)+H2O                           3.28E+13   -0.09      610.0
251. H+CH3O(+M)<=>CH3OH(+M)                         2.43E+12    0.52       50.0
     Low pressure limit:  0.46600E+42 -0.74400E+01  0.14080E+05
     TROE centering:      0.70000E+00  0.10000E+03  0.90000E+05  0.10000E+05
        H2               Enhanced by    2.000E+00
        H2O              Enhanced by    6.000E+00
        CH4              Enhanced by    2.000E+00
        CO               Enhanced by    1.500E+00
        CO2              Enhanced by    2.000E+00
        C2H6             Enhanced by    3.000E+00
252. H+CH3O<=>H+CH2OH                               4.15E+07    1.63     1924.0
253. H+CH3O<=>H2+CH2O                               2.00E+13    0.00        0.0
254. H+CH3O<=>OH+CH3                                1.50E+12    0.50     -110.0
255. H+CH3O<=>CH2(S)+H2O                            2.62E+14   -0.23     1070.0
256. H+CH3OH<=>CH2OH+H2                             1.70E+07    2.10     4870.0
257. H+CH3OH<=>CH3O+H2                              4.20E+06    2.10     4870.0
258. H+C2H(+M)<=>C2H2(+M)                           1.00E+17   -1.00        0.0
     Low pressure limit:  0.37500E+34 -0.48000E+01  0.19000E+04
     TROE centering:      0.64640E+00  0.13200E+03  0.13150E+04  0.55660E+04
        H2               Enhanced by    2.000E+00
        H2O              Enhanced by    6.000E+00
        CH4              Enhanced by    2.000E+00
        CO               Enhanced by    1.500E+00
        CO2              Enhanced by    2.000E+00
        C2H6             Enhanced by    3.000E+00
        AR               Enhanced by    7.000E-01
259. H+C2H2(+M)<=>C2H3(+M)                          5.60E+12    0.00     2400.0
     Low pressure limit:  0.38000E+41 -0.72700E+01  0.72200E+04
     TROE centering:      0.75070E+00  0.98500E+02  0.13020E+04  0.41670E+04
        H2               Enhanced by    2.000E+00
        H2O              Enhanced by    6.000E+00
        CH4              Enhanced by    2.000E+00
        CO               Enhanced by    1.500E+00
        CO2              Enhanced by    2.000E+00
        C2H6             Enhanced by    3.000E+00
```

```
        AR               Enhanced by    7.000E-01
260. H+C2H3(+M)<=>C2H4(+M)                          6.08E+12    0.27       280.0
     Low pressure limit:  0.14000E+31 -0.38600E+01  0.33200E+04
     TROE centering:      0.78200E+00  0.20750E+03  0.26630E+04  0.60950E+04
        H2               Enhanced by    2.000E+00
        H2O              Enhanced by    6.000E+00
        CH4              Enhanced by    2.000E+00
        CO               Enhanced by    1.500E+00
        CO2              Enhanced by    2.000E+00
        C2H6             Enhanced by    3.000E+00
        AR               Enhanced by    7.000E-01
261. H+C2H3<=>H2+C2H2                               3.00E+13    0.00         0.0
262. H+C2H4(+M)<=>C2H5(+M)                          5.40E+11    0.45      1820.0
     Low pressure limit:  0.60000E+42 -0.76200E+01  0.69700E+04
     TROE centering:      0.97530E+00  0.21000E+03  0.98400E+03  0.43740E+04
        H2               Enhanced by    2.000E+00
        H2O              Enhanced by    6.000E+00
        CH4              Enhanced by    2.000E+00
        CO               Enhanced by    1.500E+00
        CO2              Enhanced by    2.000E+00
        C2H6             Enhanced by    3.000E+00
        AR               Enhanced by    7.000E-01
263. H+C2H4<=>C2H3+H2                               1.33E+06    2.53     12240.0
264. H+C2H5(+M)<=>C2H6(+M)                          5.21E+17   -0.99      1580.0
     Low pressure limit:  0.19900E+42 -0.70800E+01  0.66850E+04
     TROE centering:      0.84220E+00  0.12500E+03  0.22190E+04  0.68820E+04
        H2               Enhanced by    2.000E+00
        H2O              Enhanced by    6.000E+00
        CH4              Enhanced by    2.000E+00
        CO               Enhanced by    1.500E+00
        CO2              Enhanced by    2.000E+00
        C2H6             Enhanced by    3.000E+00
        AR               Enhanced by    7.000E-01
265. H+C2H5<=>H2+C2H4                               2.00E+12    0.00         0.0
266. H+C2H6<=>C2H5+H2                               1.15E+08    1.90      7530.0
267. H+HCCO<=>CH2(S)+CO                             1.00E+14    0.00         0.0
268. H+CH2CO<=>HCCO+H2                              5.00E+13    0.00      8000.0
269. H+CH2CO<=>CH3+CO                               1.13E+13    0.00      3428.0
270. H+HCCOH<=>H+CH2CO                              1.00E+13    0.00         0.0
271. OH+C<=>H+CO                                    5.00E+13    0.00         0.0
272. OH+CH<=>H+HCO                                  3.00E+13    0.00         0.0
273. OH+CH2<=>H+CH2O                                2.00E+13    0.00         0.0
274. OH+CH2<=>CH+H2O                                1.13E+07    2.00      3000.0
275. OH+CH2(S)<=>H+CH2O                             3.00E+13    0.00         0.0
276. OH+CH3(+M)<=>CH3OH(+M)                         2.79E+18   -1.43      1330.0
     Low pressure limit:  0.40000E+37 -0.59200E+01  0.31400E+04
     TROE centering:      0.41200E+00  0.19500E+03  0.59000E+04  0.63940E+04
        H2               Enhanced by    2.000E+00
        H2O              Enhanced by    6.000E+00
        CH4              Enhanced by    2.000E+00
        CO               Enhanced by    1.500E+00
        CO2              Enhanced by    2.000E+00
        C2H6             Enhanced by    3.000E+00
277. OH+CH3<=>CH2+H2O                               5.60E+07    1.60      5420.0
278. OH+CH3<=>CH2(S)+H2O                            6.44E+17   -1.34      1417.0
279. OH+CH4<=>CH3+H2O                               1.00E+08    1.60      3120.0
280. OH+CH2OH<=>H2O+CH2O                            5.00E+12    0.00         0.0
281. OH+CH3O<=>H2O+CH2O                             5.00E+12    0.00         0.0
282. OH+CH3OH<=>CH2OH+H2O                           1.44E+06    2.00      -840.0
283. OH+CH3OH<=>CH3O+H2O                            6.30E+06    2.00      1500.0
284. OH+C2H<=>H+HCCO                                2.00E+13    0.00         0.0
285. OH+C2H2<=>H+CH2CO                              2.18E-04    4.50     -1000.0
286. OH+C2H2<=>H+HCCOH                              5.04E+05    2.30     13500.0
287. OH+C2H2<=>C2H+H2O                              3.37E+07    2.00     14000.0
288. OH+C2H2<=>CH3+CO                               4.83E-04    4.00     -2000.0
289. OH+C2H3<=>H2O+C2H2                             5.00E+12    0.00         0.0
290. OH+C2H4<=>C2H3+H2O                             3.60E+06    2.00      2500.0
291. OH+C2H6<=>C2H5+H2O                             3.54E+06    2.12       870.0
292. OH+CH2CO<=>HCCO+H2O                            7.50E+12    0.00      2000.0
293. HO2+CH2<=>OH+CH2O                              2.00E+13    0.00         0.0
294. HO2+CH3<=>O2+CH4                               1.00E+12    0.00         0.0
```

```
295. HO2+CH3<=>OH+CH3O                            3.78E+13    0.00         0.0
296. C+O2<=>O+CO                                  5.80E+13    0.00       576.0
297. C+CH2<=>H+C2H                                5.00E+13    0.00         0.0
298. C+CH3<=>H+C2H2                               5.00E+13    0.00         0.0
299. CH+O2<=>O+HCO                                6.71E+13    0.00         0.0
300. CH+H2<=>H+CH2                                1.08E+14    0.00      3110.0
301. CH+H2O<=>H+CH2O                              5.71E+12    0.00      -755.0
302. CH+CH2<=>H+C2H2                              4.00E+13    0.00         0.0
303. CH+CH3<=>H+C2H3                              3.00E+13    0.00         0.0
304. CH+CH4<=>H+C2H4                              6.00E+13    0.00         0.0
305. CH+CO(+M)<=>HCCO(+M)                         5.00E+13    0.00         0.0
     Low pressure limit:  0.26900E+29 -0.37400E+01  0.19360E+04
     TROE centering:      0.57570E+00  0.23700E+03  0.16520E+04  0.50690E+04
        H2               Enhanced by    2.000E+00
        H2O              Enhanced by    6.000E+00
        CH4              Enhanced by    2.000E+00
        CO               Enhanced by    1.500E+00
        CO2              Enhanced by    2.000E+00
        C2H6             Enhanced by    3.000E+00
        AR               Enhanced by    7.000E-01
306. CH+CO2<=>HCO+CO                              1.90E+14    0.00     15792.0
307. CH+CH2O<=>H+CH2CO                            9.46E+13    0.00      -515.0
308. CH+HCCO<=>CO+C2H2                            5.00E+13    0.00         0.0
309. CH2+O2=>OH+H+CO                              5.00E+12    0.00      1500.0
310. CH2+H2<=>H+CH3                               5.00E+05    2.00      7230.0
311. 2CH2<=>H2+C2H2                               1.60E+15    0.00     11944.0
312. CH2+CH3<=>H+C2H4                             4.00E+13    0.00         0.0
313. CH2+CH4<=>2CH3                               2.46E+06    2.00      8270.0
314. CH2+CO(+M)<=>CH2CO(+M)                       8.10E+11    0.50      4510.0
     Low pressure limit:  0.26900E+34 -0.51100E+01  0.70950E+04
     TROE centering:      0.59070E+00  0.27500E+03  0.12260E+04  0.51850E+04
        H2               Enhanced by    2.000E+00
        H2O              Enhanced by    6.000E+00
        CH4              Enhanced by    2.000E+00
        CO               Enhanced by    1.500E+00
        CO2              Enhanced by    2.000E+00
        C2H6             Enhanced by    3.000E+00
        AR               Enhanced by    7.000E-01
315. CH2+HCCO<=>C2H3+CO                           3.00E+13    0.00         0.0
316. CH2(S)+N2<=>CH2+N2                           1.50E+13    0.00       600.0
317. CH2(S)+AR<=>CH2+AR                           9.00E+12    0.00       600.0
318. CH2(S)+O2<=>H+OH+CO                          2.80E+13    0.00         0.0
319. CH2(S)+O2<=>CO+H2O                           1.20E+13    0.00         0.0
320. CH2(S)+H2<=>CH3+H                            7.00E+13    0.00         0.0
321. CH2(S)+H2O(+M)<=>CH3OH(+M)                   4.82E+17   -1.16      1145.0
     Low pressure limit:  0.18800E+39 -0.63600E+01  0.50400E+04
     TROE centering:      0.60270E+00  0.20800E+03  0.39220E+04  0.10180E+05
        H2               Enhanced by    2.000E+00
        H2O              Enhanced by    6.000E+00
        CH4              Enhanced by    2.000E+00
        CO               Enhanced by    1.500E+00
        CO2              Enhanced by    2.000E+00
        C2H6             Enhanced by    3.000E+00
322. CH2(S)+H2O<=>CH2+H2O                         3.00E+13    0.00         0.0
323. CH2(S)+CH3<=>H+C2H4                          1.20E+13    0.00      -570.0
324. CH2(S)+CH4<=>2CH3                            1.60E+13    0.00      -570.0
325. CH2(S)+CO<=>CH2+CO                           9.00E+12    0.00         0.0
326. CH2(S)+CO2<=>CH2+CO2                         7.00E+12    0.00         0.0
327. CH2(S)+CO2<=>CO+CH2O                         1.40E+13    0.00         0.0
328. CH2(S)+C2H6<=>CH3+C2H5                       4.00E+13    0.00      -550.0
329. CH3+O2<=>O+CH3O                              3.56E+13    0.00     30480.0
330. CH3+O2<=>OH+CH2O                             2.31E+12    0.00     20315.0
331. CH3+H2O2<=>HO2+CH4                           2.45E+04    2.47      5180.0
332. 2CH3(+M)<=>C2H6(+M)                          6.77E+16   -1.18       654.0
     Low pressure limit:  0.34000E+42 -0.70300E+01  0.27620E+04
     TROE centering:      0.61900E+00  0.73200E+02  0.11800E+04  0.99990E+04
        H2               Enhanced by    2.000E+00
        H2O              Enhanced by    6.000E+00
        CH4              Enhanced by    2.000E+00
        CO               Enhanced by    1.500E+00
        CO2              Enhanced by    2.000E+00
```

```
        C2H6             Enhanced by    3.000E+00
        AR               Enhanced by    7.000E-01
333. 2CH3<=>H+C2H5                                  6.84E+12    0.10    10600.0
334. CH3+HCO<=>CH4+CO                               2.65E+13    0.00        0.0
335. CH3+CH2O<=>HCO+CH4                             3.32E+03    2.81     5860.0
336. CH3+CH3OH<=>CH2OH+CH4                          3.00E+07    1.50     9940.0
337. CH3+CH3OH<=>CH3O+CH4                           1.00E+07    1.50     9940.0
338. CH3+C2H4<=>C2H3+CH4                            2.27E+05    2.00     9200.0
339. CH3+C2H6<=>C2H5+CH4                            6.14E+06    1.74    10450.0
340. HCO+H2O<=>H+CO+H2O                             1.50E+18   -1.00    17000.0
341. CH2OH+O2<=>HO2+CH2O                            1.80E+13    0.00      900.0
342. CH3O+O2<=>HO2+CH2O                             4.28E-13    7.60    -3530.0
343. C2H+O2<=>HCO+CO                                1.00E+13    0.00     -755.0
344. C2H+H2<=>H+C2H2                                5.68E+10    0.90     1993.0
345. C2H3+O2<=>HCO+CH2O                             4.58E+16   -1.39     1015.0
346. C2H4(+M)<=>H2+C2H2(+M)                         8.00E+12    0.44    86770.0
     Low pressure limit:  0.15800E+52 -0.93000E+01  0.97800E+05
     TROE centering:      0.73450E+00  0.18000E+03  0.10350E+04  0.54170E+04
        H2               Enhanced by    2.000E+00
        H2O              Enhanced by    6.000E+00
        CH4              Enhanced by    2.000E+00
        CO               Enhanced by    1.500E+00
        CO2              Enhanced by    2.000E+00
        C2H6             Enhanced by    3.000E+00
        AR               Enhanced by    7.000E-01
347. C2H5+O2<=>HO2+C2H4                             8.40E+11    0.00     3875.0
348. HCCO+O2<=>OH+2CO                               3.20E+12    0.00      854.0
349. 2HCCO<=>2CO+C2H2                               1.00E+13    0.00        0.0
350. NNH<=>N2+H                                     3.30E+08    0.00        0.0
351. NNH+O2<=>HO2+N2                                5.00E+12    0.00        0.0
352. NNH+O<=>OH+N2                                  2.50E+13    0.00        0.0
353. NNH+O<=>NH+NO                                  7.00E+13    0.00        0.0
354. NNH+CH3<=>CH4+N2                               2.50E+13    0.00        0.0
355. H2CN+N<=>N2+CH2                                6.00E+13    0.00      400.0
356. C+N2<=>CN+N                                    6.30E+13    0.00    46020.0
357. CH+N2(+M)<=>HCNN(+M)                           3.10E+12    0.15        0.0
     Low pressure limit:  0.13000E+26 -0.31600E+01  0.74000E+03
     TROE centering:      0.66700E+00  0.23500E+03  0.21170E+04  0.45360E+04
        H2               Enhanced by    2.000E+00
        H2O              Enhanced by    6.000E+00
        CH4              Enhanced by    2.000E+00
        CO               Enhanced by    1.500E+00
        CO2              Enhanced by    2.000E+00
        C2H6             Enhanced by    3.000E+00
        AR               Enhanced by    1.000E+00
358. CH2+N2<=>HCN+NH                                1.00E+13    0.00    74000.0
359. CH2(S)+N2<=>NH+HCN                             1.00E+11    0.00    65000.0
360. C+NO<=>CN+O                                    1.90E+13    0.00        0.0
361. C+NO<=>CO+N                                    2.90E+13    0.00        0.0
362. CH+NO<=>HCN+O                                  4.10E+13    0.00        0.0
363. CH+NO<=>H+NCO                                  1.62E+13    0.00        0.0
364. CH+NO<=>N+HCO                                  2.46E+13    0.00        0.0
365. CH2+NO<=>H+HNCO                                3.10E+17   -1.38     1270.0
366. CH2+NO<=>H+HCNO                                3.80E+13   -0.36      580.0
367. CH2(S)+NO<=>H+HNCO                             3.10E+17   -1.38     1270.0
368. CH2(S)+NO<=>OH+HCN                             2.90E+14   -0.69      760.0
369. CH2(S)+NO<=>H+HCNO                             3.80E+13   -0.36      580.0
370. CH3+NO<=>HCN+H2O                               9.60E+13    0.00    28800.0
371. CH3+NO<=>H2CN+OH                               1.00E+12    0.00    21750.0
372. HCNN+O<=>CO+H+N2                               2.20E+13    0.00        0.0
373. HCNN+O<=>HCN+NO                                2.00E+12    0.00        0.0
374. HCNN+O2<=>O+HCO+N2                             1.20E+13    0.00        0.0
375. HCNN+OH<=>H+HCO+N2                             1.20E+13    0.00        0.0
376. HCNN+H<=>CH2+N2                                1.00E+14    0.00        0.0
377. HNCO+OH<=>NH2+CO2                              3.30E+06    1.50     3600.0
378. HCNO+H<=>H+HNCO                                2.10E+15   -0.69     2850.0
379. HCNO+H<=>NH2+CO                                1.70E+14   -0.75     2890.0
380. HCCO+NO<=>HCNO+CO                              9.00E+12    0.00        0.0
381. CH3+N<=>H2CN+H                                 6.10E+14   -0.31      290.0
382. CH3+N<=>HCN+H2                                 3.70E+12    0.15      -90.0
383. O+CH3=>H+H2+CO                                 3.37E+13    0.00        0.0
```

```
384. O+C2H4<=>H+CH2CHO                              6.70E+06    1.83      220.0
385. O+C2H5<=>H+CH3CHO                              1.10E+14    0.00        0.0
386. OH+CH3=>H2+CH2O                                8.00E+09    0.50    -1755.0
387. CH+H2(+M)<=>CH3(+M)                            1.97E+12    0.43     -370.0
     Low pressure limit:  0.48200E+26 -0.28000E+01  0.59000E+03
     TROE centering:      0.57800E+00  0.12200E+03  0.25350E+04  0.93650E+04
        H2               Enhanced by    2.000E+00
        H2O              Enhanced by    6.000E+00
        CH4              Enhanced by    2.000E+00
        CO               Enhanced by    1.500E+00
        CO2              Enhanced by    2.000E+00
        C2H6             Enhanced by    3.000E+00
        AR               Enhanced by    7.000E-01
388. CH2+O2=>2H+CO2                                 5.80E+12    0.00     1500.0
389. CH2+O2<=>O+CH2O                                2.40E+12    0.00     1500.0
390. CH2+CH2=>2H+C2H2                               2.00E+14    0.00    10989.0
391. CH2(S)+H2O=>H2+CH2O                            6.82E+10    0.25     -935.0
392. C2H3+O2<=>O+CH2CHO                             3.03E+11    0.29       11.0
393. C2H3+O2<=>HO2+C2H2                             1.34E+06    1.61     -384.0
394. O+CH3CHO<=>OH+CH2CHO                           2.92E+12    0.00     1808.0
395. O+CH3CHO=>OH+CH3+CO                            2.92E+12    0.00     1808.0
396. O2+CH3CHO=>HO2+CH3+CO                          3.01E+13    0.00    39150.0
397. H+CH3CHO<=>CH2CHO+H2                           2.05E+09    1.16     2405.0
398. H+CH3CHO=>CH3+H2+CO                            2.05E+09    1.16     2405.0
399. OH+CH3CHO=>CH3+H2O+CO                          2.34E+10    0.73    -1113.0
400. HO2+CH3CHO=>CH3+H2O2+CO                        3.01E+12    0.00    11923.0
401. CH3+CH3CHO=>CH3+CH4+CO                         2.72E+06    1.77     5920.0
402. H+CH2CO(+M)<=>CH2CHO(+M)                       4.87E+11    0.42    -1755.0
     Low pressure limit:  0.10120E+43 -0.76300E+01  0.38540E+04
     TROE centering:      0.46500E+00  0.20100E+03  0.17730E+04  0.53330E+04
        H2               Enhanced by    2.000E+00
        H2O              Enhanced by    6.000E+00
        CH4              Enhanced by    2.000E+00
        CO               Enhanced by    1.500E+00
        CO2              Enhanced by    2.000E+00
        C2H6             Enhanced by    3.000E+00
        AR               Enhanced by    7.000E-01
403. O+CH2CHO=>H+CH2+CO2                            1.50E+14    0.00        0.0
404. O2+CH2CHO=>OH+CO+CH2O                          1.81E+10    0.00        0.0
405. O2+CH2CHO=>OH+2HCO                             2.35E+10    0.00        0.0
406. H+CH2CHO<=>CH3+HCO                             2.20E+13    0.00        0.0
407. H+CH2CHO<=>CH2CO+H2                            1.10E+13    0.00        0.0
408. OH+CH2CHO<=>H2O+CH2CO                          1.20E+13    0.00        0.0
409. OH+CH2CHO<=>HCO+CH2OH                          3.01E+13    0.00        0.0
410. CH3+C2H5(+M)<=>C3H8(+M)                        9.43E+12    0.00        0.0
     Low pressure limit:  0.27100E+75 -0.16820E+02  0.13065E+05
     TROE centering:      0.15270E+00  0.29100E+03  0.27420E+04  0.77480E+04
        H2               Enhanced by    2.000E+00
        H2O              Enhanced by    6.000E+00
        CH4              Enhanced by    2.000E+00
        CO               Enhanced by    1.500E+00
        CO2              Enhanced by    2.000E+00
        C2H6             Enhanced by    3.000E+00
        AR               Enhanced by    7.000E-01
411. O+C3H8<=>OH+C3H7                               1.93E+05    2.68     3716.0
412. H+C3H8<=>C3H7+H2                               1.32E+06    2.54     6756.0
413. OH+C3H8<=>C3H7+H2O                             3.16E+07    1.80      934.0
414. C3H7+H2O2<=>HO2+C3H8                           3.78E+02    2.72     1500.0
415. CH3+C3H8<=>C3H7+CH4                            9.03E-01    3.65     7154.0
416. CH3+C2H4(+M)<=>C3H7(+M)                        2.55E+06    1.60     5700.0
     Low pressure limit:  0.30000E+64 -0.14600E+02  0.18170E+05
     TROE centering:      0.18940E+00  0.27700E+03  0.87480E+04  0.78910E+04
        H2               Enhanced by    2.000E+00
        H2O              Enhanced by    6.000E+00
        CH4              Enhanced by    2.000E+00
        CO               Enhanced by    1.500E+00
        CO2              Enhanced by    2.000E+00
        C2H6             Enhanced by    3.000E+00
        AR               Enhanced by    7.000E-01
417. O+C3H7<=>C2H5+CH2O                             9.64E+13    0.00        0.0
418. H+C3H7(+M)<=>C3H8(+M)                          3.61E+13    0.00        0.0
```

```
     Low pressure limit:  0.44200E+62 -0.13545E+02  0.11357E+05
     TROE centering:      0.31500E+00  0.36900E+03  0.32850E+04  0.66670E+04
        H2               Enhanced by    2.000E+00
        H2O              Enhanced by    6.000E+00
        CH4              Enhanced by    2.000E+00
        CO               Enhanced by    1.500E+00
        CO2              Enhanced by    2.000E+00
        C2H6             Enhanced by    3.000E+00
        AR               Enhanced by    7.000E-01
419. H+C3H7<=>CH3+C2H5                              4.06E+06     2.19      890.0
420. OH+C3H7<=>C2H5+CH2OH                           2.41E+13     0.00        0.0
421. HO2+C3H7<=>O2+C3H8                             2.55E+10     0.26     -943.0
422. HO2+C3H7=>OH+C2H5+CH2O                         2.41E+13     0.00        0.0
423. CH3+C3H7<=>2C2H5                               1.93E+13    -0.32        0.0
424. H+O2+H2O<=>HO2+H2O                             1.13E+19    -0.76        0.0
425. H+O2+N2<=>HO2+N2                               2.60E+19    -1.24        0.0
426. H+O2+AR<=>HO2+AR                               7.00E+17    -0.80        0.0
427. BTTN=>2NO2+3CH2O+HCO+NO                        5.00E+16     0.00    40000.0
428. BTTN=>3CH2O+NO2+NO+CO+HONO                     5.00E+16     0.00    40000.0
429. N2+M=N+N+M                                     3.71E+21    -1.60   225000.0
430. NO2+NO3=NO+NO2+O2                              1.40E+11     0.00     3180.0
431. H2+O2=2OH                                      1.70E+13     0.00    47780.0
432. N2O+H=N2+OH                                    2.53E+10     0.00     4550.0
     Declared duplicate reaction...
433. N2O+H=N2+OH                                    2.23E+14     0.00    16750.0
     Declared duplicate reaction...
434. NH2+NH=N2H2+H                                  1.50E+15    -0.50        0.0
435. NH2+NH2=N2H2+H2                                5.00E+11     0.00        0.0
436. NH2+NH2=N2H3+H                                 1.79E+13    -0.35    11320.0
437. NH2+NH2+M=N2H4+M                               2.98E+47    -9.44     9680.0
438. N2H4+H=N2H3+H2                                 1.00E+12     0.50     2000.0
439. N2H4+OH=N2H3+H2O                               3.00E+10     0.68     1290.0
440. N2H4+O=N2H3+OH                                 2.00E+13     0.00     1000.0
441. N2H3=N2H2+H                                    1.20E+13     0.00    58000.0
442. N2H3+H=N2H2+H2                                 1.00E+12     0.50     2000.0
443. N2H3+OH=N2H2+H2O                               3.00E+10     0.68     1290.0
444. N2H3+O=N2H2+OH                                 2.00E+13     0.00     1000.0
445. N2H2+M=NNH+H+M                                 5.00E+16     0.00    50000.0
        H2O              Enhanced by    1.500E+01
        O2               Enhanced by    2.000E+00
        N2               Enhanced by    2.000E+00
        H2               Enhanced by    2.000E+00
446. N2H2+H=NNH+H2                                  5.00E+13     0.00     1000.0
447. N2H2+O=NH2+NO                                  1.00E+13     0.00        0.0
448. N2H2+O=NNH+OH                                  2.00E+13     0.00     1000.0
449. N2H2+OH=NNH+H2O                                1.00E+13     0.00     1000.0
450. N2H2+NH=NNH+NH2                                1.00E+13     0.00     1000.0
451. N2H2+NH2=NH3+NNH                               1.00E+13     0.00     1000.0
452. N2O+NO=N2+NO2                                  4.29E+13     0.00    47130.0
453. NO+NO+NO=N2O+NO2                               1.07E+10     0.00    26800.0
454. HOCO+M=OH+CO+M                                 2.19E+23    -1.89    35270.0
455. CH+NO2=HCO+NO                                  1.01E+14     0.00        0.0
456. NNH=N2+H                                       3.00E+08     0.00        0.0
457. HNO+NO+NO=HNNO+NO2                             1.70E+11     0.00     2100.0
458. HNNO+NO=NNH+NO2                                3.20E+12     0.00      270.0
459. HNNO+NO=N2+HONO                                2.60E+11     0.00      810.0
460. HNNO+M=H+N2O+M                                 2.20E+15     0.00    21600.0
461. HNNO+M=N2+OH+M                                 1.00E+15     0.00    25600.0
462. H+HCO(+M)<=>CH2O(+M)                           1.09E+12     0.48     -260.0
     Low pressure limit:  0.13500E+25 -0.25700E+01  0.14250E+04
     TROE centering:      0.78240E+00  0.27100E+03  0.27550E+04  0.65700E+04
        H2               Enhanced by    2.000E+00
        H2O              Enhanced by    6.000E+00
        CO               Enhanced by    1.500E+00
        CO2              Enhanced by    2.000E+00
463. H2+CO(+M)<=>CH2O(+M)                           4.30E+07     1.50    79600.0
     Low pressure limit:  0.50700E+28 -0.34200E+01  0.84350E+05
     TROE centering:      0.93200E+00  0.19700E+03  0.15400E+04  0.10300E+05
        H2               Enhanced by    2.000E+00
        H2O              Enhanced by    6.000E+00
        CO               Enhanced by    1.500E+00
```

```
        CO2              Enhanced by    2.000E+00
464. HCO+HCO=CH2O+CO                                3.00E+13    0.00        0.0
465. HCO+HCO=H2+CO+CO                               5.20E+12    0.00        0.0
466. ADN(G)+M=>NH3+HN3O4+M                          3.00E+12    0.00    12040.0
467. HN3O4=HNNO2+NO2                                2.01E+48  -10.90    42214.0
468. HNNO2+M<=>N2O+OH+M                             7.53E+24   -2.90    25150.0
469. HNNO2+M<=>NH+NO2+M                             6.35E+18   -1.10    39397.0
470. HNNO2+NO2<=>HNO+NO+NO2                         3.00E+12    0.00        0.0
471. HNNO2+OH<=>H2O+2NO                             5.00E+12    0.00        0.0
472. HNNO2+OH<=>HNO+HONO                            5.00E+12    0.00        0.0
473. NH2+NO2<=>H2NO+NO                              6.56E+16   -1.50      268.0
474. H2NO+H<=>HNO+H2                                3.00E+07    2.00     2000.0
475. H2NO+H<=>NH2+OH                                5.00E+13    0.00        0.0
476. H2NO+M<=>H2+NO+M                               7.83E+27   -4.30    60306.0
477. H2NO+M<=>HNO+H+M                               1.69E+32   -5.00    62312.0
478. H2NO+M<=>HNOH+M                                4.46E+30   -3.80    56888.0
479. H2NO+NH2<=>HNO+NH3                             3.00E+12    0.00     1000.0
480. H2NO+NO<=>HNO+HNO                              2.00E+07    2.00    13000.0
481. H2NO+NO2<=>HONO+HNO                            6.00E+11    0.00     2000.0
482. H2NO+O<=>HNO+OH                                3.00E+07    2.00     2000.0
483. H2NO+O<=>NH2+O2                                4.00E+13    0.00        0.0
484. HNNH+OH<=>H2O+N2+H                             2.50E+12    0.00        0.0
485. HNNO2+NH2<=>HNNH+HONO                          2.50E+12    0.00        0.0
486. HNNO2+NO<=>HNNO+NO2                            2.50E+12    0.00        0.0
487. HNNO2+NO<=>HONO+N2O                            2.50E+12    0.00        0.0
488. HNOH+M<=>H+HNO+M                               1.03E+04   -4.80    59527.0
489. HONO+H<=>HNO+OH                                5.64E+10    0.90     4969.0
490. HONO+H<=>NO+H2O                                8.13E+06    1.90     3846.0
491. HONO+HONO<=>NO+NO2+H2O                         9.69E+10    0.00    14132.0
492. HONO+NH<=>NH2+NO2                              1.00E+13    0.00        0.0
493. N2H2+NO<=>N2O+NH2                              3.00E+12    0.00        0.0
494. N2H3+M<=>N2H2+H+M                              3.50E+16    0.00    46000.0
495. N2H3+NH<=>N2H2+NH2                             2.00E+13    0.00        0.0
496. N2H3+O<=>NH2+HNO                               1.00E+13    0.00        0.0
497. N2H3+OH<=>NH3+HNO                              1.00E+12    0.00    15000.0
498. N2H4+NH2<=>N2H3+NH3                            3.90E+12    0.00     1500.0
499. N2H4+O<=>N2H2+H2O                              8.50E+13    0.00     1200.0
500. NH2+HO2<=>H2NO+OH                              2.50E+13    0.00        0.0
501. NH3+HNO3<=>H2NO+H2O+NO                         2.32E+01    3.50    44926.0
502. NNH<=>N2+H                                     1.00E+06    0.00        0.0
503. NO3+H<=>NO2+OH                                 6.00E+13    0.00        0.0
504. NO3+HO2<=>NO2+O2+OH                            1.50E+12    0.00        0.0
505. NO3+O<=>NO2+O2                                 1.00E+13    0.00        0.0
506. NO3+OH<=>NO2+HO2                               1.00E+13    0.00        0.0
507. HCO+HONO=CH2O+NO2                              2.39E-03    4.28     4370.0
508. HCO+HONO=H2O+CO+NO                             1.90E-08    6.12     9190.0
509. HCO+HNOH=HNO+CO+H2                             1.71E+03    2.27    -9424.0
510. HCO+HNOH=CH2O+HNO                              3.10E-01    3.52     -854.0
511. HCO+HNOH=H2NOH+CO                              2.15E+03    2.42    -8446.0
512. HCO+HNO=CH2O+NO                                5.83E-01    3.84      115.0
513. HCO+HNO=CO+H2NO                                4.89E+01    3.27     1754.5
514. HCO+HNO=HNOH+CO                                1.31E+13   -0.20     3646.0
515. C4H6+OH=2C2H2+H2+OH                            5.00E+12    0.68     1100.0
516. C4H6+CLO=2C2H2+CLOH+H                          5.00E+12    0.50     6400.0
517. C4H6+CL=2C2H2+HCL+H                            6.75E+12    0.50      100.0
518. C4H6=2C2H3                                     2.50E+18    0.00   100000.0
519. C4H6+H=C2H3+C2H2+H2                            2.30E+12    0.00    20000.0
520. C4H6+O=C2H4+CH2CO                              1.00E+12    0.00        0.0
521. NH3+NO2=NH2+HONO                               2.45E+11    0.00    25075.9
522. H2NO+OH=HNO+H2O                                2.00E+07    2.00     1000.0
523. NH2+OH+M=H2NOH+M                               5.00E+17    0.00        0.0
524. HNO3+OH=H2O+NO3                                1.03E+10    0.00    -1240.0
525. HCLO4(+M)=>OH+CLO3(+M)                         1.45E+17    0.00    52655.0
     Low pressure limit:  0.20400E+55 -0.10900E+02  0.58477E+05
526. OH+CLO3=>HCLO4                                 1.17E+60  -15.30    11012.0
527. OH+CLO3=HO2+CLO2                               1.26E+14    0.09       35.8
528. OH+CLO=HO2+CL                                  2.05E+11    0.30    -1440.6
529. OH+CLO=HCL+O2                                  3.52E+05    1.67    -3827.0
530. CLO3(+M)=>O+CLO2(+M)                           1.50E+20   -1.10    36481.3
     Low pressure limit:  0.37600E+26 -0.32800E+01  0.27599E+05
531. O+CLO2=>CLO3                                   2.41E+25   -6.16      800.8
```

```
532. O+CLO2=CLO+O2                                  5.23E+07    1.45      876.3
533. OH+CLO2=>HO2+CLO                               7.35E+01    2.75    -3342.1
534. OH+CLO2=CLOH+O2                                3.29E+04    2.07    -4101.2
535. OH+CLO2=HCLO3                                  3.01E+58  -22.36    19486.5
536. OH+CLO2(+M)=>HCLO3(+M)                         1.95E+13    0.28       35.8
     Low pressure limit:  0.10600E+36 -0.84200E+01  0.22850E+05
537. CLO+CLO(+M)=>CLOOCL(+M)                        9.64E+14   -0.67      127.2
     Low pressure limit:  0.30100E+29 -0.49600E+01  0.66760E+03
538. CLO+CLO(+M)=>CLOCLO(+M)                        3.85E+15   -0.78      151.0
     Low pressure limit:  0.62400E+34 -0.69900E+01  0.18400E+04
539. CLOOCL(+M)=>CLO+CLO(+M)                        6.30E+19   -1.32    19868.0
     Low pressure limit:  0.27900E+33 -0.52000E+01  0.20186E+05
540. CLOCLO(+M)=>CLO+CLO(+M)                        5.99E+20   -1.63    12863.8
     Low pressure limit:  0.41000E+31 -0.49000E+01  0.12892E+05
541. CLO+CLO=CL2+O2                                 6.56E+10    0.66     3759.4
542. CLO+CLO=CL+CLOO                                8.19E+10    0.77     4307.8
543. CLO+CLO=CLO2+CL                                3.77E+13    0.01     5754.4
544. CL+CLOOCL=CL2+CLOO                             9.21E+10    1.10     -234.5
     Declared duplicate reaction...
545. CL+CLOOCL=CL2+CLOO                             4.30E+12    0.86     4709.2
     Declared duplicate reaction...
546. CL+CLOOCL=CL2O+CLO                             1.32E+10    0.70     2205.6
547. HO2+CLO=CLOH+O2                                9.88E+13   -0.64     -212.6
     Declared duplicate reaction...
548. HO2+CLO=CLOH+O2                                7.83E+03    2.37     5110.6
     Declared duplicate reaction...
549. HO2+CLO=CLOH+O2                                8.37E+02    2.26     -449.1
     Declared duplicate reaction...
550. HO2+CLO=OH+CLOO                                4.58E+05    1.80     2116.2
551. HO2+CLO=>CLO2+OH                               1.34E+03    2.32     5098.6
552. HO2+CLO=HCL+O3                                 4.58E+03    2.05     1698.9
553. CLO+CLO2(+M)=CLOCLOO(+M)                       9.21E+14   -0.20      262.3
     Low pressure limit:  0.39900E+31 -0.55000E+01  0.79080E+03
554. CLO+CLO2=CLOO+CLO                              6.20E+01    2.76      155.0
555. CL+O2(+M)=>CLOO(+M)                            1.08E+14    0.00        0.0
     Low pressure limit:  0.45700E+32 -0.62200E+01  0.18737E+04
556. O+CLO(+M)=>CLO2(+M)                            2.61E+13   -0.03      -85.5
     Low pressure limit:  0.31200E+28 -0.41000E+01  0.83450E+03
557. CLO2(+M)=>CLO+O(+M)                            1.11E+16   -0.28    58749.6
     Low pressure limit:  0.98800E-23  0.11000E+02  0.33080E+05
558. O+CLO=CL+O2                                    2.48E+13   -0.06      -83.5
559. CLOO(+M)=>CL+O2(+M)                            4.87E+15   -0.59     5136.4
     Low pressure limit:  0.28100E+40 -0.41000E+00  0.37694E+04
560. CLO+CLO3=CLOO+CLO2                             1.11E+06    2.28     4802.6
561. CLO+CLO3=2CLO2                                 8.55E+05    2.11     5702.7
562. CL+NH3=NH2+HCL                                 5.49E+05    2.47     1442.6
563. CLO+NH3=NH2+CLOH                               1.13E+00    3.85     8631.5
564. CLO2+NH3=NH2+HCLO2                             8.91E+03    3.05    31110.5
565. CLO3+NH3=NH2+HCLO3                             8.19E+09    1.01     4480.7
566. CLO4+NH3=NH2+HCLO4                             5.08E+23   -3.02     1049.1
     Declared duplicate reaction...
567. CLO4+NH3=NH2+HCLO4                             1.41E+04    2.80    -8726.9
     Declared duplicate reaction...
568. CLO+NH2=HCL+HNO                                2.83E+16   -1.08      256.3
569. CLO+NH2=CL+H2NO                                1.02E+15   -0.62       47.7
570. CLO+NH2=CLOH+NH                                2.89E-05    5.11     2056.5
571. HCLO3(+M)=>CLO2+OH(+M)                         4.07E+21   -1.62    34540.0
     Low pressure limit:  0.75900E+41 -0.76000E+01  0.35245E+05
572. H+HCLO4=H2+CLO4                                8.85E+05    2.03    15815.0
573. H+HCLO4=OH+HCLO3                               2.00E+06    2.02    13667.0
574. CLO4(+M)=CLO3+O(+M)                            5.20E+20   -1.30    46128.2
     Low pressure limit:  0.95800E+47 -0.90000E+01  0.48216E+05
575. HO2+CLO2(+M)=HOOCLO2(+M)                       2.10E+14    0.00        0.0
     Low pressure limit:  0.52200E+49 -0.13100E+02  0.19130E+04
576. HO2+CLO2=HCLO2+O2                              6.02E-03    3.60     2098.0
577. CLO+NO=CL+NO2                                  3.12E+11    0.39     -761.0
578. CLNO2(+M)=CL+NO2(+M)                           1.65E+19   -1.00    33450.0
     Low pressure limit:  0.18900E+56 -0.12100E+02  0.41890E+05
579. CLO+NO2(+M)=>CLONO2(+M)                        1.39E+14    0.00        0.0
     Low pressure limit:  0.74000E+44 -0.10990E+02 -0.88450E+04
580. CLONO2(+M)=>CLO+NO2(+M)                        1.44E+23   -1.82    27175.0
```

```
     Low pressure limit:  0.79500E+15 -0.28000E+00  0.98300E+04
581. CL+NH2=HCL+NH                                  8.23E+10    0.90    -1671.1
582. CLO2+NH2=CLOH+HNO                              2.14E-01    2.98    -1746.6
583. CLO2+NH2=CLO+H2NO                              1.70E+03    2.55    -1478.3
584. CLO3+NH2=HCLO2+HNO                             3.48E+07    1.01    -1250.0
585. CLO3+NH2=CLO2+H2NO                             5.96E+15   -0.47       47.7
586. CLO4+NH2=CLO3+H2NO                             8.90E+17   -1.11     1260.0
587. NO+NO=N2+O2                                    5.00E+20    0.00    75506.0
588. NOCL+M=CL+NO+M                                 2.00E+17    0.00    37700.0
589. CL2+NO=CL+NOCL                                 2.70E+12    0.00    19900.0
590. CLOH+HNO=H2O+NOCL                              3.00E+12    0.00        0.0
591. CLO+NOCL=CL2+NO2                               1.50E+12    0.00        0.0
592. OH+HCL=H2O+CL                                  1.08E+12    0.00      477.0
593. CL+H2=HCL+H                                    2.35E+13    0.00     4590.0
594. CL+H2O2=HCL+HO2                                6.62E+12    0.00     1947.0
595. CL+HO2=HCL+O2                                  2.47E+13    0.00      894.0
596. CLOH+O=HCL+O2                                  1.20E+14    0.00        0.0
597. CLOH+HCL=CL2+H2O                               4.00E+12    0.00    10000.0
598. CL2+H=HCL+CL                                   8.40E+13    0.00     1150.0
599. HCL+O=CL+OH                                    2.30E+11    0.64      900.0
600. HCN=HNC                                        2.06E+14   -1.11    43700.0
601. HCN(+M)=H+CN(+M)                               8.30E+17   -0.93   124000.0
     Low pressure limit:  0.35700E+27 -0.26000E+01  0.12490E+06
     TROE centering:      0.95700E+00  0.10000E-89  0.83320E+04
602. HCN+CN=C2N2+H                                  1.21E+07    1.71     1530.0
603. H2CN+M=HCN+H+M                                 5.30E+16    0.00    29000.0
604. CN+H2=H+HCN                                    5.50E+02    3.18     -223.0
605. CN+CH2O=HCN+HCO                                4.22E+13    0.00        0.0
606. CH+N2<=>HCN+N                                  3.12E+09    0.88    20100.0
607. HCN+O=NCO+H                                    1.38E+04    2.64     4980.0
608. HCN+O=NH+CO                                    3.45E+03    2.64     4980.0
609. HCN+O=CN+OH                                    2.70E+09    1.58    29200.0
610. HCN+OH=H2O+CN                                  3.90E+06    1.83    10300.0
611. CH2+NO<=>OH+HCN                                2.90E+14   -0.69      760.0
612. HCNO+H<=>OH+HCN                                2.70E+11    0.18     2120.0
613. HCN=>H+CN                                      1.60E+06    0.00        0.0

 NOTE:  A units mole-cm-sec-K, E units cal/mole
```

Appendix C. JANAF Aluminum Properties

The following are the inert aluminum properties, converted from the JANAF tables, which have been used in PHASE3 and the diffusion flame model. CHEMKIN formatting is used. A condensed-phase species, AL(C), and a gas-phase species, AL(S), have been defined and both have been given the properties of solid and liquid aluminum, depending on the temperature. A condensed-phase reaction has been created in the model to convert the condensed-phase species to the gas-phase species. The files *thermo.dat* and *transport.dat* contain the thermodynamic and transport properties of the gas-phase species. These files are used in PHASE3 and the diffusion flame model. The files *fort.27* and *aphtpbc.mch* contain the thermophysical properties of the condensed-phase species and the condensed-phase mechanism. These files are only used in PHASE3.

thermo.dat

```
AL(S)              50708AL  1               S  0300.00   5000.00  0933.45      1
 3.81876324E+00 0.00000000E+00 0.00000000E+00 0.00000000E+00 0.00000000E+00    2
-1.13683371E+02-1.75511564E+01 2.50644296E+00 1.32844498E-03 2.12129517E-07    3
 0.00000000E+00 0.00000000E+00-8.07618299E+02-1.12833375E+01                   4
```

transport.dat

```
AL(S)              0  2750.000     2.655     0.000     0.000     0.000
```

fort.27

```
AL(C)
 2      26.98           0.00                                        ! # CP FITS, MW, HF298
        1.4409E-1       1.5798E-4       2.5583E+0       9.3345E+2  ! CP1     [CAL/G K]
        2.8107E-1       0.0000E+0       0.0000E+0       2.7908E+3  ! CP2     [CAL/G K]
        2.7745E+0      -2.3555E-4       0.0000E+0                  ! RHO     [G/CM3]
        6.5096E-1      -1.6184E-4       0.0000E+0                  ! K       [CAL/CM S K]
```

aphtpbc.mch

```
AL(C)=>AL(S)                                    1.00E+10 0.00 0.00E+00
```

Appendix D. AP/Al/HTPB Condensed-Phase Correlations

The following are the condensed-phase correlations used in the two-dimensional AP/Al/HTPB diffusion flame calculations. Burning rate and surface temperature are functions of the heat flux to the surface. Species mass fractions are constant for all heat fluxes.

100% AP

```
1.0          * mass fraction oxidizer in ingredient
1.756   * density of ingredient (g/cm^3)
4.94414E-03   2.51608E-04   0.000000000   * rb = a + bx + cx^2
7.66761E+02   5.31216E-03   0.000000000   * Ts = a + bx + cx^2
12           * number of inlet species mass fractions
3.69503E-02   'O2'
1.54293E-03   'OH'
2.95769E-02   'H2O'
2.23600E-02   'N2O'
2.81363E-04   'HNO'
1.27439E-01   'NH3'
2.08684E-04   'NO2'
7.57079E-03   'CLO3'
1.60817E-04   'CL'
3.30908E-02   'HCL'
7.33409E-01   'HCLO4'
7.41000E-03   'CL2'
```

40.87% AP, 31.26% Al, 27.87% HTPB

```
0.4087 * fraction oxidizer
1.572   * density of ingredient
```

```
9.15892E-04   2.77500E-04   -5.7773E-09    * rb = a + bx + cx^2
7.96317E+02  3.71022E-02   3.54275E-06   * Ts = a + bx + cx^2
17                   * # of inlet mass fractions
4.19822E-02     'C2H2'
1.32460E-01     'C4H6'
3.16352E-03     'CH4'
1.20433E-02     'CO'
2.70107E-03     'CL'
1.80071E-03     'CL2'
6.35792E-03     'CLO3'
1.49517E-02     'H2'
5.94767E-03     'H2O'
9.25954E-04     'HCL'
3.26496E-01     'HCLO4'
5.66480E-02     'NH3'
5.68844E-03     'O2'
5.08525E-04     'OH'
2.13427E-03     'N2'
7.35906E-02     'C(S)'
3.12600E-01     'AL(S)'
```